# Crystallographic analysis of hydride phase transformation and its effect on mechanical property of commercial pure titanium

Qian Wang

UNIVERSITÉ DE LORRAINE

# DISSERTATION

**Presented at**
**Université de Lorraine**

**Qian WANG**

**To obtain the doctor's degree of**
**University of Lorraine**

SPECIAL FIELD: Engineering Sciences
OPTION: Materials Science

# Crystallographic analysis of hydride phase transformation and its effect on mechanical property of commercial pure titanium

**Defended on 26th February, 2021 in front of the jury:**

| | | | |
|---|---|---|---|
| Jian WANG | Professor | University of Nebraska-Lincoln, USA | Reviewer / President |
| Salima BOUVIER | Professor | Université de Technologie de Compiègne, France | Reviewer |
| Eric FLEURY | Professor | Université de Lorraine, France | Examiner |
| Eglé CONFORTO | Doctor | Université de La Rochelle, France | Examiner |
| Christophe SCHUMAN | Doctor HDR | Université de Lorraine, France | Director |
| Jean-Sébastien LECOMTE | Doctor HDR | Université de Lorraine, France | Director |

Laboratoire d'Étude des Microstructures et de Mécanique des Matériaux, LEM3
7 rue Félix Savart, 57070 Metz, France

# Contents

# Acknowledgements

The present work is accomplished at the Laboratoire d'Étude des Microstructures et de Mécanique des Matériaux (LEM3), Université de Lorraine, Metz, France. I would like to give my sincere thanks to this laboratory for offering me opportunity to use the advanced equipment and giving me their kind help. I gratefully acknowledge the China Scholarship Council (CSC) for providing a Ph. D. scholarship to support my study in France.

Then I would like to express my deepest and sincere gratitude to my supervisor Dr. Christophe SCHUMAN and co-supervisor Dr. Jean-Sébastien LECOMTE. They are always very patient with me and put me in the first. Due to my poor french, they taught me a lot about how to use equipment and help me do plenty of deformation tests. We have discussed so much about my experiments. Many excellent ideas and methods were suggested in my work. I am so grateful to meet such kind supervisors. I am also deeply indebted to Prof. Eric FLEURY for the loan of the hydrogen charging device. He gave me friendly help on the hydrogen charging experiments. I am also grateful to Dr. Yudong ZHANG for fruitful discussions about crystal calculation. Her optimistic attitude, critical thinking and rigorous working style encourage me a lot. I would like to thank my master supervisor Prof. Xiang ZHAO of Northeastern University for giving my opportunity to further my study in French.

I greatly thank Prof. Yajun ZHAO and Prof. Shun XU, they help me a lot on my research work and give me many fruitful guidance. I also would like to thank Mr. Patrick Moll for helping me to do deformation tests and Mr. Laurent Peltier for carrying out heat treatment. I also would like to express my thanks to Mr. Jérôme SLOWENSKY, Ms. Auriane MANDRELLI, Ms. Jacqueline DECKER, Ms. Nathalie KASPRZAK, Ms. Anne-Martine BLUM, Ms Aurore HANSON, Ms. Laura Litscher and Ms. Arlette JACQUIERRE at LEM3, France for their technical and administrative help and support to my Ph. D. work. I am also grateful to all the other staffs and students in LEM3. I greatly thank my friends, Prof. Ke HUA, Prof. Chi ZHANG, Prof. Lizhao DAI, Dr. Meishuai LIU, Dr. Xiaomeng LIU, Dr. Chunyang ZHANG, Dr. Yanfeng YANG, Dr. Jianchang ZHU, Ms. Fengming QIANG, Ms. Tian ZHANG, Ms. Pengru ZHAO, Ms. Jing WEN, Mr. Hailong SHI, Mr. Wenqing CHENG and Mr. Zhengtian YANG, who shared their experiences with me and offered help to my study.

Finally, I would give my hearted thanks to my families, especially to my mother, for their patience, encouragement and support.

# Abstract

Nucleation and formation of hydride precipitates are important factors on limiting the lifetime of Ti alloys. In this work, the hydride phase transformation in commercial pure titanium is thoroughly investigated by experimental and theoretically crystallographic method.

The two dominant orientation relationships (ORs) of hydride transformation by the method of electrolytic hydrogen charging are $\{0001\}//\{001\}$ $<1\bar{2}10>//<110>$ with interface plane of $\{10\bar{1}0\}//\{1\bar{1}0\}$ (OR1) and $\{0001\}//\{1\bar{1}1\}$ $<1\bar{2}10>//<110>$ with interface plane of $\{10\bar{1}3\}//\{1\bar{1}0\}$ (OR2). The grain orientations of $\{10\bar{1}0\}$ or $\{10\bar{1}3\}$ interface planes parallel to the diffusion surface are most favorable for OR1 and OR2 hydride transition, respectively. The hydride variants with interface plane parallel to the diffusion surface is preferentially selected because of the highest capacity for strain accommodation. The *c*-axis or *a*-axis parallel to the diffusion direction are unfavorable orientations, due to the complicated interactions between different hydride variants.

The multi-dimensional microstructures of hydride layer were characterized to investigate the accommodation mechanisms for hydride transformation. Plastic accommodation behaviors are necessary inside hydride layer. Both $\{10\bar{1}2\}$ extension and $\{11\bar{2}2\}$ contraction twins are induced at the interface of OR2 hydride platelets. The selected twin variant has the highest accommodation capacity for local distortion of hydride nucleation. The $\{10\bar{1}2\}$ twins are transformed into $\{10\bar{1}1\}$ twins in order to the further growth of hydride platelet. Hydride microstructure on the cross section of hydride layer were observed for the first time, the interactions of different hydride variants relax the anisotropic misfit strain inside hydride layer. The intergranular hydride pair is another accommodation behavior during hydrogenation, which prefer to be formed at the grain boundary with both low angle ($< 30^{o}$) and high angle ($75^{o} < \theta c < 85^{o}$) boundaries.

The mechanical property of titanium surface changed by hydrogen charging was investigated by nanoindentation tests and tensile deformation tests. After hydrogenation, the nanohardness increases while elastic modulus decreases due to the formation of hydride precipitation. The orientation dependent hardness of δ-hydride formed after 168 h charging is less sensitive than that of α-Ti. The average $H_{IT}$ value of δ-hydride is 3.8 ± 0.3 GPa, which is higher than titanium matrix (2.8 ± 0.3 GPa) showing the hard nature of hydride phase. During tensile deformation, hydride layer shows a poor deformability, but the interactions between dislocations and twins occur for

OR2 hydride platelets: the transmissions of prismatic slips into hydride precipitations and the hindering of hydrides on the growth and thickening of $\{10\bar{1}2\}$ tension twins.

***Keywords:*** Titanium; Hydride; Variant selection; Accommodation; Mechanical property;

# Résumé

La nucléation et la formation d'hydrures jouent un rôle important sur la durée de vie des alliages de Ti. Dans ce travail, la transformation d'hydrure en fonction de l'orientation cristalline dans le titane commercial pur est étudiée expérimentalement et théoriquement.

Les deux relations d'orientation dominantes (OR) de la transformation des hydrures obtenus par une méthode de chargement électrolytique de l'hydrogène sont {0001} // {001} <1$\bar{2}$10> // <110> avec le plan d'interface (OR1) et {0001} // {1$\bar{1}$1} <1$\bar{2}$10> // <110> avec le plan d'interface de {10$\bar{1}$3} // {1$\bar{1}$0} (OR2). Les orientations des grains avec des plans d'interface {10$\bar{1}$0} ou {10$\bar{1}$3} parallèles à la surface de diffusion sont les plus favorables à la formation des hydrures ayant les OR1 et OR2, respectivement. Les variants d'hydrure avec un plan d'interface parallèle à la surface de diffusion sont choisis préférentiellement en raison de leur plus grande capacité d'adaptation à la déformation. L'axe c ou l'axe a parallèle à la direction de diffusion sont des orientations défavorables, en raison des interactions complexes entre les différents variants des hydrures.

Les microstructures de la couche d'hydrure ont été caractérisées afin d'étudier les mécanismes d'accommodation lors de la transformation des hydrures. Des mécanismes d'accommodation plastique sont nécessaires à l'intérieur de la couche d'hydrure. Des macles d'extension {10$\bar{1}$2} et de contraction {11$\bar{2}$2} sont induits à l'interface des platelets d'hydrure OR2. Le variant de macle sélectionnée a la plus grande capacité d'accommodation de la distorsion locale lors de la nucléation des hydrures. Les macles {10$\bar{1}$2} sont transformées en macles {10$\bar{1}$1} afin de poursuivre la croissance des platelets d'hydrure. La microstructure des hydrures dans la section transversale de la couche d'hydrure a été observée. Les interactions des différentes variants d'hydrure relaxent la déformation anisotrope à l'intérieur de la couche. La paire d'hydrures intergranulaires est un autre comportement d'accommodation pendant l'hydrogénation. Ce mécanisme se forme sur des joints à faible désorientation ($< 30^o$) et à forte désorientation ($75^o < \theta c < 85^o$).

Les propriétés mécaniques de la surface du titane modifiée par le chargement en hydrogène a été étudiée par nanoindentation et en traction. Après l'hydrogénation, la dureté augmente tandis que le module élastique diminue en raison de la formation d'hydrures. La dureté dépendant de l'orientation de l'hydrure δ- formé après 168 h de charge est moins sensible que celle de α-Ti. La valeur HIT moyenne de l'hydrure δ est de 3.8 ± 0.3 GPa, ce qui est supérieur à la matrice de titane (2.8 ± 0.3 GPa). L'hydrure est plus dur que la matrice. En traction, la couche d'hydrure est peu

déformable. Des interactions entre les dislocations et les macles se produisent pour les platelets OR2. On observe que du glissement prismatique traverse les hydrures et que les hydrures limitent la croissance et l'élargissement des macles de tension $\{10\bar{1}2\}$.

**Mots-clés:** Titane ; Hydrure ; Sélection de variant ; Accommodation ; Propriétés mécanique

# List of abbreviation

| | |
|---|---|
| B <***a***> | Basal <***a***> slip |
| $C_i^I$ | $\{11\bar{2}2\}<11\bar{2}\bar{3}>$ compression twin |
| $C_i^{II}$ | $\{10\bar{1}1\}<10\bar{1}\bar{2}>$ compression twin |
| $C_i^{III}$ | $\{11\bar{2}4\}<\bar{2}\bar{2}43>$ compression twin |
| CRSS | Critical resolved shear stress |
| CP-Ti | Commercial pure titanium |
| DGA | Displacement gradient accommodation |
| EBSD | Electron backscatter diffraction |
| $E^*$ | Plane strain modulus |
| FCC | Face-centered cubic |
| FCT | Face-centered tetragonal |
| FSD | Forescatter diodes |
| GB | Grain boundary |
| GMM | Gaussian mixture model |
| GSF | generalized Schmid factor |
| HCP | Hexagonal closed packed |
| $H_{IT}$ | Indentation hardness |
| HPN | Twin habit plane |
| IGMA | Intragranular misorientation axis |
| IPF | Inverse pole figure |
| MVC | Micro-void coalescence |
| ND | Normal direction |
| NDD | Nucleation via dislocation dissociation |
| OR | Orientation relationship |
| OR1 ($P_i$) | $\{0001\}$ //$\{001\}$ $<1\bar{2}10>$//<110> interface plane $\{10\bar{1}0\}$//$\{1\bar{1}0\}$ |
| OR2 ($B_i$) | $\{0001\}$//$\{1\bar{1}1\}$ $<1\bar{2}10>$//<110> interface plane $\{10\bar{1}3\}$//$\{1\bar{1}0\}$ |
| OR3 | $\{10\bar{1}0\}$//$\{1\bar{1}\bar{1}\}$, $<1\bar{2}10>$//<110> interface plane $\{0001\}$//$\{1\bar{1}2\}$ |
| OR4 | $\{\bar{1}011\}$//$\{001\}$, $<1\bar{2}10>$//<110> interface plane $\{10\bar{1}1\}$//$\{1\bar{1}\bar{1}\}$ |
| P <***a***> | Prismatic <***a***> slip |
| RD | Rolling direction |

| | |
|---|---|
| SD | Twinning shear direction |
| SEM | Scanning electron microscopy |
| SF | Schmid factor |
| SPN | Normal of twinning shear plane |
| $T_i^I$ | $\{10\bar{1}2\}\langle\bar{1}011\rangle$ tension twin |
| $T_i^{II}$ | $\{11\bar{2}1\}\langle\bar{1}\bar{1}26\rangle$ tension twin |
| TD | Transverse direction |
| TE | Total elongation |
| TEM | Transmission electron microscopy |

# Chapter 1 Literature review

**Contents**



## 1.1 Hexagonal closed packed structure

The hexagonal closed packed (HCP) crystal structure is a common close packed structure, shown in Fig.1.1. The hexagonal structure of alternating layers is shifted, so its atoms are aligned to the gaps of the adjacent layer. The closest arrangement of atoms in an atom plane forms a regular hexagon around a central atom. The middle layer has three atoms nestle in the triangular "grooves" of the top and bottom plane. The lattice parameters for the hexagonal system can be presented by $\{a, a, c, 90°, 90°, 120°\}$. In an ideal hexagonal close-packed structure, the axial ratio $\gamma = c/a$ is equal to $\sqrt{8/3} \approx 1.633$.

The HCP structure is very common for elemental metals and some examples include Zirconium, Titanium, Magnesium, Zinc, etc. They have a lot of industry applications. Due to high specific strength, high corrosion resistance and high biocompatibility, titanium alloys are widely used in aerospace, marine, chemical engineering and biomedicine industries. Zirconium alloys are famous in the nuclear industry because of high resistance to waterside corrosion and a low absorption cross

section for thermal neutrons; Magnesium alloys are widely used in automobile, aerospace, and computer industries due to their low density, desirable mechanical property and thermal conductivity. The main uses of zinc alloys are galvanizing steel for corrosion protection and die castings owning to their lower melting point. The mechanical properties of these material (hardness, strength, ductility, etc.) are sensitive to different material microstructures (grain size, morphology, orientation, alloy content, etc.) and working conditions (strain rate, temperature, stress level, etc.). The improvement of mechanical property is an ongoing and long-term issue.

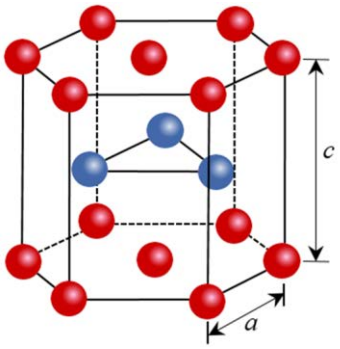


| HCP | Axial ratio *c*/*a* |
|---|---|
| Ti | 1.586 |
| Zr | 1.594 |
| Mg | 1.626 |
| Zn | 1.856 |

**Fig. 1.1** Schematic of a reduced sphere unit cell of HCP structure.

### 1.1.1 Deformation modes

#### 1.1.1.1 Slip

There are five common slip modes in HCP structure materials, as shown in Table 1.1. The corresponding Taylor axes are obtained from the reference [1]. The limited slip systems have a large difference in their critical resolved shear stress (CRSS) [2], thus yielding anisotropy is more severe in HCP structure metals than in cubic structure metals. The most common slip systems in HCP material at room temperature are basal <***a***> slip and prismatic <***a***> slip [2,3], see Fig. 1.2. Yoo and Wei [4] calculated the relative ease of gliding (CRSS value) by the method of anisotropic elasticity theory of dislocations, which explains the choice of prevailing slip systems in some HCP materials. The dominating prismatic <***a***> slip in Ti and Zr alloys, the basal <***a***> slip in Mg and the second-order pyramidal slip in Zn alloys always have lower CRSS. However, the lower CRSS is not the decisive factor for the selection of dominating deformation mode. The actual stimulation of slip system is governed by the combination of the Schmid factor (SF) and CRSS (i.e., activation stress=CRSS/SF) [5–7]. The SF is the ratio of the applied stress to the component of shear stress on the corresponding slip system [8], which is calculated by the angle relationship between the

loading direction and crystal orientation. Therefore, in addition to CRSS, both the loading direction and crystal orientation play important roles on the activation of different slip systems.

**Table 1.1** Slip mode of HCP structure and corresponding Taylor axes.

| Slip mode | Slip type | Notation | Variant number | Taylor axis |
|---|---|---|---|---|
| {0001} <1$\bar{2}$10> | Basal <***a***> | B <***a***> | 3 | <1$\bar{1}$00> |
| {10$\bar{1}$0} <1$\bar{2}$10> | Prismatic <***a***> | P <***a***> | 3 | <0001> |
| {10$\bar{1}$1} <1$\bar{2}$10> | Pyramidal <***a***> | $\pi_1$ <***a***> | 6 | <10$\bar{1}\bar{2}$> |
| {10$\bar{1}$1} <11$\bar{2}\bar{3}$> | Pyramidal-I <***c+a***> | $\pi_1$ <***c+a***> | 12 | <$\bar{8}$13$\bar{5}$3> |
| {11$\bar{2}$2} <11$\bar{2}\bar{3}$> | Pyramidal-II <***c+a*** > | $\pi_2$ <***c+a***> | 6 | <$\bar{1}$100> |

Normally, the initial yield of HCP material is attributed to slip modes. A huge amount of work has been done on the effect of slip on strain accommodation and deformation texture evolution. Many methods were proposed to accurately identify the active slip systems. By transmission electron microscopy (TEM) technique, both the type (screw, edge or mixed) and the Burgers vector, ***b***, can be determined via the simple $\boldsymbol{g}\cdot\boldsymbol{b} = 0$ invisibility criterion [9], where ***g*** is diffraction vector. The in situ TEM is uniquely capable to investigate complex dislocation reactions, while only a few grains can be processed using this method because of the complexity of sample preparation and small sample volume.

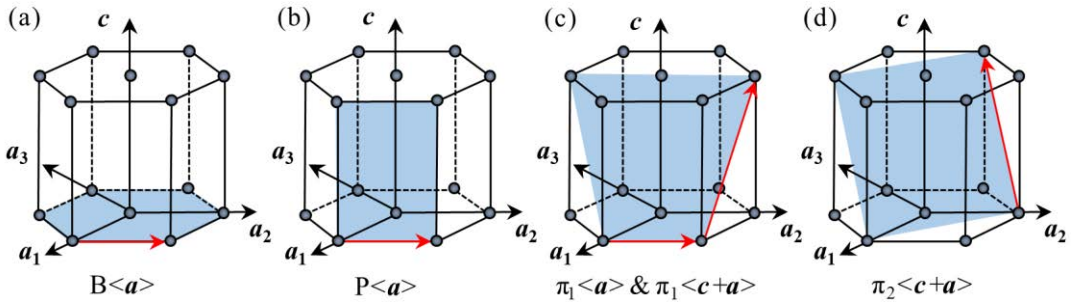


**Fig. 1.2** Main slip systems in HCP materials.

Electron Backscatter Diffraction (EBSD) based slip trace analysis is another technique to determine the active slip modes [10]. Slip planes can be identified by comparison between the angle of the slip trace at the sample surface and the one computed from the Euler angles of the grain. Recently, this method was also used on the strain maps obtained by high resolution digital image correlation [11]. Sometimes, more than one slip systems have similar slip trace angles to the experimental one and thus this method cannot differentiate the slip systems sharing the identical

slip plane with different slip directions. In this case, the second criteria of CRSS-SF is also required for the slip system determination. Sometimes, the constraint of SF is not enough, because the loading direction used to calculate SF within individual grain was assumed identical with the nominal applied stress. A method was proposed to supplement the existing analysis, that is, relative displacement ratio analysis [12]. This approach can increase the confidence by the combination of both experimentally-measured and theoretically-calculated relative displacement ratios obtained by digital image correlation and EBSD measurements, respectively.

The limited number of processed grains and the existing calculation error of the above approaches may introduce an uncertainty in drawing general conclusion on how individual grains with different orientations in polycrystalline material response to mechanical loading. For this purpose, an experimental technique was introduced to determine the dominant slip systems for individual grain or a large number of deformed grains [1]. The slip induced lattice rotation axis can be expressed by the Taylor axis, which is lying in the slip plane and perpendicular to the slip direction,

$$\boldsymbol{T} = \boldsymbol{n} \times \boldsymbol{b} \tag{1-1}$$

where $\boldsymbol{T}$, $\boldsymbol{n}$ and $\boldsymbol{b}$ are Taylor axis, slip plane normal, and slip direction, respectively. The Taylor axes of slip systems are given in Table 1.1. The dominant slip mode in a deformed grain can be determined by matching the experimentally obtained intragranular misorientation axis (IGMA) distribution from EBSD measurement to the Taylor axis of a known slip system. The limited angular resolution of the EBSD analysis needs to be treated with caution in this technique.

#### 1.1.1.2 Twinning

Due to the limited slip systems in some crystalline structures, twinning is an important deformation mechanism to allow arbitrary shape changes of a grain, which is usually necessary to maintain polycrystalline compatibility. A deformation twin is produced by a homogeneous simple shear of lattice. The schematic diagram of twinning is illustrated in Fig. 1.3, the twin frame is set up by: twinning shear direction (**SD**), normal of twin habit plane (**HPN**) and normal of shear plane (**SPN**). Twinning shear happens on the twinning plane (invariant plane, $\boldsymbol{K_1}$) along the twinning direction $\boldsymbol{\eta_1}$. The second undistorted plane is $\boldsymbol{K_2}$, it rotates to $\boldsymbol{K_2'}$ in the twin. $\boldsymbol{\eta_2}$ is the conjugate twinning direction which becomes $\boldsymbol{\eta_2'}$ after twinning. The twinning directions of different HCP materials are dependent on the corresponding axial ratio $c/a$ [13]. For an example, the $\{10\bar{1}2\}$ twin

in HCP materials with $c/a > 1.633$ is extension twin with shear direction along $<\bar{1}011>$, but it is a compression twin along $<10\bar{1}\bar{1}>$ in the $c/a < 1.633$ material.

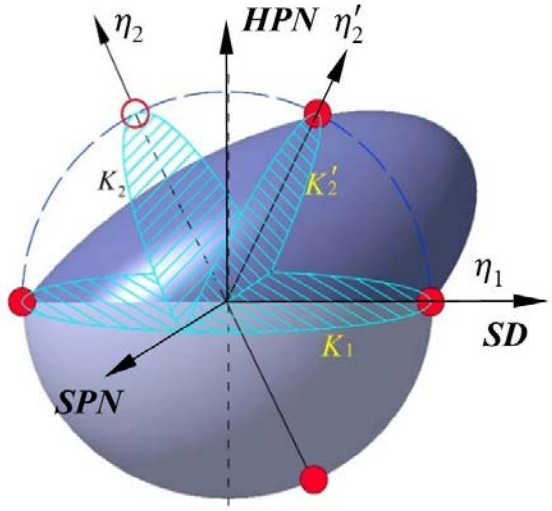


**Fig. 1.3** Schematic of four twinning elements [14].

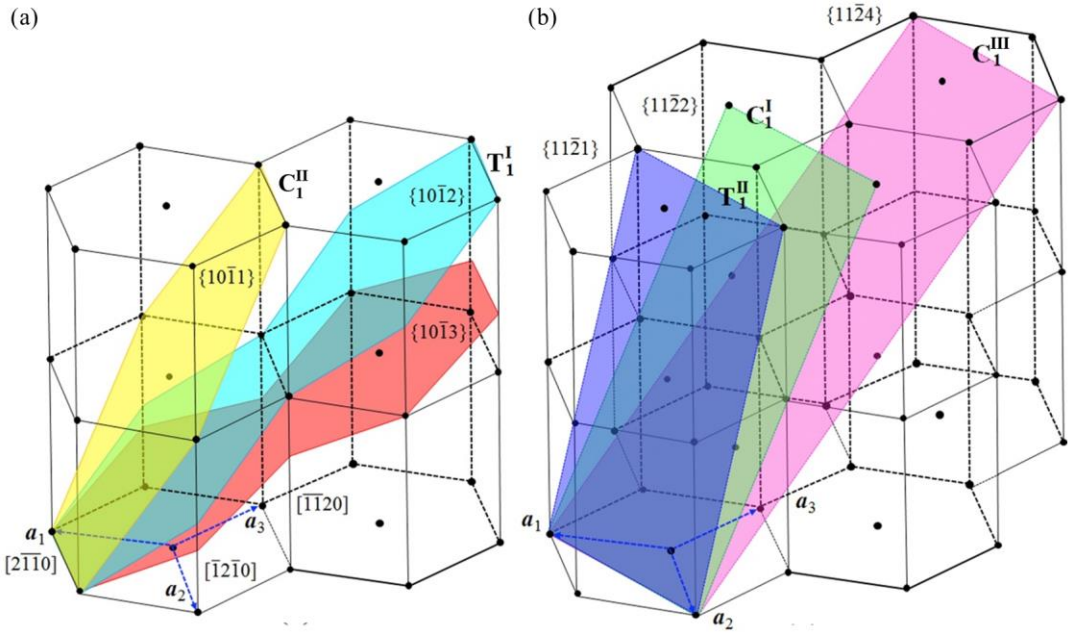


**Fig. 1.4** Six twinning systems in α-titanium: **(a)** $\{10\bar{1}1\}$ twinning plane in yellow, $\{10\bar{1}2\}$ twinning plane in light blue and $\{10\bar{1}3\}$ twinning plane in red. **(b)** $\{11\bar{2}1\}$ twinning plane in purple, $\{11\bar{2}2\}$ twinning plane in green and $\{11\bar{2}4\}$ twinning plane in pink [15].

There exist six common twinning systems in HCP materials [15]. Fig. 1.4 illustrates the classification of the six twin modes into two groups according to the zone axes, $<11\bar{2}0>$ zone axis (Fig. 1.4a) and $<10\bar{1}0>$ zone axis (Fig. 1.4b). Extension twins can be easily activated when ***c***-axis

is parallel to tensile direction or perpendicular to compression direction, while compression twins occur when ***c***-axis parallel to compression direction or perpendicular to tensile direction. Five main twinning modes in α-titanium are shown in Table 1.2. In deformed α-titanium, $\{10\bar{1}2\}<\bar{1}011>$ extension twinning and $\{11\bar{2}2\}<11\bar{2}\bar{3}>$ compression twinning are commonly observed at room temperature [16]. The fractions of $\{11\bar{2}1\}<\bar{1}\bar{1}26>$ and $\{11\bar{2}4\}<22\bar{4}\bar{3}>$ increase when titanium is deformed at high strain rate [17]. However, the $\{10\bar{1}1\}<10\bar{1}\bar{2}>$ are rarely observed in titanium.

**Table 1.2** Common twinning systems in α-Titanium

| Type | Notation (i=1…6) | $K_1$ | $\eta_1$ | $K_2$ | $\eta_2$ | Misorientation axis | Misorientation angle |
|---|---|---|---|---|---|---|---|
| Compression twinning | $C_i^I$ | $\{11\bar{2}2\}$ | $<11\bar{2}\bar{3}>$ | $\{\bar{1}\bar{1}24\}$ | $<\bar{2}\bar{2}43>$ | $<\bar{1}100>$ | ~64º |
| | $C_i^{II}$ | $\{10\bar{1}1\}$ | $<10\bar{1}\bar{2}>$ | $\{10\bar{1}\bar{3}\}$ | $<30\bar{3}2>$ | $<\bar{1}2\bar{1}0>$ | ~57º |
| | $C_i^{III}$ | $\{11\bar{2}4\}$ | $<\bar{2}\bar{2}43>$ | $\{\bar{1}\bar{1}22\}$ | $<\bar{1}\bar{1}2\bar{3}>$ | $<\bar{1}100>$ | ~77º |
| Extension twinning | $T_i^I$ | $\{10\bar{1}2\}$ | $<\bar{1}011>$ | $\{\bar{1}012\}$ | $<10\bar{1}1>$ | $<\bar{1}2\bar{1}0>$ | ~85º |
| | $T_i^{II}$ | $\{11\bar{2}1\}$ | $<\bar{1}\bar{1}26>$ | $\{0001\}$ | $<11\bar{2}0>$ | $<\bar{1}100>$ | ~35º |

When a load is applied on polycrystalline material, the inhomogeneity of local stress is enhanced due to the different shapes and orientations of individual grains. Twinning nucleation can be induced by both external and local stress and thus can significantly influence the microstructure evolution and flow stress during deformation, which further affects the mechanical property. A lot of studies have been carried out on the twin variant selection. The SF is a conveniently criterion, which is effective on the general variant activation of twin [18,19], as shown in Fig. 1.5. Under uniaxial stress,

$$SF = \cos(\theta)\cos(\lambda) \tag{1-2}$$

where $\theta$ is the angle between twinning plane normal (**HPN**) and loading direction, and $\lambda$ is the angle between shear direction (**SD**) and loading direction. The generalized Schmid factor (GSF) can be used under multi-axial loading states.

$$GSF = \boldsymbol{d}\cdot(\mathbf{G}^{-1}\cdot\boldsymbol{\sigma}\cdot\mathbf{G})\cdot\boldsymbol{n} \tag{1-3}$$

where $\boldsymbol{d}$ is shear direction, $\boldsymbol{n}$ is twinning plane normal, $\boldsymbol{\sigma}$ is normalized stress tensor and $\boldsymbol{G}$ is the orientation matrix obtained by Euler angle. The variant with the highest SF is preferentially activated.

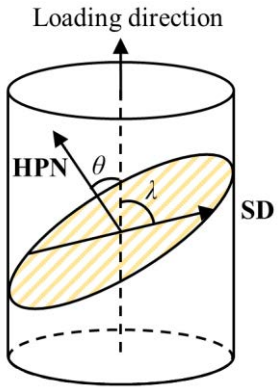


**Fig. 1.5** Schematic of Schmid factor calculation method

During mechanical loading, the first formed twinning cuts across the equiaxed grain into thin, uniform pieces, and the change of grain shape and size influences the further twinning in the produced grain pieces. Schuman et al. [20,21] proposed a criterion to explain the variant activation of primary twin, which considered the change of grain size by the first formed twin via the Hall-Petch type relation. This criterion was verified in rolled CP-Ti to 10% reduction [22], and it could accurately predict the activation of primary twinning.

Furthermore, due to the local stress concentration, low SF or anomalous twinning usually occurs. The displacement gradient accommodation (DGA) criterion was also widely used in recent decades to explain the local accommodation of twin-dislocation or twin-twin interaction. The original DGA criterion was proposed by Martin et al. [23] to explain the strong variant selection during double twinning in tensile deformed Mg–3.4%Al–0.33%Mn with the combination of SF criterion. They found that the preferred secondary twins do not always obey the SF criterion, while they always have a better compatibility on primary twin by transforming the displacement gradient tensors of secondary twins into the reference frame of primary twin. This method was further used to explore the twinning accommodated by slip systems in neighbor grain through rotating the twinning displacement gradient tensor into the crystal reference frame of neighboring grain [24]. The contraction twins in stretched AM30 and AZ31 magnesium alloys with lower SF are activated when they can be easily accommodated by basal slip or extension twin (favorable accommodation modes in Mg), while the twins need accommodation from difficult deformation systems, such as prismatic slip, are restricted. The accommodation effect was also explored in tensile CP-Ti by Wang et al. [25]: it was shown that the twins with high SF and that deformation accommodated by twins in neighbor grains have higher capacity to propagate, whereas the ones accommodated by

dislocations are difficult to grow up. Xu et al. [16] also used DGA criterion to explore the twin-twin interaction inside grain, and they demonstrated that $\{10\bar{1}2\}$ extension twin can be stimulated to accommodate the twin-twin junction of two primary $\{11\bar{2}1\}$ twins.

In addition to the constraint of SF and DGA criterions, for the analysis of double twin mechanism, the dislocation reaction principle was developed from Beyerlein et al. [26]. The model considered that the dominant two types of double twin variants can nucleate by a dissociation reaction of basal <***a***> slip and only one type double twin is energetic favorable. For the rarely formed double twin variants, both the dissociations of mixed <***c***+***a***> pyramidal slip and dislocation climb are necessary, which are more difficult than the dissociation of basal slip. Besides the unfavorable energy factor, the nucleation and motion of <***c***+***a***> slip in Mg are much more difficult than basal <***a***> slip. Xu et al. [15] systematically studied the variant selection of four types of double twin (co-family: $\{11\bar{2}2\}\rightarrow\{11\bar{2}1\}$ and $\{11\bar{2}1\}\rightarrow\{11\bar{2}4\}$, non-family: $\{11\bar{2}2\}\rightarrow\{10\bar{1}2\}$ and $\{11\bar{2}4\}\rightarrow\{10\bar{1}2\}$) in compressed CP-Ti sheet by the combination of SF, DGA and nucleation via dislocation dissociation (NDD). Both the DGA and NDD can predict the only one prevailed secondary twin variant in co-family double twin. For non-family double twin, the DGA and NDD are used to obtain the prevailed group of secondary twin variants, the SF is needed to further determine the most preferred variant.

#### 1.1.1.3 Kinking

Compared with slip and twining, “deformation kinking” is a less common deformation mode, but important for materials showing strong plastic anisotropy, such as Zn [27,28], Mg/LPSO two-phase alloys [29,30], where LPSO phase is a long-period stacking ordered phase in Mg alloy. Hess and Barrett [27] first proposed a dislocation-based model to explain kink band formation, as shown in Fig. 1.6a. In this model, cooperative operation followed by arrangement of basal dislocations to align perpendicular to the slip plane were believed to be the basic process to form the deformation kink boundary. For HCP phase, the deformation kink band boundary was mainly constructed by the array of basal dislocations [28,31]. In LPSO phase, the kink band can be classified into three types according to Taylor axes: $<1\bar{1}00>$ or $<0\bar{1}10>$ rotation type, <0001> rotation type and $<1\bar{2}10>$ rotation type, which are produced by basal <***a***> slip, prismatic <***a***> sip and a combination of two basal slip variants, respectively [32].

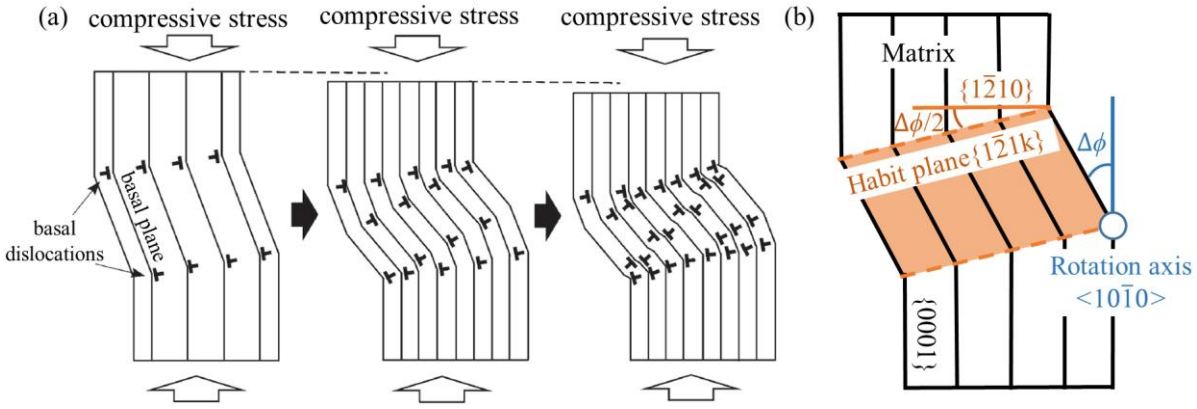


**Fig. 1.6 (a)** Model of deformation kink band formed in the Zn single crystal [27]. **(b)** Schematic on the crystal rotation angle (misorientation angle) and crystal rotation axis of kink band.

The kink band in HCP material induced by basal slip with the misorientation axis focus on <10$\bar{1}$0> is illustrated in Fig. 1.6b. The rotation axis can be determined through intragranular misorientation axis (IGMA) analysis of EBSD measurement and the askew rotation axis from Taylor axis <10$\bar{1}$0> due to the other slip systems activated near the kink band. The rotation angle $\Delta\phi$ is between the basal planes of kink band and matrix, which is related to the dislocation density and the dislocation wall thickness [32]. The habit plane {1$\bar{2}$1k} of each type kink band is rotated from {1$\bar{2}$10} around <10$\bar{1}$0> axis, the value $k$ varies with the rotation angle $\Delta\phi$. The angle between {1$\bar{2}$10} and {1$\bar{2}$1k} is equal to the $\Delta\phi$/2.

Furthermore, kink bands play an important role on the twin nucleation. Wang et al. [33] found that, in binary Mg-Y alloy, {10$\bar{1}$2} twin nucleation was almost concomitant with the kink propagation through a mechanism of basal dislocation dissociation. Some researchers have argued that {11$\bar{2}$1} twin can be regarded as "geometry-fixed deformation kink band" [34]. Jin et al. [31] studied twinning behavior and kinking behavior in CP-Ti under dynamic plastic deformation at room temperature. They proposed that {11$\bar{2}$1} twin is formed by a gradual increased misorientation angle of kink band boundary through accumulative basal dislocations.

### 1.1.2 Solute effect on plastic deformation

There are two types of interstitial sites for solute atoms in HCP structure, octahedral (O) and tetrahedral (T) sites, as shown in Fig. 1.7. Based on the solubility and lattice parameter change, Ehrlich et al. [35] suggested that oxygen atoms occupy O sites in titanium. Due to the limit of solubility, only one half of these sites are occupied. Inelastic neutron scattering measurements have

been used to determine the hydrogen site occupied in α-Zr and α-Ti, the result shows that hydrogens are located in T sites [36]. With the framework of the density functional theory, H occupancy is confirmed in T interstitial in Zr at low temperature [37]. Although the O site is unfavorable for H atoms, it also plays an important role for the H atom diffusion. Both jumps between adjacent T and O sites in the basal plane and between O sites along the *c*-axis were observed. Besides, the H atoms can share the bonds of Zr atom and lead to a local softening of the bond between these Zr atoms and the surrounding bulk, which may change the cohesion property of Zr.

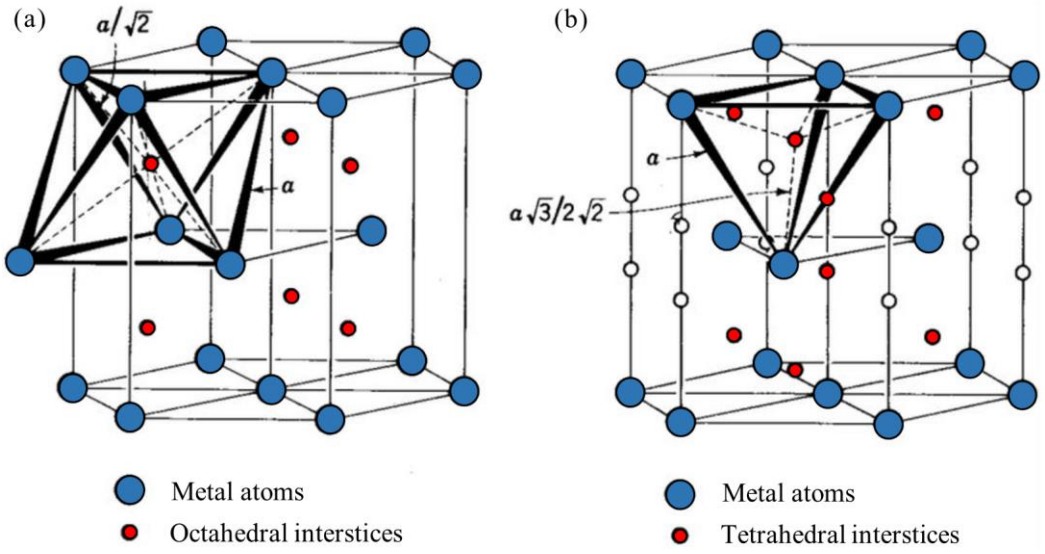


**Fig. 1.7** Interstitial sites in HCP lattice. **(a)** Octahedral site. **(b)** Tetrahedral sites.

Hydrogen embrittlement is strongly related to the interaction of hydrogen with specific plasticity mechanisms in HCP material under applied loading. In α-Ti and α-Zr, the principal slip mode is prismatic <***a***> slip, and secondary slip systems include <***a***> dislocation gliding in basal plane and in first order pyramidal $\{10\bar{1}1\}$, plus <***c***+***a***> dislocation in second order pyramidal $\{11\bar{2}2\}$. The <***a***> screw dislocations can control the activity of <***a***> slip systems, and thus play an especial role on the ductility and work hardening in α-Ti and α-Zr [38]. The addition of oxygen and hydrogen atoms or their interactions with dislocation core affects the dislocation mobility, and therefore the mechanical property of material [39].

Oxygen atoms effect on the plastic behavior of Ti and Zr alloys has been widely researched and can be regarded as a reference to understand the effect of hydrogen solutes. Churchman [40] investigated the influence of titanium purity on the slip modes during tensile deformation. The combined oxygen and nitrogen contents of two group single crystals were 0.01 wt.% and 0.1 wt. %,

respectively. The principle prismatic <***a***> slips and a few basal <***a***> slips were observed in 0.01 wt.% group and all types of <***a***> slip in prismatic, basal and pyramidal planes happen in 0.1 wt. % samples. The significantly increased critical resolved shear stress (CRSS) for basal and prismatic slip show stronger restriction produced by oxygen content (especially prismatic slip) than pyramidal one.

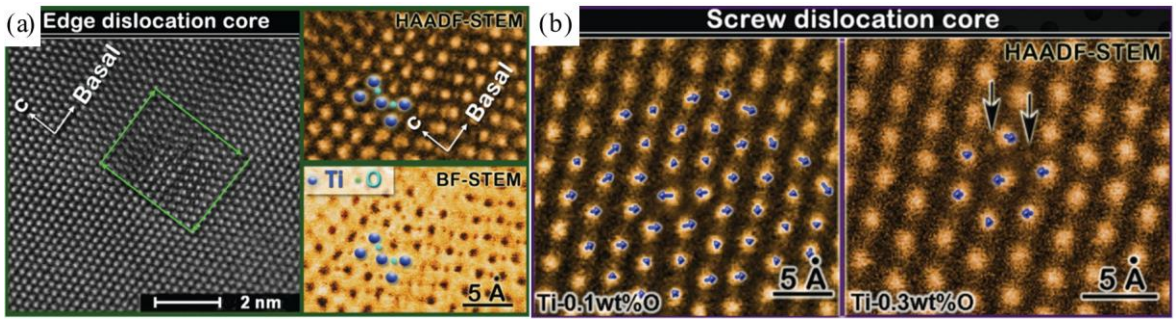


**Fig. 1.8** TEM image of oxygen atoms at octahedral sites and their effect on the dislocation cores in Ti. **(a)** High-angle annular dark-field scanning (HAADF)–STEM image of an edge dislocation core in 0.1 wt % O sample with zone axis of $[2\bar{1}\bar{1}0]$. The higher-magnification HAADF-STEM (top) and the corresponding bright-field STEM image (bottom) are shown at right. **(b)** HAADF-STEM image of a screw dislocation core in Ti-0.1 wt % O (left) and Ti-0.3 wt % O (right) with beam direction along $[11\bar{2}0]$. The in-plane displacement vectors are plotted where each blue vector represents the actual physical displacement of Ti atoms. The black arrows point to the oxygen atom columns in the screw dislocation core [41].

Ti and Zr alloys are mainly deformed by the prismatic <***a***> slip, the edge dislocations are usually with a planar structure and have a greater mobility than screw ones [42]. The gliding motion of screw dislocations is different in Ti and Zr. In Ti alloys [43], the jerky glide follows a non-planar structure with a locking-unlocking mechanism, where the locked period means a slow and limited glide in pyramidal plane and the unlocked period shows a rapid and extended glide in prismatic plane. By contrast, the prismatic gliding core is the most stable in Zr and leads to a rapid motion. Yu et al. [41] explored the oxygen strengthening mechanism by the interaction between oxygen and the core of screw dislocation using titanium samples with oxygen content of 0.1, 0.2 and 0.3 wt.%. Both the core structure of "near-edge" and screw prismatic dislocations were observed. The "near-edge" dislocations always included both <***a***> and <***c***> components (shown in the Burgers circuit in green in Fig. 1.8a), the oxygen atoms occupied octahedral sites of dislocation core and were nearly unchanged with the increase of oxygen content. In Fig. 1.8b, the in-plane displacement field projection of screw core in the 0.1 wt.% sample significantly reduced in 0.3 wt.% sample and

the oxygen interstitials were observed close to the screw core of 0.3 wt.% sample. Due to the similar core of edge dislocation in sample with different oxygen content, the mechanical property influenced by oxygen solutes was mainly related to the interaction between oxygen atoms and screw dislocations.

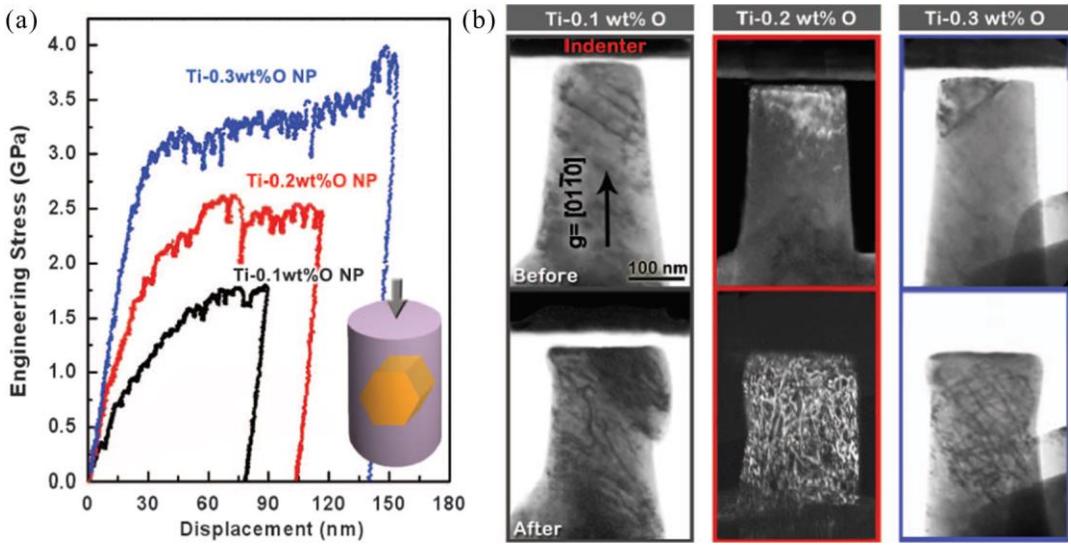


**Fig. 1.9** In situ TEM nanocompression tests of Ti with 0.1, 0.2, and 0.3 wt % O, respectively. **(a)** The engineering stress-displacement curves of pillar compression tests at different oxygen concentrations with the loading direction along [01$\bar{1}$0]. **(b)** Corresponding TEM images of the pillars before and after compression with ***g*** vector along [01$\bar{1}$0]. The 0.1 wt % O and 0.3 wt % O samples were tested under bright-field TEM mode, whereas this 0.2 wt % O sample was tested under dark-field mode [41].

Mechanical behavior was explored by in situ TEM nanocompression performed on the pillars with different oxygen contents [41] (Fig. 1.9a). Both yield strength and durability were increased in the sample with higher oxygen content. Besides, in Fig. 1.9b, during the compression on pillars with 0.1 wt.% O, obvious localized shear was observed. In the 0.3 wt.% O pillars, complex dislocation network happened and the deformation was almost homogeneous. These results were attributed to the increased interaction of oxygen-screw dislocation as the oxygen content was raised. Two effect mechanisms were proposed on the interaction of screw dislocation and oxygen interstitial. First, after the passage of a screw slip, the shear significantly decreases the volume of octahedral site, after that, oxygen atoms were squeezed out of the interstitial sites and stucked into a basal plane site. Second, the cross slip of screw dislocation can be produced by the effected oxygen atoms near the dislocation core, which further led to the dislocation pinning thus eventually finally the strengthening of material.

Due to the low solubility of hydrogen in Ti and Zr alloys, the research of hydrogen effect on the mechanical behavior is limit. The interaction of hydrogen and plane defects in Zr was investigated by ab initio calculation based on density functional theory [44]. The result shows that hydrogen atoms can reduce stacking fault energies and enhancing the spreading of intrinsic dislocation core in the prismatic plane, and consequently hinders cross-slip. But no experiment observation can be used to verify these calculation results. By a repulsive effect, the presence of hydrogen on the tetrahedral sites near the dislocation core can be inferred to decrease the oxygen atoms on the octahedral sites, which would reduce the oxygen effect on dislocation gliding. Besides, according to the effect mechanism of oxygen, it can be inferred that hydrogen interstitials also produce a barrier opposing the dislocation motion and thus improving the yield strength of material.

## 1.2 Hydrogen damage

In practice, engineering materials, such as steel, aluminium, titanium, and zirconium, are usually exposed to hydrogen and they may interact with it resulting in various kinds of structural damage. Hydrogen embrittlement, hydrogen attack, cracking due to precipitation of internal hydrogen, hydrogen induced blistering and cracking due to hydride formation are some hydrogen induced damage to metals and alloys [45]. There are many mechanisms responsible for hydrogen damage in material, such as hydrogen enhanced decohesion mechanism, hydrogen enhanced local plasticity, hydrogen assisted micro-void coalescence and hydride formation [46–52]. The initiation of hydrogen induced degradation and embrittlement is the combination of these mechanisms.

### 1.2.1 Practical cases

A most common effect of hydrogen in high strength material such as steels are known as hydrogen embrittlement [53–55]. Hydrogen embrittlement is a phenomenon that makes steel brittle where hydrogen gases get trapped in the interior of the liquid metal during the solidification process and penetrate the interior of the base material causing decohesion and/or the generation of crack [56]. Hydrogen can also enter into material during processes like electroplating, cathodic charging and welding. The strength of a material can be reduced significantly by introduction of hydrogen atom. Simultaneously, decreased ductility of a material makes it brittle.

Austenitic stainless steel has widely used in high-pressure hydrogen applications, such as pipelines and valves, for fuel cell storage systems or hydrogen refueling stations because they are less susceptible to hydrogen embrittlement. But after a period of time, embrittlement problem still

occurs. Cold work hardening by pre-straining is used to improve the mechanical properties of austenitic stainless steel. All of the initial dislocation and prior martensite by pre-strain and the dynamic martensite during service are the important factors for hydrogen-induced cracking affecting hydrogen environment embrittlement [57–59]. Due to the need of environmental protection and energy saving, the lightweight aluminum alloy becomes the new trend in the field of high-speed train and automobile [60]. During the welding process, hydrogen source dissolves in aluminum alloy weld as intermetallic particles and influences the welding consumable quality [61,62]. The most prominent defect appeared in the weld is H-induced porosity, which deteriorates the impact property. H atoms can also interact with lattice defects like dislocations, grain boundary, and inclusions [63], these defects will be the failure initiation when subjected to the impact load.

Zirconium alloys are the most exclusive material for fuel cladding and pressure tubes in high temperature water cooled reactors. The precipitation of hydride platelet can significantly affect the ductility of cladding even when they are formed homogeneously and aligned in the circumferential (in-plane) direction of the cladding tube [64–66]. The hydrogen embrittlement is enhanced by the stress-reorientation of hydrides or in presence of radial hydrides [67,68]. The delayed hydride cracking is an important potential mechanism for stress corrosion cracking [69]. The hydrogen mobile is related to the concentration, stress and temperature gradients in the fuel cladding. By the hydrogen redistribution and local maxima in hydride precipitate concentrations in the fuel rod, hydrides may preferentially precipitate in a so-called “hydride rim” near the outer cladding surface [64,70] or in hydride blisters - if oxide spallation occurs creating a cold spot in the cladding [71,72]. The cladding ductility can be drastically reduced by these two processes of local hydride aggregation [66,73]. If the hydride reorientation happens under a high hoop stress, the ductility is reduced more [74].

The embrittlement problem is also serious in hydrogen transportation and storage system directly exposed to high pressure hydrogen environment. The widely used nuclear technologies including energy, medical science, manufacture, agriculture and so on brings with high-level nuclear waste which has extremely long decay time, strong radioactivity and high toxicity [75]. Titanium is considered as a candidate material for high-level nuclear waste container due to its superior corrosion resistance [76,77]. Although titanium has reasonably resistant to chemical attack, severe problems can also arise when titanium-based alloys come in contact with hydrogen-containing environments, where they can pick up large amounts of hydrogen, especially at elevated

temperatures [78]. Hydrogen embrittlement in titanium occurs by hydrogen absorption near the crack tip and the precipitation of brittle hydride, thus promoting crack formation in a stress corrosion cracking process [79,80]. The hydrogen embrittlement mechanisms in Ti alloys are similar to that in Zr alloys, due to similar HCP structure. Despite a large research effort in attempting to understand the mechanisms of hydrogen damage, the hydrogen embrittlement mechanism in hydride forming metals (Zr and Ti) are too complicated and still not completely understood.

### 1.2.2 Hydrogen damage mechanism

Hydrogen enhanced decohesion mechanism is a simple mechanism. When hydrogen atoms are available inside the material, the internal stress gradient drives the diffusion of hydrogen atoms towards crack tips and results in the decrease of interatomic strength or cohesive strength [47]. Simultaneously, the surface energy is reduced by the decreased cohesive strength and so that fracture stress is also reduced and cleavage like fracture occurs below its permissible value. The hydrogen accumulation near crack tips can also decrease the resistance for dislocation motion [81]. The local yield stress drop accelerates the dislocation movement which corresponds to the slip bands at the crack tips on the fracture surface [82]. The increase of dislocation mobility also leads to the local plastic deformation inside embrittled material. By fractography examination, there appears more local plastic deformation with the reduction of macroscopic ductility, but not direct link is observed between hydrogen enhanced local plasticity and actual embrittlement.

Micro-void coalescence (MVC) is inherently a ductile fracture mechanism [83,84]. The MVC crack propagation happens in various stages such as void nucleation, void growth, void coalescence and crack extension. The MVC crack growth happens in a zig-zag pattern by joining of voids in crack propagation direction. MVC dimple produced by the effect of hydrogen possesses poor ductility and final fracture occurs due to shear stress. This is called hydrogen assisted micro-void coalescence. Besides, the previous research on Zr alloy [85] with various hydrogen contents proposed that the increase in void density with strain is enhanced by the presence of hydrogen, and the ductility decreases with increasing hydrogen content. The increased number of void nucleation sites is due to the formation of hydride precipitates, which increase the void nucleation kinetics [86].

In some materials with low solubility of hydrogen, such as titanium and zirconium, formation of hydride usually takes places once the local hydrogen solubility limit is exceeded. The hydride is a brittle phase, which actually causes the embrittlement of the material. Hydrogen agglomeration at crack tips with high stress intensities also results in the hydrogen-embrittlement behaviors due to delayed hydride cracking, which is a subcritical crack growth mechanism and crack propagates in a discontinuous mode [80,87–89]. A crack growth cycle includes stress-directed diffusion of hydrogen towards the crack-tip, hydride formation, which subsequently induces cleavage in front of a growing crack. Regardless of whether the hydride formation is driven by high internal hydrogen concentration or by stress-gradient driven high hydrogen flux at a crack tip, it leads to detrimental effects on mechanical properties, such as loss of ductility and sustained load cracking. Thus, it is significant to develop a more comprehensive understanding of room temperature hydride formation, and of its influence on the damage evolution mechanisms.

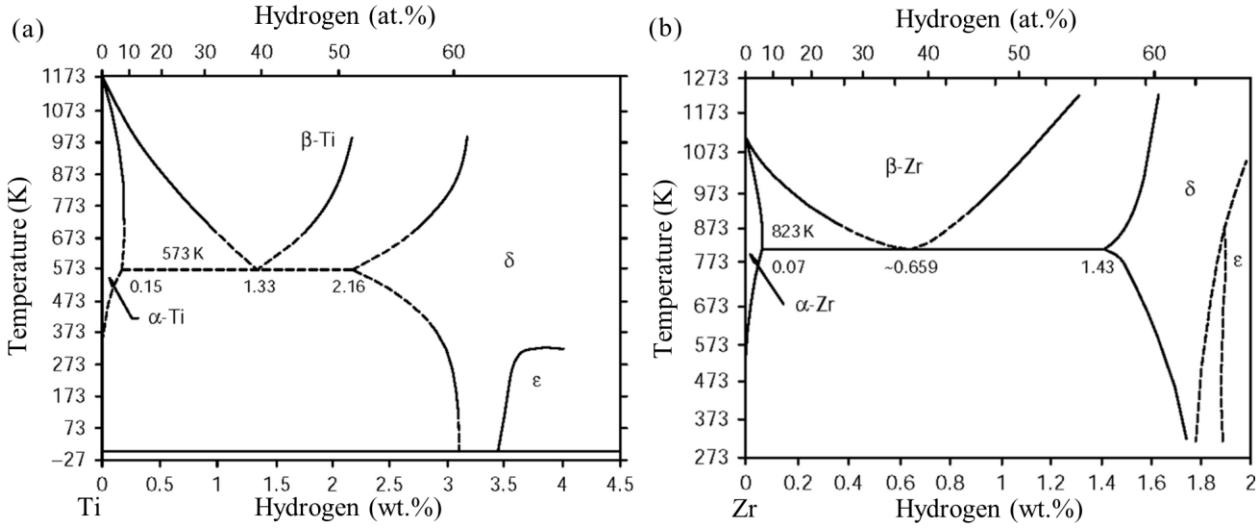


**Fig. 1.10** Binary phase diagrams **(a)** Ti-H system. **(b)** Zr-H system [90].

## 1.3 Hydride phase transformation

Hydrogen atoms in solid solution state can diffuse very fast in Ti and Zr alloys towards the areas of local stress concentrations, such as crystal defects, precipitates, grain and phase boundaries. Thus, these areas are the preferential nucleation position for hydride precipitations in order to reduce the activation energy. When hydrogen concentration surpasses the terminal solubility limit, hydride nucleation happens and then the hydrogen atoms will be bonded in the interstitial sites of the crystal lattice. The Ti-H and Zr-H binary phase diagram is shown in Fig. 1.10 [90]. At 300 ºC,

the hydrogen solubility is around 0.15 wt. % in α-Ti and 0.07 wt. % in α-Zr, which rapidly decreases as the temperature drops. Thus, hydrides are extremely easy to precipitate at room temperature (especially for Zr) due to the low hydrogen solubility.

### 1.3.1 Hydride phases and orientation relationships

Various hydride phases were found in titanium at room temperature depending on hydrogen concentration, metastable γ-hydride (TiH, face-centered tetragonal (FCT), $c/a > 1$), stable δ-hydride ($TiH_x$, $1.5 < x < 1.99$, face-centered cubic (FCC)) and ε-hydride ($TiH_2$, FCT, $c/a < 1$)) [91–95]. The δ-phase hydride is the most commonly observed hydride phase formed by multi-step process. Bair et al. [96] proposed that the shape evolution of the δ-hydride is highly dependent on the intermediate ζ and γ phase, which was explored by a multiphase field model. The γ, δ and ε phase hydrides also happen in Zr alloys [97,98], while the fourth hydride phase ξ-$Zr_2H$, a metastable hexagonal phase, was first observed in [99] with a trigonal symmetry structure fully coherent with HCP Zr matrix.

**Table 1.3** Four orientation relationships of hydride transition.

| | Orientation relationship | Interface plane |
|---|---|---|
| OR1 | {0001} //{001}, <1$\bar{2}$10>//<110> | {10$\bar{1}$0}//{1$\bar{1}$0} |
| OR2 | {0001}//{1$\bar{1}$1} (angle of 4°), <1$\bar{2}$10>//<110> | {10$\bar{1}$3}//{1$\bar{1}$0} |
| OR3 | {10$\bar{1}$0}//{1$\bar{1}\bar{1}$}, <1$\bar{2}$10>//<110> | {0001}//{1$\bar{1}$2} |
| OR4 | {$\bar{1}$011}//{001}, <1$\bar{2}$10>//<110> | {10$\bar{1}$1}//{1$\bar{1}\bar{1}$} |

Four types of orientation relationships (ORs) between HCP matrix and FCT and FCC hydrides have been reported in [91–94], which are shown in Table 1.3. OR1 and OR2 are most common orientation relationships. For OR1 transformation {0001} //{001} <1$\bar{2}$10>//<110> with interface plane {10$\bar{1}$0}//{1$\bar{1}$0}, the atoms on basal plane are moved into face-centered arrangement by the partial dislocation on prismatic plane, and an additional rearrangement of atoms (shuffles) are also needed for the rearrangement along the {10$\bar{1}$0} invariant plane normal [100]. The OR2 adopts habit plane {0001}//{1$\bar{1}$1} <1$\bar{2}$10>//<110> with interface plane {10$\bar{1}$3}//{1$\bar{1}$0} accomplished by the gliding of Shockley partial dislocation on every two (0001) planes to change the stacking sequence from …ABABAB… to …ABCABC… [100]. This transformation is hardly achieved by mechanical stress, but feasible by the chemical stress produced by the high hydrogen concentration. OR3 and OR4 are firstly observed in [91] and the transformation mechanisms is not clear.

### 1.3.2 Misfit accommodation

Hydride phase transformation is usually associated with large volume expansion (around 15%), causing high internal stresses [101]. The complicate mechanism of OR1 and OR2 hydride transformations results in the anisotropic misfit strain which is regarded as the origin of several important alloy properties decease, such as ductility and toughness [102]. Both the volume expansion and misfit strain can be accommodated through the effect of crystal defect, grain boundary, surface relaxation, external loading, etc. Thus, the research on the accommodation behavior induced by hydride transition is significant on the improvement of the hydrogen embrittlement.

Dislocations are necessary to accommodate the dilatation misfit between hydrides and the hexagonal matrix. The OR1 hydride is nucleated via a simple shear mechanism, the internal twinning is required to against the shear induced rigid body rotation and keep the undistorted $\{10\bar{1}0\}$ habit plane [100]. The growth of OR1 hydride were observed via a ledge mechanism [92] including a shear component along $<1\bar{2}10>$ and the normal dilatation component along $<10\bar{1}0>$. Conforto and Caillard [91] proposed that the OR1 transition produces two opposite prismatic loops along the interface, which contributes to relax the misfit in the $<1\bar{2}10>$ direction. In previous studies, twinning is rarely observed for the hydride accommodation. Carpenter [103] suggested that the hydride in OR2 can be formed by the dissociation of the normal $1/3 <1\bar{2}10>$ dislocations. Through the examination of strain field surrounding the hydride, the hydride is formed by the means of hydrogen diffusion plus a shear transformation caused by the glide of $1/3 <10\bar{1}0>$ Shockley partial dislocations on alternate basal plane [103]. Around the top and bottom ends of the hydride precipitate, shear loop dislocations on the basal plane with $\boldsymbol{b} = 1/3 <1\bar{2}10>$ are punched out and extend in the direction of their Burgers vectors [93]. Besides, up to now, the formation mechanism of the hydride following OR3 and OR4 still not clear.

Crystal orientation is also an important factor for hydride transformation in alloys. Hydride precipitation always appears a platelet-like shape controlled by anisotropy interfacial energy and elastic energy [104]. For OR2 hydride, although elastic energy of the large shear lattice mismatch on the basal plane tilts the hydride from the basal plane, the broad interface is still close to (0001) plane with smallest interface energy. The broad interface of OR1 hydride is $\{10\bar{1}0\}$ invariant plane [100]. Furthermore, Long et al. [105] examined the section surface microstructure of a hydride

blister grown on normal direction (**ND**) surface of Zircaloy-4 specimen. The grains with basal normal parallel to **ND** (blister growth direction) have more hydrides and less residual matrix, which shows that the crystal orientation with ***c***-axis parallel to **ND** is favorable for hydride formation. Both OR1 and OR2 hydride transformations were observed inside the blister. It is found that OR1 hydrides exhibit a larger resistance on nucleation and growth and more frequently occur in the grains with *c*-axis away from **ND**.

Grain boundary (GB) is a preferential site for second-phase nucleation because of the high energy and the high density of dislocation which can accommodate the large misfit strain of phase transformation. The physical origins are GB-solute interaction-induced nucleation and GB relaxation-induced nucleation [106]. Wang et al. [107] explored the hydride nucleation of Zircaloy-4 alloy under moderately slow cooling process. They found that most of hydrides are formed at grain boundaries in the fine grain and higher proportion of intragranular hydrides in the large grain sample. Silva et al. [108] proposed that hydride precipitation at grain boundary is directional depending on the different grain misorientation angle. The response of different hydride variants to the GB nucleation also corresponds to the geometric relationship between GB plane orientation and hydride growth direction. The effective growth direction of the hydride macro-platelet prefer to be aligned with the grain boundary plane orientation [109]. Besides, the precipitation of δ-hydride at grain boundary produces orientation gradient in the adjacent grain, and further results in the cross-boundary hydride via an auto-catalytic mechanism [107]. The cross-boundary hydride is preferred at both low-angle and high-angle grain boundary, which is related to grain boundary energy and the combined effect of collective shear on the slip plane in both grains.

The stress state is another important factor strongly affecting the formation of hydride. Sharma et al. [110] investigated the stress reorientation of hydride in Zr-2.5%Nb alloy pressure tube, which is usually used in pressurized heavy-water reactors after cold worked and stress relieved treatment. Only circumferential hydrides are formed in the pressure tube under unstressed condition. The reoriented or radial hydride happens when the fuel cladding tubes are cooled from solution state under tensile stress produced by the temporary storage and internal pressure of fission gas, which significantly increases the embrittlement in Zr-2.5%Nb alloy along circumferential direction. The hydride reorientation was also explored in CP-Ti [111]. The randomly orientated hydrides produced by cathodic hydrogenation followed by a thermal diffusion treatment were shown in Fig. 1.11a. When the tensile load applied during cooling process, the precipitated hydride platelets are

aligned to perpendicular to tensile axis (Fig. 1.11b). The external stress can decrease the critical nucleation energy of the grain boundary normal to the stress direction and further induce hydride nucleation in it [109]. In fact, the macroscopic hydrides are formed by the stacking of the micro hydride plates. Han et al. [104] proposed a micromechanical phase-field model for the formation and transition of the δ-hydrides stacking structure in Zr. The results suggested that hydride grows by repetitive nucleation, growth and coarsening near the pre-existing hydride platelet. The nucleation driving force is dependent on the elastic interaction energy around the pre-existing hydride, which can determine the preferred nucleation site and nucleation probability. The applied stress changes the energetically favored nucleation site and stacked hydride variant type, therefore transforms the orientation of macro-hydride stacking structure.

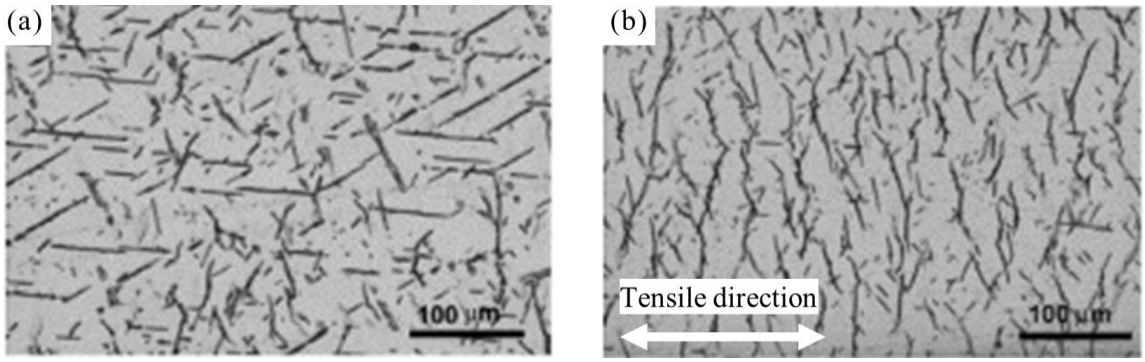


**Fig. 1.11** Hydride distribution **(a)** before and **(b)** after tensile tests [111].

### 1.3.3 Hydride enhanced hardening process

With the hardness increase by the generation of hydride precipitation, the material failure occurs easier due to the decrease of plastic and ductile deformation. The origin of such failure is attributed to the brittle nature of the hydride, micro-crack or void nucleation by the interaction between hydride and dislocation at the hydride interface [112]. The internal stress produced by strain incompatibility between hydride and matrix material is the reason for the hydride enhanced hardening process. The hardening is dependent on the crystal orientation and the relationship between slip plane and hydride habit plane; it has been shown that the hardening is more significant when the slip plane is close to the habit plane of hydride [113]. Sometimes, the effect of hardening is weakened because hydrides can also experience plastic yielding under certain working conditions, which was confirmed by Guillot et al. [114] in α-titanium using TEM technique. After plastic strain, the cross slip and dislocation loops debris were observed inside hydride. Thus, hydrides cannot always be regarded as a hard phase in a soft matrix. By the method of ab initio

calculation, Udagawa et al. [112] suggested that {111} plane slip in FCC hydride shows less resistance to both detachment and slip than that in {001} and {110} planes.

Chen et al. [115] deeply studied the deformation behaviors of γ-hydride platelet in CP-Ti with 77 ppm hydrogen during cyclic process. Both OR1 and OR2 γ-hydrides were observed under scanning electron microscopy (SEM) and TEM techniques and OR1 hydrides are easier sheared by slip band, which is due to the interface structure and the relative orientation of hydride with matrix. The OR1 hydrides were deformed by the crossed slip through the coherent interface (Fig. 1.12). The equation for slip crossing process can be written as:

$$\frac{1}{3}[11\bar{2}0]_{(10\bar{1}0)\alpha} \leftrightarrow \frac{1}{2}[1\bar{1}0]_{(110)\gamma} + \boldsymbol{b_r} \tag{1-4}$$

$\boldsymbol{b_r}$ is a residual partial dislocation left on the interface equal to 1/10 $[\bar{2}3\bar{1}0]$ when $a_\gamma = 0.420$ nm and $a_\alpha = 0.295$ nm. Under the moderate strain maximum 0.25 %, γ-hydrides have a good deformability, especially OR1 hydride, which results in the perfect continuity between hydride and matrix during deformation. Thus, no void nucleation occurs when the hydride is fragmented and separated by titanium matrix. However, voids were observed in hydride platelets and increase significantly at the necked region under monotonic tensile deformation after a large plastic strain [116].

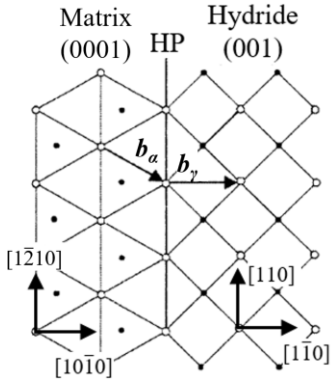


**Fig. 1.12** Schematic illustrations of atomic arrangements in the γ-hydride and matrix OR1 $\{0001\}_\alpha//\{001\}_\gamma$ $<1\bar{2}10>_\alpha//<110>_\gamma$, HP $=\{1\bar{1}00\}$ [115].

The interaction between dislocation and hydride were further investigated by focusing on the OR1 γ-hydride precipitation [117]. Two families of <100> slips on (001) plane occur and intersect with each other in large hydride plate, while in the thin hydride lamella, the activated dislocations deviate from (001) plane. The dislocation cells are usually observed near a hydride plate accompanied by hydride bending around $[0001]_\alpha//[001]_\gamma$ axis leading to the alignment of slip

direction during slip crossing process in Fig. 1.12, which reduces the residual dislocation left at hydride interface and relaxes the strain incompatibility. Besides, hydride dissolution and strain-induced hydride caused by the hydrogen/hydride-dislocation interactions further result in the shape change (refinement) and redistribution of hydride precipitation.

The deformation behaviors of OR1 γ- and δ- hydride was investigated during cyclic deformation and monotonic tensile tests in the titanium with 350, 720 and 930 wt ppm hydrogen concentration in [118]. When δ hydride has the similar size with γ hydride, they experience the same slip transfer mechanism, the kink deformation by twinning shear also occurs in both thin γ and δ hydride, but can be difficult in the thicker hydride. The δ hydrides deformed by slip bands and twinning processes are shown in Fig. 1.13a and b. Besides, the cleavage usually happens on {111}, {110}, {100} planes in massive hydride plates, while on {110} transverse plane in thin precipitation. In the hydride nearly parallel to tensile axis, the cracks are induced by large internal stress and oriented normal to tensile axis (Fig. 1.13c). Those hydride plates normal to tensile direction are difficult to be fractured because the inhomogeneous stress can be accommodated by the residual compressive stress of hydride transformation and slip transfer process at the interface.

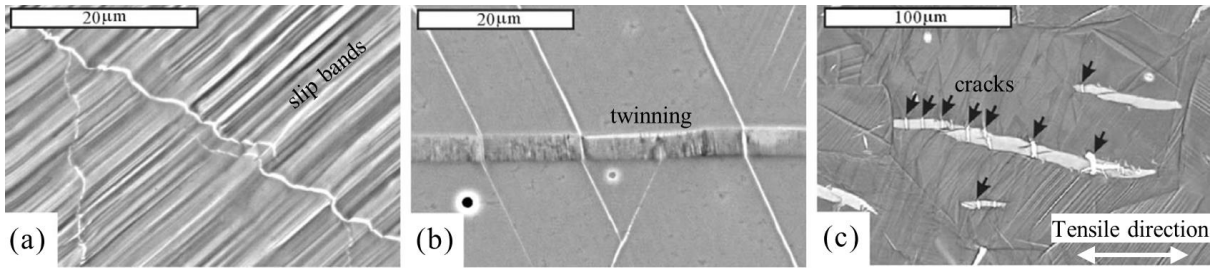


**Fig. 1.13** SEM image **(a)** δ-hydride deformed by slip bands **(b)** δ-hydride deformed by twinning **(c)** cracks normal to tensile axis in the δ-hydride parallel to tensile axis [118].

## 1.4 Chapter summary

In this chapter, the researches on plastic deformation and hydride transformation in HCP materials in the last decades were introduced. The formation of brittle hydride in Zr and Ti alloys is an important factor for hydrogen damage when materials are applied in hydrogen-rich environment. Thus, it is significant to study the relationship between hydride precipitation, crystal orientation and plastic deformation to improve the hydrogen embrittlement process. In the next chapter, the experiment processes and the crystallographic calculation principles used in this work will be given.

# Chapter 2 Experimental procedures and crystallographic calculations

Contents



## 2.1 Experimental procedures

### 2.1.1 Material

The as-received material in the present work was hot-rolled and then annealed CP-Ti sheet T40 (ASTM grade 2) with the thickness of 1.5 mm. The composition of material is shown in Table 2.1. To obtain fully recrystallized microstructure, the sample cut from Ti sheet was sealed in a vacuum quartz tube to do the heat treatment. The samples with various grain size can be achieved when the heat treatment was performed under different temperatures and lengths of time. The texture of annealed sample is split basal texture (see Chapter 3).

**Table 2.1** Chemical composition of CP-Ti T40 sheet

| Element | H | C | N | O | Fe | Ti |
|---|---|---|---|---|---|---|
| Composition (wt. ppm) | 3 | 52 | 41 | 1062 | 237 | Balance |

### 2.1.2 Hydrogen charging procedure

Hydrogen atoms were introduced into the specimens through concentration gradient by an electrolytic method [119,120]. A platinum anode of cylindrical shape was used and the specimen was located in the center of the electrolytic cell as illustrated in Fig. 2.1. The specimens were charged with hydrogen in an electrolyte consisting of 1/3 volume phosphoric acid (85 wt%) and 2/3 volume glycerin (85 wt%) [121] under an applied current density of 2 kA/m$^2$. A hydride layer formed on the sample surface when the hydrogens were supersaturated at the surface and then restrained further inward diffusion of hydrogen [119]. The structure of hydride layer is presented in Fig. 2.2, and the thickness $d$ of hydride layer is around 7 μm (see Fig. 4.8). The hydrogen concentration was measured by thermal desorption analysis (TDA) at the Welding and Joining Institute (ISF) of the RWTH Aachen University using the analyzer G8 GALILEO (Bruker, Billerica, USA).

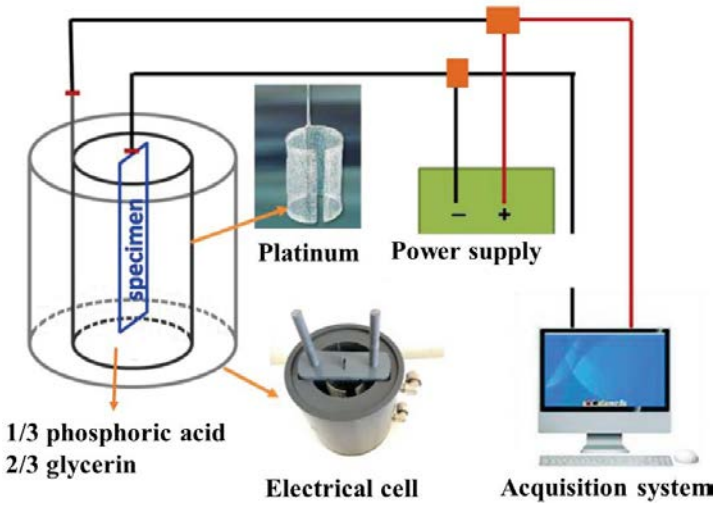


**Fig. 2.1** Schematic presentation of hydrogen charging system [120].

### 2.1.3 Polishing preparation

For orientation detection of initial material, the specimens were ground with SiC papers of grits from 1200$^{\#}$ to 2400$^{\#}$ manually on a Struers LabPol-21S equipment. After that, electrolytic polishing was performed at 35 V 5 ºC for 5 s using a solution of 10 vol% perchloric acid in methanol with

Struers LectroPol-3 machine. Leica Stereomicroscope was used to verify the surface quality for SEM-EBSD analysis.

In order to perform interrupted in-situ microstructural observation before and after hydrogen charging, the pre-charged surface was ground and electrolytic polished at 35 V 5 ºC for 5 s, and then the hydride layer can be determined directly under EBSD after charging. For the characterization of hydride precipitates inside the hydride layer, the polishing processes were carried out pertinently for different regions: Region I close to titanium matrix and Region II near diffusion surface, as shown in Fig. 2.2. To observe Region I, the pre-charged surface was ground to 2000# SiC papers, the hydride layer surface was electropolished for 1 s at 30 V. As for Region II, the pre-charged surface was ground and electrolytic polished at 35 V 5 ºC for 5, the hydrogenated surface was milled by Ar ion beam (Gatan PECS II) with 5kV for 2h. For the observation of diffusion cross section, the hydrogenated sample were mounted with Struers Polyfast resin to protect the diffusion layer during the metallographic preparation process. After ground and chemical-mechanical polished with OPS (Struers), the cross-section surface was embellished by argon ion polishing using Gatan PECS II apparatus with 5kV for 2h.

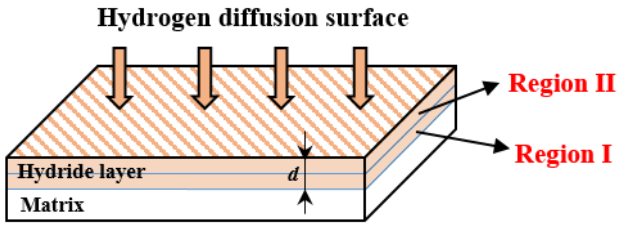


**Fig. 2.2** Illustration of hydride diffusion layer (*d*: thickness of hydride layer).

### 2.1.4 Nanoindentation test

Nanoindentation is employed to measure the mechanical property of α-grains before and after hydrogenation. Compared with conventional hardness test, it provides high spatial resolutions to place the indents and a real-time load-displacement data while the indentation is in progress, thus both plastic and elastic deformations of the material can be measured. In this work, nanoindentation tests were conducted using the nanoindenter $NHT_2$ from Anton Paar equipped with a continuous stiffness measurements modulus and Berkovich tip indenter (142.3°). This nanoindentation tester is available for the measurement of hardness, elastic modulus, and other surface properties from the nanometer to the micrometer scale. With the unique top surface referencing technique (a

reference ring taking the depth reference directly on the specimen surface), an instrumented indentation measurement can be made immediately without waiting for thermal drift stabilization.

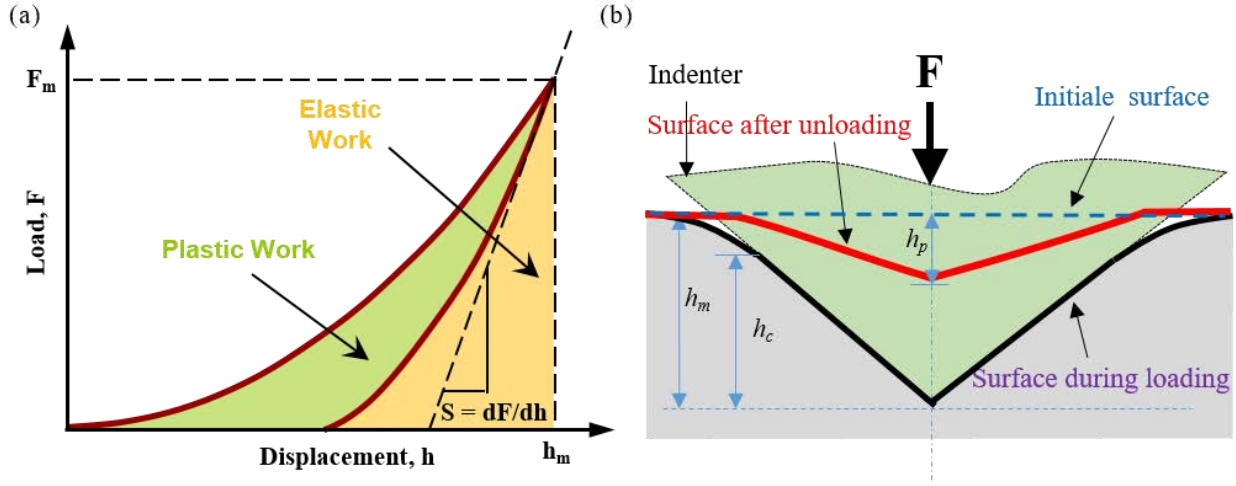


**Fig. 2.3 (a)** Schematic of load-displacement curve of nanoindentation experiment. **(b)** Definition of the different penetration depths. ($S$ is unloading stiffness; $F_m$ is maximum applied load; $h_m$ is maximum penetration depth; $h_c$ is contact depth, $h_p$ is the final displacement after unloading).

A typical load-displacement curve is shown in Fig. 2.3a, which is measured dynamically during a load-unload cycle of indentation test. The area below the loading curve is the work done by indentation compression. The area between the loading the unloading curves represents the work done to deform the material permanently (plastic work) and below the unloading curve is elastic work. Pharr and Bolshakov [122] founded that unloading curves are well described by the following power-law relationship:

$$F = F_m \left( \frac{h-h_p}{h_m-h_p} \right)^m \tag{2-1}$$

where $F_m$ is the maximal load and $m$ is fitted (by the least squares) to best adjust the unload curve. Many experiments performed by Pharr and Bolshakov [122] leaded to an average value for $m$ close to 1.5 for the Berkovich indenter. The Definition of the different penetration depths during interaction between indenter and sample surface is shown in Fig. 2.3b, $h_p$ is the final displacement after complete unloading, $h_m$ is the maximum depth and $h_c$ is contact depth during loading. The stiffness $S$ is determined by differentiating the equation (2-1).

$$S = \left(\frac{\mathrm{d}F}{\mathrm{d}h}\right)_{h=h_m} = mF_m\left(h_m\text{-}h_p\right)^{-1} \tag{2-2}$$

The indentation hardness ($H_{IT}$) is measured by:

$$H_{IT} = \frac{F_m}{A_p} \tag{2-3}$$

where $A_p$ is projected contact area. The reduced modulus $E_r$ measured by the instrument is

$$E_r = \frac{\sqrt{\pi}}{2}\frac{S}{\sqrt{A_p}} \tag{2-4}$$

which represents the elastic deformation in both sample and indenter tip. The plane strain modulus $E^*$ of the tested material is calculated using the following equation:

$$\frac{1}{E_r} = \frac{1}{E^*} + \frac{(1\text{-}\nu_i^2)}{E_i} \tag{2-5}$$

An indenter modulus $E_i$ and Poisson's ratio $\nu_i$ of 1140 GPa and 0.07 were used in accordance with the properties of diamond tip [123]. Then the indentation modulus ($E_{IT}$) can be calculated from the plane strain modulus using a hypothetic Poisson's ratio of tested material ($\nu$):

$$E_{IT} = E^*\times(1\text{-}\nu^2) \tag{2-6}$$

It is sometime difficult to estimate the Poisson's ratio ($\nu$), even if the influence on the error made on it is not large. Thus, in this work, the plane strain modulus $E^*$ is used to show the modulus of tested material.

The value of the projected area $A_p$ is needed to calculate both indentation hardness and modulus. The interaction between indenter tip and sample in Fig. 2.3b shows a typical sink-in effect. In fact, both pile-up and sink-in effects can be observed in the indentation test, which depends on the indentation depth and strain hardening coefficient of the target material [124]. In many materials, the projected contact area ($A_p$ calculated from the contact depth, $h_c$) is a good approximation to the projected residual print area.

$$A_p(h_c) = C_0h_c^2 + C_1h_c + C_2h_c^{\frac{1}{2}} + \ldots \tag{2-7}$$

However, the values $h_c$ are significantly different between pile-up and sink-in effects, as shown in Fig. 2.4a. This is generally of critical concerns in determining hardness of material as pile-up and sink-in affecting the contact area which is used to calculate the hardness. Before calculating the $h_c$, sink-in or pile- up effect need to be determined. The work of N'jock et al. [125] proposed a criterion to identify the pile-up or sink-in deformation behavior during indentation experiments, according to the methodology of Giannakopoulos and Suresh [126]. After analysis of Vickers or Berkovich indentation tests on a wide range of materials, the following criterion is established.

$$\Delta = \frac{h_p}{h_m} \tag{2-8}$$

As $\Delta < 0.83$, sink-in happens, $\Delta > 0.83$ corresponds to pile-up, while for $\Delta = 0.83$, none of the modes is preponderant. The critical value for a similar criterion in the work of Giannakopoulos and Suresh [126] is around 0.875. The models to calculate indenter contact depth $h_c$ with respective pile-up and sink-in deformation modes are as follows:

The Oliver and Pharr Model for sink-in case [127]:

$$h_c = h_m - \varepsilon \frac{F_m}{S} \tag{2-9}$$

To determine the contact depth, it is necessary to deduce the value of $\varepsilon$. When $\varepsilon$ is considered as fixed, $\varepsilon = 0.72$ is for a conical indenter ($m = 2$), and $\varepsilon = 0.75$ for a paraboloid of revolution ($m = 1.5$). The value $\varepsilon$ can also be expressed as a function of the exponent of the power law $m$ in equation (2-1) [122]:

$$\varepsilon = m\left(1 - \frac{2\Gamma\left(\frac{m}{2(m-1)}\right)}{\sqrt{\pi}\,\Gamma\left(\frac{1}{2(m-1)}\,(m-1)\right)}\right) \tag{2-10}$$

where $\Gamma$ is the factorial (gamma) function. In the case of pile-up ($\Delta > 0.83$), we use the model of Hochstetter et al. [128]:

$$h_c = \alpha\left(h_m - \frac{F_m}{S} + h_{tip}\right) \tag{2-11}$$

where α is a constant function of the material (usually around 1.2) and $h_{tip}$ is the Berkovich tip defect around 60 nm.

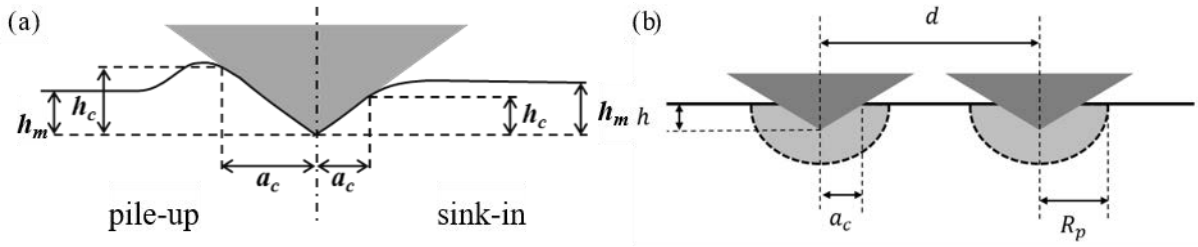


**Fig. 2.4 (a)** Cross section of pile-up and sink-in deformation. **(b)** Cross-sectional scheme of 2 indents, with the definition of geometrical parameters, contact radius $a_c$ and plastic radius $R_p$.

Furthermore, the important parameters for any indentation test, apart from the selection of load and indenter geometry, is indentation depth and spacing of indents. According to Constantinides et al. [129], the indentation depth $h$ should be at most 1/10 of the characteristic size of the microstructure $D$ (e.g.: particle size in a matrix, grain or void diameter…), in order to apply continuum indentation analysis to heterogeneous systems and to access phase properties. To characterize thick coatings on a substrate, Rother and Jehn [130] proposed a range of indentation depths over coating thickness ratios between 1/10 (10%) and 1/7 (14.3%), to avoid the imperfections of the indenters, the roughness and the surface pollution. Once the maximum indentation depth is defined, it is required to well define the distance between each indents. The cross-sectional scheme of two indents is presented in Fig. 2.4b. To avoid overlap of indents, the distance $d$ between two indents has to be larger than the plastic radius $R_p$ below each indent. Usually, the plastic radius in metals is between 3 and 6 times the contact radius $a_c$, between the indenter and the sample surface. And finally, the contact radius is roughly estimated to be 3.5 times the indentation depth $h$ in the case of Berkovich indentation. According to all of the above, to obtain accurate results for a Berkovich indenter, indent spacing should be at least 10.5 times the indentation depth.

### 2.1.5 Tensile tests

The tensile deformation was performed to investigate the mechanical property of hydride diffusion layer and the interaction between hydride and plastic modes, such as slip and twinning. The tensile tests were carried out at room temperature using a DEBEN (Suffolk, UK) machine with a maximum load cell of 1 kN (see Fig. 2.5a). The measurements were taken under an imposed force

and with a tensile speed of 200 μm/min. Fig. 2.5b shows the gauge dimensions of the tensile sample with the thickness of 0.5mm, which were designed for the tensile machine. A small pre-load was typically put on the sample and the slope out of the load train was then used to correct for zero extension to avoid any compliance issues for the machine.

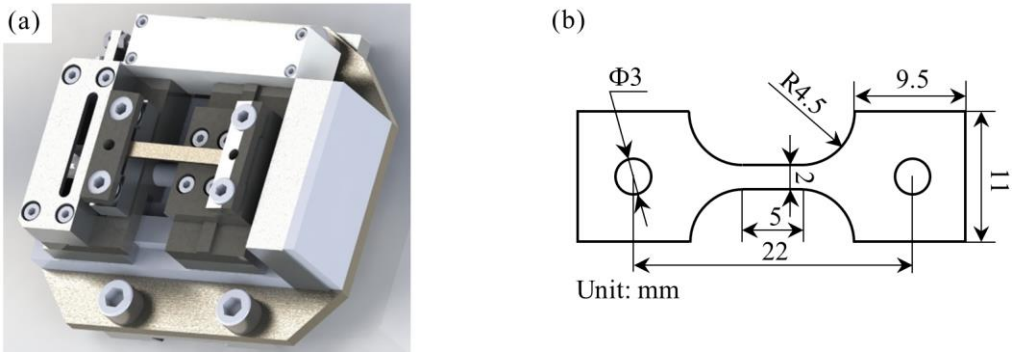


**Fig. 2.5 (a)** Illustration of tensile machine. **(b)** Gauge dimensions of the tensile sample.

### 2.1.6 Microstructural characterization

Microstructure characterization was performed using a tungsten thermionic emission Jeol-6490 and field emission gun Jeol-6500F SEM. They are equipped with an EBSD detector to provide crystallographic orientation information of the observed surface and the AZtec acquisition software package (Oxford Instruments) for data acquisition. Secondary electron imaging and forward scattered detectors was used to obtain the morphology details. To save the characterization time and obtain enough information for statistics, Jeol-6490 was used to make EBSD measurements in large area. Specifically, EBSD patterns were acquired on Jeol-6500F for obtaining more detailed examination. The HKL Channel 5 software was used to produce orientation image maps and perform quantitative metallography analysis. Pole figures were processed by using ATEX software [131].

## 2.2 Crystallographic calculations

### 2.2.1 Coordinate transformation

In the present work, there are two phases: hydride (cubic: FCC/FCT) and α-Ti (hexagonal: HCP), thus only FCC, FCT and HCP phase were involved in the crystallographic calculations. Before the discussion of coordinate transformation, the different types of coordinate systems used in HKL Channel 5 acquisition system should be introduced. To obtain the relative crystal orientation, the orientation image map uses sample surface to define the orthogonal Cartesian

sample frame ($\boldsymbol{X_1}$-$\boldsymbol{X_2}$-$\boldsymbol{X_3}$), as shown in Fig. 2.6a. On the sample surface, each crystal has corresponding frame, that is Cartesian crystal coordinate frame ($\boldsymbol{x_1}$-$\boldsymbol{x_2}$-$\boldsymbol{x_3}$). A crystal orientation is defined as the rotation between crystal and sample coordinate frame. The crystal coordinate frames corresponding to the Bravais lattice coordinate systems of different crystal structures are presented in Fig. 2.6b and c. In cubic structure, the Bravais coordinate system is $\boldsymbol{a_\delta}$-$\boldsymbol{b_\delta}$-$\boldsymbol{c_\delta}$ ($a=b=c$ and $\alpha=\beta=\gamma=90^o$) for FCC and $\boldsymbol{a_\gamma}$-$\boldsymbol{b_\gamma}$-$\boldsymbol{c_\gamma}$ ($a=b\neq c$ and $\alpha=\beta=\gamma=90^o$) for FCT, while the relationship between crystal and Bravais system is $\boldsymbol{x_1}$//$\boldsymbol{a}$, $\boldsymbol{x_2}$//$\boldsymbol{b}$ and $\boldsymbol{x_3}$//$\boldsymbol{c}$. The Bravais coordinate system of HCP structure is $\boldsymbol{a_1}$-$\boldsymbol{a_2}$-$\boldsymbol{a_3}$-$\boldsymbol{c_\alpha}$ ($a_1=a_2=a_3\neq c_\delta$, $\alpha=\beta=90^o$ and $\gamma=120^o$), the relationship with crystal system is $\boldsymbol{x_2}$//$\boldsymbol{a_2}$, $\boldsymbol{x_3}$//$\boldsymbol{c_\alpha}$ and $\boldsymbol{x_1}$//($\boldsymbol{a_2}\times\boldsymbol{c_\alpha}$).

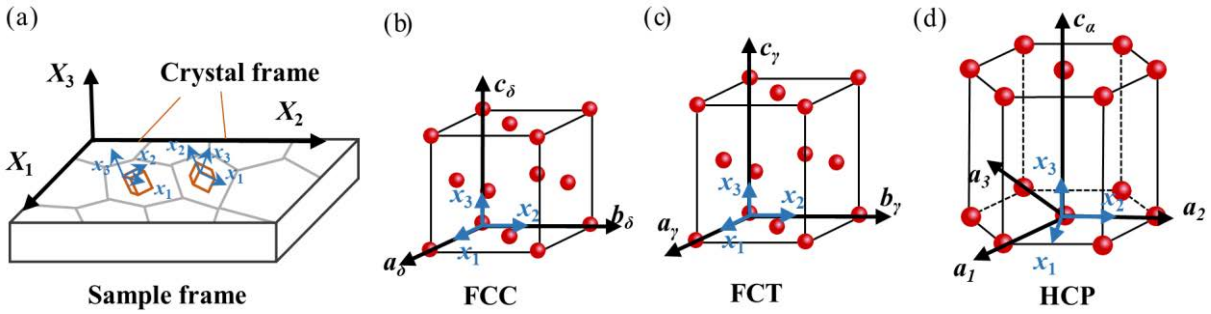


**Fig. 2.6 (a)** Relationship between the Cartesian coordinate system for sample frame ($\boldsymbol{X_1}$-$\boldsymbol{X_2}$-$\boldsymbol{X_3}$) and crystal frame ($\boldsymbol{x_1}$-$\boldsymbol{x_2}$-$\boldsymbol{x_3}$) **(b)** FCC Bravais lattice basis ($\boldsymbol{a_\delta}$-$\boldsymbol{b_\delta}$-$\boldsymbol{c_\delta}$) and crystal coordinate frame **(c)** FCT Bravais lattice basis ($\boldsymbol{a_\gamma}$-$\boldsymbol{b_\gamma}$-$\boldsymbol{c_\gamma}$) and crystal coordinate frame **(d)** HCP Bravais lattice basis ($\boldsymbol{a_1}$-$\boldsymbol{a_2}$-$\boldsymbol{a_3}$-$\boldsymbol{c_\alpha}$) and crystal coordinate frame

### 2.2.1.1 Bravais ↔ crystal coordinate system

The Bravais coordinate system of FCC structure coincides with crystal system, while the Bravais and Miller systems of FCT crystal are not orthogonal. To obtain the vector of FCT lattice in crystal system, the transformation should be done as following,

$$\begin{bmatrix} U_c \\ V_c \\ W_c \end{bmatrix} = \begin{bmatrix} 1 & 0 & 0 \\ 0 & 1 & 0 \\ 0 & 0 & \boldsymbol{c_\gamma}/\boldsymbol{a_\gamma} \end{bmatrix} \begin{bmatrix} U_B \\ V_B \\ W_B \end{bmatrix} \tag{2-12}$$

The matrix for vector transformed from FCT Miller to crystal system is named by $\mathbf{M_{cb}}$. But, this matrix is not suitable for the Miller-crystal system transformation of FCT crystal plane. In FCC crystal frame, the normal of ($H_cK_cL_c$) plane is the same vector as <$H_cK_cL_c$>, but in FCT system they are different. Thus, to get <$H_cK_cL_c$>, the plane normal of ($H_BK_BL_B$) needs to be calculated. For this purpose, reciprocal matric tensor ($\mathbf{M}^*$) [132] of corresponding lattice structure is introduced:

$$\mathbf{M}^* = \begin{bmatrix} a^*\cdot a^* & a^*\cdot b^* & a^*\cdot c^* \\ b^*\cdot a^* & b^*\cdot b^* & b^*\cdot c^* \\ c^*\cdot a^* & c^*\cdot b^* & c^*\cdot c^* \end{bmatrix}$$
$$= \frac{1}{V^2}\begin{bmatrix} b^2c^2\sin^2\alpha & abc^2(\cos\alpha\cos\beta-\cos\gamma) & ab^2c(\cos\alpha\cos\gamma-\cos\beta) \\ abc^2(\cos\alpha\cos\beta-\cos\gamma) & a^2c^2\sin^2\beta & a^2bc(\cos\beta\cos\gamma-\cos\alpha) \\ ab^2c(\cos\alpha\cos\gamma-\cos\beta) & a^2bc(\cos\beta\cos\gamma-\cos\alpha) & a^2b^2\sin^2\gamma \end{bmatrix} \quad (2\text{-}13)$$

$$V^2 = a^2b^2c^2(1+2\cos\alpha\cos\beta\cos\gamma-\cos^2\alpha-\cos^2\beta-\cos^2\gamma) \quad (2\text{-}14)$$

where $a^*$, $b^*$, $c^*$ are three basis vectors of crystal in reciprocal space, $a$, $b$, $c$ are lattice parameters, α, $\beta$, γ are lattice angles. The plane normal of $(H_BK_BL_B)$ can be obtained when $(H_BK_BL_B)$ is multiplied by $\mathbf{M}^*$, and then $<H_cK_cL_c>$ can be calculated using the above-mentioned matrix $\mathbf{M_{cb}}$.

$$\begin{bmatrix} H_c \\ K_c \\ L_c \end{bmatrix} = \mathbf{M_{cb}}\cdot\mathbf{M}^*\cdot\begin{bmatrix} H_B \\ K_B \\ L_B \end{bmatrix} \quad (2\text{-}15)$$

The $(H_cK_cL_c)$ is the corresponding plane of $(H_BK_BL_B)$ transformed from Miller system into crystal coordinate frame.

As for HCP structure, the Bravais system is not orthogonal and need to be transformed into orthogonal system during crystallographic calculations. First, the 4-index Miller-Bravais system of HCP structure $(hkil)<uvtw>$ should be changed into 3-index Miller system $(H_BK_BL_B)<U_BV_BW_B>$:

$$\begin{bmatrix} U_B \\ V_B \\ W_B \end{bmatrix} = \begin{bmatrix} 2 & 1 & 0 & 0 \\ 1 & 2 & 0 & 0 \\ 0 & 0 & 0 & 1 \end{bmatrix}\begin{bmatrix} u \\ v \\ t \\ w \end{bmatrix} \quad (2\text{-}16)$$

$$\begin{bmatrix} H_B \\ K_B \\ L_B \end{bmatrix} = \begin{bmatrix} 1 & 0 & 0 & 0 \\ 0 & 1 & 0 & 0 \\ 0 & 0 & 0 & 1 \end{bmatrix}\begin{bmatrix} h \\ k \\ i \\ l \end{bmatrix} \quad (2\text{-}17)$$

The transformation matrices from 4 index to 3 index are given by $\mathbf{M_{43}}$. After transformed into 3-index system, the $<U_BV_BW_B>$ vector of HCP Miller system is given in crystal coordinate frame by:

$$\begin{bmatrix} U_c \\ V_c \\ W_c \end{bmatrix} = \begin{bmatrix} \sqrt{3}/2 & 0 & 0 \\ -1/2 & 1 & 0 \\ 0 & 0 & \boldsymbol{c_\alpha/a_\alpha} \end{bmatrix}\begin{bmatrix} U_B \\ V_B \\ W_B \end{bmatrix} \quad (2\text{-}18)$$

$\boldsymbol{c_\alpha/a_\alpha}$ is the axial ratio of HCP material and it is equal to 1.587 for Ti. The plane normal of $(H_BK_BL_B)$ can be obtained by the same method as FCT system.

### 2.2.1.2 Rotation of crystal coordinate system

The rotation of coordinate system is often involved in crystallographic calculation. The object itself stays fixed during coordinate rotation, the object can be a vector (1st-rank tensor) such as crystal direction or force, or a 2st-rank tensor such as stress or strain. For an example, the $\boldsymbol{x_1}$-$\boldsymbol{x_2}$-$\boldsymbol{x_3}$ Cartesian crystal frame is rotated into $\boldsymbol{a}$-$\boldsymbol{b}$-$\boldsymbol{c}$ frame. A general method to formulate a transformation matrix is based on the cosines of the angles between the axes of two coordinate systems:

$$\mathbf{R} = \begin{bmatrix} \cos(\boldsymbol{a},\boldsymbol{x_1}) & \cos(\boldsymbol{a},\boldsymbol{x_2}) & \cos(\boldsymbol{a},\boldsymbol{x_3}) \\ \cos(\boldsymbol{b},\boldsymbol{x_1}) & \cos(\boldsymbol{b},\boldsymbol{x_2}) & \cos(\boldsymbol{b},\boldsymbol{x_3}) \\ \cos(\boldsymbol{c},\boldsymbol{x_1}) & \cos(\boldsymbol{c},\boldsymbol{x_2}) & \cos(\boldsymbol{c},\boldsymbol{x_3}) \end{bmatrix} = \begin{bmatrix} a_1 & a_2 & a_3 \\ b_1 & b_2 & b_3 \\ c_1 & c_2 & c_3 \end{bmatrix} \tag{2-19}$$

where $\mathbf{R}$ is an orthogonal matrix and $\mathbf{R^T} = \mathbf{R^{-1}}$. In a Cartesian crystal frame, $|\boldsymbol{x_1}|=|\boldsymbol{x_2}|=|\boldsymbol{x_3}|=1$, $\cos(\boldsymbol{a},\boldsymbol{x_1})$ is equal to the value of $\boldsymbol{a}$ projection onto $\boldsymbol{x_1}$ axis, that is, the $\boldsymbol{x_1}$-component ($a_1$) of $\boldsymbol{a}$ vector. Thus, in Cartesian crystal system, the coordinate rotation matrix $\mathbf{R}$ can also be expressed by the 9 components of $\boldsymbol{a}$-$\boldsymbol{b}$-$\boldsymbol{c}$. Then, the vector ($\boldsymbol{v}$) and tensor ($\mathbf{T}$) transformed from Cartesian crystal frame ($\boldsymbol{x_1}$-$\boldsymbol{x_2}$-$\boldsymbol{x_3}$) to frame ($\boldsymbol{a}$-$\boldsymbol{b}$-$\boldsymbol{c}$) can be obtained by:

$$\boldsymbol{v'} = \mathbf{R}\cdot\boldsymbol{v} \text{ and } \mathbf{T'} = \mathbf{R}\cdot\mathbf{T}\cdot\mathbf{R^{-1}} \tag{2-20}$$

### 2.2.1.3 Crystal ↔ sample coordinate system

The crystal orientations measured by EBSD are referred to the fixed sample coordinate frame, as shown in Fig. 2.7a. A crystal orientation is defined as a triplet rotation from sample frame to crystal frame, which is usually described with Euler angles introduced by Leonhard Euler [133]. The Euler angles ($\varphi_1$, $\Phi$, $\varphi_2$) from HKL system are given by Bunge convention [134,135], which are adopt in this work. The definition of three successive counterclockwise rotations about different axes of sample system is illustrated in Fig. 2.7b-d, which in order to realize the transformation from sample to crystal coordinates in Fig. 2.7a. First, the sample coordinates are changed into $\boldsymbol{X_1'}$-$\boldsymbol{X_2'}$-$\boldsymbol{X_3'}$ by the rotation of $\varphi_1$ around $\boldsymbol{X_3}$ axis (Fig. 2.7b). After that, the $\boldsymbol{X_1'}$-$\boldsymbol{X_2'}$-$\boldsymbol{X_3'}$ are rotated into $\boldsymbol{X_1''}$-$\boldsymbol{X_2''}$-$\boldsymbol{X_3''}$ by $\Phi$ around $\boldsymbol{X_1'}$ (Fig. 2.7c), which is followed by the rotation $\varphi_2$ about $\boldsymbol{X_3''}$ into $\boldsymbol{X_1'''}$-$\boldsymbol{X_2'''}$-$\boldsymbol{X_3'''}$ ($\boldsymbol{x_1}$-$\boldsymbol{x_2}$-$\boldsymbol{x_3}$) as shown in Fig. 2.7d. When the crystal coordinate frame coincides with sample frame, that is, $\boldsymbol{x_1}$//$\boldsymbol{X_1}$, $\boldsymbol{x_2}$//$\boldsymbol{X_2}$ and $\boldsymbol{x_3}$//$\boldsymbol{X_3}$, the Euler angles are (0°, 0°, 0°).

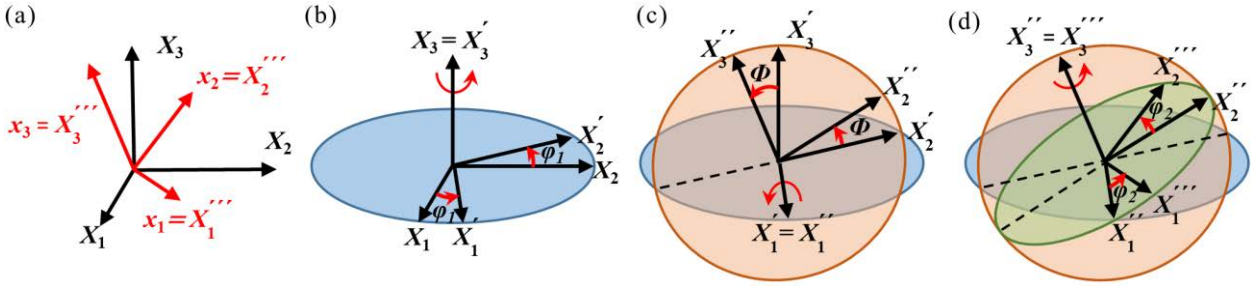


**Fig. 2.7** Presentation of the three successive rotations in Euler angle (Bunge notation) **(a)** spatial relationship between sample ($X_1$-$X_2$-$X_3$) and crystal ($x_1$-$x_2$-$x_3$) frame. **(b)** first rotation $\varphi_1$ around $X_3$ axis. **(c)** second rotation $\Phi$ around $X_1'$ axis. **(d)** third rotation $\varphi_2$ around $X_3''$ axis.

The rotation of Euler angles can be represented as rotation matrices of trigonometric functions of the angles. The matrices for three successive rotations around $X_3$-$X_1'$-$X_3''$ are given as following:

$$\mathbf{R}_{\varphi_1} = \begin{bmatrix} \cos\varphi_1 & \sin\varphi_1 & 0 \\ -\sin\varphi_1 & \cos\varphi_1 & 0 \\ 0 & 0 & 1 \end{bmatrix} \tag{2-21}$$

$$\mathbf{R}_{\Phi} = \begin{bmatrix} 1 & 0 & 0 \\ 0 & \cos\Phi & \sin\Phi \\ 0 & -\sin\Phi & \cos\Phi \end{bmatrix} \tag{2-22}$$

$$\mathbf{R}_{\varphi_2} = \begin{bmatrix} \cos\varphi_2 & \sin\varphi_2 & 0 \\ -\sin\varphi_2 & \cos\varphi_2 & 0 \\ 0 & 0 & 1 \end{bmatrix} \tag{2-23}$$

A final matrix for Bunge rotation can be obtain by multiplication of these three matrices:

$$\mathbf{R}_{cs} = \mathbf{R}_{\varphi_2} \cdot \mathbf{R}_{\Phi} \cdot \mathbf{R}_{\varphi_1} \tag{2-24}$$

The vector or plane in crystal frame transformed from sample system is given by:

$$\boldsymbol{v}_c = \mathbf{R}_{cs} \cdot \boldsymbol{v}_s \text{ or } \mathbf{T}_c = \mathbf{R}_{cs} \cdot \mathbf{T}_s \cdot \mathbf{R}_{cs}^{-1} \tag{2-25}$$

### 2.2.2 Misorientation (Disorientation)

Misorientation is the orientation difference between two crystal cells or between two local crystal frames in a polycrystalline material, which usually defined by the angle-axis pair $\theta$ <$r_1$ $r_2$ $r_3$>. One crystal coordinate system can be superimposed onto the other by rotating an angle $\theta$ around axis <$r_1$ $r_2$ $r_3$>. For equivalent rotation axes <$r_1$ $r_2$ $r_3$>, the misorientation angle $\theta$ is defined as the smallest angle relating two given crystal orientations. The rotation operation can be also

described by misorientation matrix $\Delta\mathbf{M}$. The schematic with respect to calculate $\Delta\mathbf{M}$ between Crystal A and Crystal B is presented in Fig. 2.8.

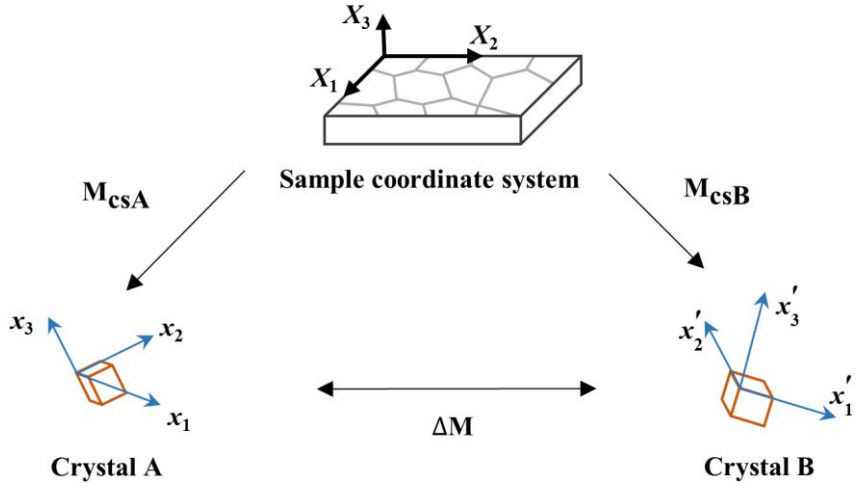


**Fig. 2.8** Schematic of misorientation between Crystal A and Crystal B. $\mathbf{M}_{csA}$ and $\mathbf{M}_{csB}$ are coordinate transformation matrices from sample to crystal frame, $\Delta\mathbf{M}$ is the misorientation matrix.

During the misorientation calculation, crystal symmetries are considered to present all possible misorientation relationships. For cubic crystal system, there exist 24 symmetry elements by combination of 4-fold <001> axes (3×4 = 12) and 3-fold <111> axes (4×3 = 12). There are 12 symmetry elements for hexagonal structure, 6-fold [0001] axis (1×6 = 6) plus 2-fold $<\bar{1}2\bar{1}0>$ (3×2 = 6). The definition of the symmetry rotation axis of order $n$ is that a crystal can coincide with itself in an anticlockwise rotation of 360°/$n$. Besides, the misorientations from A to B and B to A are the same. Thus, the misorientation matrix $\Delta\mathbf{M}$ is given as follows:

$$\Delta\mathbf{M} = (\mathbf{M}_{csA}\cdot\mathbf{S}_i)^{-1}\cdot\mathbf{M}_{csB}\cdot\mathbf{S}_j = \begin{bmatrix} g_{11} & g_{12} & g_{13} \\ g_{21} & g_{22} & g_{23} \\ g_{31} & g_{32} & g_{33} \end{bmatrix} \tag{2-26}$$

where $\mathbf{S}_i$ and $\mathbf{S}_j$ are the rotation symmetry elements of Crystal A and Crystal B, respectively. The misorientation angles $\theta$ and axes $<r_1\ r_2\ r_3>$ can be calculated according to $\Delta\mathbf{M}$:

$$\theta = \arccos\left(\frac{g_{11}+g_{22}+g_{33}-1}{2}\right) \tag{2-27}$$

when $\theta = 0^o$

$$[r_1\ r_2\ r_3] = [1\ 0\ 0] \tag{2-28}$$

when $0^o < \theta < 180^o$

$$r_1 = \frac{g_{23}-g_{32}}{2\sin\theta};\ r_2 = \frac{g_{31}-g_{13}}{2\sin\theta};\ r_3 = \frac{g_{12}-g_{21}}{2\sin\theta} \tag{2-29}$$

when $\theta = 180^o$

$$r_1 = \pm\sqrt{\frac{g_{11}+1}{2}};\ r_2 = \pm\sqrt{\frac{g_{22}+1}{2}};\ r_3 = \pm\sqrt{\frac{g_{33}+1}{2}} \tag{2-30}$$

with $r_m = \max(|r_i|, i = 1, 2, 3)$, $\forall\ i \neq m$, $r_i = \text{sign}(g_{im}) \cdot |r_i|$.

The misorientation fundamental zone for cubic-cubic, hexagonal-hexagonal and cubic-hexagonal are 24×24, 12×12 and 24×12, respectively. Disorientation is introduced to describe the misorientation with the smallest possible rotation angle among all symmetrically equivalent misorientations in the fundamental zone between two crystals. It is also denoted by the angle-axis pair $\theta_{min} <r_1\ r_2\ r_3>$, where $\theta_{min}$ is the disorientation angle, which is minimum of misorientation angle, and corresponding disorientation axis $<r_1\ r_2\ r_3>$.

### 2.2.3 Trace analysis

During plastic deformation or phase transformation, slip plane, twinning plane or habit plane of a second phase can be observed on the sample surface. Trace analysis method is an efficient method to determine the as-mentioned planes.

Stereographic projection is a special mapping, which can represent a three-dimensional sphere onto a two-dimensional plane. In crystallography, pole figure in the form of stereographic projection is used to present the orientation distribution of crystal lattice planes or directions on sample surface. The axes of the projection sphere are aligned with the axes of the sample coordinates $\boldsymbol{X_1}$-$\boldsymbol{X_2}$-$\boldsymbol{X_3}$. Fig. 2.9a illustrates a projection example of $(1\,\bar{1}\,1)$ plane normal in a Cartesian crystal system $\boldsymbol{x_1}$-$\boldsymbol{x_2}$-$\boldsymbol{x_3}$ with Euler angle of (0º, 0º, 0º). ***OP*** $[U_s V_s W_s]$ is the normal of $(1\bar{1}1)$ plane, the length of ***OP*** is equal to Sphere radius $R$, that is, $|\boldsymbol{OP}|=R=1$. $P$ is the pole of $(1\bar{1}1)$ plane normal on the sphere with the coordinates of $(U_s, V_s, W_s)$ and $P'$ is the projection of $P$ on equatorial plane. The coordinates of $P'$ $(U_s', V_s')$ can be calculated from normalized ***OP*** $[U_s V_s W_s]$ as follows:

$$U_s^{'} = \frac{U_s}{|W_s|+1}; V_s^{'} = \frac{V_s}{|W_s|+1}; \tag{2-31}$$

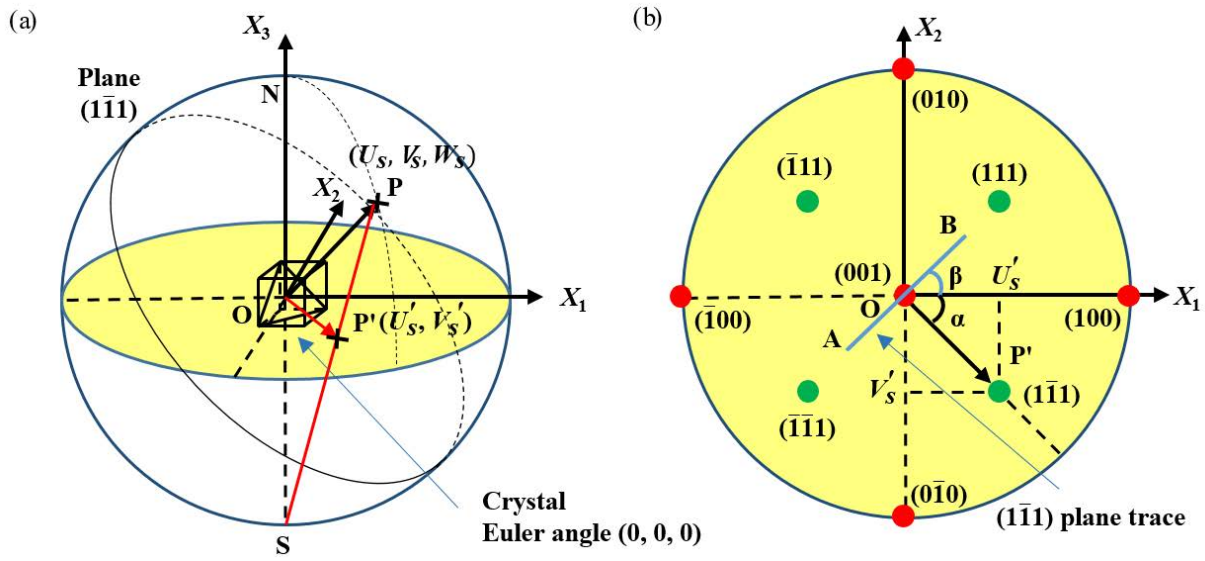


**Fig. 2.9 (a)** Illustration of stereographic projection with respect to (1$\bar{1}$1) plane normal in an example crystal. $X_1$-$X_2$-$X_3$ are sample coordinates, OP is (1$\bar{1}$1) plane normal and corresponding projection OP' on equatorial plane. **(b)** $X_1OX_2$ projection plane and the poles of {111} (green) and {001} (red) planes. AB is the plane trace of (1$\bar{1}$1) plane on $X_1OX_2$ plane.

The projection plane is shown in Fig. 2.9b. ***OP'*** is the projection of ***OP*** with the angle of $\alpha$ from $X_1$ axis.

$$|OP'| = \sqrt{U_s^{'2} + V_s^{'2}}; \alpha = \arctan\left(\frac{V_s^{'}}{U_s^{'}}\right) \tag{2-32}$$

AB is the trace of (1$\bar{1}$1) plane on sample surface, which is perpendicular to ***OP'***. The angle $\beta$ between the trace and $X_1$ axis is equal to 90°-$\alpha$. The poles of {001} (red) and other {111} planes (green) are also drawn out on the projection plane in Fig. 2.9b using the same method.

Therefore, every crystal plane in sample space can be calculated using the Euler angles EBSD data with the transformation matrix $\mathbf{M_{cs}}$. After that, the crystallographic plane can be identified by comparing the theoretical direction and actual direction on SEM or EBSD map. When using the trace analysis method, some auxiliary conditions are always needed as constraints because some planes share similar trace angles. For an example, CRSS and SF are necessary for the slip or twinning plane determination in a deformed material.

### 2.2.4 Deformation theory

#### 2.2.4.1 Basic concepts

The lattice displacement has two components: a rigid-body displacement and a shape deformation. Fig. 2.10 illustrates the deformation of a crystal lattice. For convenience, the Cartesian coordinate systems $\boldsymbol{Y_1}$-$\boldsymbol{Y_2}$-$\boldsymbol{Y_3}$ and $\boldsymbol{y_1}$-$\boldsymbol{y_2}$-$\boldsymbol{y_3}$ for the undeformed and deformed configuration are superimposed. $\boldsymbol{Y}$ and $\boldsymbol{y}$ are the position vector of respective point $P$ and $p$ from the origin of coordinate system. $\boldsymbol{u}(\boldsymbol{Y})$ is displacement tensor between undeformed particle $P$ and deformed $p$. The displacement gradient tensor ($\mathbf{D}_{ij}$) can be produced by the partial derivative of the displacement vector with respect to the spatial coordinates, which is given by:

$$\mathbf{D}_{ij}=\frac{\partial u_i}{\partial Y_i}=\begin{bmatrix}\frac{\partial u_1}{\partial Y_1} & \frac{\partial u_1}{\partial Y_2} & \frac{\partial u_1}{\partial Y_3}\\ \frac{\partial u_2}{\partial Y_1} & \frac{\partial u_2}{\partial Y_2} & \frac{\partial u_2}{\partial Y_3}\\ \frac{\partial u_3}{\partial Y_1} & \frac{\partial u_3}{\partial Y_2} & \frac{\partial u_3}{\partial Y_3}\end{bmatrix} \tag{2-33}$$

The point $Q$ is neighboring $P$ with the position vector $\boldsymbol{Y}+d\boldsymbol{Y}$, the position of $q$ in deformed lattice is $\boldsymbol{y}+d\boldsymbol{y}$. The small segments between $PQ$ and $pq$ are expressed by respective $d\boldsymbol{Y}$ and $d\boldsymbol{y}$. The $d\boldsymbol{y}$ after deformation can be obtained from $d\boldsymbol{Y}$ by:

$$d\boldsymbol{y}=\frac{\partial \boldsymbol{y}}{\partial \boldsymbol{Y}}\,d\boldsymbol{Y} \tag{2-34}$$

Then the deformation gradient tensor to present local deformation at neighboring point is shown as following:

$$\mathbf{F}_{ij}=\frac{\partial Y_i}{\partial Y_i}=\begin{bmatrix}\frac{\partial y_1}{\partial Y_1} & \frac{\partial y_1}{\partial Y_2} & \frac{\partial y_1}{\partial Y_3}\\ \frac{\partial y_2}{\partial Y_1} & \frac{\partial y_2}{\partial Y_2} & \frac{\partial y_2}{\partial Y_3}\\ \frac{\partial y_3}{\partial Y_1} & \frac{\partial y_3}{\partial Y_2} & \frac{\partial y_3}{\partial Y_3}\end{bmatrix} \tag{2-35}$$

As shown in Fig. 2.10, the $d\boldsymbol{y}$ can also be obtained as follows:

$$d\boldsymbol{y}=d\boldsymbol{Y}+d\boldsymbol{u}\approx d\boldsymbol{Y}+\frac{\partial \boldsymbol{u}}{\partial \boldsymbol{Y}}\,d\boldsymbol{Y}=(\mathbf{I}+\frac{\partial \boldsymbol{u}}{\partial \boldsymbol{Y}})\,d\boldsymbol{Y}=(\mathbf{I}+\mathbf{D})\,d\boldsymbol{Y}=\mathbf{F}\,d\boldsymbol{Y} \tag{2-36}$$

Thus,

$$\mathbf{F}_{ij} = \mathbf{I} + \mathbf{D}_{ij} \tag{2-37}$$

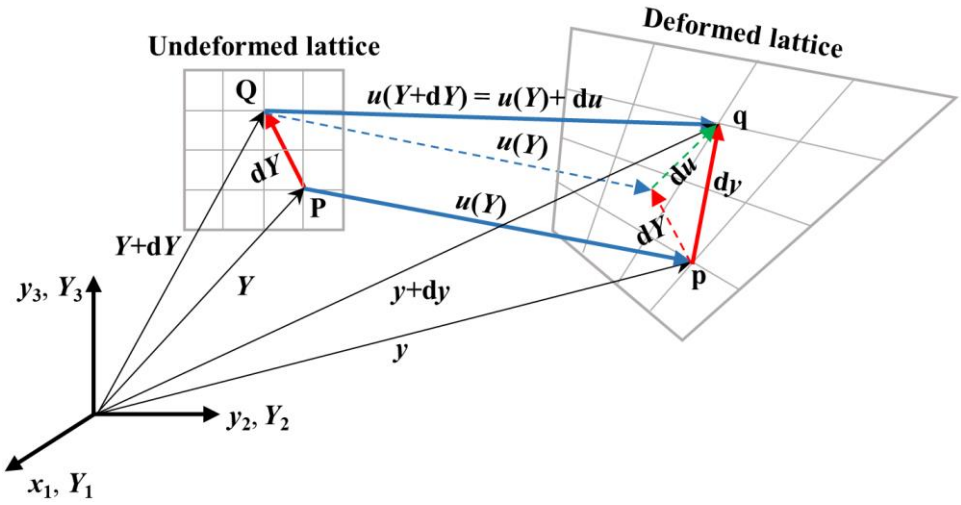


**Fig. 2.10** Schematic of lattice deformation. *P* and *Q* are the particles in undeformed lattice in the material (body-frame) coordinate system $Y_1$-$Y_2$-$Y_3$. For deformed lattice, the corresponding particle positions are given by *p* and *q* in spatial (lab-frame) coordinate system $y_1$-$y_2$-$y_3$. $\boldsymbol{Y}$ and $\boldsymbol{y}$ are the position vector of respective particle *P* and *p*.

The displacement gradient tensor can be divided into two parts: symmetric and antisymmetric,

$$\mathbf{D} = \boldsymbol{\varepsilon} + \boldsymbol{\Omega} \tag{2-38}$$

where $\boldsymbol{\Omega}$ is the antisymmetric tensor correlated to rigid body rotation. The symmetric part is strain tensor $\boldsymbol{\varepsilon}$ indicating the shape change of crystal lattice during deformation.

$$\boldsymbol{\varepsilon} = \frac{1}{2}\left(\mathbf{D}^{\mathrm{T}} + \mathbf{D}\right) \tag{2-39}$$

The volume expansion can be calculated by the sum of diagonal elements of displacement gradient tensor or strain tensor. For plastic deformation, the sum of diagonal elements is equal to zero because of the volume conservation.

### 2.2.4.2 Twinning

A deformation twin is produced by a homogeneous simple shear of lattice, and the region twinned with a macroscopic change of shape is described by the same simple shear. The schematic diagram of twinning is illustrated in Fig. 2.11. The twin frame is set up by: $\boldsymbol{Z_1}$ // twinning shear direction (***SD***(***n***)), $\boldsymbol{Z_3}$ // normal of twin habit plane (***HPN***(***m***)) and $\boldsymbol{Z_2}$ // normal of shear plane

(***SPN***(***p***)). The displacement gradient tensor of twinning ($\mathbf{D}^{\mathbf{t}}$) has a simple form in the twinning frame [23]:

$$\mathbf{D}^{\mathbf{t}} = \frac{\partial u_i}{\partial Z_i} = \begin{bmatrix} 0 & 0 & s \\ 0 & 0 & 0 \\ 0 & 0 & 0 \end{bmatrix} \tag{2-40}$$

where ***u***(***Z***) is displacement vector at position $Z_i$ and $s$ is the magnitude of twinning shear in Ti ($c/a$=1.587). The only non-zero component is the twinning shear ($s = \frac{\partial u_1}{\partial Z_3}$), $u_1$ is a line function of the distanse to the twinning plane ($Z_3$). The $s$ value calculation of different twinning modes in α-titanium are shown in Table 2.2.

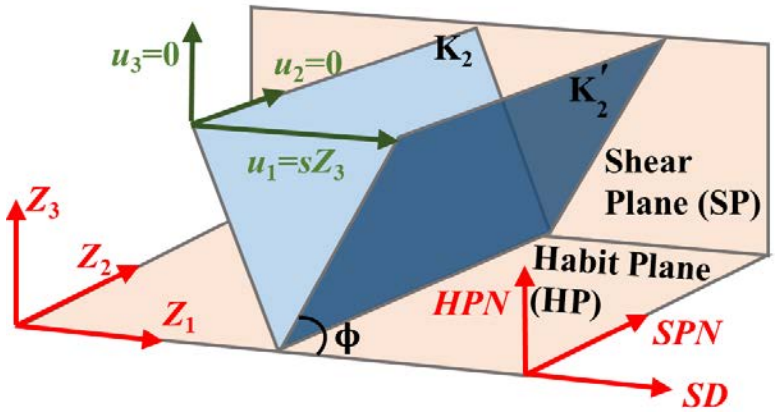


**Fig. 2.11** Schematic diagram of twinning

**Table 2.2** The calculation of twinning shear ($\gamma = c/a$)

| | $C^{I}$ $\{11\bar{2}2\}\langle 11\bar{2}\bar{3}\rangle$ | $C^{II}$ $\{10\bar{1}1\}\langle 10\bar{1}\bar{2}\rangle$ | $C^{III}$ $\{11\bar{2}4\}\langle \bar{2}\bar{2}43\rangle$ | $T^{I}$ $\{10\bar{1}2\}\langle \bar{1}011\rangle$ | $T^{II}$ $\{11\bar{2}1\}\langle \bar{1}\bar{1}26\rangle$ |
|---|---|---|---|---|---|
| Twinning shear ($s$) | 0.218 | 0.099 | 0.218 | 0.173 | 0.631 |
| | $2(\gamma^2-2)/3\gamma$ | $(4\gamma^2-9)/4\sqrt{3}\gamma$ | $2(\gamma^2-2)/3\gamma$ | $(3-\gamma^2)/\sqrt{3}\gamma$ | $1/\gamma$ |

To investigate the accommodation mechanism of twinning, $\mathbf{D}^{\mathbf{t}}$ is always transformed into other coordinate systems, such as crystal system, another twinning system or neighboring grain crystal system. First, the coordinate rotation matrix from crystal system to twinning system is built.

$$\mathbf{R}_{\mathbf{tc}} = \begin{bmatrix} n_1 & n_2 & n_3 \\ p_1 & p_2 & p_3 \\ m_1 & m_2 & m_3 \end{bmatrix} \tag{2-41}$$

The transformation of $\mathbf{D}^{\mathbf{t}}$ between crystal $\mathbf{D}_{\mathbf{c}}^{\mathbf{t}}$ and twinning frame $\mathbf{D}_{\mathbf{t}}^{\mathbf{t}}$ can be obtained:

$$\mathbf{D}_t^t = \mathbf{R}_{tc} \cdot \mathbf{D}_c^t \cdot \mathbf{R}_{tc}^{-1} \tag{2-42}$$

The transformation of $\mathbf{D}^t$ from Twin 1 $\mathbf{D}_{t1}^{t1}$ to crystal to Twin 2 $\mathbf{D}_{t2}^{t1}$ is:

$$\mathbf{D}_{t2}^{t1} = \mathbf{R}_{t2c} \cdot \mathbf{D}_c^{t1} \cdot \mathbf{R}_{t2c}^{-1} = \mathbf{R}_{t2c} \cdot \mathbf{R}_{t1c}^{-1} \cdot \mathbf{D}_{t1}^{t1} \cdot \mathbf{R}_{t2c} \cdot \mathbf{R}_{t1c}^{-1} \tag{2-43}$$

The transformation of $\mathbf{D}^t$ from Grain1 $\mathbf{D}_{c1}^t$ to Grain 2 $\mathbf{D}_{c2}^t$ is:

$$\mathbf{D}_{c2}^t = \mathbf{R}_{c2s} \cdot \mathbf{D}_s^t \cdot \mathbf{R}_{c2s}^{-1} = \mathbf{R}_{c2s} \cdot \mathbf{R}_{c1s}^{-1} \cdot \mathbf{D}_{c1}^t \cdot \mathbf{R}_{c1s} \cdot \mathbf{R}_{c2s}^{-1} \tag{2-44}$$

### 2.2.4.3 Hydriding

The hydride coordinate systems of four hydride transformations (OR1-OR4 in Table 1.3) are expressed in the different coordination frame in HCP and FCC/FCT crystal (see Fig. 2.12), where OR1 transformation is from $\boldsymbol{x_1}$-$\boldsymbol{y_1}$-$\boldsymbol{z_1}$ (red) to $\boldsymbol{l_1}$-$\boldsymbol{m_1}$-$\boldsymbol{n_1}$ (green), OR2/OR4 from $\boldsymbol{x_1}$-$\boldsymbol{y_1}$-$\boldsymbol{z_1}$ (red) to $\boldsymbol{l_2}$-$\boldsymbol{m_2}$-$\boldsymbol{n_2}$ (blue) and OR3 from $\boldsymbol{x_1}$-$\boldsymbol{y_1}$-$\boldsymbol{z_1}$ (red) to $\boldsymbol{l_3}$-$\boldsymbol{m_3}$-$\boldsymbol{n_3}$ (pink). OR2 and OR4 have the same coordination frame but different interface planes and transformation mechanisms. These hydride transformations include both HCP-FCT/FCC structure and lattice transformation, the corresponding deformation gradient tensors are calculated by the following methods:

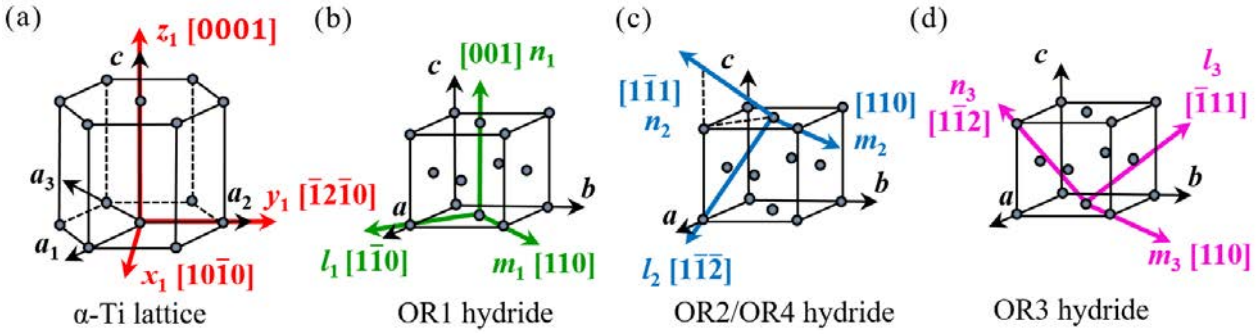


**Fig. 2.12** Crystal coordinate frame of α-Ti (red) and corresponding coordinate systems for OR1-OR4 hydride.

a) OR1 hydride transformation:

The HCP-FCT/FCC structure transformation of OR1 hydride is achieved by prismatic partial dislocation, which is accommodated by internal deformation mechanisms (slip or twinning) [100]. Thus only lattice transformation is considered to calculate the OR1 deformation gradient tensor. Three OR1 variants ($P_i$) are defined by $\{10\bar{1}0\}$ interface planes in the Table 2.3. The hydride frame of each variant is determined by interface normal along $\boldsymbol{x}$, basal plane normal $\boldsymbol{z}$ and $\boldsymbol{y}$ ($\boldsymbol{y}$=$\boldsymbol{z}$×$\boldsymbol{x}$). The

deformation gradient tenors are first calculated in the hydride frames and then transformed into crystal frame.

**Table 2.3** Hydride variants and coordinate frames of OR1 transitions

| Variant | $P_1$ | $P_2$ | $P_3$ |
|---|---|---|---|
| | $(10\bar{1}0)$ | $(01\bar{1}0)$ | $(\bar{1}100)$ |
| Coordinate frame | $\boldsymbol{x_1}$: $[10\bar{1}0]$<br>$\boldsymbol{y_1}$: $[\bar{1}2\bar{1}0]$<br>$\boldsymbol{z_1}$: $[0001]$ | $\boldsymbol{x_2}$: $[01\bar{1}0]$<br>$\boldsymbol{y_2}$: $[\bar{2}110]$<br>$\boldsymbol{z_2}$: $[0001]$ | $\boldsymbol{x_3}$: $[\bar{1}100]$<br>$\boldsymbol{y_3}$: $[\bar{1}\bar{1}20]$<br>$\boldsymbol{z_3}$: $[0001]$ |

HCP α-Ti is first transformed into γ-hydride ($a_\gamma$ = 0.420 nm, $c_\gamma$ = 0.470 nm) and then into δ-hydride ($a_\delta$ = 0.440 nm). The atomic spacing along coincident axes and corresponding lattice misfit of α-γ and γ-δ hydride transition are shown in Table 2.4. The lattice dilatation matrix $\mathbf{M_1}$ from α-Ti to FCT hydride is:

$$\mathbf{M_1} = \begin{bmatrix} r_x & 0 & 0 \\ 0 & r_y & 0 \\ 0 & 0 & r_z \end{bmatrix} \tag{2-54}$$

The lattice transformation matrix $\mathbf{M_2}$ from metastable γ-structure to FCC δ-hydride is:

$$\mathbf{M_2} = \begin{bmatrix} s_x & 0 & 0 \\ 0 & s_y & 0 \\ 0 & 0 & s_z \end{bmatrix} \tag{2-55}$$

The deformation gradient tensor of δ-hydride transformation in hydride frame is:

$$\mathbf{F_1} = \mathbf{M_2 M_1} = \begin{bmatrix} 1.218 & 0 & 0 \\ 0 & 1.055 & 0 \\ 0 & 0 & 0.940 \end{bmatrix} \tag{2-56}$$

**Table 2.4** Calculation of atomic spacing and misfit strain of OR1 hydride transformation

| Hydride frame | Coincident atomic spacing | | | | | | Misfit strain | |
|---|---|---|---|---|---|---|---|---|
| | α-Ti ($d_\alpha$) | | γ-hydride ($d_\gamma$) | | δ-hydride ($d_\delta$) | | α-γ: $d_\gamma/d_\alpha$ | γ-δ: $d_\delta/d_\gamma$ |
| $\boldsymbol{x}$ | $<10\bar{1}0>$ | $d_{\alpha x}=\sqrt{3}a_\alpha$ | $[1\bar{1}0]$ | $d_{\gamma x}=\sqrt{2}a_\gamma$ | $[1\bar{1}0]$ | $d_{\delta x}=\sqrt{2}a_\delta$ | $r_x=\frac{\sqrt{6}a_\gamma}{3a_\alpha}$ | $s_x=\frac{a_\delta}{a_\gamma}$ |
| $\boldsymbol{y}$ | $<\bar{1}2\bar{1}0>$ | $d_{\alpha y}=a_\alpha$ | $[110]$ | $d_{\gamma y}=\frac{a_\gamma}{\sqrt{2}}$ | $[110]$ | $d_{\delta y}=\frac{a_\delta}{\sqrt{2}}$ | $r_y=\frac{a_\gamma}{\sqrt{2}a_\alpha}$ | $s_y=\frac{a_\delta}{a_\gamma}$ |
| $\boldsymbol{z}$ | $<0001>$ | $d_{\alpha z}=c_\alpha$ | $[001]$ | $d_{\gamma z}=c_\gamma$ | $[001]$ | $d_{\delta z}=a_\delta$ | $r_z=\frac{c_\gamma}{c_\alpha}$ | $s_z=\frac{a_\delta}{c_\gamma}$ |

Then, the deformation gradient tensors of three hydride variants are transformed into crystal frame of α-Ti by the following equation:

$$\mathbf{F_1^{H\text{-}C}} = \mathbf{R_{hc}^{-1}} \cdot \mathbf{F_1} \cdot \mathbf{R_{hc}} \tag{2-57}$$

The coordinate rotation matrix from crystal frame to OR1 hydride frames are shown as follows:

$$\mathbf{R_{hc}} = \begin{bmatrix} \boldsymbol{x}^{\mathbf{T}} \\ \boldsymbol{y}^{\mathbf{T}} \\ \boldsymbol{z}^{\mathbf{T}} \end{bmatrix} \tag{2-58}$$

where $\boldsymbol{x}$, $\boldsymbol{y}$ and $\boldsymbol{z}$ are the coordinate axes of hydride frames in Table 2.3. The transformed deformation gradient tensors of three OR1 hydride variants can be found in Table 2.5.

**Table 2.5** Deformation gradient tensor $\mathbf{F_1^{H\text{-}C}}$ of OR1 hydride in crystal frame

| Deformation gradient tensor $\mathbf{F_1^{H\text{-}C}}$ | | |
|---|---|---|
| $P_1$ | $P_2$ | $P_3$ |
| $\begin{bmatrix} 1.218 & 0 & 0 \\ 0 & 1.055 & 0 \\ 0 & 0 & 0.940 \end{bmatrix}$ | $\begin{bmatrix} 1.096 & 0.071 & 0 \\ 0.071 & 1.177 & 0 \\ 0 & 0 & 0.940 \end{bmatrix}$ | $\begin{bmatrix} 1.096 & -0.071 & 0 \\ -0.071 & 1.177 & 0 \\ 0 & 0 & 0.940 \end{bmatrix}$ |

The transformation strain $\varepsilon_1$ along an arbitrary orientation can be calculated as follows:

$$\varepsilon_1 = (|\boldsymbol{v}|-|\boldsymbol{u}|)/|\boldsymbol{u}| \tag{2-59}$$

where $\boldsymbol{v} = \mathbf{F_1^{H\text{-}C}}\boldsymbol{u}$, $|\boldsymbol{v}| = \sqrt{v_1^2+v_2^2+v_3^2}$ and $|\boldsymbol{u}| = \sqrt{u_1^2+u_2^2+u_3^2}$. The Matlab script for calculating the deformation tensors and transformation strains is attached in Appendix.

b) OR2 hydride transformation:

The OR2 phase transformation can be achieved by the passage of $1/3\langle 10\bar{1}0\rangle$ partial dislocations on the basal plane associated with lattice transformation [95]. Six OR2 variants are listed in the Table 2.6 defined by $\{10\bar{1}3\}$ interface planes and corresponding dislocation shear directions. The hydride frame of each variant is determined by shear direction along $\boldsymbol{x}$, shear plane normal $\boldsymbol{z}$ and $\boldsymbol{y}$ ($\boldsymbol{y}=\boldsymbol{z}\times\boldsymbol{x}$). The deformation gradient tenors are first calculated in the hydride frames and then transformed into crystal frame.

**Table 2.6** Hydride variants and coordinate frames of OR2 transitions

| Variant | $B_1$ | $B_2$ | $B_3$ | $B_4$ | $B_5$ | $B_6$ |
|---|---|---|---|---|---|---|
| | $(10\bar{1}3)[10\bar{1}0]$ | $(01\bar{1}3)[01\bar{1}0]$ | $(\bar{1}103)[\bar{1}100]$ | $(\bar{1}013)[\bar{1}010]$ | $(0\bar{1}13)[0\bar{1}10]$ | $(1\bar{1}03)[1\bar{1}00]$ |
| Coordinate frame | $\boldsymbol{x_1}$: $[10\bar{1}0]$<br>$\boldsymbol{y_1}$: $[\bar{1}2\bar{1}0]$<br>$\boldsymbol{z_1}$: $[0001]$ | $\boldsymbol{x_2}$: $[01\bar{1}0]$<br>$\boldsymbol{y_2}$: $[\bar{2}110]$<br>$\boldsymbol{z_2}$: $[0001]$ | $\boldsymbol{x_3}$: $[\bar{1}100]$<br>$\boldsymbol{y_3}$: $[\bar{1}\bar{1}20]$<br>$\boldsymbol{z_3}$: $[0001]$ | $\boldsymbol{x_4}$: $[\bar{1}010]$<br>$\boldsymbol{y_4}$: $[1\bar{2}10]$<br>$\boldsymbol{z_4}$: $[0001]$ | $\boldsymbol{x_5}$: $[0\bar{1}10]$<br>$\boldsymbol{y_5}$: $[2\bar{1}\bar{1}0]$<br>$\boldsymbol{z_5}$: $[0001]$ | $\boldsymbol{x_6}$: $[1\bar{1}00]$<br>$\boldsymbol{y_6}$: $[11\bar{2}0]$<br>$\boldsymbol{z_6}$: $[0001]$ |

To realize HCP-FCT/FCC structure transition, shearing along <10$\bar{1}$0> is necessary to change of stacking sequence AB/ABC, leading to γ/δ-phase generation. By physical or crystallographic studies, we know the shear plane normal $\boldsymbol{p_0}$ and the shear vector $\boldsymbol{d} = n\boldsymbol{d_0}$, $\boldsymbol{p_0}$ and $\boldsymbol{d_0}$ are taken as unit vectors and identified on the basis $\boldsymbol{x_1}$-$\boldsymbol{y_1}$-$\boldsymbol{z_1}$ frame, then the pure shear matrix can be written directly:

$$\mathbf{S} = \mathbf{I} + n\boldsymbol{d_0}\,\boldsymbol{p_0}^{\mathbf{T}} \tag{2-45}$$

where $n$ is shear of Shockley dislocation ($\boldsymbol{b}$ = 1/3 <10$\bar{1}$0>):

$$n = \frac{|\boldsymbol{b}|}{\text{basal plane spacing}} = \frac{a_\alpha/\sqrt{3}}{c_\alpha} \tag{2-46}$$

with lattice parameter $a_\alpha$ = 0.295 nm and $c_\alpha$ = 0.468 nm. The shear matrix of $B_1$ variant ($\boldsymbol{d_0}$ [100] and $\boldsymbol{p_0}$ [001]) can be written as:

$$\mathbf{S} = \mathbf{I} + n\begin{bmatrix}1\\0\\0\end{bmatrix}[001] = \begin{bmatrix}1&0&0\\0&1&0\\0&0&1\end{bmatrix} + \frac{a_\alpha}{\sqrt{3}\,c_\alpha}\begin{bmatrix}0&0&1\\0&0&0\\0&0&0\end{bmatrix} \tag{2-47}$$

The lattice dilatation of hydride transformation includes two steps. HCP α-Ti is first transformed into γ-hydride ($a_\gamma$ = 0.420 nm, $c_\gamma$ = 0.470 nm) and then into δ-hydride ($a_\delta$ = 0.440 nm). The atomic spacing along coincident axes and corresponding lattice misfit of α-γ and γ-δ hydride transition are shown in Table 2.7.

**Table 2.7** Calculation of atomic spacing and misfit strain of OR2 hydride transformation

| Hydride frame | Coincident atomic spacing | | | | | | Misfit strain | |
|---|---|---|---|---|---|---|---|---|
| | α-Ti ($d_\alpha$) | | γ-hydride ($d_\gamma$) | | δ-hydride ($d_\delta$) | | α-γ: $d_\gamma/d_\alpha$ | γ-δ: $d_\delta/d_\gamma$ |
| $\boldsymbol{x}$ | <10$\bar{1}$0> | $d_{\alpha x}=\sqrt{3}a_\alpha$ | [$\bar{1}$12] | $d_{\gamma x}=\sqrt{\frac{a_\gamma^2}{2}+c_\gamma^2}$ | [$\bar{1}$12] | $d_{\delta x}=\frac{\sqrt{6}a_\delta}{2}$ | $r_x=\frac{\sqrt{a_\gamma^2+2c_\gamma^2}}{\sqrt{6}a_\alpha}$ | $s_x=\frac{\sqrt{3}a_\delta}{\sqrt{a_\gamma^2+2c_\gamma^2}}$ |
| $\boldsymbol{y}$ | <$\bar{1}$2$\bar{1}$0> | $d_{\alpha y}=a_\alpha$ | [110] | $d_{\gamma y}=\frac{a_\gamma}{\sqrt{2}}$ | [110] | $d_{\delta y}=\frac{a_\delta}{\sqrt{2}}$ | $r_y=\frac{a_\gamma}{\sqrt{2}a_\alpha}$ | $s_y=\frac{a_\delta}{a_\gamma}$ |
| $\boldsymbol{z}$ | <0001> | $d_{\alpha z}=c_\alpha$ | [1$\bar{1}$1] | $d_{\gamma z}=\frac{2\sqrt{2a_\gamma^2+c_\gamma^2}}{3}$ | [1$\bar{1}$1] | $d_{\delta z}=\frac{2a_\delta}{\sqrt{3}}$ | $r_z=\frac{2\sqrt{2a_\gamma^2+c_\gamma^2}}{3c_\alpha}$ | $s_z=\frac{\sqrt{3}a_\delta}{\sqrt{2a_\gamma^2+c_\gamma^2}}$ |

The lattice dilatation matrix $\mathbf{M_1}$ from α-Ti to FCT hydride is:

$$\mathbf{M_1} = \begin{bmatrix} r_x & 0 & 0 \\ 0 & r_y & 0 \\ 0 & 0 & r_z \end{bmatrix} \tag{2-48}$$

The lattice transformation matrix $\mathbf{M_2}$ from metastable γ-structure to FCC δ-hydride is:

$$\mathbf{M_2} = \begin{bmatrix} s_x & 0 & 0 \\ 0 & s_y & 0 \\ 0 & 0 & s_z \end{bmatrix} \tag{2-49}$$

Combining these steps, the deformation gradient tensor of δ-hydride transformation in hydride frame is:

$$\mathbf{F_2 = M_2 M_1 S} = \begin{bmatrix} 1.055 & 0 & 0.384 \\ 0 & 1.055 & 0 \\ 0 & 0 & 1.085 \end{bmatrix} \tag{2-50}$$

Then, the deformation gradient tensors of six hydride variants are transformed into crystal frame of α-Ti by the following equation:

$$\mathbf{F_2^{H\text{-}C}} = \mathbf{R_{hc}^{-1} \cdot F_1 \cdot R_{hc}} \tag{2-51}$$

The coordinate rotation matrix from crystal frame to OR2 hydride frames are shown as follows:

$$\mathbf{R_{hc}} = \begin{bmatrix} \boldsymbol{x}^{\mathbf{T}} \\ \boldsymbol{y}^{\mathbf{T}} \\ \boldsymbol{z}^{\mathbf{T}} \end{bmatrix} \tag{2-52}$$

Rhcwhere $\boldsymbol{x}$, $\boldsymbol{y}$ and $\boldsymbol{z}$ are the coordinate axes of hydride frames in Table 2.6. The transformed deformation gradient tensors of six OR2 hydride variants can be found in Table 2.8.

**Table 2.8** Deformation gradient tensor $\mathbf{F_2^{H\text{-}C}}$ of OR2 hydride in crystal frame

| Deformation gradient tensor $\mathbf{F_2^{H\text{-}C}}$ | | |
|---|---|---|
| $B_1$ | $B_2$ | $B_3$ |
| $\begin{bmatrix} 1.055 & 0 & 0.384 \\ 0 & 1.055 & 0 \\ 0 & 0 & 1.085 \end{bmatrix}$ | $\begin{bmatrix} 1.055 & 0 & 0.192 \\ 0 & 1.055 & -0.332 \\ 0 & 0 & 1.085 \end{bmatrix}$ | $\begin{bmatrix} 1.055 & 0 & 0.192 \\ 0 & 1.055 & 0.332 \\ 0 & 0 & 1.085 \end{bmatrix}$ |
| $B_4$ | $B_5$ | $B_6$ |
| $\begin{bmatrix} 1.055 & 0 & -0.192 \\ 0 & 1.055 & -0.332 \\ 0 & 0 & 1.085 \end{bmatrix}$ | $\begin{bmatrix} 1.055 & 0 & -0.192 \\ 0 & 1.055 & 0.332 \\ 0 & 0 & 1.085 \end{bmatrix}$ | $\begin{bmatrix} 1.055 & 0 & -0.384 \\ 0 & 1.055 & 0 \\ 0 & 0 & 1.085 \end{bmatrix}$ |

If an arbitrary vector $\boldsymbol{u}$ in the crystal frame of the α phase is transformed to $\boldsymbol{v}$ due to the hydriding transformation, the transformation strain $\varepsilon_2$ can be calculated as follows:

$$\varepsilon_2 = (|\boldsymbol{v}|-|\boldsymbol{u}|)/|\boldsymbol{u}| \tag{2-53}$$

where $\boldsymbol{v} = \mathbf{F}_2^{\mathbf{H\text{-}C}}\boldsymbol{u}$, $|\boldsymbol{v}| = \sqrt{v_1^2+v_2^2+v_3^2}$ and $|\boldsymbol{u}| = \sqrt{u_1^2+u_2^2+u_3^2}$. The Matlab script for calculating the deformation tensors and transformation strains is attached in Appendix.

c) OR3 and OR4 hydride transformation:

Up to now, detailed study on the formation mechanism with variant definition related to the OR3 and OR4 hydrides have not been done yet. Thus, for the strain calculation of OR3 and OR4 hydrides transformation, only lattice expansions are considered. The coincident coordinate systems of OR3 transformation is:

$\boldsymbol{x_1}$ : $[10\bar{1}0] \rightarrow [\bar{1}11]$

$\boldsymbol{y_1}$ : $[\bar{1}2\bar{1}0] \rightarrow [110]$

$\boldsymbol{z_1}$ : $[0001] \rightarrow [1\bar{1}2]$

The atomic spacing along coincident axes and corresponding lattice misfit of α-γ and γ-δ hydride transition are shown in Table 2.9.

**Table 2.9** Calculation of atomic spacing and misfit strain of OR3 hydride transformation

| Hydride frame | Coincident atomic spacing | | | | | | Misfit strain | |
|---|---|---|---|---|---|---|---|---|
| | α-Ti ($d_\alpha$) | | γ-hydride ($d_\gamma$) | | δ-hydride ($d_\delta$) | | α-γ: $d_\gamma/d_\alpha$ | γ-δ: $d_\delta/d_\gamma$ |
| $\boldsymbol{x_1}$ | $[10\bar{1}0]$ | $d_{\alpha x}=\sqrt{3}a_\alpha$ | $[\bar{1}11]$ | $d_{\gamma x}=\frac{2\sqrt{2a_\gamma^2+c_\gamma^2}}{3}$ | $[\bar{1}11]$ | $d_{\delta x}=\frac{2a_\delta}{\sqrt{3}}$ | $r_x=\frac{2\sqrt{2a_\gamma{}^2+c_\gamma{}^2}}{3\sqrt{3}a_\alpha}$ | $s_x=\frac{\sqrt{3}a_\delta}{\sqrt{2a_\gamma{}^2+c_\gamma{}^2}}$ |
| $\boldsymbol{y_1}$ | $[\bar{1}2\bar{1}0]$ | $d_{\alpha y}=a_\alpha$ | $[110]$ | $d_{\gamma y}=\frac{a_\gamma}{\sqrt{2}}$ | $[110]$ | $d_{\delta y}=\frac{a_\delta}{\sqrt{2}}$ | $r_y=\frac{a_\gamma}{\sqrt{2}a_\alpha}$ | $s_y=\frac{a_\delta}{a_\gamma}$ |
| $\boldsymbol{z_1}$ | $[0001]$ | $d_{\alpha z}=c_\alpha$ | $[1\bar{1}2]$ | $d_{\gamma z}=\sqrt{\frac{a_\gamma^2}{2}+c_\gamma^2}$ | $[1\bar{1}2]$ | $d_{\delta z}=\frac{\sqrt{6}a_\delta}{2}$ | $r_z=\frac{\sqrt{a_\gamma{}^2+2c_\gamma{}^2}}{\sqrt{2}c_\alpha}$ | $s_z=\frac{\sqrt{3}a_\delta}{\sqrt{a_\gamma{}^2+2c_\gamma{}^2}}$ |

The lattice transformation matrix from HCP α-Ti to FCT γ-hydride is:

$$\mathbf{M_1} = \begin{bmatrix} r_1 & 0 & 0 \\ 0 & r_2 & 0 \\ 0 & 0 & r_3 \end{bmatrix} \tag{2-60}$$

The lattice transformation matrix from γ-hydride to δ-hydride in the second step is:

$$\mathbf{M_2} = \begin{bmatrix} s_1 & 0 & 0 \\ 0 & s_2 & 0 \\ 0 & 0 & s_3 \end{bmatrix} \tag{2-61}$$

Thus, the deformation gradient tensor of OR3 α-Ti/δ-hydride transformation can be written as follows:

$$\mathbf{F_3} = \mathbf{M_2 M_1} = \begin{bmatrix} 0.994 & 0 & 0 \\ 0 & 1.055 & 0 \\ 0 & 0 & 1.151 \end{bmatrix} \tag{2-62}$$

The coordinate systems of OR4 transformation is:

$\boldsymbol{x_1}$ : $[10\bar{1}0] \rightarrow [\bar{1}12]$

$\boldsymbol{y_1}$ : $[\bar{1}2\bar{1}0] \rightarrow [110]$

$\boldsymbol{z_1}$ : $[0001] \rightarrow [1\bar{1}1]$

The atomic spacing along coincident axes and corresponding lattice misfit of α-γ and γ-δ hydride transition are shown in Table 2.10.

**Table 2.10** Calculation of atomic spacing and misfit strain of OR4 hydride transformation

| Hydride frame | Coincident atomic spacing | | | | | | Misfit strain | |
|---|---|---|---|---|---|---|---|---|
| | α-Ti ($d_\alpha$) | | γ-hydride ($d_\gamma$) | | δ-hydride ($d_\delta$) | | α-γ: $d_\gamma/d_\alpha$ | γ-δ: $d_\delta/d_\gamma$ |
| $\boldsymbol{x_1}$ | $[10\bar{1}0]$ | $d_{\alpha x}=\sqrt{3}a_\alpha$ | $[\bar{1}12]$ | $d_{\gamma x}=\sqrt{\frac{a_\gamma^2}{2}+c_\gamma^2}$ | $[\bar{1}12]$ | $d_{\delta x}=\frac{\sqrt{6}a_\delta}{2}$ | $r_x=\frac{\sqrt{a_\gamma^2+2c_\gamma^2}}{\sqrt{6}a_\alpha}$ | $s_x=\frac{\sqrt{3}a_\delta}{\sqrt{a_\gamma^2+2c_\gamma^2}}$ |
| $\boldsymbol{y_1}$ | $[\bar{1}2\bar{1}0]$ | $d_{\alpha y}=a_\alpha$ | $[110]$ | $d_{\gamma y}=\frac{a_\gamma}{\sqrt{2}}$ | $[110]$ | $d_{\delta y}=\frac{a_\delta}{\sqrt{2}}$ | $r_y=\frac{a_\gamma}{\sqrt{2}a_\alpha}$ | $s_y=\frac{a_\delta}{a_\gamma}$ |
| $\boldsymbol{z_1}$ | $[0001]$ | $d_{\alpha z}=c_\alpha$ | $[1\bar{1}1]$ | $d_{\gamma z}=\frac{2\sqrt{2a_\gamma^2+c_\gamma^2}}{3}$ | $[1\bar{1}1]$ | $d_{\delta z}=\frac{2a_\delta}{\sqrt{3}}$ | $r_z=\frac{2\sqrt{2a_\gamma^2+c_\gamma^2}}{3c_\alpha}$ | $s_z=\frac{\sqrt{3}a_\delta}{\sqrt{2a_\gamma^2+c_\gamma^2}}$ |

The lattice transformation matrix from HCP α-Ti to FCT γ-hydride is:

$$\mathbf{M_1} = \begin{bmatrix} r_1 & 0 & 0 \\ 0 & r_2 & 0 \\ 0 & 0 & r_3 \end{bmatrix} \tag{2-63}$$

The lattice transformation matrix from γ-hydride to δ-hydride is:

$$\mathbf{M_2} = \begin{bmatrix} s_1 & 0 & 0 \\ 0 & s_2 & 0 \\ 0 & 0 & s_3 \end{bmatrix} \tag{2-64}$$

Thus, the deformation gradient tensor of OR4 α-Ti/δ-hydride transformation can be written as follows:

$$\mathbf{F_4} = \mathbf{M_2M_1} = \begin{bmatrix} 1.055 & 0 & 0 \\ 0 & 1.055 & 0 \\ 0 & 0 & 1.085 \end{bmatrix} \tag{2-65}$$

## 2.3 Chapter summary

In this chapter, the experimental procedures and crystallographic calculation principles used in this work were given. The research results are presented in the following chapters. In Chapter 3, orientation dependence and variant selection of hydride precipitation was investigated. Multi-dimensional characterization of hydride layer and the plastic accommodation induced by hydride transformation are explored in Chapter 4. Chapter 5 studied the effect of hydride precipitation on the mechanical properties of CP-Ti by nanoindentation compression and tensile deformation.

# Chapter 3 Crystallographic orientation dependence of hydride precipitation in commercial pure titanium

Contents



## 3.1 Introduction

Long et al. [105] examined the microstructure of a hydride blister grown in a Zircaloy-4 specimen, indicating that the orientation of parent α-grain can significantly influence hydride transformation. The hydride precipitation is less preferential in the parent grains with *c*-axis away from the normal direction. However, the reason for the crystal orientation dependence on hydride transformation has never been thoroughly researched. Zirconium and Titanium alloys benefit from a huge literature because they are widely used in the nuclear industry due to their low neutron absorption, good mechanical properties and excellent high-temperature corrosion resistance. The embrittlement induced by hydrogen limits their performance. Crystal orientation is an important factor for hydride precipitation in alloys.

In this chapter, we investigate the orientation dependence of hydride precipitation in commercially pure titanium via interrupted in-situ electron backscatter diffraction (EBSD)

measurements. The deformation gradient tensor based accommodation was used to explore the origin of orientation dependence and hydride variant selection.

### 3.2 Experimental process

In the current work, the material used was rolled commercially pure titanium T40 (ASTM grade 2) sheet with the thickness of 1.5 mm, which was first annealed under high vacuum condition at 800 ºC for 3 h. The obtained material was fully recrystallized with an average grain size of ~30 μm and the texture is a typical split basal texture with basal pole oriented ±20° away from **ND** of the sheet towards the transverse direction (**TD**). The specimens were charged with hydrogen under an applied current density of 2 $kA/m^2$ for 168 h. Under this condition, enough hydrides can precipitate on the diffusion surface and the sample is not over-corroded. A hydrogen concentration of 123 wt ppm was measured by thermal desorption analysis using the analyzer G8 GALILEO.

To obtain diffusion surfaces with different textures, two sets of samples are prepared, i.e., hydrogen diffusion direction is along **ND** of the rolled titanium sheet and along the rolling direction. The former set is designated as Sample A and the latter one as Sample B. Interrupted in-situ microstructural observation before and after hydrogen charging was performed by EBSD measurements. In addition, to observe the microstructure of hydride nucleation in the Region I of hydride layer (see Fig. 2.2), another sample was prepared with **ND** parallel to diffusion direction like Sample A. Especially, it is difficult to accurately distinguish multiple hydride phases (FCC and FCT) by EBSD. Thus, only FCC δ-hydride, the most prevalent hydride phase, was chosen as indexed phase during EBSD measurements on the hydrogen-charged samples for determining the orientation relationship between the hydride precipitation and the parent grain. To save the characterization time and obtain enough information for statistics, Jeol-6490 was used to make EBSD measurements in large area at a step size of 0.5 μm. Specifically, EBSD patterns were acquired on a Jeol-6500F for obtaining more detailed examination of hydrides platelet at a step size of 0.1 μm.

### 3.3 Character of hydride layer

#### 3.3.1 Microstructure characterization before and after hydrogen charging

In order to determine the microstructure of the initial α-Ti grains and the produced hydrides, EBSD maps were acquired on the diffusion surface of Sample A and Sample B (Surface A and Surface B) before and after hydrogen charging. Fig. 3.1a and c present the microstructure of the

initial material with equiaxed grains after heat treatment in form of inverse pole figure (IPF) map, where the $\boldsymbol{X_3}$ axis (normal direction of the surface or diffusion direction of hydrogen) is projected with the shown color bar. The length direction and width direction are defined as $\boldsymbol{X_1}$ and $\boldsymbol{X_2}$, respectively. The average grain size of Sample A and Sample B is 30.6±17.2 and 29.4±16.4 μm, respectively. The observation plane in Fig. 3.1 is diffusion surface. The scattered points of the grains on the two surfaces are presented in the IPFs shown in Fig. 3.1a and c. The diffusion direction is close to <0001> of most grains on Surface A, while it is away from <0001> of the grains on Surface B. Thus, almost all kinds of orientations can be obtained from these two surfaces to investigate the orientation dependence of hydride precipitation.

After hydrogen charging, the microstructure is shown in Fig. 3.1b and d, in forms of phase map. In the phase maps, the blue color refers to the transformed FCC δ-hydride, while the red is the remnant HCP α-Ti phase. The grains appearing in blue in phase map are preferential for hydride formation, while the grains with large amount of red phase are difficult for hydriding. It should be noted that there are certain areas shown in white color, which are the non-indexed. Zero solutions generally arise when patterns are too blur for the automated band detection and indexing algorithms to work reliably. Blur patterns can arise for various reasons, for example highly deformed materials and fine-grained materials tend to produce patterns of lower quality due to resolution limitations related to the size of the interaction volume and the fine scale of the structure in such materials [136]. Indeed, large lattice misfit is caused due to the phase transformation from HCP α-Ti to FCC δ-hydride [91]. The non-indexed grains are difficult to accommodate the distortion of hydride transition and thus are not considered for hydride formation.

On Surface A in Fig. 3.1b, 57.33% of the total areas are identified as δ-hydride, 8.05% are α-Ti and the rest have zero solutions. As for the phase map of Surface B (Fig. 3.1d), significant increase of the red phase (HCP α-Ti, 57.02%) can be observed, while the proportions for the blue phase (FCC δ-hydride, 24.03%) and zero solutions decrease. Thus, Surface A is easier to form hydride than Surface B. Besides, the area fraction of the δ-hydride varies from one grain to another in phase maps, which indicates that the formation of hydride layer exhibits strong grain orientation dependence. This effect can be inferred from the comparison between the initial microstructure (Fig. 3.1a and c) and the hydrogen-charged microstructure (Fig. 3.1b and d), which will be discussed in details in the following sections.

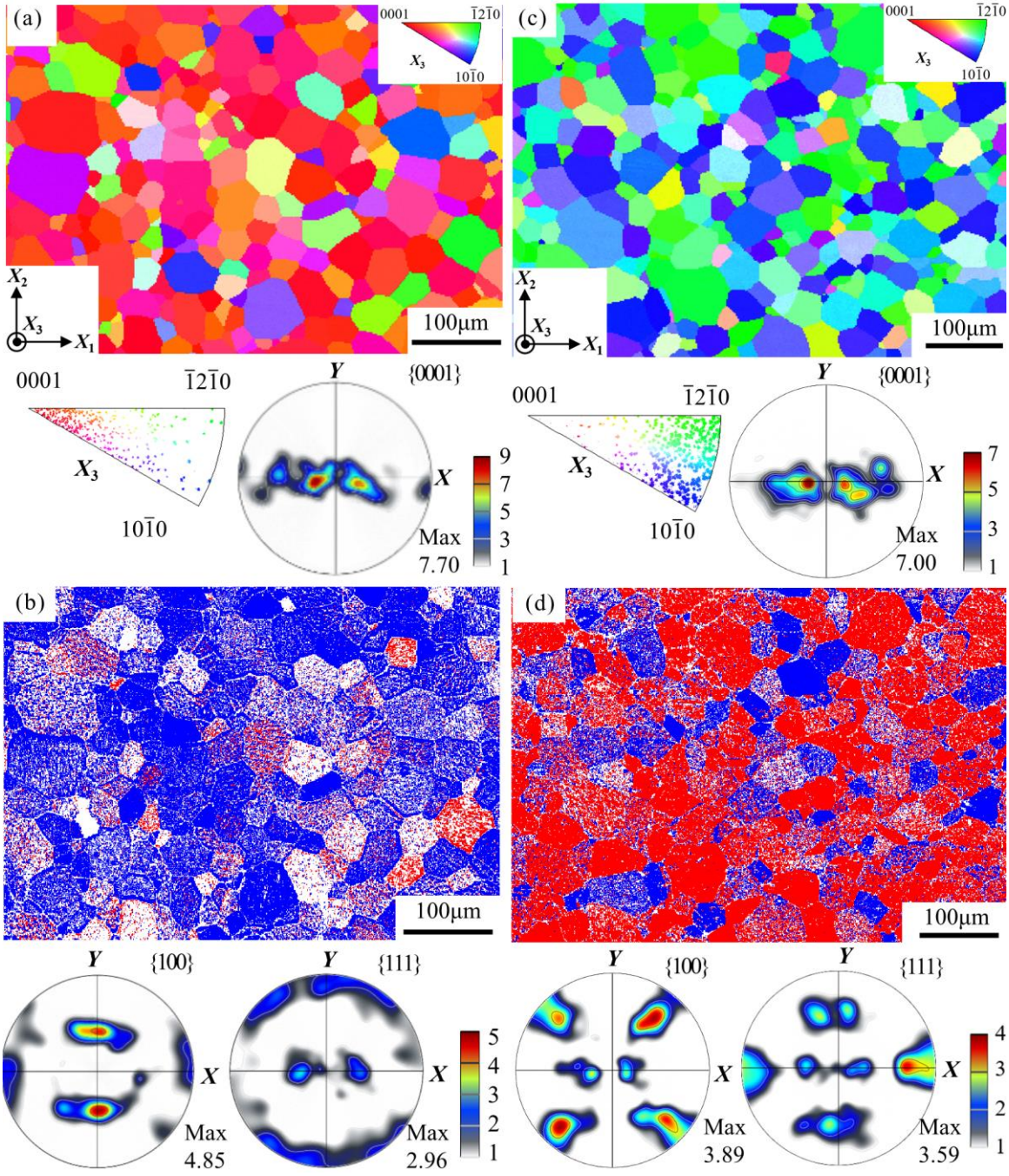


**Fig. 3.1 (a)** IPF map of initial grains on Surface A, corresponding IPF and pole figure **(b)** Phase map of Surface A after hydrogen charging and corresponding pole figures **(c)** IPF map of initial grains on Surface B, corresponding IPF and pole figure **(d)** Phase map of Surface B after hydrogen charging and corresponding pole figures (In phase maps, red: α-Ti, blue: δ-hydride, white: zero solution)

To compare the texture change during hydriding on two surfaces, all the grain orientations are projected under the same coordinate, which is set up as ***X*** // ***TD***, ***Y*** // ***RD*** and ***Z*** // ***ND***. The grain orientations of Surface A and Surface B (rolled α-Ti sheet after heat treatment) before hydrogen

charging are projected into {0001} pole figure (Fig. 3.1a and c). They exhibit similar split basal texture. After hydrogen charging, the {100} and {111} pole figures of δ-hydride (blue phase in phase map) are shown in Fig. 3.1b and d. The difference between the texture of hydride precipitation on Surface A and on Surface B suggests that the ORs of hydride transition on these two surface are different. Specially, at the same peak in {0001} pole figure of initial α-Ti, there are also two peaks in {001} pole figure of δ-hydride on Surface B, but no peaks in the {001} pole figure of surface A. It reveals that more hydrides follow OR1 ($\{0001\}_\alpha//\{001\}_\delta$ $<1\bar{2}10>_\alpha//<110>_\delta$) with the initial matrix on Surface B than on Surface A. There are also two peaks in {111} pole figure of δ-hydride at the same location of {0001} pole figure of α-Ti. However, $\{0001\}_\alpha//\{111\}_\delta$ is followed by both OR2 and OR4. Thus, the OR2 was identified by comparing their pole figures of interface planes, which are different between these two ORs (see Table 1.3). These results are in agreement with that of zirconium reported in [105]. The OR1 can be usually observed in the grains with *c*-axis away from the normal direction.

### 3.3.2 Classification of initial α-Ti grains

According to the different area fractions of hydride layer in grains after hydrogen charging (see in Fig. 3.1b and d), the initial grains of α-Ti can be divided into two groups as listed in Table 3.1. Group I represents the grains covered by hydride layer after hydriding (blue color in the phase maps). In this group, some grains with almost full blue in phase map means that they are fully covered by hydride layer, while some other grains with more than half blue phase are partially covered by hydride layer. According to the two ORs of hydride transition, the as-received grains in Group I are further divided into OR1 and OR2, which prefer to form OR1 hydride layer and OR2 hydride layer during hydriding, respectively. The grains with almost white (non-indexed) or red (remnant α-Ti matrix) in phase map are classified into Group II, which are difficult to form hydride layer during hydrogen charging. The number of the grains belonging to the two groups on Surface A and Surface B is shown in the Table 3.1.

Fig. 3.2a and d show the grains of Group I on Surface A and Surface B, respectively. By identifying the type of the orientation relationship between the initial α-Ti grain and the precipitated δ-hydride, the initial grains in Fig. 3.2a are further separated into OR1 grains (Fig. 3.2c) and OR2 grains (Fig. 3.2d). Excluding grains at the scanning border, 180 of the 186 grains in Fig. 3.2a are OR2 grains in Fig. 3.2c and only 6 are OR1 grains in Fig. 3.2b. On Surface B, just 7 in the total 62

of as-received α-Ti grains (Fig. 3.2f) which can form hydride layer are covered by OR2 hydride (see Fig. 3.2e) and the other 55 grains (Fig. 3.2e) form OR1 hydride layer. Therefore, OR2 hydride is easier to be formed on Surface A during hydriding, while the formation of OR1 hydride is more favorable on Surface B.

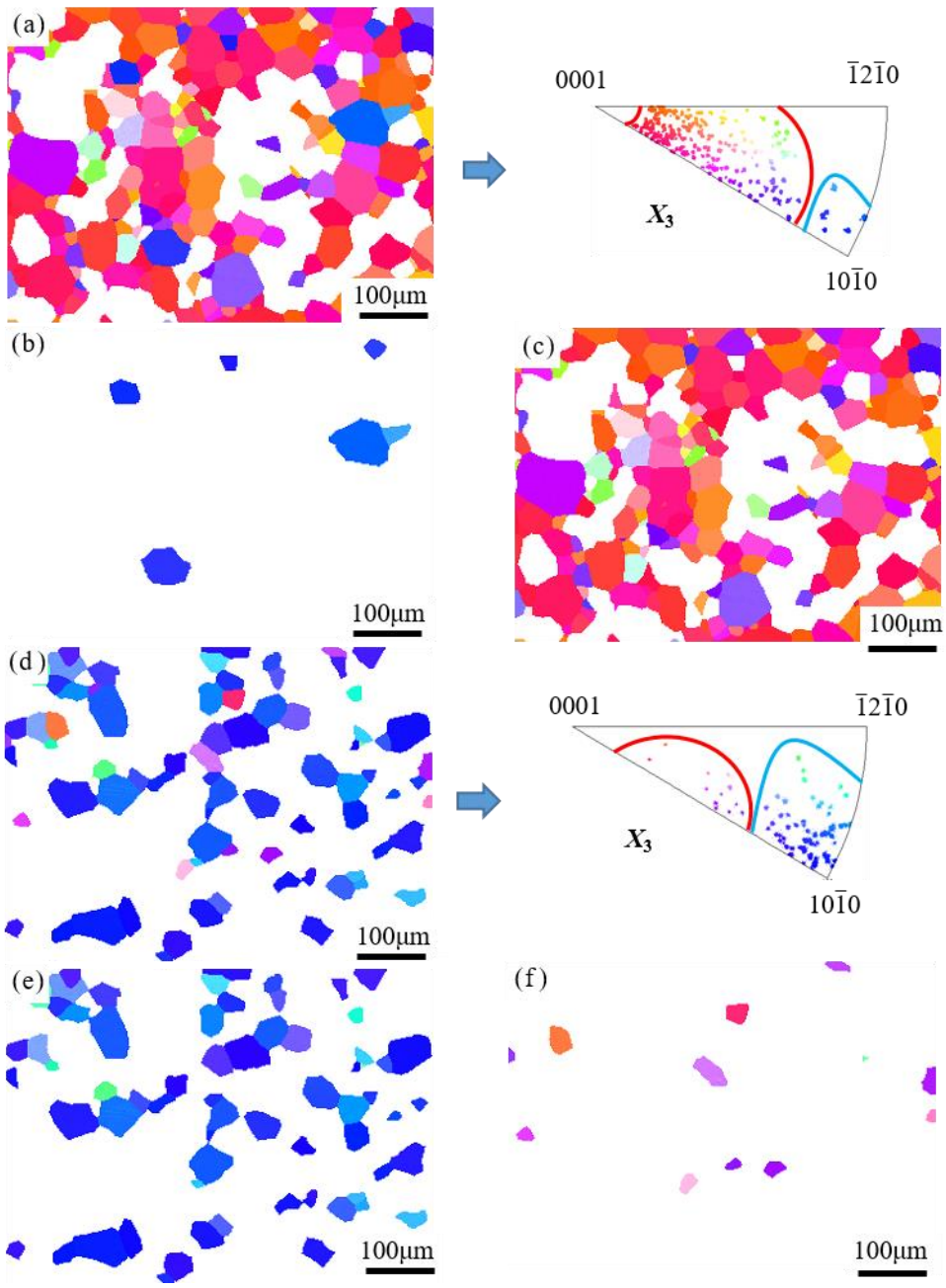


**Fig. 3.2 (a)** IPF map of initial Group I grains and corresponding IPF on Surface A **(b)** IPF map of initial OR1 grains on Surface A **(c)** IPF map of initial OR2 grains on Surface A **(d)** IPF map of initial Group I grains and corresponding IPF on Surface B **(e)** IPF map of initial OR1 grains on Surface B **(f)** IPF map of initial OR2 grains on Surface B.

**Table 3.1** Classification of grains on Surface A and Surface B

| Number of grains | Group I | | | Group II | Total |
|---|---|---|---|---|---|
| | OR1 | OR2 | Total | | |
| Surface A | 6 | 180 | 186 | 73 | 259 |
| Surface B | 55 | 8 | 63 | 295 | 358 |

Comparing the two IPFs of α-Ti grains in Fig. 3.2a and d, more orientations on Surface A are favorable for hydride formation than Surface B, which attributes to the formation of more hydride on Surface A. Moreover, the IPFs are also divided into two areas, i.e., the OR2 grains are located in the area inside red lines and the OR1 grains are concentrated in the corner of the IPF (inside blue line). The area inside red lines on Surface A (Fig. 3.2a) is larger than that on Surface B (Fig. 3.2d), which indicates more OR2 grain orientations on Surface A. Thus, more OR2 hydrides are formed on Surface A. Similarly, more OR1 grains formed on Surface B because more orientations on Surface B are favorable for OR1 hydride transition as revealed in Fig. 3.2d. Interestingly, some OR2 orientations on Surface A change into OR1 on Surface B. It seems that the type of hydrides can be influenced by the preferentially formed hydrides in the neighboring grains. Indeed, Conforto and Caillard [94] proposed that the elastic strains produced by hydride volume expansion play an important role on the close interconnection between precipitates.

### 3.3.3 Crystal orientation dependence of hydride precipitation

According to the grain microstructures after hydrogen charging as shown in the phase maps (Fig. 3.1b and d), four groups of initial Ti grains were chosen from Surface A or B into subsets to explore the orientation dependence of hydride precipitation. EBSD maps and corresponding IPFs are shown in Fig. 3.3. Fully-covered OR1 and OR2 hydride layer form within the grains in Fig. 3.3a and b after hydriding, respectively. Fig. 3.3c and d present two kinds of grains, which are difficult to form hydride layer. One kind of grains in Fig. 3.3c is almost non-indexed after hydriding and the other in Fig. 3.3d is nearly full of remnant α-Ti matrix.

The grains in Fig. 3.3a exhibit the most favorable orientations for OR1 transition with $\{10\bar{1}0\}$ plane parallel to surface. Fig. 3.3c shows that the orientations most favorable for OR2 transition are focused in the position where the $\boldsymbol{X}_3$ axis deviates 30° from <0001> direction to $<10\bar{1}0>$ direction, which implies that $\{10\bar{1}3\}$ plane is parallel to the diffusion surface. As shown in Fig.

3.3b and 3.3d, the most unfavorable orientations for the formation of hydride are in the position where *c*-axis and *a*-axis are normal to the diffusion surface, respectively.

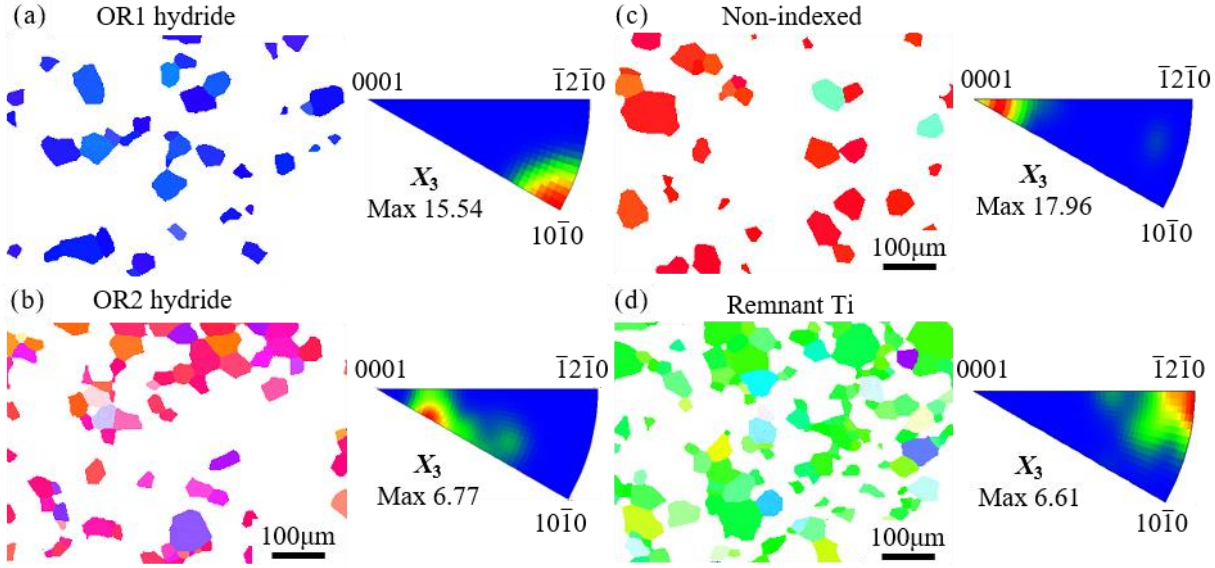


**Fig. 3.3** Subsets of initial Ti grains and corresponding IPF. **(a)** Grains forming full-covered OR1 hydride layer after hydrogen charging **(b)** Grains forming full-covered OR2 hydride layer after hydrogen charging **(c)** Grains which are non-indexed after hydrogen charging **(d)** Grains with remnant Ti after hydrogen charging.

According to the phase maps in Fig. 3.1b and d together with Fig. 3.3, more non-indexed grains (white color) exist on Surface A after hydriding than on Surface B. It results from more initial grains on Surface A with the orientation of *c*-axis parallel to the diffusion direction. More grains with *a*-axis parallel to the diffusion direction on Surface B result in more remnant α-Ti matrix (red color) after hydriding (Fig. 3.1d). The reason will be further discussed in Section 3.6.2.2.

### 3.4 Orientation relationship preference of α-Ti / δ-hydride transition

Four types of orientation relationships have been reported in [91–94], which are shown in Table 1.3 (Chapter 1). The volume strain of phase transition is calculated by the change of volume per atom ($V$) from α-Ti ($a_\alpha = 0.295$ nm, $c_\alpha = 0.468$ nm) to δ-hydride ($a_\delta = 0.440$ nm). The volume per atom is defined as the volume of a lattice cell of the crystal ($3\sqrt{3}\,a_\alpha^2 c_\alpha/2$ for HCP α-Ti and $a_\delta^3$ for FCC δ-hydride) divided by the nominal atom number of the lattice cell (6 atoms for HCP Ti and 4 for FCC hydride). The calculated results for α-Ti ($V_\alpha$) and δ-hydrides ($V_\delta$) are $1.76\times10^{-29}$ m$^3$ and $2.13\times10^{-29}$ m$^3$, respectively. The volume strain during α-Ti / δ-hydride transformation is constant for different ORs and can be obtained by: $(V_\delta - V_\alpha)/V_\alpha$, equal to 21.0%.

The phase transformation mechanisms for four OR hydrides are extremely different, which always include both structure and lattice transformations. For OR1 hydride transformation, there also exist a shear of 30° along $[1\bar{2}10]$ on prismatic plane in Fig. 4.13a. The shear is produced by prismatic partial dislocations, which bring the hexagonal atoms into face-centered arrangement, where atom shuffles are also needed for the rearrangement along the $\{10\bar{1}0\}$ invariant plane normal. Furthermore, a shear is always accompanied with rigid body rotation, which will destroy the undistorted $\{10\bar{1}0\}$ interface plane. Internal deformation mechanisms (like slip, twinning or shuffling) are necessary to accommodate the shear on $\{10\bar{1}0\}$ plane and achieve the experimental orientation relationship of OR1. Indeed, internal twins and dislocations were observed by TEM at hydride-matrix interfaces [100], but not detected by EBSD measurement in this work.

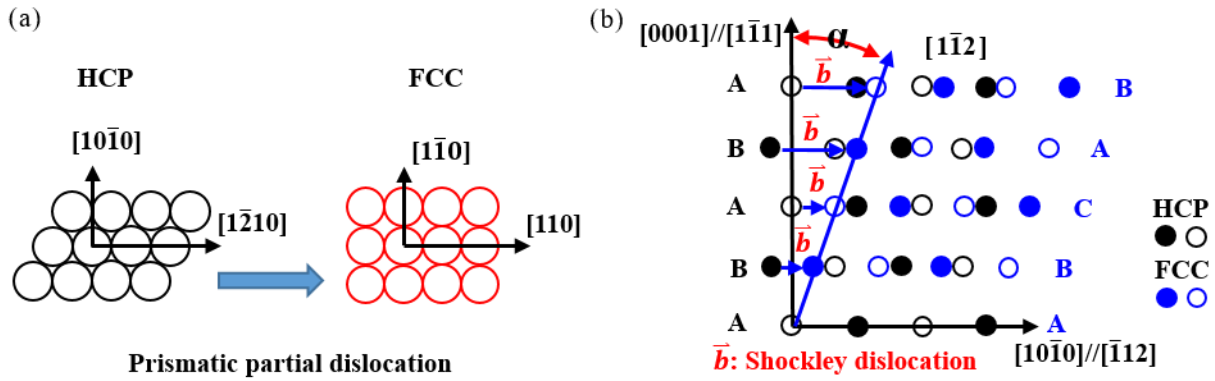


**Fig. 4.13** Illustration of HCP-FCC structure transformation of **(a)** OR2 and **(b)** OR1 hydride. The filled and open circles are in the different atom layers.

δ-hydride will be formed by the HCP-FCC transformation combined with lattice dilatation. The misfit parameters of the α-Ti / δ-hydride transition are examined by the calculation method proposed in [137]. The details can be found in Section 2.2.4.3 (Chapter 2). For the misfit strain of OR1, i.e., $\{0001\}_\alpha//\{001\}_\delta$ $<1\bar{2}10>_\alpha//<110>_\delta$, atomic spacing reduced by -6.0% from 0.234 nm to 0.220 nm along <0001>, while increased by 5.5% along $<1\bar{2}10>$ from 0.295 nm to 0.311 nm and by 21.8% along $<10\bar{1}0>$ from 0.511 nm to 0.622 on the basal plane. The large strain along $<10\bar{1}0>$ (21.8%) produces strong distortion on the basal plane. Conforto and Caillard [91] proposed that the transition of OR1 produces two opposite prismatic loops along the interface, contributing to the relaxation of misfit in the $<1\bar{2}10>$ direction.

As for OR2 transformation shown in Fig. 4.13b, a simple shear introduced by the slip of Shockley dislocation along $[10\bar{1}0]$ on (0001) plane converts the hexagonal lattice (filled circle) into cubic structure (open circle). The angle $\alpha$ produced by $\boldsymbol{b} = 1/3[10\bar{1}0]$ is around 20.0º:

$$\alpha = \arctan\left(\frac{|\boldsymbol{b}|}{c}\right) = \arctan\frac{a}{\sqrt{3}c} \tag{4-1}$$

where $a$ = 0.295 nm and $c$ = 0.468 nm are the lattice parameters of α-Ti. Weatherly et al. [100] claimed that shearing caused by 1/3 <10$\bar{1}$0> Shockley partial dislocations to realize the change of stacking sequence AB→ABC associated with δ-hydride transition could not occur easily if driven only by mechanical stress, but it is feasible under the influence of a chemical stress driven by the high hydrogen concentration.

For OR2, i.e., $\{0001\}_\alpha // \{1\bar{1}1\}_\delta$ $<1\bar{2}10>_\alpha // <110>_\delta$, the atomic spacing on the basal plane along the <1$\bar{2}$10> and <10$\bar{1}$0> direction expand from 0.295 nm to 0.311 nm and from 0.511 nm to 0.539 nm, respectively. The atomic spacing perpendicular to the basal plane expands along <0001> from 0.234 nm to 0.254 nm. These atomic spacing expansions in each direction corresponds to lattice strains of 5.5%, 5.5% and 8.6%, respectively. Compared with the misfit parameters of OR1, OR2 hydride transformation is less anisotropic. Therefore, OR2 hydride transition in α-Ti is more favorable than OR1. To accommodate the large misfit strains, shear loop dislocations on the basal plane with $b$ = 1/3 <1$\bar{2}$10> are punched out and extending in the direction of their Burgers vectors around the top and bottom ends of the hydride precipitate [93]. In addition, twins were also observed together with OR2 hydride precipitates [107,138].

In addition, the other two ORs (OR3 $\{10\bar{1}1\}_\alpha // \{1\bar{1}1\}_\delta$ $<1\bar{2}10>_\alpha // <110>_\delta$ and OR4 $\{\bar{1}011\}_\alpha // \{001\}_\delta$ $<1\bar{2}10>_\alpha // <110>_\delta$) are rarely observed. Up to now, detailed study on the structure transformation related to the OR3 and OR4 hydrides have not been reported. The misfit strains are calculated to explain the unfavorable OR3 hydride. The expansion strain along <0001> is 15.0%. Such a large strain along $c$-axis is difficult to be accommodated by dislocations in titanium. Interface energy also play important role on OR preference. The average density of coinciding atoms in the interface plane was calculated by Conforto and Caillard [91]. The ORs correspond to maximum order and then, to the minimum interface energy. However, the average density of coinciding atoms in the interface plane of OR3 is the lowest among these four ORs. Thus, the formation of OR3 hydride is less favorable than OR1 and OR2 hydrides.

OR4 and OR2 are quite close except different interface planes, which is $\{10\bar{1}1\}$ for OR4 and $\{10\bar{1}3\}$ for OR2. In fact, the average density of coinciding atoms in $\{10\bar{1}1\}$ and $\{10\bar{1}3\}$ interface planes are the same and higher than $\{10\bar{1}0\}$ interface plane of OR1 hydride. But, the slightly less favorable OR1 than OR2 hydride can be due to its larger distortion on the basal plane. As for the preference between OR2 and OR4 hydride, $\{10\bar{1}3\}$ is favorable interface plane for strain release during hydride transition (see the details in the next section). Therefore, OR1 and OR2 are the dominant orientation relationships in α-Ti.

### 3.5 Strain anisotropy of α-Ti / δ-hydride phase transformation

The δ-hydride phase transformation is multi-step process in zirconium and the shape evolution of the δ-hydride is highly dependent on the intermediate ζ and γ phase [96]. Different from zirconium, only one type of intermediate phase (γ phase) has been observed in titanium so far. In this section, anisotropic strain in α-Ti matrix caused by the two-step phase transformation is calculated based on the transformation of deformation gradient tensors to explore the origins of orientation dependence for the hydride formation.

First, different variants of OR1 and OR2 hydrides are defined in Table 3.2, OR1 hydride transformation only considers the lattice dilatation, while OR2 hydride variants are given by the interface plane with shear of Shockley dislocation. Their variants are notated as $P_i$ and $B_j$, respectively ($i$=1,2,3 and $j$=1,2,3…6). The deformation gradient tensors (**F**) of OR1 and OR2 transformations under ***x*-*y*-*z*** hydride frame are shown in Table 3.3. The transformed deformation gradient tensors of different hydride variants in crystal frame are shown in Table 2.5 and 2.8 in Chapter 2. The details of the calculation of the deformation gradient tensors are shown in Section 2.2.4.3. The diagonal elements, $F_{ij}$ ($i$=$j$, $i, j$ = 1, 2 3), mean elongation ($F_{ii}$> 1) or contraction ($F_{ii}$ < 1), whereas, the off diagonal elements, ( $F_{ij}$, $i \neq j$) indicate shear in the direction of $i$ on the plane normal to $j$.

For the tensor of OR1 transition in Table 3.3, there appear larger expansion along ***x*** axis and contraction along ***z*** axis. For the tensor of OR2 transition, $F_{11} = F_{22}$, it shows the isotropic misfit on the basal plane, while the misfit dilatation along ***c***-axis (***z*** axis), $F_{33}$, is higher. A large shear occurs on the basal plane in ***x*** direction, $F_{13}$, which achieve the hydride structure transformation. These anisotropic misfits indicate a possible platelet-like shape of δ-hydride precipitation and anisotropic growth to minimize the deformation energy.

**Table 3.2** Hydride variants of OR1 and OR2 transitions

| Hydride | Variant 1 | Variant 2 | Variant 3 | Variant 4 | Variant 5 | Variant 6 |
|---|---|---|---|---|---|---|
| OR1 hydride ($P_i$) | $P_1$ $(10\bar{1}0)$ | $P_2$ $(01\bar{1}0)$ | $P_3$ $(\bar{1}100)$ | | | |
| OR2 hydride ($B_j$) | $B_1$ $(10\bar{1}3)[10\bar{1}0]$ | $B_2$ $(01\bar{1}3)[01\bar{1}0]$ | $B_3$ $(\bar{1}103)[\bar{1}100]$ | $B_4$ $(\bar{1}013)[\bar{1}010]$ | $B_5$ $(0\bar{1}13)[0\bar{1}10]$ | $B_6$ $(1\bar{1}03)[1\bar{1}00]$ |

**Table 3.3** Deformation gradient tensors of OR1 and OR2 hydrides in hydride frame

| OR1 | OR2 |
|---|---|
| $\begin{bmatrix} 1.218 & 0 & 0 \\ 0 & 1.055 & 0 \\ 0 & 0 & 0.940 \end{bmatrix}$ | $\begin{bmatrix} 1.055 & 0 & 0.384 \\ 0 & 1.055 & 0 \\ 0 & 0 & 1.085 \end{bmatrix}$ |

The anisotropic misfit strains of α-Ti / δ-hydride transition were calculated along different crystal directions by the method in Section 2.2.4.3. The results are projected into the full inverse pole figure with the shown color bar (see Fig. 3.4). The Matlab scripts to draw these IPF maps can be found in Appendix. In Fig. 3.4, the red area shows the crystal directions with the largest misfit strain. The grains with these crystal directions normal to diffusion surface can relax the largest expansion misfit of hydride transition through the free surface. Thus, they are the most favorable ones for the hydride formation. Conversely, the most unfavorable grains are those with crystal directions in white area normal to diffusion surface.

For OR1 transition, the peak area (red) of the strain IPF for Variant 1 in Fig. 3.4a is around $\{10\bar{1}0\}$ plane normal with the maxima of 21.8%. It can be seen in Fig. 3.4b with all the six variants of OR1 hydride that the six high peak areas are around $\{10\bar{1}0\}$ plane normal, while the area with minimal strain value is located around ***c***-axis. Thus, for OR1 hydride transformation, the orientations with $\{10\bar{1}0\}$ and $\{0001\}$ plane parallel to the sample surface are the most preferential and unfavorable orientation, respectively. This conclusion for OR1 transition is in good agreement with the experimental result.

The strain IPF for Variant 1 of OR2 transition is shown in Fig. 3.4c. The high strain area (red) is nearly an ellipse with the maxima of 27.9% along the $\{10\bar{1}\ 2.6\}$ plane normal, which is 3.76° deviated from the most favorable orientation, i.e., $\{10\bar{1}3\}$ interface plane normal. In fact, the energy of phase transformation can be adjusted by anisotropy interfacial energy through reducing the tilt angle of the hydride interface plane towards basal plane [104]. Fig. 3.4d is a full strain IPF projected by the maximum strain of all six OR2 hydride variants during the transition. The strain map is six-

fold symmetric around *c*-axis. It shows that the grain orientations with $\{10\bar{1}3\}$ plane parallel to the sample surface are the most preferential and those with basal plane normal to the surface are the most unfavorable for OR2 hydride transformation.

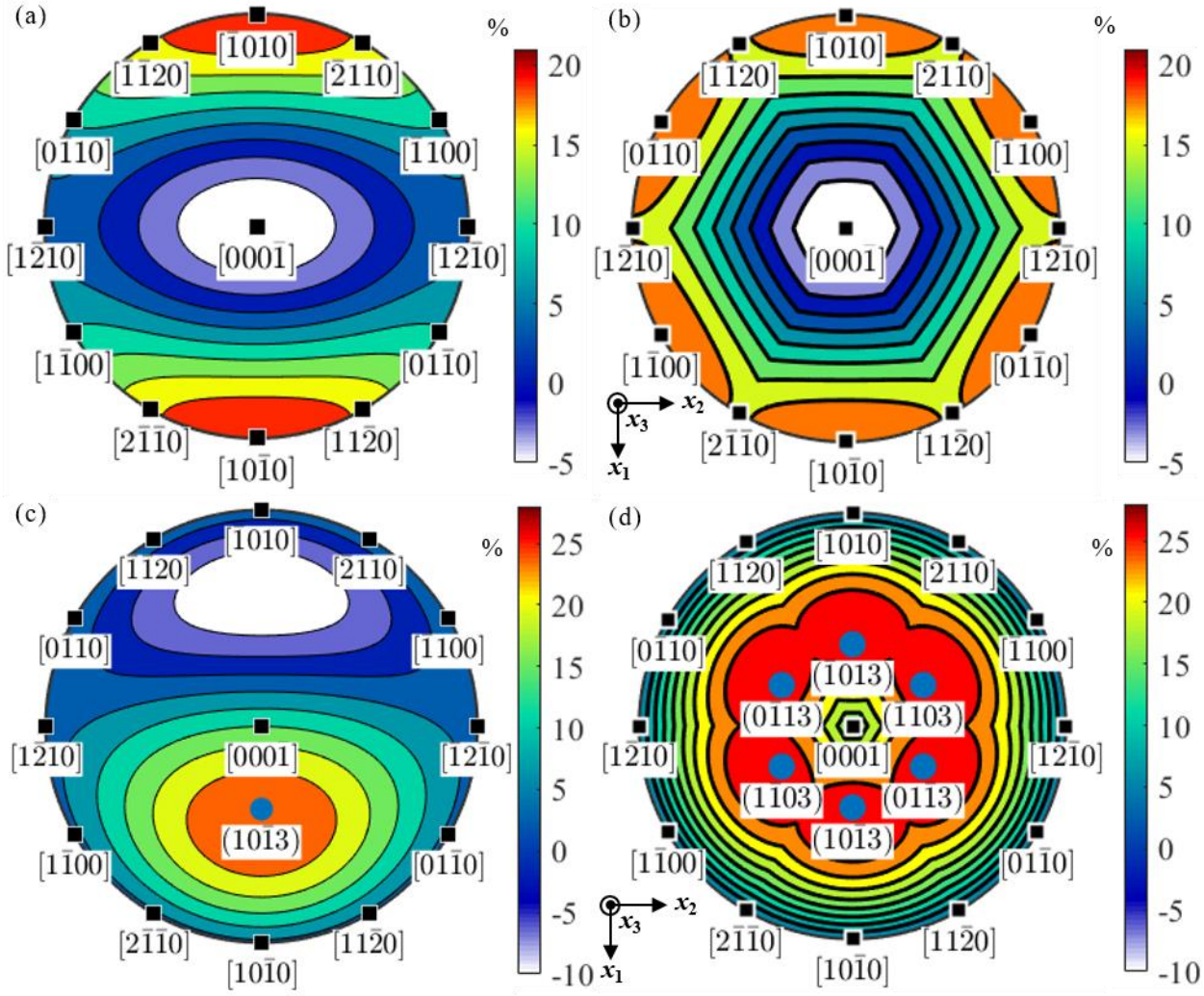


**Fig. 3.4** Full inverse pole figure of strain **(a)** Variant 1 of OR1 hydride **(b)** Six variants of OR1 hydride **(c)** Variant 1 of OR2 hydride **(d)** Six variants of OR2 hydride

## 3.6 Anisotropy of hydride nucleation

### 3.6.1 Microstructure of hydride platelets

During hydrogen absorption, hydride plates are formed randomly at the early stage on the Ti surface and eventually become a hydride layer [139]. Further understanding of the hydride nucleation process can be provided through the characterization of hydride platelets, which was conducted by removing the thin hydride layer from sample surface via electrolytic polishing.

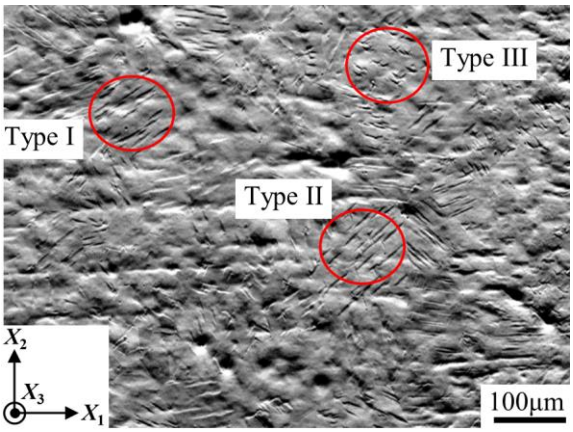


**Fig. 3.5** FSD map of α-Ti matrix with hydride platelets

The hydride platelets are imbedded in the α-Ti matrix, as shown in Fig. 3.5. The contrast of the Forescatter diodes (FSD) map (Fig. 3.5) based on diffraction events at each pixel indicates the deformation and strain gradient in the material. The different contrasts show the various degrees of lattice deformation upon the formed hydrides. The dark platelets contain large lattice deformation, while the hydrides with little distortion are light. Similar to the hydride layer, the microstructure of hydride platelets also varies from one grain to another. Three types of microstructures (inside red circles) are observed within the field-of-view: Type I (parallel hydride platelets), Type II (crossed hydride platelets) and Type III (clustered hydride platelets). The multiple morphologies of hydride platelets suggest that the hydride process involves variant selection of hydride precipitation and interaction of different variants. To characterize different microstructures of hydride platelets, detailed EBSD measurement was performed, which will be presented in next section.

### 3.6.2 Variant selection of hydride platelets

According to Section 3.5, the hydride variants with interface plane parallel to the diffusion surface is the most preferred due to the highest capacity of strain release. Thus, hydride variant selection can be evaluated by the distance ($d = |\boldsymbol{OP'}|$) between the interface plane pole of different variants (P′) and the center of pole figure (O), as shown in Fig. 3.6, where $\boldsymbol{X_1\text{-}X_2\text{-}X_3}$ is sample frame and $\boldsymbol{OP}$ ($|\boldsymbol{OP}|=1$) shows the interface plane normal of OR1 or OR2 hydride. The method for the calculation of $|\boldsymbol{OP'}|$ is presented in Section 2.2.3 (Chapter 2). The hydride variants with smaller $d$ among all the variants of OR1 or OR2 hydride are favorable to be selected because larger distortion can be accommodated through free surface. It should be noted that the value of $d$ cannot be used for the variant selection between OR1 and OR2 hydride.

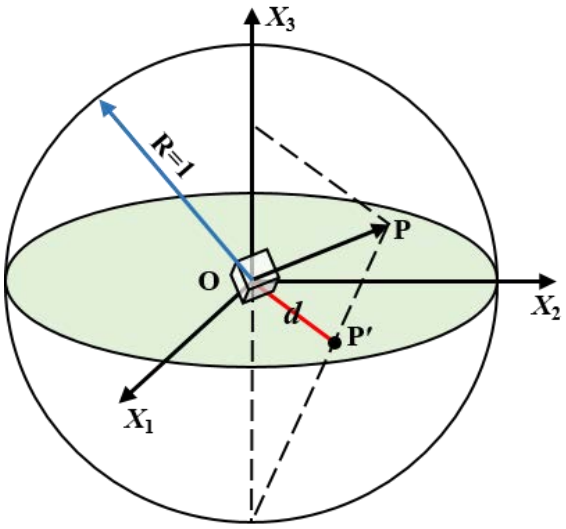


**Fig. 3.6** Illustration of the *d* value calculation.

To research the relationship between hydride nucleation and crystal orientation, EBSD measurements were performed on five typical grains. As presented in Fig. 3.7, five areas are labeled in the inverse pole figure (Areas 1-5). In Area 1 and Area 2, the grains are fully covered by hydride layer after hydriding. In Area 3, partially covered hydride layer is generated in the grains. All the grains with orientations in Areas 1-3 belong to Group I. In addition, Areas 4-5 represent the orientations of grains belonging to Group II. After hydriding, the grains in Area 4 are almost non-indexed and those in Area 5 are full of remnant α-Ti matrix. The morphologies of hydride platelets were acquired in five representative grains (Grains 1-5) with the orientations chosen from Areas 1-5, respectively (see Fig. 3.8 and Fig. 3.9).

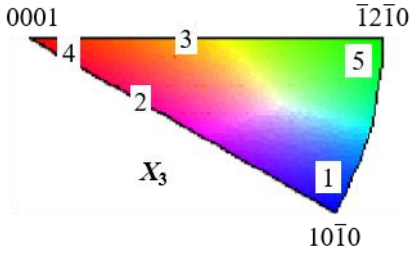


**Fig. 3.7** Positions of five areas in inverse pole figure

### 3.6.2.1 Grains with one or two preferential hydride variants (Group I)

Fig. 3.8a presents Grain 1 with the orientation favorable for OR1 hydride, i.e., $\{10\bar{1}0\}$ plane nearly parallel to the sample surface. Due to the large distortion on basal plane of OR1 transition,

the formation of hydride layer is difficult and the thickness is extremely thin. Therefore, after electrolytic polishing, only a few parallel platelets of OR1 hydrides are left in Grain 1 and they are always accompanied by some OR2 hydrides and micro twins (see Fig. 3.8b). From the pole figures in Fig. 3.8a, the hydride variants are $P_2$ and $B_5$. The $\{1\bar{1}0\}$ pole of $P_2$ is much closer to the center of pole figure than the $\{1\bar{1}0\}$ pole of B5. Besides, the value $d$ of $P_2$ and $B_5$ in Table 3.4 is the smallest among the variants of OR1 and OR2, respectively. Thus, $P_2$ is the most preferential hydride variant in Grain 1. It seems that $B_5$ is stimulated by the OR2 hydride in the neighboring grain (pink), which is favorable for OR2 transition like Grain 2.

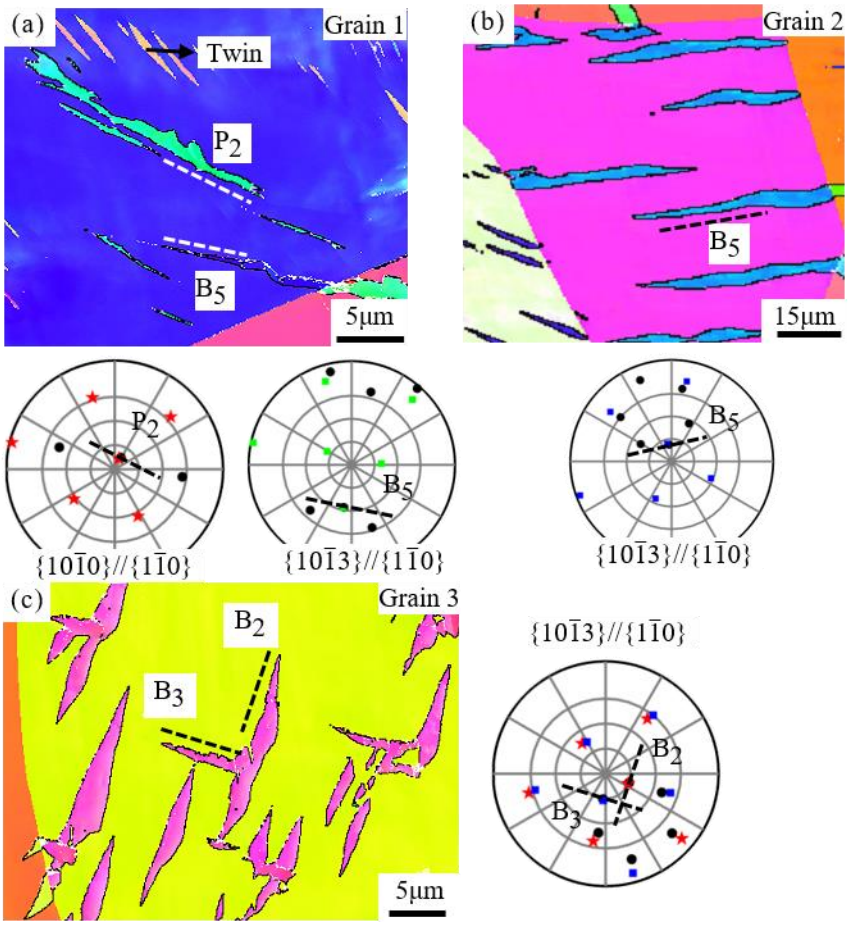


**Fig. 3.8** IPF maps of Group I grains with hydride platelets and corresponding pole figures of hydride interface planes **(a)** Grain 1, Euler angle: 167.3, 103.2, 34.0 **(b)** Grain 2, Euler angle: 17.7, 129.8, 23.9 **(c)** Grain 3, Euler angle: 31.8, 48.9, 1.8. The black dots represent the $\{10\bar{1}0\}$ or $\{10\bar{1}3\}$ interface planes of Ti matrix and the colors represent the $\{1\bar{1}0\}$ interface planes of hydrides. The dotted lines represent the traces of the corresponding hydride interface planes.

Grain 2 in Fig. 3.8b first form several parallel hydride platelets before fully covered by OR2 hydride layer. These platelets grow and merge with each other. As a result, they cover the whole

grain quickly and then hinder subsequent diffusion of hydrogen. In the $\{10\bar{1}3\}//\{1\bar{1}0\}$ pole figure (Fig. 3.8b), $B_5$ is the only hydride variant and the $\{1\bar{1}0\}$ pole of the selected variant is the closest to the center of the pole figure. For Grain 2, the value *d* of possible six OR2 variants is shown in the Table 3.4. Among all the variants of OR2 transition, $B_5$ has the minimum *d* of 0.169 and thus it is the most favorable OR2 variant. In conclusion, the grains with such orientation only favor one hydride variant. The $\{10\bar{1}3\}//\{1\bar{1}0\}$ interface plane of the selected variant is nearly parallel to the diffusion surface. Besides, Fig. 3.8b also shows that the hydrides near grain boundaries can stimulate the hydride nucleation in neighboring grains. The growth of both intragranular hydrides and adjoining hydrides at grain boundaries is achieved via an auto-catalytic mechanism [107].

**Table 3.4** The value *d* of OR1 and OR2 hydrides in Grain 1, Grain 2 and Grain 3 (no unit)

| OR1 | Grain 1 | Grain 2 | Grain 3 | OR2 | Grain 1 | Grain 2 | Grain 3 |
|---|---|---|---|---|---|---|---|
| $P_1$ | 0.543 | 0.725 | 0.977 | $B_1$ | 0.915 | 0.667 | 0.521 |
| $P_2$ | 0.121 | 0.366 | 0.449 | $B_2$ | 0.724 | 0.862 | 0.221 |
| $P_3$ | 0.634 | 0.614 | 0.468 | $B_3$ | 0.973 | 0.726 | 0.236 |
| | | | | $B_4$ | 0.594 | 0.413 | 0.540 |
| | | | | $B_5$ | 0.419 | 0.169 | 0.804 |
| | | | | $B_6$ | 0.641 | 0.350 | 0.794 |

For Grain 3, it is partially covered by hydride layer after hydriding. The hydrides inside with crossed-lamellar microstructure is shown in Fig. 3.8c. Two OR2 variants precipitate and intersect with each other. These two variants are $\{111\}<11\bar{2}>$ twins (similar to the observation in zirconium reported by Wang et al. [107]). The stress concentration caused by the boundaries between the two variants restrains their further growth. Thus, only partial grain is covered by hydride layer after hydriding. The pole figure in Fig. 3.8c shows that the two variants are $B_2$ and $B_3$. The $\{1\bar{1}0\}$ poles of them align most closely to the center of the pole figure and they have similar values (*d*) shown in Table 3.3. If two OR2 variants are selected simultaneously in one grain, they are definitely adjacent variants, i.e., $B_i$ and $B_{i+1}$. However, two or three OR1 variants formed in the same grain can only occur when they are in pairs with OR2 variants, which will be presented in Fig. 3.9b.

### 3.6.2.2 Grains with more than three hydride variants (Group II)

Grain 4, with *c*-axis normal to the sample surface, are almost non-indexed after hydriding. Fig. 3.9a shows the morphology of the microstructure after removing the non-indexed hydride layer via electropolishing. The fine platelets in Grain 4 are intercrossed. Some $\{10\bar{1}2\}<\bar{1}011>$ extension

twins are induced at the $\{10\bar{1}3\}$ interface of hydride platelets. According to the pole figures in Fig. 3.9a, all the six OR2 variants are formed in this grain. It is because that the $\{10\bar{1}3\}$ poles of α-Ti matrix are nearly six-fold symmetric around surface normal and the distance values (*d*) of them are similar (see Table 3.5). According to the misorientation between them, the six OR2 hydride variants can be divided into two groups: $B_i \rightarrow B_{i+1}$, $B_{i+3}$ and $B_{i+5}$ (twin 60° / $<11\bar{1}>$); $B_i \rightarrow B_{i+2}$ and $B_{i+4}$ (no obvious misorientation). The multi-directional deformation and complicated phase boundaries of multiple variants in Grain 4 produce Kikuchi patterns of lower quality, which cannot be identified. Thus, the reason why the grains with the orientations like Grain 4 are always non-indexed after hydrogen charging is the large distortion and complicated phase boundaries produced by the multiple variants.

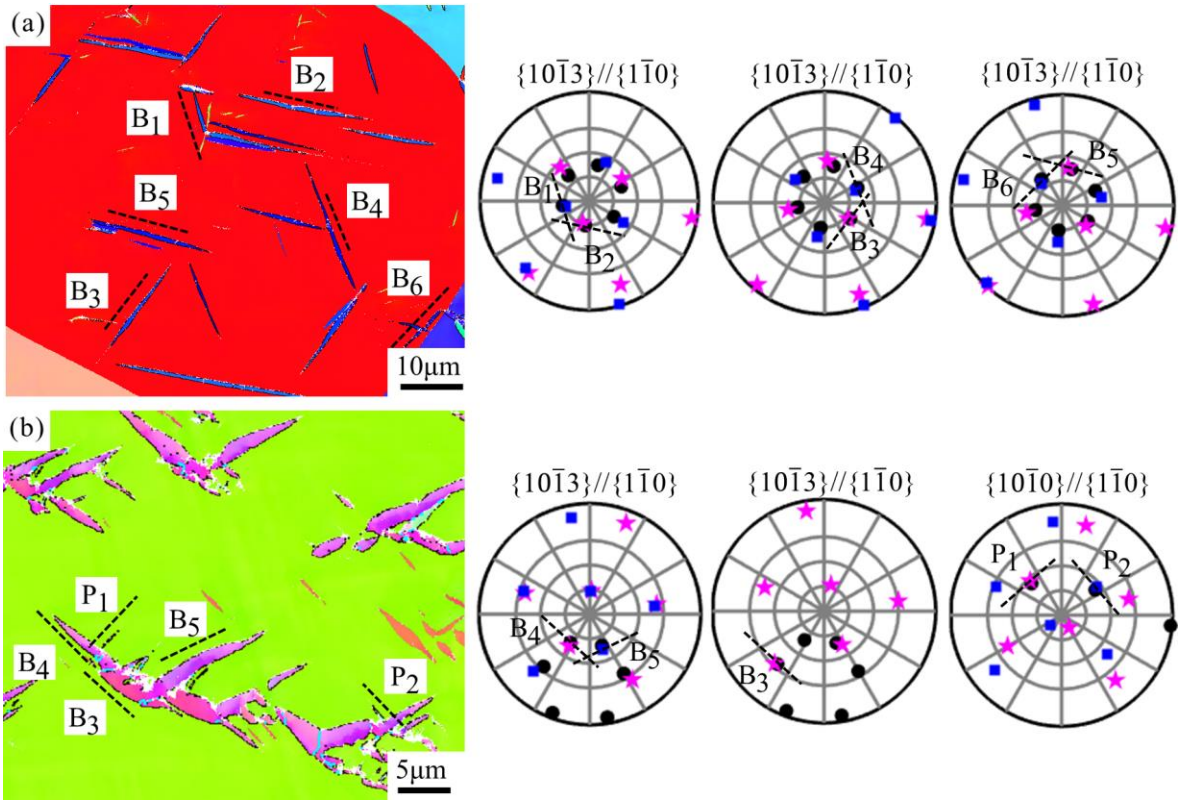


**Fig. 3.9** IPF maps of Group II grains with hydride platelets and corresponding pole figures of hydride interface planes **(a)** Grain 4, Euler angle: 155.2, 6.4, 43.3 **(b)** Grain 5, Euler angle: 175.0, 120.5, 58.5. In IPF map of (b), the blue curves represent the boundaries between hydride variants. In the pole figures of hydride interface planes, the black dots represent the $\{10\bar{1}3\}$ or $\{10\bar{1}0\}$ interface planes of Ti matrix and the colors represent the $\{1\bar{1}0\}$ interface planes of hydrides. The dotted line represents the trace of the corresponding hydride interface planes.

**Table 3.5** The value *d* of OR1 and OR2 hydrides in Grain 4 and Grain 5 (no unit)

| OR1 | Grain 4 | Grain 5 | OR2 | Grain 4 | Grain 5 |
|---|---|---|---|---|---|
| $P_1$ | 0.926 | 0.391 | $B_1$ | 0.244 | 0.951 |
| $P_2$ | 0.897 | 0.372 | $B_2$ | 0.224 | 0.963 |
| $P_3$ | 0.969 | 0.978 | $B_3$ | 0.270 | 0.638 |
| | | | $B_4$ | 0.326 | 0.318 |
| | | | $B_5$ | 0.341 | 0.307 |
| | | | $B_6$ | 0.304 | 0.620 |

The *a*-axis of Grain 5 is nearly parallel to the surface normal. After hydriding, the grains with this kind of orientation usually remain large amount of α-Ti matrix. The clustered hydride platelets are observed in Fig. 3.9b after electropolishing. From the pole figures in Fig. 3.9b, the clusters include both OR1 and OR2 hydride platelets. The OR1 variants are $P_1$ and $P_2$, and the OR2 hydride variants are $B_4$ and $B_5$. Occasionally, $B_3$ can be stimulated near the junction of B4 and B5. According to the misorientation, three OR1 variants are classified into two groups: $P_i \rightarrow P_{i+1}$ (30º / <0001>); $P_i \rightarrow P_{i+2}$ (no obvious misorientation). Besides, $P_i \rightarrow B_i$ and $B_{i+3}$ are often observed in pairs, with the misorientation of 60º around $<11\bar{2}0>$, i.e., *a*-axis of the surrounding titanium matrix. It is therefore speculated that the $P_i$ is stimulated by $B_i$ or $B_{i+3}$ through dislocation reaction on the basal plane of the Ti matrix. Furthermore, the formation of OR2 hydride is difficult in Grain 5 because the minimum value *d* (Table 3.4) is larger than that in Grain 1 and Grain 3 (Table 3.3). The finer OR1 hydride platelets show that OR1 hydride is more difficult to nucleate in Grain 5. Besides, the interaction of different OR1 and OR2 hydride variants in each cluster restrains the growth of hydride clusters. They finally result in large amount of remnant α-Ti matrix in the grain with the orientation like Grain 5 after hydriding.

### 3.7 Chapter summary

In this chapter, the orientation dependence of hydride precipitation formed by electrolytic hydrogen charging in commercially pure titanium was investigated via interrupted in-situ EBSD measurements.

After hydrogen charging on both **ND** and **RD** surface, two orientation relationships of α-titanium/δ-hydride transition (OR1: $\{0001\}_\alpha//\{001\}_\delta$ $<1\bar{2}10>_\alpha//<110>_\delta$ with interface plane $\{10\bar{1}0\}_\alpha//\{1\bar{1}0\}_\delta$ and OR2: $\{0001\}_\alpha//\{1\bar{1}1\}_\delta$ $<1\bar{2}10>_\alpha//<110>_\delta$ with interface plane

$\{10\bar{1}3\}_{\alpha}//\{1\bar{1}0\}_{\delta}$) are observed on diffusion surfaces. The texture of **ND** and **RD** surface are more favorable for respective OR1 and OR2 hydride transition.

The grain orientations with $\{10\bar{1}3\}$ and $\{10\bar{1}0\}$ interface planes parallel to the diffusion surface are most favorable for OR1 and OR2 hydride transition, respectively. However, *c*-axis and *a*-axis of α-Ti grains parallel to the diffusion direction are unfavorable orientations for the formation of hydride precipitation. The calculation of anisotropic strain caused by hydride transition in α-Ti matrix indicates that the direction with largest misfit strain is $\{10\bar{1}0\}$ interface plane normal for OR1 hydride and $\{10\bar{1}3\}$ interface plane normal for OR2 hydride. Thus, the grains which are more favorable for hydride formation can more effectively accommodate the strain of OR1 and OR2 hydride transition through free surface.

There appear three types of hydride platelet microstructures: parallel hydride platelets (Type I), crossed hydride platelets (Type II) and clustered hydride platelets (Type III). The hydride variants with interface plane parallel to the diffusion surface is selected due to the highest capacity of strain release. In the OR1 and OR2 favorable grain, less than two hydride variants are activated. For the grain with basal plane parallel to the sample surface, all the OR2 hydride variants can be formed. The interaction between the multiple variants leads to that the grain is non-indexed after hydrogen charging. The reason for lots of remnant α-Ti matrix in the grain with *a*-axis parallel to the surface normal is the difficulties on the growth of the formed clusters including both OR1 and OR2 hydrides.

# Chapter 4 Multi-dimensional hydride characterization and accommodation behavior in pure titanium

Contents



## 4.1 Introduction

Brittle hydride precipitation is an important reason for the hydrogen damage of titanium alloys in hydrogen-rich environment [102]. The hydride phase transformation is usually associated with large volume expansion (around 15%), which induces high internal stresses as the origin of a decreased toughness. The large misfit strain of hydride transition can be self-accommodated to improve hydride-induced material damage by plastic deformations, interactions between different variants, grain boundary and free surface relaxation, etc. The different accommodation behaviors induced by hydride transition are deserved to be researched. In this chapter, the surface and section microstructures of hydride layer were explored by EBSD characterization. Three micro accommodation behaviors were observed and will be discussed considering plastic accommodation, interaction between hydride variants and grain-boundary accommodation.

## 4.2 Experimental process

Four sets of CP-Ti samples were prepared for research in this chapter. Samples with different average grain sizes were achieved by different annealing processes: Sample A and Sample C (coarse grain sample) with an average grain size of ~50 μm was annealed at 800 ºC for 3 h; Sample B and Sample D (fine grain sample) with an average grain size of ~30 μm was annealed at 700 ºC for 3 h. The obtained materials were fully recrystallized with a typical split basal texture.

The microstructure evaluation of diffusion surface in Sample A and Sample B with different grain sizes were examined under EBSD before and after hydrogen charging for 24 h and 72 h, respectively. Sample C and Sample D were charged for 168h to investigate the accommodation behaviors inside diffusion layer. The hydride microstructure on **ND** surface inside hydride layer and the section microstructure of hydride layer formed on **RD** and **TD** surfaces were observed in Sample C, while cross-boundary hydride was researched on **ND** surface of Sample D. Specially, to examine the section microstructures of hydride layer formed in the grains with different orientations, both **RD** and **TD** surfaces of Sample C were prepared as diffusion surface. The details of sample preparation processes are shown in Section 2.1.3.

Microstructure characterization was performed using JSM 6490 SEM and JEOL 6500F field emission gun microscopy equipped with an EBSD camera and Aztec software package (Oxford Instruments). For doing statistical analysis on phase evolution, the hydride layer on large diffusion surfaces of Sample A and Sample B were indexed by both FCT γ-hydride ($a_\gamma$ = 0.420 nm, $c_\gamma$ = 0.470 nm) and FCC δ-hydride ($a_\delta$ = 0.440 nm). Only FCC δ-hydride was chosen as indexed phase for Sample C and D, due to that all the hydrides have transformed into FCC phase after 168 h.

## 4.3 Microstructure evolution of diffusion surface

The initial microstructures of as-received Sample A (coarse-grained) and Sample B (fine-grained) are shown in Fig. 4.1a and d in form of inverse pole figure (IPF) maps, where **ND** is projected with the shown color bar (see subgraph in Fig. 4.1a). After hydrogen charging for 24 h, the fraction of Ti matrix and γ-hydride are much higher in the coarse-grained Sample A (Fig. 4.1b) than that in the fine-grained Sample B (Fig. 4.1e), indicating a facilitating effect of grain boundaries on the formation of δ-hydride. While almost all of the Ti matrix and γ-hydride have transformed into δ-hydride after 72 h (as shown in Fig. 4.1c and f), revealing that the FCC δ-hydride has the highest stability during room temperature hydrogen charging. Noting that, certain grains in the

phase maps are always non-indexed because of large lattice distortion. The fact that higher percentage of zero solutions always appear in the grains with *c*-axis nearly parallel to the hydrogen diffusion direction has been explored in Section 3.2.3 (Chapter 3). Inside such grains, Kikuchi patterns are too blur to be detected due to the multi-directional deformation and complicated phase boundaries of multiple hydride variants.

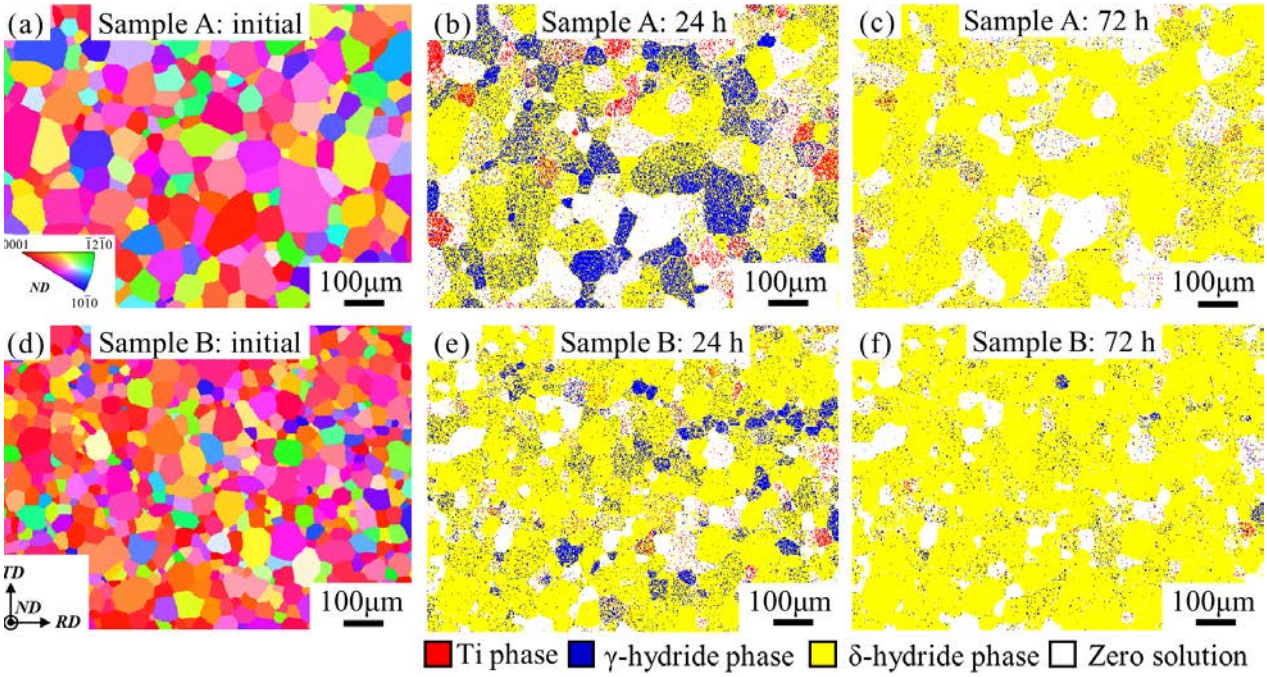


**Fig. 4.1 (a)** IPF map of initial grains in Sample A with coarse grain. **(b)** Phase map after hydrogen charging for 24 h. **(c)** Phase map after hydrogen charging for 72 h. **(d)** IPF map of initial grains in Sample B with fine grain. **(e)** Phase map after hydrogen charging for 24 h. **(f)** Phase map after hydrogen charging for 72 h. In the phase maps, red: Ti matrix, blue: γ-hydride, yellow: δ-hydride, white: zero solution.

In order to clarify the phase evolution process of hydride layers during hydrogen charging, the phase components in Sample A and B were further plotted in form of bar chart (Fig. 4.2) according to the data from EBSD measurements. In Fig. 4.2, red label refers to Ti matrix, while yellow and blue are δ-hydride and γ-hydride respectively, white is zero solution. Before hydriding charging, there appears single Ti phase in both samples. The evolution of Sample A is observed first.

After hydrogen charging for 24 h, close to 100% of the Ti phase has transformed into hydrides (γ and δ phase) and/or non-indexed areas. Due to the highest stability, the FCC δ-hydride occupy the majority of the diffusion surface rapidly during hydriding process, the surface fraction of δ phase (45%) is much higher than that of γ-phase (13%) after 24 h charging. The proportion of δ-

hydride continually increases with further hydrogen atoms diffusion, consuming the γ-hydride phase. After 72 hours, γ-hydride nearly disappears and the diffusion surface consists of only δ-hydride and non-indexed areas. According to the observation, metastable γ-hydrides can be firstly formed under the chemical force driven by the high hydrogen concentration in the titanium matrix, but gradually transformed into the stable FCC structure over time. It is worth mentioning that the non-indexed areas also occupy a large proportion of the diffusion surface after 24 h charging, but slightly decreases during hydrogen diffusion from 24 h to 72 h. This change indicates the activation of some accommodation modes that relax the hydride distortion. Indeed, both dislocations and twins have been observed to accommodate the misfit strain of hydride transition [93,100].

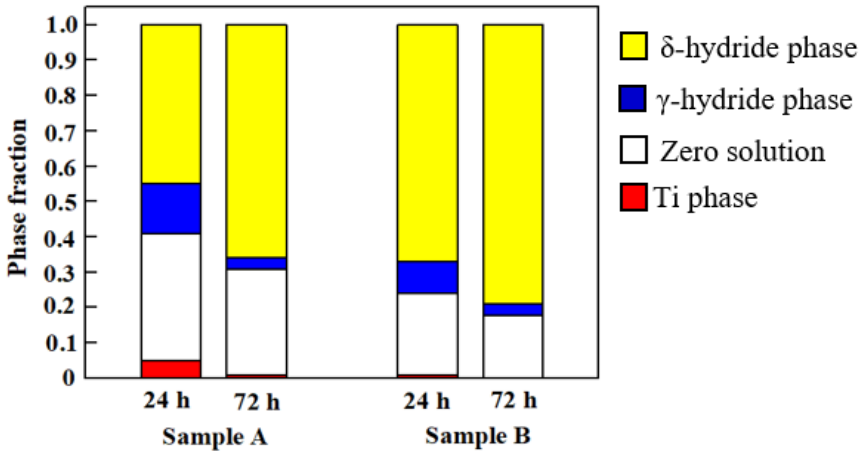


**Fig. 4.2** Evolution of phase composition during hydrogen charging in Sample A and Sample B.

Phase evolution of Sample B (fine-grained) is also examined to study the effect of grain size on the hydride transition process, as shown in Fig. 4.2. During hydrogen charging, Sample B follows the similar phase evolution tendency to that of Sample A, while showing significant difference on the proportion of each phase. Compared to Sample A, more δ-hydride, but less remnant Ti matrix and γ-hydride are observed in Sample B after charging for 24 h, indicating that the phase transformation process from Ti to stable δ-hydride is faster in Sample B, due to the higher volume fraction of grain boundaries in the fine-grained sample.

The nucleation of hydrides tends to form preferentially at grain boundaries because of the high interface energy and relatively weak bonding. Indeed, more hydrides are detected at grain boundaries in fine-grained material [107], in which the high volume fraction of grain boundaries can accelerate the strain accommodation of hydride transition and shorten the phase transformation process. Furthermore, lower fraction of non-indexed area is observed inside Sample B after

diffusing for 24 h, which is the result of reduced hydride interaction inside matrix that due to less intragranular hydrides formed in the fine-grained sample. The decrease slopes of the zero solution from 24 h to 72 h charging in both samples are similar, showing that the plastic accommodation induced by the accumulated misfit strain is independent on grain size.

### 4.4 Hydride microstructure inside hydride layer

In this section, the hydride microstructure inside the diffusion layer is examined, for which the **ND** surface is taken as the diffusion surface. According to the depth, the hydride layer is divided into two parts: Region I: hydride nucleation near the Ti matrix and Region II: large hydride precipitation near the sample surface (see Fig. 2.2, Chapter 2). Hydride platelets have already been observed near the Ti matrix in Section 3.6 (Chapter 3) to investigate the variant selection. In this section, the various microstructures and plastic behaviors induced by hydride transformation are further studied through the thickness of the hydride layer. For convenience, $P_i$ and $B_j$ are employed to denote the three OR1 and six OR2 hydride variants ($j$=1,2,3 and $i$=1,2,3…6) as listed in Table 4.1. More importantly, twin variants are studied in detail, by employing the same expression method in [15]: $T_i^I$ (i = 1, 2,… 6) denoted the six $\{10\bar{1}2\}$ ($T_i^I$) tension twin variants, while the six $\{11\bar{2}2\}$ and $\{10\bar{1}1\}$ compression twin variants are represented by $C_i^I$ and $C_i^{II}$ (i = 1, 2, …6) respectively, as presented in Table 4.1. No $\{11\bar{2}4\}<22\bar{4}\bar{3}>$ and $\{11\bar{2}1\}<\bar{1}\bar{1}26>$ twins appears in our experiments, they are usually activated when titanium is deformed at high strain rate [17].

**Table 4.1** Variants of hydrides and deformation twins

| | Variant 1 | Variant 2 | Variant 3 | Variant 4 | Variant 5 | Variant 6 |
|---|---|---|---|---|---|---|
| OR1 hydride ($P_i$) | $P_1$ $(10\bar{1}0)$ | $P_2$ $(01\bar{1}0)$ | $P_3$ $(\bar{1}100)$ | | | |
| OR2 hydride ($B_i$) | $B_1$ $(10\bar{1}3)[10\bar{1}0]$ | $B_2$ $(01\bar{1}3)[01\bar{1}0]$ | $B_3$ $(\bar{1}103)[\bar{1}100]$ | $B_4$ $(\bar{1}013)[\bar{1}010]$ | $B_5$ $(0\bar{1}13)[0\bar{1}10]$ | $B_6$ $(1\bar{1}03)[1\bar{1}00]$ |
| $\{10\bar{1}2\}$ twin ($T_i^I$) | $T_1^I$ $(10\bar{1}2)[\bar{1}011]$ | $T_2^I$ $(01\bar{1}2)[0\bar{1}11]$ | $T_3^I$ $(\bar{1}102)[1\bar{1}01]$ | $T_4^I$ $(\bar{1}012)[10\bar{1}1]$ | $T_5^I$ $(0\bar{1}12)[01\bar{1}1]$ | $T_6^I$ $(1\bar{1}02)[\bar{1}101]$ |
| $\{11\bar{2}2\}$ twin ($C_i^I$) | $C_1^I$ $(11\bar{2}2)[11\bar{2}\bar{3}]$ | $C_2^I$ $(\bar{1}2\bar{1}2)[\bar{1}2\bar{1}\bar{3}]$ | $C_3^I$ $(\bar{2}112)[\bar{2}11\bar{3}]$ | $C_4^I$ $(\bar{1}\bar{1}22)[\bar{1}\bar{1}2\bar{3}]$ | $C_5^I$ $(1\bar{2}12)[1\bar{2}1\bar{3}]$ | $C_6^I$ $(2\bar{1}\bar{1}2)[2\bar{1}\bar{1}\bar{3}]$ |
| $\{10\bar{1}1\}$ twin ($C_i^{II}$) | $C_1^{II}$ $(10\bar{1}1)[10\bar{1}\bar{2}]$ | $C_2^{II}$ $(01\bar{1}1)[01\bar{1}\bar{2}]$ | $C_3^{II}$ $(\bar{1}101)[\bar{1}10\bar{2}]$ | $C_4^{II}$ $(\bar{1}011)[\bar{1}01\bar{2}]$ | $C_5^{II}$ $(0\bar{1}11)[0\bar{1}1\bar{2}]$ | $C_6^{II}$ $(1\bar{1}01)[1\bar{1}0\bar{2}]$ |

### 4.4.1 Near-matrix hydride nucleation (Region I)

Microstructure of the near-matrix hydrides in Region I is shown in Fig. 4.3. For an explicit study of the hydrides and twins, two maps are drawn: **ND**-IPF map (Fig. 4.3a) and Phase map (Ti: silver, Hydride: white) with colored boundaries (Fig. 4.3b). The corresponding color definitions are presented under individual map. In Fig. 4.3a, the near-matrix hydrides are in platelet shape and show strong orientation dependence, which is consistent with the results in Section 3.6 (Chapter 3). In Fig. 4.3b, the interface planes of OR1 hydrides are colored by pink lines and blue lines for OR2 hydride interfaces. The fraction of OR2 hydrides is much higher than that of OR1 hydrides showing the favorable texture on **ND** surface for OR2 transformation. Two types of twins are observed near OR2 hydride interfaces: majority of $\{10\bar{1}2\}$ extension twins (green lines) and a smaller quantity of $\{11\bar{2}2\}$ contraction twins (orange lines) as well. Although no twins are activated around OR1 hydride, significant orientation change is observed in the grains with OR1 favorable orientation.

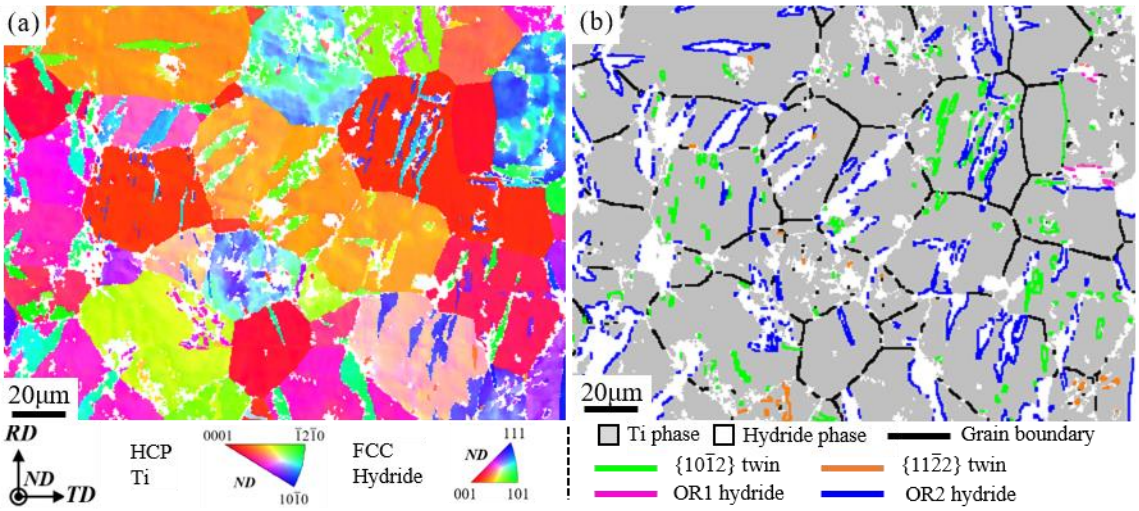


**Fig. 4.3** Microstructure of the near-matrix hydrides in Region I **(a) ND**-IPF map of Ti matrix and hydride precipitates with corresponding color code. **(b)** Phase map with Ti matrix in silver and white hydride. The hydride and twin boundaries are highlighted by color lines: $\{10\bar{1}2\}$ extension twins (green), $\{11\bar{2}2\}$ contraction twins (orange), interface planes of OR1 hydrides (pink) and OR2 hydrides (blue). Black lines refer to grain boundaries (>5°).

#### 4.4.1.2 Grains with internal orientation change

Fig. 4.4a shows the IPF map of a typical grain (Grain I) with OR1 hydrides formed at grain boundary. The $\{10\bar{1}0\}$ interfaces of OR1 hydrides are not straight as the $\{10\bar{1}3\}$ interfaces of OR2

hydrides. Grain boundary and curved interface can accommodate the large misfit dilatation of OR1 transformation along <10$\bar{1}$0> (about 20%). Furthermore, the intragranular orientation changes are more significant in the OR1 favorable grains due to a high density of geometrically necessary dislocation, which can be the favorable nucleation positions for OR1 hydride in the grain interior.

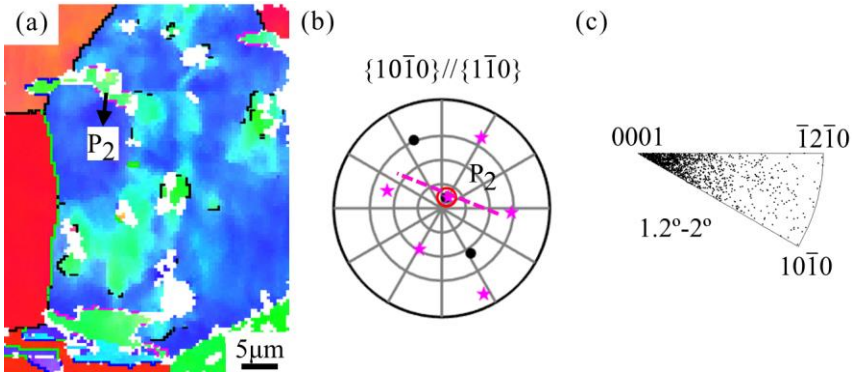


**Fig. 4.4 (a)** IPF map of Grain I (Euler angles: 116.0, 98.2, 21.1) containing OR1 hydrides. The color code for the IPF maps is the same as that of Fig. 4.3. **(b)** {10$\bar{1}$0} pole figure, the black dots represent the planes of Ti matrix and the color ones represent the hydride planes. The dotted lines represent the traces of corresponding interface planes of hydrides. **(c)** IGMA distributions obtained from the misorientation angles of Grain I.

Using the method of Chun et al. [1], IGMA (In-Grain Misorientation Axes) analysis of EBSD date is performed to explore the activated slip mode. The lower cutoff misorientation angle in IGMA analysis is taken as 1.2º, because of the limited angular resolution of the EBSD analysis. Actually, the IGMA distributions of material-point pairs between 1.2º and 2º is enough for the investigation of active slip mode. In this work, IGMA distributions of Grain I with angle range of 1.2º-2º are plotted in Fig. 4.4c, showing strong intensities around <0001>. By matching the Taylor axis, such IGMA distributions are attributed to the predominant activation of prismatic <*a*> slip. According to Weatherly et al. [100], the HCP-FCC transformation of OR1 hydrides is formed by the partial dislocations on prismatic plane. Thus, it can be inferred that the accumulation of prismatic <*a*> dislocations is a significant factor for the nucleation of intragranular OR1 hydrides.

#### 4.4.1.1 {10$\bar{1}$2} and {11$\bar{2}$2} twin induced by OR2 hydride

To study the hydride-stimulated twinning, the OR2 hydride-twin pairs are examined in detail. Two specific grains (Grain II and Grain III) containing respective {10$\bar{1}$2} and {11$\bar{2}$2} twins are shown in IPF maps (Fig. 4.5a and e) and corresponding phase maps (Fig. 4.5b and f) with the same color definition as Fig. 4.3. In Fig. 4.5a and b, relatively large {10$\bar{1}$2} twins are formed on both

sides of OR2 hydride interfaces. According to the pole figures in Fig. 4.5c, inside the red circles, the hydride variant $B_5$ and twin variant $T_2^I$ are selected. The $\{10\bar{1}2\}$ twin orientation existing a large deviation OR2 favorable orientation ($\{10\bar{1}3\}$ plane parallel to diffusion surface), and thus restrains further thickening of hydride lamellas. While for the grain containing $\{11\bar{2}2\}$ twins in Fig. 4.5e and f, the larger shear necessary for the formation of $\{11\bar{2}2\}$ twins make their growth more difficult than $\{10\bar{1}2\}$ extension twins, only small $\{11\bar{2}2\}$ twin plates are observed. The hydride platelets are gradually thinned or/and breaking off when $\{11\bar{2}2\}$ twins are formed near the hydride tips. The growth of intragranular hydrides can be explained via the auto-catalytic nucleation mechanism [140,141]. The chemical potential wells produced by the misfit strain at the growth front attract the hydrogen atoms and then control the path for further nucleation and growth of hydride. However, the local strain can be relaxed by the activation $\{10\bar{1}2\}$ or $\{11\bar{2}2\}$ twins, which decrease the chemical potential wells and also their relative hydrogen affinities. Therefore, when a hydride stimulates the twinning process or intersects with an impinging twin, further growth will be restrained or changed.

All the grains containing $\{10\bar{1}2\}$ and $\{11\bar{2}2\}$ twins are selected from Fig. 4.3, their orientations are projected into IPF, as shown in form of IPF contouring maps in Fig. 4.5d and h, where the red points represent the most favorable orientation for OR1 and OR2 transformation. According to Fig. 4.5d, the $\{10\bar{1}2\}$ twins prefer to stimulate in the grains with ***c***-axis aligned to hydrogen diffusion direction (ND). Grains with such orientation, due to the large lattice distortion induced by hydrogen charging, are difficult to be indexed by EBSD characterization, as presented in Fig. 3.3 in Chapter 3. Noting that, during hydrogen charging from 24 h to 72 h, the non-indexed area with large lattice distortion is reduced in Fig. 4.2, which can be due to the formation of $\{10\bar{1}2\}$ twins. For $\{11\bar{2}2\}$ twins, the preferred grain orientations are located in the transition area between OR1 and OR2 favorable orientations (red points), as shown in Fig. 4.5h. Large misfit strain can be induced during OR2 hydride transformation in the grains with OR1-OR2 transition orientations leading to the nucleation of $\{11\bar{2}2\}$ twins. The accommodation mechanism of hydride-twin pairs will be discussed in Section 4.7.1.

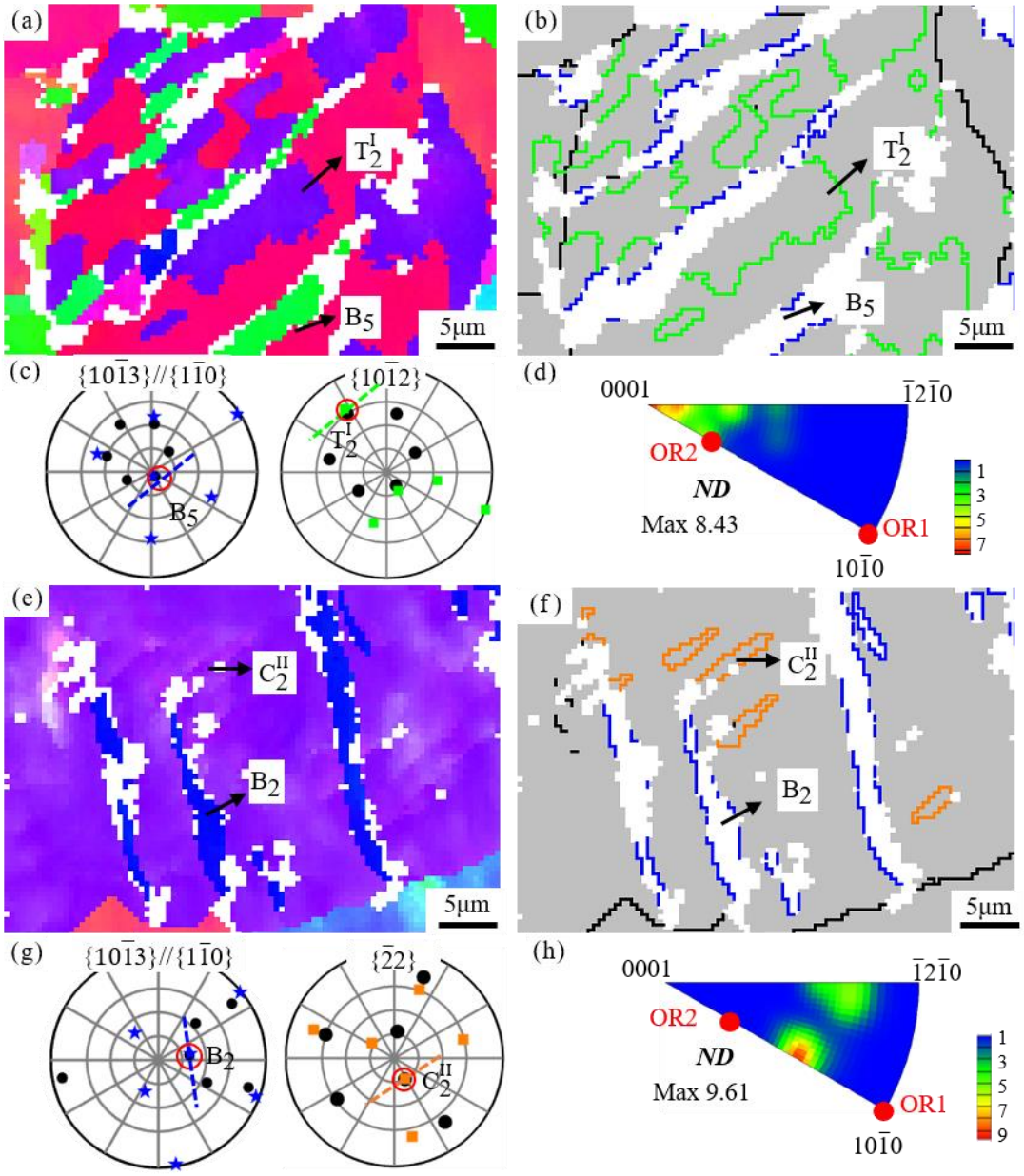


**Fig. 4.5 (a)** and **(e) ND**-IPF map of Grain II (Euler angles: 33.2, 155.5, 29.2) containing {10$\bar{1}$2} extension twins and Grain III (Euler angles: 100.2, 62.6, 25.1) containing {11$\bar{2}$2} contraction twins. **(b)** and **(f)** Corresponding phase maps of Grain II and Grain III. The color code for the EBSD maps is the same as that in Fig. 4.3. **(c)** and **(g)** Pole figures of {10$\bar{1}$3}, {10$\bar{1}$2} and {11$\bar{2}$2} planes. The black dots represent the planes of Ti matrix and the color ones are the planes of hydrides or twins. **(d)** and **(h)** IPF contouring map of all the grains with respective {10$\bar{1}$2} and {11$\bar{2}$2} twins. The positions of OR1 and OR2 favorable orientations in IPF are indicated by red points.

### 4.4.2 Near-surface hydride precipitation (Region II)

Microstructure of the large hydride precipitations near diffusion surface in Region II are examined and shown in Fig. 4.6. In Fig. 4.6a, titanium grains and hydrides are colored by the IPF

color code, phase map with colored boundaries is in Fig. 4.6b. After ion beam milling, partial hydride inside diffusion layer are removed and the underneath titanium matrix can be observed. The grains with high indexing rate form single hydride variant, thus the nearly unindexed grains are due to the complex interactions between different hydride variants. The near-surface hydrides with irregular shapes shows different morphology feature comparing with the platelet ones formed near Ti matrix in Fig. 4.3. In Fig. 4.6b, only OR2 hydride interfaces are determined. Specially, except for $\{10\bar{1}2\}$ and $\{11\bar{2}2\}$ twins, $\{10\bar{1}1\}$ contraction twins are found with $\{10\bar{1}1\}$ ($K_1$) as twining plane and the corresponding second undistorted plane $\{10\bar{1}\bar{3}\}$ ($K_2$), which is the same as the $\{10\bar{1}3\}$ interface plane of OR2 hydride. According to previous researches, $\{10\bar{1}1\}$ twins usually occur in the deformed titanium under high temperature [142,143]. In the present work, $\{10\bar{1}1\}$ twin induced by hydride phase transformation at room temperature is identified for the first time.

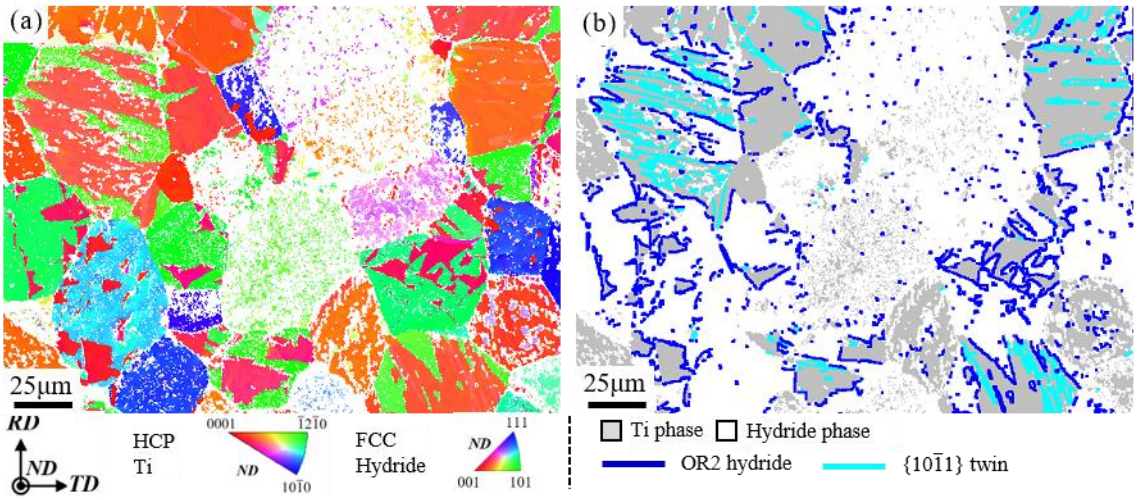


**Fig. 4.6** Microstructure of the near-surface area in Region II **(a)** ND-IPF map of Ti matrix and hydride with corresponding color code. **(b)** Phase map with Ti matrix in silver and white hydride. The hydride and twin boundaries are highlighted by color lines: $\{10\bar{1}1\}$ contraction twins (aqua) and interface plane of OR2 hydrides (blue).

A specific grain containing $\{10\bar{1}1\}$ twins is selected for detailed examination. The IPF map is shown in Fig. 4.7a, where $\{10\bar{1}1\}$ twins have similar IPF color (pink) with titanium matrix and hydrides are green. From the phase map in Fig. 4.7b with $\{10\bar{1}1\}$ twin and hydride boundaries colored by respective aqua and blue, $\{10\bar{1}1\}$ twins are determined to be activated near OR2 hydride interface. According to the $\{10\bar{1}1\}$ and $\{10\bar{1}3\}$ pole figures (Fig. 4.7c), the activated twin and hydride variants are $C_2^{II}$ and $B_5$ shown inside red circles. The twin plane trace of $C_2^{II}$ in pole figure

is consistent with the boundary in Fig. 4.7b. However, in EBSD maps, the boundaries of $B_5$ hydrides nearly parallel to $C_2^{II}$ twins have a large deviation from the calculated $\{10\bar{1}3\}$ interface trace in the pole figure. Therefore, with the growth of hydride precipitates, the interface plane is deviated from $\{10\bar{1}3\}$ plane and gradually approaches $\{10\bar{1}1\}$ twin plane.

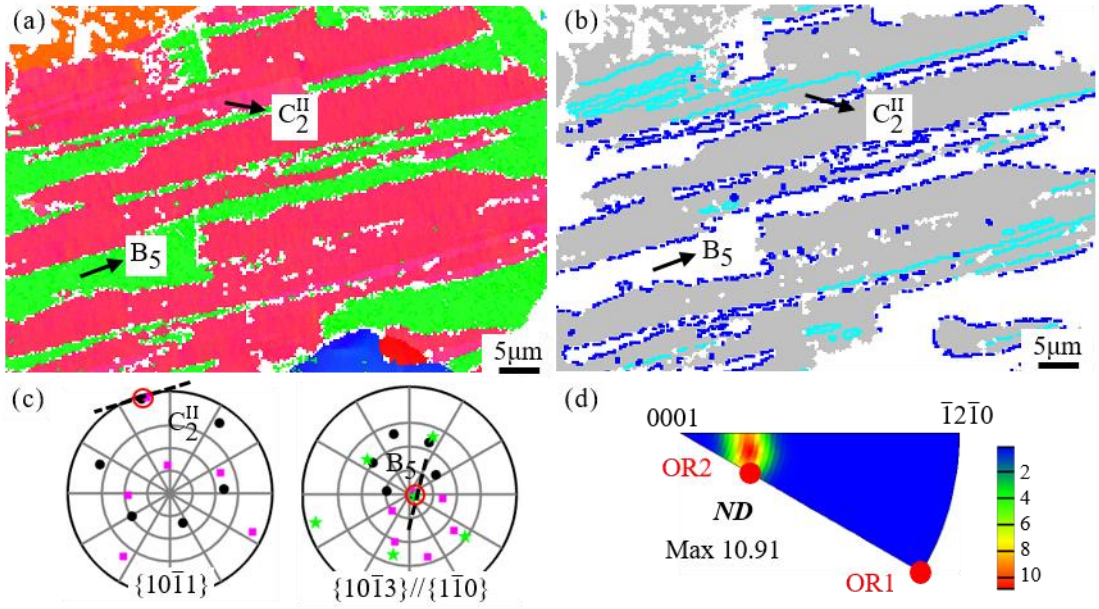


**Fig. 4.7 (a)** IPF map of selected Ti grains containing $\{10\bar{1}1\}$ twins (Euler angle of Ti grain 8.0, 151.5, 19.4). **(b)** corresponding phase map. The color code is the same as that of Fig. 4.6. **(c)** $\{10\bar{1}1\}$ and $\{10\bar{1}3\}$ pole figures. In pole figures, the poles of Ti matrix are black, pink is for $\{10\bar{1}1\}$ twin and green is hydride. **(d)** IPF contouring map of all the grains with $\{10\bar{1}1\}$ twins. The positions of OR1 and OR2 favorable orientations in IPF are indicated by red points.

Furthermore, as shown in $\{10\bar{1}3\}$ pole figure, one of the six $\{10\bar{1}3\}$ planes of matrix (black dots) are overlapped by that of $C_2^{II}$ variant (pink dots) shown inside the red circle, which is the second undistorted plane of $\{10\bar{1}1\}$ twin. Simultaneously, the $\{10\bar{1}3\}$ second undistorted plane parallel to one $\{1\bar{1}0\}$ plane of $B_5$ hydride (green dot), indicating that hydride variant with the same orientation can be formed in both the matrix grain and $\{10\bar{1}1\}$ twin. It means that $B_5$ hydrides formed in the matrix can transfer into $\{10\bar{1}1\}$ twin directly without orientation change, and thus with further hydrogen diffusion, the whole grain can be covered by a hydride layer with single hydride variant ($B_5$).

The grains containing $\{10\bar{1}1\}$ twins are selected from Fig. 4.6 and projected into IPF, as shown in Fig. 4.7d, where the positions of OR1 and OR2 favorable orientations are indicated by red points. The grain orientations were concentrated near the OR2 favorable position. Compared with Fig.

4.4d, the peak in Fig. 4.7d is included in the intensity area for $\{10\bar{1}2\}$ twin favorable orientations. Partial favorable orientations for $\{10\bar{1}2\}$ twin coincide with the ones preferring $\{10\bar{1}1\}$ twin, the others forming various hydride variants and corresponding $\{10\bar{1}2\}$ twin variants in Region I are non-indexed in Region II. However, by the combination of the microstructures in Region I and Region II, it can be inferred that the nucleation of $\{10\bar{1}1\}$ twin, difficult in titanium at room temperature, is related to the pre-existing $\{10\bar{1}2\}$ twin induced by hydride nucleation, which will be further discussed in Section 4.7.2.

## 4.5 Cross section of hydride layer

In this section, the hydride microstructure was investigated on the cross section of the diffusion layer. The SEM – Secondary Electron Image showing the section microstructure of the hydride layer is shown in Fig. 4.8a. It can be seen that the sample and the resin are bonded tightly, with a stress-free area at the junction (the area between red dotted lines), which is ion polishing area and can be indexed by EBSD measurement. Inside the stress-free area, the hydride layer ($TiH_x$) is marked by the yellow lines with a thickness of around 7 μm. The higher-magnification SEM map of the black box area in Fig. 4.8a is shown in Fig. 4.8b. In which, the section microstructure of diffusion layer can be observed more clearly, the light gray curve (labeled by yellow dotted line) is the interface between Ti matrix and hydride layer. The cross section structure under SEM are nearly the same no matter it was formed on which diffusion surface (**TD**, **RD** or **ND**), while the microstructures of hydride inside diffusion layer are strongly dependent on grain orientation.

Fig. 4.8c and d present the **RD**-IPF and **TD**-IPF maps of diffusion layer sections formed on respective **RD** and **TD** diffusion surfaces, which are colored by hydrogen diffusion directions. The IPF maps include two regions: FCC hydride layer (upper side) and HCP titanium matrix (lower side). It is obvious that the hydride layer has much lower indexing rates, especially at the junction area between hydride layer and titanium matrix, where Kikuchi patterns are too blur to be detected due to the large lattice distortion induced by hydride transformation. Inside hydride layer, the hydride microstructures are dependent on the grain orientations of Ti matrix. According to Fig. 4.8c and d, some grains form homogeneous hydride layers with almost single hydride variant, and some hydride layers contain complicated interactions between different hydride variants. Although there exist multiple hydride microstructures, the hydride layers are continuous and uniform in thickness, and the hydride – matrix interfaces are approximately parallel to the diffusion surface.

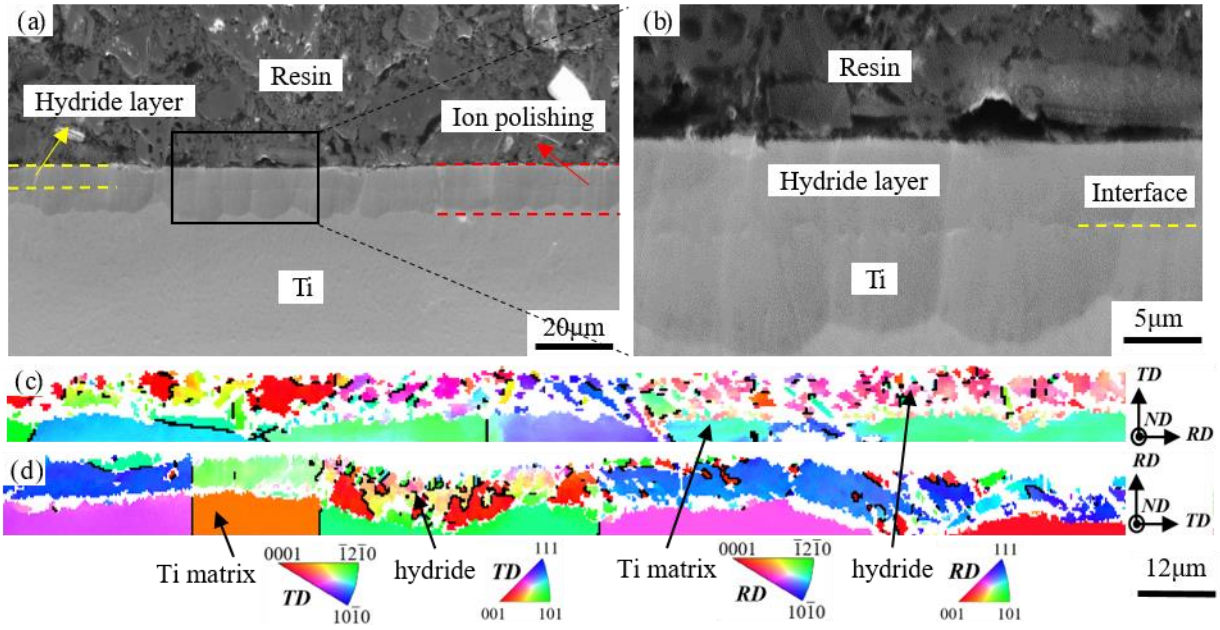


**Fig. 4.8 (a)** SEM image of section microstructure of hydride layer. **(b)** The higher-magnification SEM of the area in the black box. **(c)** IPF maps of hydride layer formed on **RD** surface. **(d)** IPF and phase maps of hydride layer formed on **TD** surface. Grain boundaries are indicated by black line in the IPF maps.

According to the characterization of hydride platelets in Section 3.6 (Chapter 3), there appears four typical titanium matrix orientations: the orientations of $\{10\bar{1}0\}$ and $\{10\bar{1}3\}$ interface planes parallel to the diffusion surface are favorable for single OR1 and OR2 hydride variant, respectively; the grain with *c*-axis parallel to diffusion direction prefers multiple OR2 variants; the OR1-OR2 hydride clusters are formed in the grain with *a*-axis parallel to diffusion direction. In the present research, the section microstructures of hydride layers in the grains (G1-G4) with above four typical orientations are characterized, as shown in Fig. 4.9. G1 and G2 (Fig. 4.9a and b) are selected from **RD** diffusion surface (Fig. 4.8c), while G3 and G4 (in Fig. 4.9c and d) from **TD** surface (Fig. 4.8d). According to Fig. 4.9, no matter the grain orientation is favorable for hydride transformation or not, more than one hydride variant is activated inside hydride layer to relax the anisotropic misfit strain.

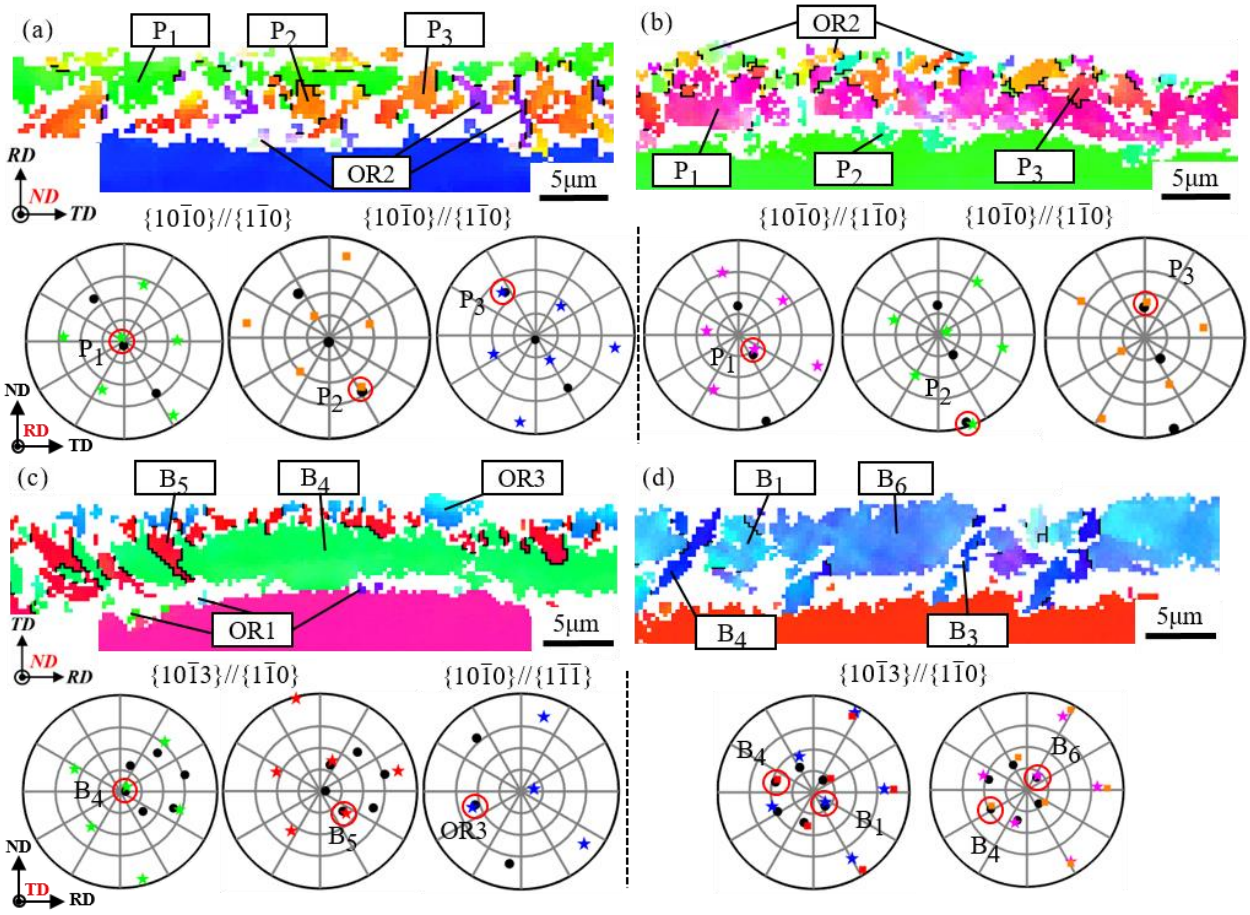


**Fig. 4.9** IPF maps of hydride layer and corresponding pole figures of hydride variants in **(a)** Grain 1, Euler angle: 101.1, 73.3, 22.9 **(b)** Grain 2, Euler angle: 86.7, 57.1, 5.2 **(c)** Grain 3, Euler angle: 37.9, 82.5, 13.3 and **(d)** Grain 4, Euler angle: 166.2, 87.1, 26.3. The IPF maps are colored with hydrogen diffusion direction. Grain boundaries are indicated by black line in the IPF maps. The black dots in pole figures represent the {10$\bar{1}$0} or {10$\bar{1}$3} interface planes of Ti matrix and the colors refer to the {1$\bar{1}$0} or {1$\bar{1}\bar{1}$} planes of hydrides.

As mentioned above, Fig. 4.9a shows the hydride layer in G1 with the orientation of {10$\bar{1}$0} parallel to the rolling surface (diffusion surface), which is the favorable orientation for the precipitation of OR1 hydrides. All of the three OR1 hydride variants are detected in G3. As shown in the pole figures, apart from the most favorable variant $P_1$, $P_2$ and $P_3$ variants with their {10$\bar{1}$0} interfaces ~60º away from **RD** surface are also formed. OR1 transformation has larger anisotropic misfit strain than OR2, as discussed in Section 3.4 (Chapter 3), thus the interaction of symmetric dilatations along <10$\bar{1}$0> between three variants can accommodate the large strain inside hydride layer. During hydrogen diffusion, $P_1$ preferentially precipitated on the sample surface, where the large misfit strain along [10$\bar{1}$0] can be relaxed, $P_2$ and $P_3$ then formed interconnecting with $P_1$. In

addition, OR2 hydrides are not favorable in G3, eventhough a few OR2 hydrides are also induced inside the diffusion layer and/or at the hydride-matrix junction. Conforto and Caillard [94] suggested that, due to the nearly perpendicular misfit strain direction, the interconnection between OR1 and OR2 hydrides can decrease the total stored elastic energy.

G2 represents the grain with <$\bar{1}2\bar{1}0$> parallel to the hydrogen diffusion direction (**RD**), dominated by OR1 hydrides in the hydride layer, as shown in Fig. 4.9b. Specifically, $P_1$ variant is the main component of hydride layer in G2, while some $P_3$ hydrides are also observed embedding into $P_1$ hydride layer and few $P_2$ variants formed at the junction of hydride layer and Ti matrix. According to the pole figures (Fig. 4.9b), $P_2$ variant is extremely unfavorable in G2, presenting a large deviation of its $(01\bar{1}0)$ pole from the pole figure center, thus the interaction between three symmetric OR1 variants in G1 hardly occurs inside the hydride layer of G2.

The orientation of G3 in Fig. 4.9c ($\{10\bar{1}3\}$ interface plane parallel to **TD** diffusion surface) is favorable for the formation of OR2 hydrides, specifically, a major variant ($B_4$) almost occupy the entire hydride layer. According to the pole figures in Fig. 4.9c, the $(\bar{1}013)$ interface plane of $B_4$ is the closest one to the **TD** surface. This accords with the investigation of variant selection reported in Chapter 3, the hydride variant with its interface closest parallel to diffusion surface is selected because it has the highest capacity to accommodate the distortion through free surface. In general, inside hydride layer, more than one hydride variants are activated. Some $B_5$ variants with $(0\bar{1}13)$ interface is slightly deviated from **TD** surface also precipitate near the diffusion surface and embeds into $B_4$ hydride layer, which can, to some extent, relax the accumulated misfit strain of $B_4$. Only a few of small OR1 particles are induced at the matrix-hydride junction because of the unfavorable orientation of G1 for OR1 transformation. It should be noticed that some OR3 hydrides appear along the upside sample edge. Normally, OR3 hydride transformation is difficult in α-Ti matrix because of large misfit (around 15%) along ***c***-axis, while the high density of dislocations on the free surface provides the possibility for the formation of OR3 hydrides. Besides, the OR3 precipitates are only observed on the surface of OR2 hydride layer like G3 indicating that the pre-existing OR2 hydrides play an important role on the nucleation of OR3 precipitates. The nucleation mechanism of OR3 hydrides will be discussed in Section 4.7.1.

Grain 4 (Fig. 4.9d) has the orientation of ***c***-axis nearly parallel to **TD**, in which four kinds of OR2 hydride variants ($B_1$, $B_3$, $B_4$ and $B_6$) are formed inside hydride layer. According the pole

figures, $B_1$ and $B_6$ are the most favorable two variants occupying a large proportion of hydride layer and small amount of lamellar $B_3$ and $B_4$ are activated. Noting that, $B_1$-$B_4$ and $B_3$-$B_6$ usually occur in pairs. The dislocation accumulation produced by the formation of $B_6$ and $B_1$ would induce the formation of $B_3$ and $B_4$ respectively, due to the fact that the Shockley dislocations are along opposite directions between $B_i$ and $B_{i+3}$. The large distortion produced by the interaction of different variants results in a thicker non-indexed area at the hydride-matrix junction than G3. Besides, $\{10\bar{1}2\}$ twins are always observed at the hydride interface in the grain with G4 orientation, as presented in Fig. 4.4, but not detected on the cross section.

### 4.6 Intergranular hydride

According to Fig. 4.2, hydride transformation is faster in fine-grained sample because of increased grain boundary area, where is energy favorable for priority hydride nucleation. Thus, fine-grained Sample D was chosen to research grain boundary accommodation. After polishing out the hydride layer, hydride platelets occur on the diffusion surface (**ND** surface), as shown in Fig. 4.10. Fig. 4.10a shows IPF map, both hydride and titanium are colored by **ND**, while corresponding phase map with colored boundaries is presented in Fig. 4.10b. Hydrides phase mainly follows OR2 with the surrounding matrix, because the texture of **ND** diffusion surface is favorable for OR2 transformation. Some $\{10\bar{1}2\}$ tension twins labeled by green lines are determined at hydride interface, which is also observed in coarse-grained Sample C (Fig. 4.3).

The adjoining hydrides at grain boundaries can be observed in Fig. 4.10. The preferred boundaries for connected intergranular hydrides are explored. Firstly, the ***c***-axis misorientation angles ($\theta_c$) of 200 random grain boundaries selected from Fig. 4.10 are calculated to reveal the intrinsic ***c***-axis misorientation distribution of the textured plate. After that, $\theta_c$ of 210 grain boundaries with adjoining hydride pairs are obtained for the analysis of boundary preference for intergranular hydride. The results are presented in Fig. 4.11. For the distribution of intrinsic ***c***-axis misorientation (black bars) from $0^o$ and $90^o$, there appear three peaks focus on the angle around $35\text{-}40^o$, $60\text{-}65^o$ and $85\text{-}90^o$. Compared with the data set of all boundaries, the peaks of boundaries with adjacent hydrides (red bars) are shifted towards left and right side, respectively. The formation of intergranular hydride prefers the grain boundaries with both the low $\theta_c$ ($< 30^o$) and the high $\theta_c$ ($75^o < \theta_c < 85^o$), while the grain boundaries with the ***c***-axis misorientation angle between $30^o$ and

75° and larger than 85° are unfavorable. The reason for the grain boundary dependence of adjacent hydride will be further discussed in Section 4.7.3.

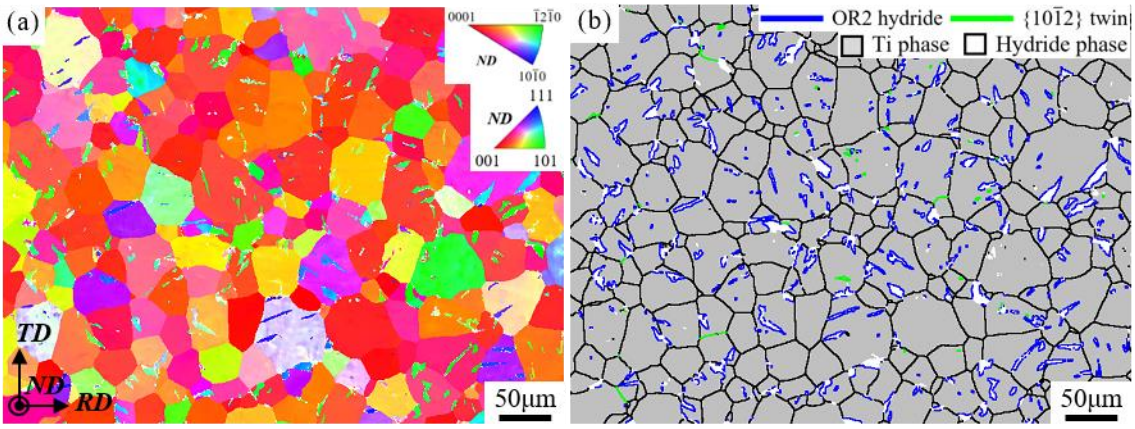


**Fig. 4.10 (a)** IPF map of hydride platelets in Sample D. **(b)** EBSD map to show the $\{10\bar{1}2\}$ twin boundary and OR2 hydride phase boundary. All the indexed phases are color by gray. Green line shows the twin boundaries of $\{10\bar{1}2\}$ extension twin. Blue line is interface plane of OR2 hydride, respectively. Grain boundaries are colored by black.

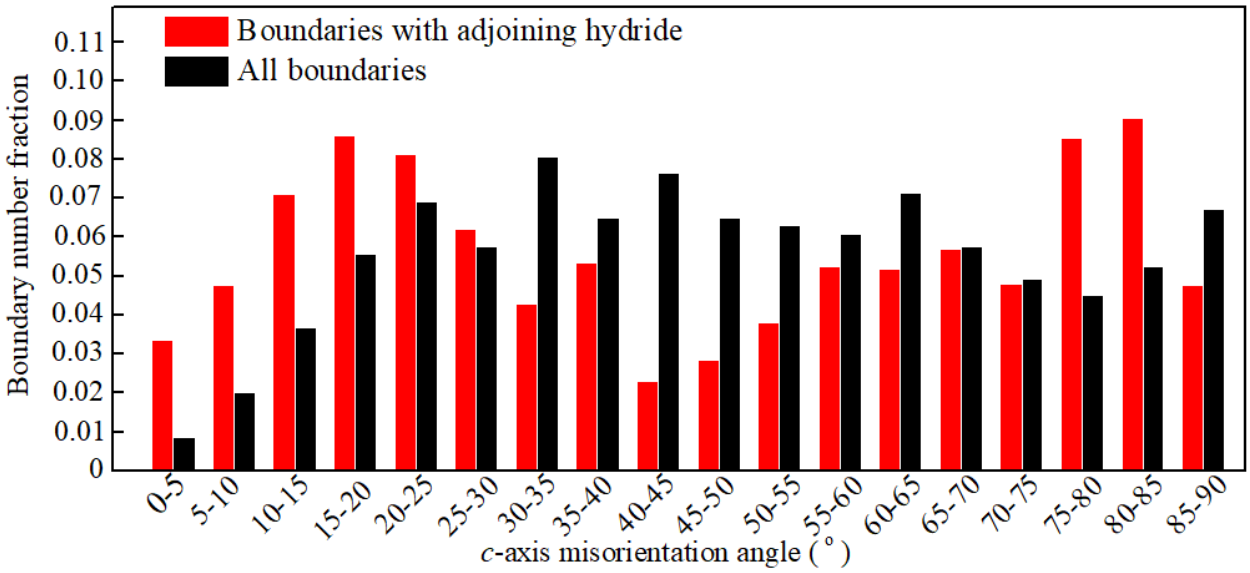


**Fig. 4.11** EBSD-based distribution of grain boundaries and hydride crossing at grain boundaries with ***c***-axis misorientation angle.

There appears an abnormal decrease of boundary fraction at high $\theta_c$ value of 85-90° in Fig. 4.11. During the statistics of grain boundary with adjoining hydride, to ensure the accuracy, the identified hydrides must be more than 5 pixels in Fig. 4.10. With the increase of ***c***-axis misorientation, the grain orientations can deviate from the favorable orientation for hydride nucleation leading to the

small hydride size. The excluded hydrides less than 5 pixels finally result in the decrease of hydride pair at 85-90° $\theta_c$ boundary. However, according to the tendency at 75-85°, it can be speculated that the actual number of hydride pair at 85-90° boundary is larger than the calculated value.

The details of adjoining hydride pairs at low angle and high angle grain boundaries are shown in Fig. 4.12a and b. The disorientation angle is 10.2° between Grain 1 and Grain 2, while 82.9° between Grain 3 and Grain 4. In the pole figures, the selected hydride variant in each grain is marked by the red circle. The hydride variant selection follows the principle studied in Section 3.6.2 (Chapter 3), which is not influenced by the neighboring hydride and grain boundary. The selected OR2 variant are always the most favorable one to accommodate the misfit strain of hydride transformation with the $\{10\bar{1}3\}$ interface plane closest to hydrogen diffusion surface. Thus, it can be inferred that, when the grains at both sides of boundary have preferential orientation for OR2 transformation, the nucleation probability of hydride pair is higher. However, adjoining hydride is restrained if the neighboring grain orientation is unfavorable.

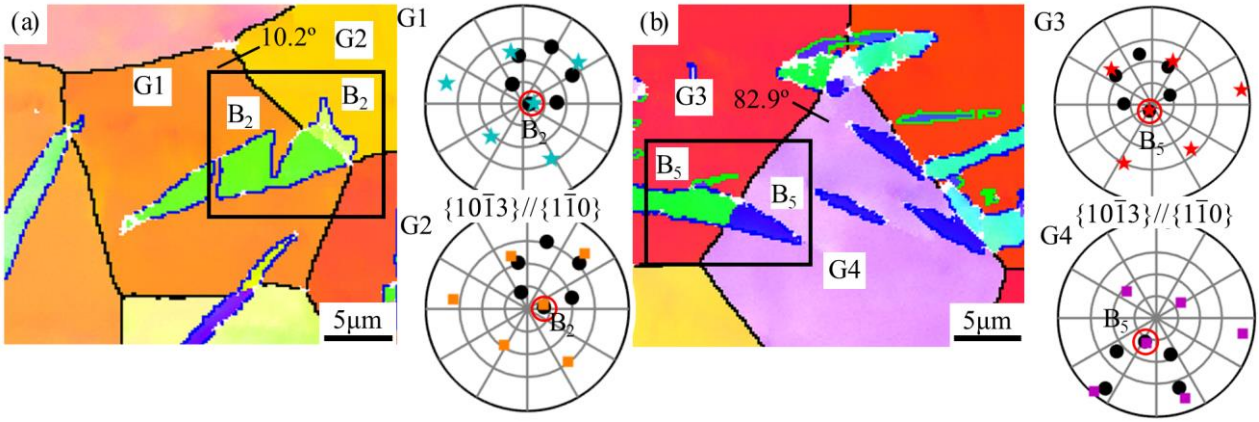


**Fig. 4.12** IPF maps of adjoining hydrides **(a)** at low angle boundary (Grain 1 and Grain 2) and **(b)** high angle boundary (Grain 3 and Grain 4). The black dots represent the $\{10\bar{1}3\}$ interface planes of Ti matrix and the colors represent the $\{1\bar{1}0\}$ interface planes of hydrides. The twin, grain and OR2 hydride boundaries are colored by green, black and blue, respectively. (Euler angle of G1: 145.9° 35.9° 53.6°, G2: 149.3° 40.4° 59.6°, G3: 21.1° 155.6° 42.8, G4: 167.7° 120.5° 18.5°)

## 4.7 Discussion

### 4.7.1 Hydride transformation mechanism

The multiple plastic accommodation modes for OR1 and OR2 transformation: the accumulation of prismatic dislocations are found in OR1 favorable grains and twins are commonly induced by

OR2 hydrides are due to different transformation mechanisms (see Section 3.4 in Chapter 3). The shear of prismatic partial dislocations and lattice misfit are attributed to OR1 hydride transformation. Thus, the accumulation of prismatic dislocations in Fig. 4.4 can be the origin of OR1 transformation. Internal twins and dislocations were observed by TEM at OR1 hydride-matrix interfaces [100], but not detected by EBSD measurement in this work. OR2 hydride is formed by shear of Shockley dislocation combined with lattice dilatation, which can be accommodated by dislocations and/or twins, such as $\{10\bar{1}2\}$ and $\{11\bar{2}2\}$ twins as observed before in Fig. 4.5.

OR3 transformation is difficult to be activated due to the large misfit strain along *c*-axis in α-Ti matrix, while it was observed close to the diffusion surface in the OR2 hydride layer, as mentioned before in Fig. 4.9c. The habit planes of activated OR2 and OR3 variants are respective $(\bar{1}013)//(1\bar{1}0)$ and $(\bar{1}010)//(\bar{1}11)$ with the same zone axis $<\bar{1}2\bar{1}0>//<\bar{1}\bar{1}0>$, the experimental misorientation between the two variants is ~26.6º/$<\bar{1}\bar{1}0>$. To explore the special nucleation of OR3 hydrides, the HCP-FCC transformations of observed OR2 and OR3 variants are illustrated in Fig. 4.13. If not considering lattice dilatation, the difference between the FCC structures of OR2 and OR3 hydrides is only a simple lattice rotation ~20º around $<\bar{1}2\bar{1}0>//<\bar{1}\bar{1}0>$. The deviation of misorientation angles between 20º and 26.6º/$<\bar{1}\bar{1}0>$ is due to the lattice distortion during phase transformation. Thus, it could be derived that the OR3 precipitates are rotated from the pre-existing OR2 variant $B_4$ induced by the accumulated Shockley shear inside $B_4$ hydride layer and/or the interaction between $B_4$ and $B_5$. The stress concentration on the diffusion surface also plays an important role in the formation of OR3.

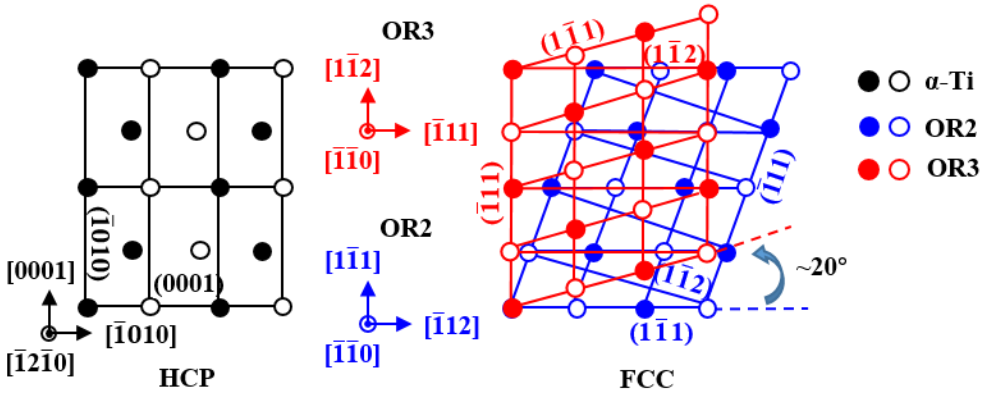


**Fig. 4.13** The relationship of HCP-FCC structure transformation between OR2 and OR3 hydrides. The filled and open circles are in the different atom layers.

### 4.7.2 Variant selection of {10$\bar{1}$2}, {11$\bar{2}$2} and {10$\bar{1}$1} twin

OR2 hydride transformation includes both lattice expansion and shear of 1/3 <10$\bar{1}$0> Shockley partial dislocation. When grain orientations are oriented from OR2 favorable ones, only dislocation slip is not enough to accommodate such complicated misfit strain, but also twinning is always induced. {10$\bar{1}$2} and {11$\bar{2}$2} induced by OR2 hydride nucleation were observed in our work. During plastic deformation at room temperature, {10$\bar{1}$2} extension twins and {11$\bar{2}$2} contraction twins are commonly observed in α-Ti [16]. The nucleation of {10$\bar{1}$2} and {11$\bar{2}$2} twins induced by hydride transformation is dependent on the grain orientation, as shown in Fig. 4.5. {10$\bar{1}$2} twin prefers the orientation with ***c***-axis parallel to diffusion direction and {11$\bar{2}$2} is easier to be activated in the grain with transition orientation between OR2 and OR1 favorable ones.

In the current work, we use DGA (deformation gradient accommodation) criterion to explore the accommodative twin nucleation which can relax the local distortion at the interface of hydrides. The original DGA criterion was employed to predict the secondary twinning in magnesium alloys [23] and also extended for the exploration of the accommodation between different twin variants in titanium alloys [16]. According to the transformation mechanism, the OR2 hydriding frame is set up by: ***x*** // gliding direction of partial dislocation <10$\bar{1}$0>, ***z*** // normal of basal plane and ***y*** // the zone axis (***y*** = ***z*** × ***x***). The twin frame is set up by: ***n*** // twinning shear direction, ***m*** // normal of twin habit plane and ***p*** // normal of shear plane. The calculated displacement gradient tensors of OR2 hydride $\mathbf{D_H}$ and twins $\mathbf{D_T}$ in their defined reference frames are summarized in Table 4.1.

**Table 4.1** Displacement gradient tensor of OR2 hydride and twinning in α-titanium (c/a=1.587).

| OR2 hydride ($\mathbf{D_H}$) | Twinning ($\mathbf{D_T}$) | | |
|---|---|---|---|
| | $C^{I}$ {11$\bar{2}$2}<11$\bar{2}\bar{3}$> | $C^{II}$ {10$\bar{1}$1}<10$\bar{1}\bar{2}$> | $T^{I}$ {10$\bar{1}$2}<$\bar{1}$011> |
| $\begin{bmatrix} 0.055 & 0 & 0.384 \\ 0 & 0.055 & 0 \\ 0 & 0 & 0.086 \end{bmatrix}$ | $\begin{bmatrix} 0 & 0 & 0.218 \\ 0 & 0 & 0 \\ 0 & 0 & 0 \end{bmatrix}$ | $\begin{bmatrix} 0 & 0 & 0.099 \\ 0 & 0 & 0 \\ 0 & 0 & 0 \end{bmatrix}$ | $\begin{bmatrix} 0 & 0 & 0.173 \\ 0 & 0 & 0 \\ 0 & 0 & 0 \end{bmatrix}$ |

At first, the accommodation of twinning on the hydride-induced surface expansion is considered as a constraint for the variant selection between {10$\bar{1}$2} and {11$\bar{2}$2} twins. The contribution of hydride and twin variants in Grain II and Grain III (see Fig. 4.5) to the expansion along surface normal is evaluated by transforming their displacement gradient tensor **D** into sample frame $\mathbf{D^s}$:

$$\mathbf{D^s} = \mathbf{R_{cs}^{-1}} \cdot \mathbf{D} \cdot \mathbf{R_{cs}} \tag{4-2}$$

where $\mathbf{R_{cs}}$ is Bunge rotation matrix, calculated by equation (2-24) in Chapter 2. The $D_{33}^{S}$ values of $B_5$ hydride +0.228 in Grain II is larger than that of $B_2$ hydride 0.220 in Grain III, while the $D_{33}^{S}$ values of $\{10\bar{1}2\}$ and $\{11\bar{2}2\}$ twins in these two grains are summarized in Table 4.2. The twin variants with larger $D_{33}^{S}$ values has higher capacity to accommodate the expansion along sample surface. As for Grain II with ***c***-axis parallel to the surface normal, the surface expansion coincides with ***c***-axis extension, thus all the $D_{33}^{S}$ of $\{10\bar{1}2\}$ tension twin is positive but negative for $\{11\bar{2}2\}$ twin, indicating all the six $\{10\bar{1}2\}$ twin variants are favorable to accommodate the surface expansion of $B_5$ hydride. In contrast, only one $\{10\bar{1}2\}$ twin variant has positive $D_{33}^{S}$ in Grain III, while three $\{11\bar{2}2\}$ twin variants are preferred with larger $D_{33}^{S}$ ($\mathbf{C_2^I}$, $\mathbf{C_4^I}$ and $\mathbf{C_5^I}$). The basal plane of Grain III is oriented away from diffusion surface, thus the surface expansion of $B_2$ hydride trends to perpendicular to ***c***-axis, which is favorable to be accommodated by $\{11\bar{2}2\}$ contraction twinning.

**Table 4.2** The value $D_{33}^{S}$ transformed from $\{10\bar{1}2\}$ and $\{11\bar{2}2\}$ twin frames into sample frame

| | Variant 1 | Variant 2 | Variant 3 | Variant 4 | Variant 5 | Variant 6 |
|---|---|---|---|---|---|---|
| Grain II | **$T_1^I$ +0.071** | **$T_2^I$ +0.063** | **$T_3^I$ +0.071** | **$T_4^I$ +0.066** | **$T_5^I$ +0.052** | **$T_6^I$ +0.065** |
| | $C_1^I$ -0.038 | $C_2^I$ -0.038 | $C_3^I$ -0.081 | $C_4^I$ -0.100 | $C_5^I$ -0.100 | $C_6^I$ -0.082 |
| Grain III | $T_1^I$ +0.004 | $T_2^I$ -0.056 | $T_3^I$ -0.008 | $T_4^I$ -0.009 | $T_5^I$ -0.044 | $T_6^I$ -0.001 |
| | $C_1^I$ 0.000 | **$C_2^I$ +0.008** | $C_3^I$ -0.024 | **$C_4^I$ +0.063** | **$C_5^I$ +0.078** | $C_6^I$ -0.017 |

To further explore the variant selection among six twin variants of respective $\{10\bar{1}2\}$ and $\{11\bar{2}2\}$ twins, the displacement gradient tensor of OR2 hydride are transformed into different twin frames. The coordinate rotation matrix from OR2 hydride system and twinning system to crystal frame are shown as follows:

$$\mathbf{R_{hc}} = \begin{bmatrix} x_1 & x_2 & x_3 \\ y_1 & y_2 & y_3 \\ z_1 & z_2 & z_3 \end{bmatrix} \text{ and } \mathbf{R_{tc}} = \begin{bmatrix} n_1 & n_2 & n_3 \\ p_1 & p_2 & p_3 \\ m_1 & m_2 & m_3 \end{bmatrix} \tag{4-3}$$

The transformed displacement gradient tensor ($\mathbf{D^{H\text{-}T}}$) from OR2 frame to twinning frame can be expressed as:

$$\mathbf{D^{H\text{-}T}} = \mathbf{R_{tc}} \cdot \mathbf{R_{hc}^{-1}} \cdot \mathbf{D_H} \cdot \mathbf{R_{hc}} \cdot \mathbf{R_{tc}^{-1}} \tag{4-4}$$

The $D_{13}^{H\text{-}T}$ component of transformed tensor indicates the displacement gradient of hydride transformation happens along the shear direction on the twin plane, the twin variants with larger $D_{13}^{H\text{-}T}$ corresponding to higher capability to accommodate the resultant strain of hydrides are preferentially selected.

The $D_{13}^{H\text{-}T}$ transformed from activated OR2 hydride variants ($B_5$ and $B_2$ in Fig. 4.5) into corresponding twin variants of $T^I$ and $C^I$ are shown in Table 4.3. The bold variants have largest $D_{13}^{H\text{-}T}$ values among six variants of each twin mode and thus are most capable for hydride accommodation. In Grain II, the most favorable hydride-twin pair $B_5$-$T_2^I$ is consistent with the experimental result. Thus, for the grains like Grain II with *c*-axis close to diffusion direction, the accommodative hydride-twin pair can be denoted by $B_i$-$T_{i+3}^I$. Furthermore, both $C_1^I$ and $C_2^I$ have the same largest $D_{13}^{H\text{-}T}$ (+0.080) in Grain III, while the larger $D_{33}^S$ of $C_2^I$ (+0.008) than $C_1^I$ (0.000) results in the final activation of $B_2$-$C_2^I$ pair. It can be derived that, in the grains with transition orientation between OR1 and OR2 favorable ones like Grain III, the $B_i$-$C_{i-1}^I$/$C_i^I$ hydride-twin pair can be determined by displacement gradient accommodation, the accommodation on surface expansion leading to the selection between $C_{i-1}^I$ and $C_i^I$ variants is orientation dependent.

**Table 4.3** The value $D_{13}^{H\text{-}T}$ transformed from hydriding frame into the twinning frame.

| | Variant 1 | Variant 2 | Variant 3 | Variant 4 | Variant 5 | Variant 6 |
|---|---|---|---|---|---|---|
| $B_5$ (Grain II) | $T_1^I$ +0.120 | $T_2^I$ +**0.224** | $T_3^I$ +0.120 | $T_4^I$ +0.089 | $T_5^I$ -0.193 | $T_6^I$ -0.089 |
| $B_2$ (Grain III) | $C_1^I$ +**0.080** | $C_2^I$ +**0.080** | $C_3^I$ -0.014 | $C_4^I$ -0.108 | $C_5^I$ -0.108 | $C_6^I$ -0.014 |
| $B_5$ ($\{10\bar{1}1\}$ twins) | $C_1^{II}$ -0.057 | $C_2^{II}$ **-0.101** | $C_3^{II}$ -0.057 | $C_4^{II}$ +0.031 | $C_5^{II}$ +0.075 | $C_6^{II}$ +0.031 |

Furthermore, $C^{II}$ $\{10\bar{1}1\}$ twins were activated inside hydride layer near diffusion surface in Fig. 4.7, which are usually formed when titanium is deformed under high temperature [142,143]. The observed hydride-twin pairs is $B_5$-$C_2^{II}$ denoted by $B_i$-$C_{i+3}^{II}$. However, as shown in Table 4.3, $C_2^{II}$ with a negative $D_{13}^{H\text{-}T}$ value (-0.101) cannot accommodate the distortion of $B_5$ hydride, which is induced by the accumulative distortion inside Ti matrix during hydride growth. As the hydride grows, the plate shape is unable to be maintained and the hydride interface will overlap with twin plane. The $\{10\bar{1}1\}$ twin ($C_{i+3}^{II}$) prefers the hydride variant with the same orientation as $B_i$ according to the results in Section 4.4.2. Thus, $B_i$ can continue to grow up through $\{10\bar{1}1\}$ twin and finally cover the whole grain.

### 4.7.3 Formation mechanism of adjoining hydride pair

Hydride transformation (OR2), similar to a martensitic transformation, consists of a shear deformation on basal plane and a lattice expansion, while twinning is a pure shear deformation mode. The twin transmission at grain boundary has already been investigated in-depth [144]. Thus, before the discussion of hydride pair, twinning can be considered as a reference. Kumar et al. [144] suggested that twin transmission frequency in HCP materials decreases with the increase of grain boundary misorientation, which is commonly attributed to the misalignment in the twin plane and shear direction at the grain boundary with large misorientation. The tendency of twin transmission frequency should be nearly the same when grain boundary misorientation is replaced by ***c***-axis misorientation angle used in this paper.

Specially, the boundary frequency with hydride pair is not monotonically decreasing with the increased ***c***-axis misorientation, as shown in Fig. 4.10, where the peaks occur on both low and high angle regions. The intergranular hydride has also been investigated in zirconium when hydride nucleates during moderately slow cooling process [107]. The precipitation of intergranular hydride pair favors the grain boundaries with both the low $\theta_c$ ($< 40^o$) and the high $\theta_c$ ($> 80^o$), which is slightly different from our results, the low $\theta_c$ ($< 30^o$) and the high $\theta_c$ ($75^o < \theta_c < 85^o$), probably due to the different materials or hydriding process (electrolytic hydrogen charging in our work).

The favorable formation of hydride pair at low $\theta_c$ boundary is mainly due to the shear accommodation like the transmission of twin. The shear inside the formed hydride platelet results from the 1/3 $<10\bar{1}0>$ Shockley partial dislocation. The alignment of slip planes and slip directions ($\{0001\}$ and $<1\bar{1}00>$) at the grain boundary are responsible for the adjoining hydride. For any grain boundary, the $<1\bar{1}00>$ misorientation angle is always low, allowing for easy collective shear [107]. Thus, the alignment of $\{0001\}$ plane is of particular importance and responsible for the preferable formation of intergranular hydride pair in low $\theta_c$ range. The analysis should be associated with the auto-catalytic mechanism proposed by Wang et al. [107]. For low $\theta_c$ boundaries, basal slip can be easily induced by the strain misfit produced by hydride tip in the neighbor grain with aligned slip plane ($\{0001\}$ basal plane). Solute hydrogen atoms nearby tend to diffuse towards the dislocated area, that is, chemical potential well. The chemical stress accompanying hydrogen agglomeration stimulates the dissociation of 1/3 $<11\bar{2}0>$ dislocations into 1/3 $<10\bar{1}0>$ partial dislocations [103] and then the hydride nucleation occurs.

The effect of collective shear on intergranular hydride pair is weakened with the increase of ***c***-axis misorientation angle. The again appearance of strong intensity at high $\theta_c$ grain boundaries confirms that the adjoining hydride should not only induced by the pure shear accommodation like twin transmission. Indeed, as mentioned before, OR2 hydride transformation contains both shear misfit and large dilatation along ***c***-axis. Thus, for the adjoining hydride at high $\theta_c$ boundary, ***c***-axis dilatation difficult accommodated by misfit dislocations should be regarded as the major factor. Prismatic slip $\{10\bar{1}0\}<1\bar{2}10>$ is the dominant slip family at room temperature in α-titanium [145]. Carpenter [103] proposed that the $1/3<10\bar{1}0>$ Shockley dislocation for OR2 hydride nucleation can be dissociated from a screw segment of prismatic dislocation by chemical stress accompanying hydrogen agglomeration. Thus, the stimulation of prismatic slip is another important part for the hydride nuclear reaction. SF criterion is used to evaluate the probability of slip activation in Grain A under the effect of ***c***-axis dilatation in neighbor grain (Grain B), which is equivalent to a uniaxial compressive stress for Grain A. Under uniaxial stress, the SF of prismatic slip in Grain A can be obtained by the stress projection on the slip systems:

$$SF = \cos(\theta)\cos(\lambda) \tag{4-5}$$

where $\theta$ is the angle between slip plane normal $<10\bar{1}0>$ and stress direction, and $\lambda$ shows the angle between slip direction $<1\bar{2}10>$ and stress direction [146]. The different types of grain boundaries can be obtained by manipulating the Euler angle of Grain A using the method of Wang et al. [107]. The $[\varphi_1, \phi, \varphi_2] = [90^o, 90^o, 0]$ is taken as reference Euler angles of neighbor Grain B, while three types of initial orientations are taken for Grain A: Type I $[90^o, 90^o, 0]$ (red square), Type II $[90^o, 90^o, 15^o]$ (black round) and Type III $[90^o, 90^o, 30^o]$ (blue star), of which ***c***-axes are all aligned to that of Grain B. Grain A is misoriented through altering the angle $\phi$ (rotation around $[10\bar{1}0]$) from 90º to 0º, in which the SFs for prismatic slip systems are calculated every time $\phi$ goes down $5^o$. The maximum SFs corresponding to $\Delta\phi$ (***c***-axis misorientation between Grain A and Grain B) are shown in Fig 4.14, indicating increased SFs with the increase of $\Delta\phi$ in all types of Grain A. Due to the symmetry of HCP crystal, the SFs for Type I and Type III Grain A are the same, while increase faster up to 0.5 (the maximum of SF) for Type II Grain A. Especially, when ***c***-axis misorientation is higher than $75^o$, all the SFs are larger than 0.4, indicating the easier activation of prismatic slip. Above all, high frequency hydride pairs at high $\theta_c$ grain boundaries is due to the activation of prismatic slip by the neighboring hydride which can further induce the nucleation of adjacent

hydride. In addition, the high $\theta_c$ grain boundaries with higher energy can also as the preferential position of hydride nucleation during hydrogen diffusion.

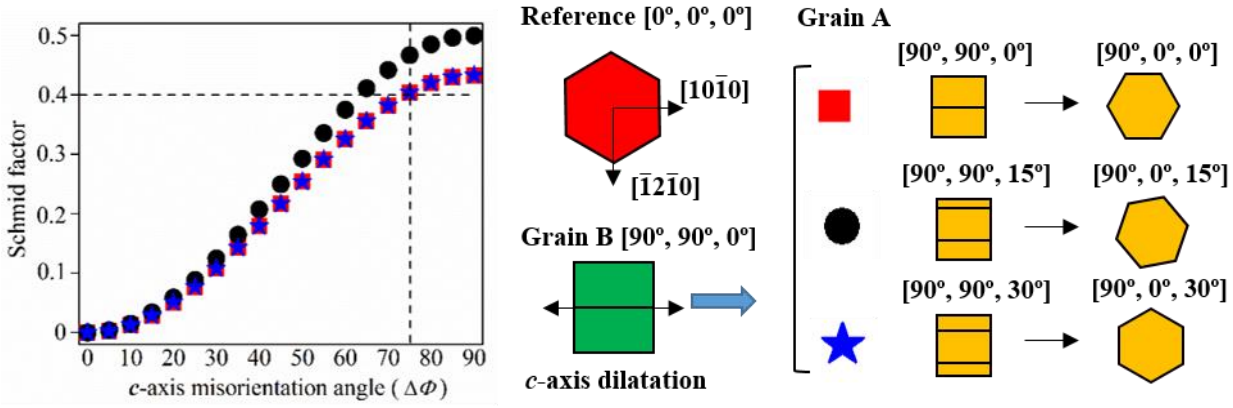


**Fig. 4.14** Change in the Schmid factor of prismatic slip system as a function of ***c***-axis misorientation

## 4.8 Chapter summary

Due to the large misfit strain of hydride transformation, certain accommodation operations are necessary for the strain relaxation. In this chapter, the accommodation mechanisms of plastic deformation, hydride interaction and grain boundary on hydride phase transformation were investigated through multi-dimensional characterization of hydride diffusion layer.

The microstructure evolution of hydride layer during hydrogen charging on the free diffusion surface was observed via interrupted in-situ EBSD measurement. Four different microstructures can be observed on the free surface of hydrogen diffusion: non-indexed area, Ti matrix, γ and δ phase hydride. After diffusing for 72 h, the non-indexed area and δ-hydride are the major segment of hydride layer. The non-indexed area decreases after charging more than 24 h due to the accommodation behavior of Ti matrix. Besides, in the fine grain sample, more grain boundaries result in the faster hydride transformation from γ to stable δ hydride and less distortion than large grain sample.

Inside hydride layer, deformation twins are observed to accommodate the misfit strain of OR2 hydride. {10$\bar{1}$2} extension and {11$\bar{2}$2} contraction twins are activated at the interface of hydride platelets. {10$\bar{1}$2} twin prefers to be formed in the grain with ***c***-axis parallel to diffusion direction and {11$\bar{2}$2} twin in the grain with transition orientation between OR1 and OR2 favorable ones. The twin variant with larger $D_{13}^{H\text{-}T}$ and $D_{33}^{S}$ is selected due to the highest accommodation capacity

for local distortion of the nucleated hydride platelet. $\{10\bar{1}1\}$ twin is induced by the accumulative stress inside Ti matrix during hydride growth.

The section microstructure of hydrogen diffusion layer was observed for the first time, which is dependent on grain orientation. The hydride layer in the grains with the oriantations of $<\bar{1}2\bar{1}0>$ and/or $<10\bar{1}0>$ parallel to diffusion direction mainly consists of OR1 hydrides. Three symmetric OR1 variants are usually precipitated together to accommodate the large misfit strain of each other. The grains with $\{10\bar{1}3\}$ and/or basal plane parallel to diffusion surface are favorable for the OR2 hydride layer. OR3 particles are usually stimulated at the edge of hydride layer composed of almost single OR2 variant due to the stress concentration on the diffusion surface.

The formation of intergranular hydride pair is a kind of grain boundary accommodation behavior, which prefers both the low θc ($< 30^{o}$) and the high θc ($75^{o} < \theta c < 85^{o}$) grain boundary. The reason for the preference at low $\theta_c$ boundaries is the aligned {0001} slip plane of grains on both sides of grain boundary. Prismatic slip induced by ***c***-axis dilatation of neighbor grain results in the amount of hydride pairs at the high $\theta_c$ boundaries ($75^{o} < \theta c < 85^{o}$).

# Chapter 5 Hydride induced hardening in commercial pure titanium

Contents



## 5.1 Introduction

Environment sensitive failure, particularly the hydrogen assisted mechanical degradation or hydrogen embrittlement, is a longstanding problem in material science. The failure occurs easily with the increase of hardening and yield stress by the generation of hydride precipitation. The hard and brittle nature of the hydride and the strain incompatibility between hydride and matrix material is the reason for the hydride enhanced hardening process. Yamanaka et al. [147] suggested that hydrides with composition range of $ZrH_{1.5}$–$ZrH_{1.7}$ unusually have higher values of Young's modulus and Vickers hardness than zirconium matrix. Nano-indentation hardness tests were performed in the α-Zr sample with hydride in [113] indicating that δ-hydride has higher $H_{IT}$ and similar $E_{IT}$ value with α-Zr phase. However, the influences to those values by the difference of crystal orientation of δ-hydrides were unknown.

Conforto et al. [148,149] studied the mechanical characteristics of epitaxial hydride layer, plastic deformation has been demonstrated in indentation tests and in tension up to more than 1% strain. The internal stress concentration induced by the interaction between hydride and plastic deformation modes is the origin of micro-crack or void nucleation. Such hydride-induced hardening is dependent on the crystal orientation and relationship between slip plane and hydride habit plane [113], which is more significant when the slip plane close to the habit plane of δ-hydride. Furthermore, hydrides can also experience plastic yielding in certain working conditions. The interaction between dislocation and hydride is investigated by Chen et al. [115], OR1 hydride can be easily sheared by the slip bands in deformed titanium and has good deformability. They deeply studied the dislocation transfer mechanism across OR1 hydride, while the related research on OR2 hydride is lacking due to a few OR2 hydrides were observed in their experiments.

OR2 hydride is the dominant hydride precipitation in the CP-Ti sheet during electrolytic hydrogen charging. In this chapter, the mechanical properties of titanium influenced by the formed OR2 hydride was investigated. Nanoindentation hardness tests were performed to investigate the change of anisotropic hardness and modulus before and after hydrogenation. Furthermore, tensile deformation was performed on the hydrogenated titanium sample, the interactions between OR2 hydride and plastic behaviors were observed by EBSD measurement.

## 5.2 Experimental process

In the current work, the material used was rolled commercially pure titanium T40 (ASTM grade 2) sheet with the thickness of 1.5 mm and annealed at 800 ºC for 3 h under high vacuum conditions. The obtained material was fully recrystallized with an average grain size of ~50 μm and a typical split basal texture. SEM and EBSD microstructure characterization was performed using JSM 6490 SEM and JEOL 6500F field emission gun microscopy.

The nano-indentation test with maximum load of 10 mN and loading/unloading rate 20 mN/min was performed to measure the mechanical properties of pre- and post-H-charged sample surface. 20×20 indentation matrices with spacing of 20 μm was done on the initial surface and hydrogenated surface after every 8 h charging until 24 h. The average indentation hardness ($H_{IT}$) and plane strain modulus ($E^*$) were calculated for each matrix to study the evolution of mechanical properties with charging time. The calculation method for hardness and modulus was presented in Section 2.1.4 of Chapter 2. The orientation dependence of hardness evolution was studied through performing

nanoindentation test on the same area of sample surface before and after 168 h hydrogenation. The anisotropy of elastic modulus was not involved because it is less sensitive to grain orientation [150]. The mechanical property of pre-charged α-Ti was measured by 30×40 indent matrix with the indent spacing of 20 μm along the X and 10 μm along Y axis. After hydrogenation, 8 sets of 15×10 indent matrices with above-mentioned spacing were inserted into initial 30×40 matrix successively to determine the anisotropic properties of hydride diffusion layer and also the hardness evolution during hydrogen charging. The influence of the grain boundaries was minimized by choosing indents in the grain interior more than 2 μm from grain boundaries [151].

The thickness of hydride layer after 7-days hydrogen charging is around 7 μm according to Fig. 4.8 in Chapter 4, which is too thin to influence the tensile property of Ti sheet. Thus, for the **TD** tensile samples with and without 168 h hydrogenation, only the lateral surface morphology near fractured edge of were compared under SEM. Besides, to investigate the interaction of dislocation and twin with hydride precipitates, another **TD** tensile sample with hydride platelets was prepared and stretched until 20% elongation. The samples were stretched using a DEBEN machine with a maximum load cell of 1 kN and a strain rate of 200 μm/min, while the tensile machine and sample dimensions are shown in Fig. 2.5a of Chapter 2.

## 5.3 Nano-indentation test

### 5.3.1 Mechanical property of α-Ti at different hydrogen charging times

During hydrogen charging, hard hydride phase precipitates when hydrogen concentration is supersaturated changing the surface properties of α-Ti. Fig. 5.1 shows the evolution of indentation hardness ($H_{IT}$) and plane strain modulus ($E^*$) during hydrogen charging measured by nanoindentation test. Before hydrogen charging, the mean nanohardness and modulus obtained from 400 indents are 2.8±0.3 GPa and 142.1±5.6 GPa, respectively, which coincide with the normal indentation properties of CP-Ti [150]. With hydrogen charging, the hardness of the sample clearly tends to increase while the modulus decreases. The gradual evolution of hydrogen-induced hardening and elastic modulus reduction is due to the formation of titanium hydride. However, the hardness and elastic modulus tend to maintain a constant level after 16 h of hydrogen charging time, respective 3.7±0.4 GPa and 130.9±6.8 GP. With the growth of hydride precipitation, the sample surface is gradually covered by hydride layer, then the nanohardness and modulus are

unchanged. Indeed, nearly whole titanium matrix on the diffusion surface has been transformed into hydride precipitates after 24 h hydrogen charging in Fig. 4.1 (Chapter 4).

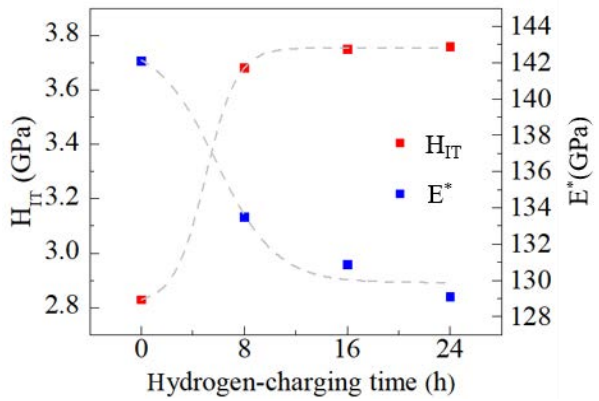


**Fig. 5.1** Hardness ($H_{IT}$: red) and modulus ($E^*$: blue) of CP-Ti depending on hydrogen-charging time

The results are consistent with the previous work of Xu et al. [152], in which the indentation was performed on the cross section of hydride layer, and the hardness was found to be about 30% higher than Ti matrix. The increased hardness of post-charged titanium surface shows the hard nature of hydride layer and thus the poor plastic deformability. Besides, the hydride has a slightly lower modulus than Ti matrix. The reduced $E^*$ means the lower resistance of hydride layer to elastic (recoverable) deformation under indentation load. Setoyama et al. [153] also found that Ti hydride is elastically softer than matrix and the elastic modulus is dependent on the hydrogen content. By using acoustic emission technique, Shi et al. [154] found that the micro-cracks in hydride can be initiated below the yield strength of Zr alloy and the stresses for crack initiation depend on the hydride length. During elastic deformation, the initiated micro-cracks can result in the reduction of macroscopic elastic modulus [155]. Thus, the formation of defects, such as micro-cracks or void, on the hydride layer can be the reason for the reduced elastic modulus of post-charged surface.

### 5.3.2 Anisotropic hardness of α-Ti before and after hydrogen charging

#### 5.3.2.1 Microstructure of grid indentation array

To study the anisotropic hardness evolution of Ti surface, the interrupted in-situ EBSD maps before and after 168 h hydrogenation are performed and shown in Fig. 5.2. The indents of 30×40 matrix on pre-charged titanium surface are presented on the band contrast map overlaid with IPF map in Fig. 5.2a, while the hydride microstructure of the same area after hydrogen charging is shown in Fig. 5.2b. The indents in α-Ti matrix produce large distortion during hydrogenation

leading to the corresponding non-indexed areas in Fig. 5.2b. To make sure that the indent matrix for δ-hydride measurement can be accurately inserted into initial α-Ti indent matrix, the large matrix is separated into 8 groups and 15×10 indent matrix for each group. The δ-hydride indents can be partially observed in the band contrast map of Fig. 5.2b. However, due to the instrument error, some δ-hydride indents, which are close to the initial α-Ti ones, will be excluded in subsequent analysis.

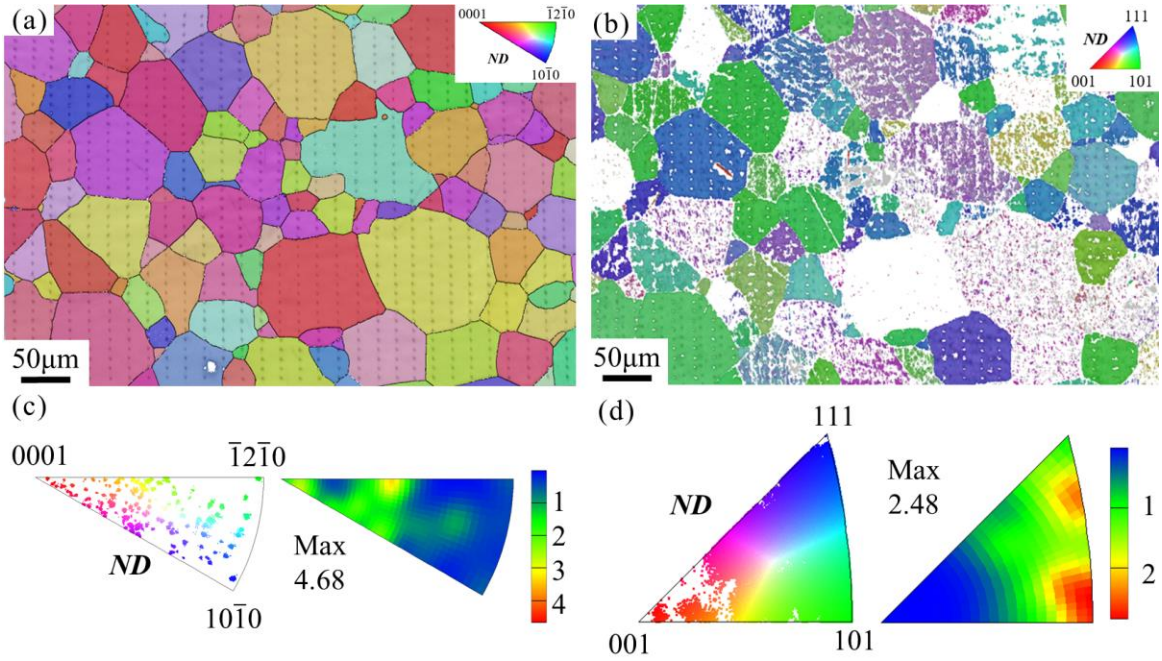


**Fig. 5.2** EBSD band contrast image overlaid with an IPF-**ND** orientation colored map of **(a)** α-Ti before charging and (b) δ-hydride layer after charging. The zero solution and remnant α-Ti matrix in **(b)** are shown by white and silver colors. **(c)** and **(d)** are the corresponding scatter and contour maps of IPF distribution of respective α-Ti and hydride.

Fig. 5.2c and d present **ND**-IPF distributions of initial α-Ti and δ-hydride precipitation in Fig. 5.2a and b, respectively. According to the scattered map of Fig. 5.2c, the selected area of initial sample includes enough grain orientations to investigate the anisotropic mechanical properties of α-Ti. Some orientation intensities are observed around 40º oriented from **ND** in IPF contour map favorable for the formation of OR2 hydride (Chapter 2). The orientation distribution of hydride is shown in Fig. 5.2d showing larger internal misorientation of hydride precipitation than titanium matrix due to the distortion of phase transformation. Indeed, the mean misorientation of the titanium and hydride grains in Fig. 5.2 are respective 0.27º and 1.55º. Hydride orientations mainly focus on the <101> parallel to **ND** corresponding to the orientation intensities of Ti matrix,

indicating that the majority hydrides follow OR2 orientation relationship $\{10\bar{1}3\}//\{1\bar{1}0\}$. Besides, the hydride with {001} plane normal parallel to **ND** is difficult to be formed.

The magnification of local indentation array is shown in SEM images (see Fig. 5.3). Fig. 5.3a presents the indents in α-Ti with the size of around 2.9 μm. In this chapter, the indent spacing 10 μm along Y direction is enough to avoid the influence of the plastically deformed zones around the existing indents on the mechanical properties. The large gap 20 μm in the X direction is left for indent insertion after hydrogen charging. The maximum load of 10 mN is unchanged before and after hydrogenation. The grain surface after hydrogenation are not smooth as shown in Fig. 5.3b due to the complex interactions between hydride variants. The indent size of δ-hydride (~2.5 μm) is smaller than that of α-Ti indicating the different hardness between $TiH_x$ and Ti matrix.

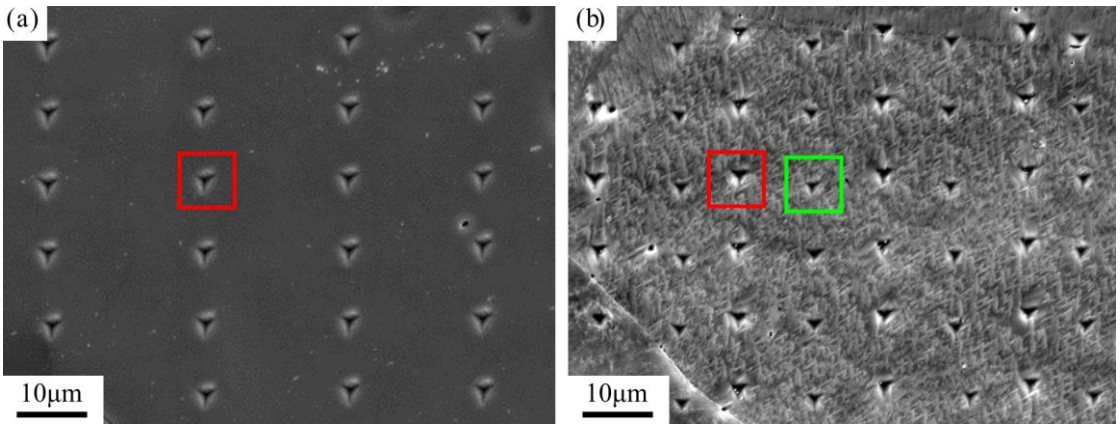


**Fig. 5.3** SEM magnification of grid indentation array **(a)** α-Ti before charging and **(b)** δ-hydride layer after charging. Red box shows the indenter of α-Ti and green box is the indenter on δ-hydride after hydrogenation.

### 5.3.2.2 Anisotropic hardness of α-Ti

To calculate anisotropic hardness of α-Ti, 55 α-Ti grains and 229 indentation tests in total (3-5 indents for each grain) are chosen from Fig. 5.2a. IPF with indentation hardness ($H_{IT}$) scales are drawn in Fig. 5.4a, which allow the observation of the relationship between the crystallographic orientation of a chosen single grain and corresponding mechanical properties. As shown in Fig. 5.4a, a clear rainbow appears in the fundamental triangle of IPF showing a significant tendency between the hardness values and specific orientations of individual grains. The hardness values decrease as the *c*-axis of the HCP crystal deviated from **ND**. The $H_{IT}$ values of α-Ti are in the range from 3.5 to 2.3 GPa with an average of 2.8 ± 0.3 GPa. The anisotropic hardness of CP-Ti was also measured using indentation (Berkovich tip, maximum load 50 mN) by Fizanne-Michel [150]. The

observed orientation dependence of hardness is consistent with our results, while the mean hardness 2.9 ± 0.4 GPa is similar to that in our work (2.8 ± 0.3 GPa). The slight deviation is likely due to the difference in applied load, instrument measurement error or the condition of indented surface.

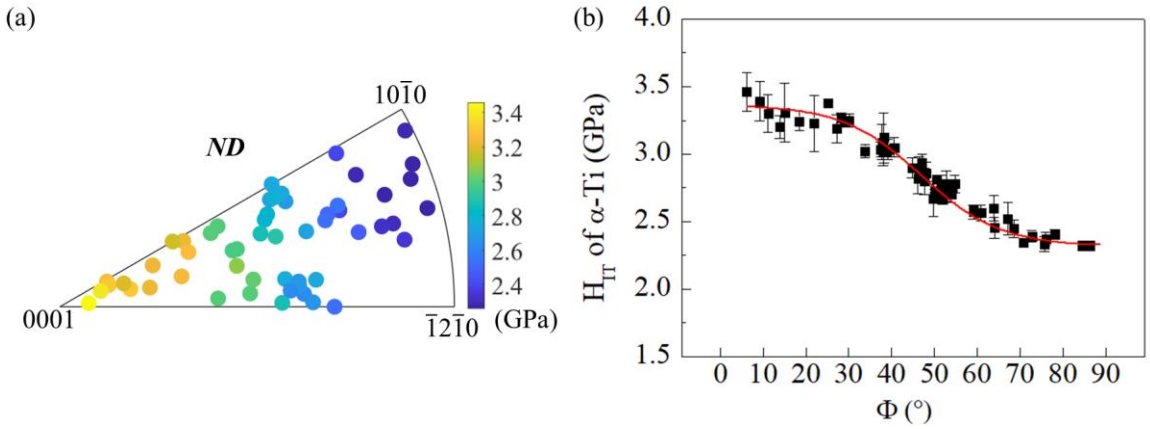


**Fig. 5.4** (a) Indentation Hardness IPF of α-Ti before charging. (b) Indentation hardness versus declination angle (Φ). Error bars are ± one standard deviation which incorporates multiple measurements in the same grain.

According to the IPF of hardness in Fig. 5.4a, there appears the variation of $H_{IT}$ along radial direction but not obvious circumferential variation. Thus, the $H_{IT}$ of CP-Ti is a function of the declination angle (Φ). The declination angle is between *c*-axis of the HCP crystal and the normal of sample surface (**ND**), which is equal to the second angle Φ of Euler angle ($\varphi_1$, Φ, $\varphi_2$). The only radial variation of hardness shows negligible influence of ($\varphi_1$, $\varphi_2$). Indeed, the result of crystal elastic finite element simulation on hardness of CP-Ti proposed negligible influence of ($\varphi_1$, $\varphi_2$) [156]. Fig. 5.4b shows the relationship between indentation hardness and declination angle (Φ). In generally, the $H_{IT}$ values monotonously decrease from 3.5 to 2.3 GPa as the indentation direction (stress axis) deviates from *c*-axis. It marginally decreases 5.7% at 0º<Φ<25° and 3.4% at 70º<Φ<90°, decreases steeply by approximately 29.1% within 25º<Φ<70°. These trends demonstrate strongly dependence between indentation hardness of individual grains and the orientation of indentation direction. The *c*-axis parallel to stress axis (Φ=0º) is the hardest orientation, while the <$10\bar{1}0$> or <$1\bar{2}10$> along stress axis (Φ=90º) is softest orientation for indentation test.

Indentation hardness measures the resistance of CP-Ti to local plastic deformation produced by compression load from an indenter, thus the orientation dependent $H_{IT}$ is attributed to the anisotropic activation of slip and twinning systems. The stress to activate a given slip or twinning

system is proportional to CRSS/SF. Viswanathan et al. [157] characterized plastic zone of α-Ti beneath nanoindents with focused-ion-beam (FIB) and TEM techniques. <***c***+***a***> slip is most favorable system in the hardest grain, all three types of <***a***> slips (prismatic, basal and pyramidal) are activated in the medium grain and screw prismatic <***a***> slip is predominant in softest grain. For CP-Ti, the CRSS for activation of <***c***+***a***> and prismatic <***a***> dislocations at room temperature are around 141 and 350 MPa, respectively [158]. It means that, if the SFs of <***c***+***a***> and prismatic <***a***> dislocation are the same, the stress needed for <***c***+***a***> dislocation is 2.5 times larger than that of prismatic <***a***>. Thus, the difference on activation stresses of multiple slip systems is the main reason for the anisotropic hardness. Twinning was not observed whether outside or beneath the residual indent [156,157]. Because of significant size dependence, large indenter size is needed to activate deformation twinning [159].

The SF calculated by indentation direction is suitable to predict the slip activation [157], although an arbitrary shape change is produced by indenter in a localized region indenter. In this chapter, SF is calculated to evaluate the probability of slip activation in the grain with different orientation under indentation compression. The grains with Euler angles of [0º, 0º, 0º] and [0º, 0º, 15º] are taken as two initial orientations, which are the hardest orientations with *c*-axes parallel to stress direction, and then misoriented through alter the angle Φ from 0º to 90º. For each orientation, the maximum SFs among the variants in each slip system are calculated and shown in Fig. 5.5. The lines with different colors represent five slip systems in CP-Ti. The solid and dotted lines show the SFs of the grain oriented from respective [0º, 0º, 0º] and [0º, 0º, 15º]. At Φ=0º, all the SFs of <***a***> slips are almost zero, the activation of them is severely limited, thus <***c***+***a***> slips with large SF (>0.4) are favorable in this orientation leading to the larger hardness. As the angle Φ increases, the orientation gradually favors <***a***> slips and the hardness also decreases. In the medium grain (Φ=45º), the SF of basal slip is highest, while the other <***a***> slips with slightly lower SF can also be activated due to the lower CRSS. The softest orientation of Φ=90º has the highest SFs for prismatic slip, which is the most common slip system in CP-Ti. Therefore, in this orientation, plastic deformation can be easily stimulated with low applied stress of indentation test.

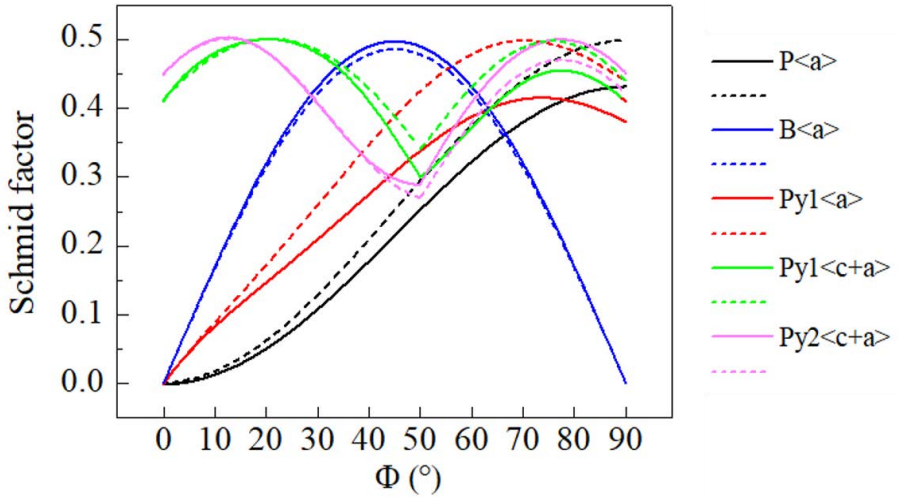


**Fig. 5.5** Schmid factor value of the dislocation slip systems with angle between the *c*-axis and loading direction.

### 5.3.2.3 Anisotropic hardness of δ-hydride

After hydrogen charging, 215 indentation tests (3-5 indents for each grain) were chosen from the same 55 titanium grains in order to compare the hardness change of hydride layer. The mechanical properties of hydride layer are obviously different from Ti matrix. The $H_{IT}$ values of δ-hydride are in the range from 3.2 to 4.4 GPa with an average of 3.8 ± 0.3 GPa, which is around +31.0% larger than the hardness of α-Ti (2.8 ± 0.3 GPa). The result is similar to that in Section 5.3.1.

Two hardness IPFs of the hydride hardness corresponding to respective titanium matrix orientations and hydride orientations are drawn in Fig. 5.6a and b. Fig. 5.6a shows the relationship between hydride hardness and the corresponding orientations of 55 titanium matrices, showing less sensitive orientation dependence of hydride hardness than α-Ti. The hydrides with higher hardness (inside red circle) are always formed in the titanium grain with $\{10\bar{1}3\}$ parallel to **ND** surface, which is the most favorable orientation for OR2 hydride. The summary of $H_{IT}$ versus declination angle Φ is shown in Fig. 5.6c. Indeed, there appears a peak at around Φ=25º with the orientation close to the $\{10\bar{1}3\}$ plane parallel to sample surface. According to the OR2 orientation relationship ($\{10\bar{1}3\}//\{1\bar{1}0\}$), the hydrides with orientations of $\{1\bar{1}0\}$ parallel to sample surface should also be harder. As shown in Fig. 5.2b, partial hydride grains are nearly non-indexed after charging. To calculate the dependence of hydride hardness on their own orientation, the non-indexed grains are excluded from the total 55 grains. The hardness IPF based on the orientations of 44 hydride grains

is presented in Fig. 5.6b, where the hydrides with orientations focus on {1$\bar{1}$0} normal parallel to **ND** have higher hardness (inside red circle). We also calculated the relationship between hydride hardness and declination angle $\theta$, which is the angle between <1$\bar{1}$0> direction of FCC hydride and **ND** (see Fig. 5.6d). It can be seen that $H_{IT}$ values slightly decrease with the increase of <1$\bar{1}$0> declination angle $\theta$. According to above, the OR2 hydrides formed from titanium grain with the orientation of {10$\bar{1}$3} plane parallel to **ND** surface have higher indentation hardness.

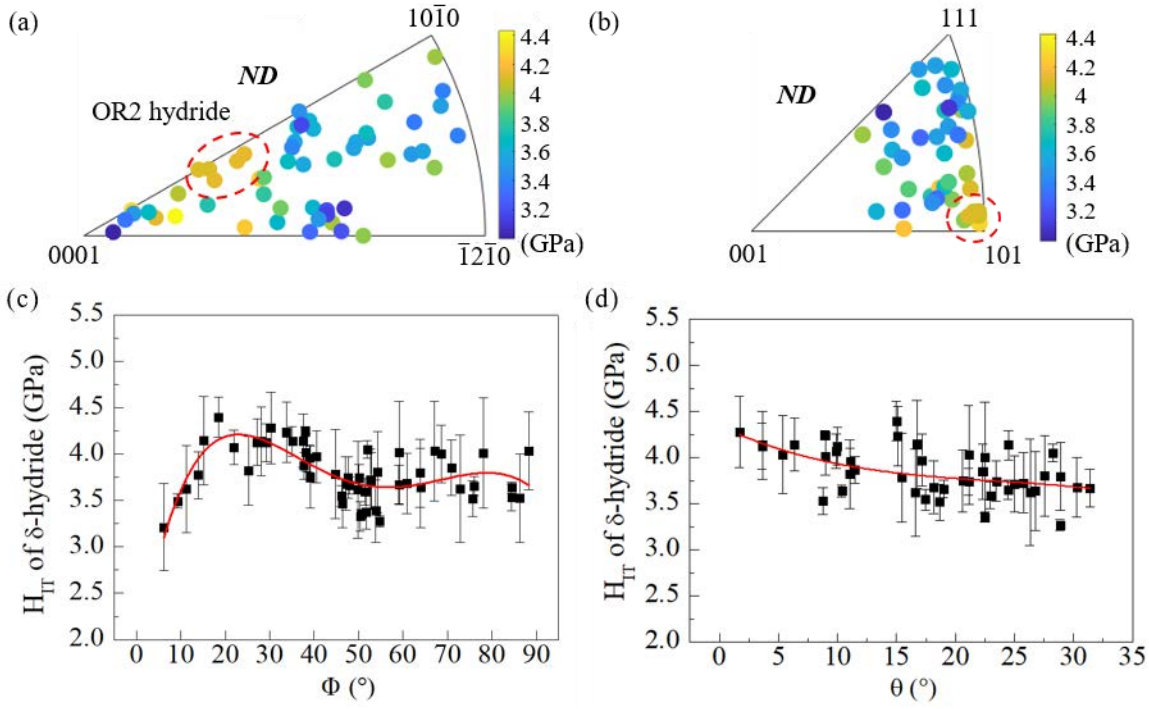


**Fig. 5.6** Hardness of δ-hydride layer after charging. **(a)** Hardness IPF drawn with orientation of Ti matrix **(b)** Hardness IPF drawn with orientation of δ-hydride **(c)** Indentation hardness of δ-hydride layer versus declination angle Φ **(d)** Indentation hardness of δ-hydride layer versus declination angle θ. Error bars are ± one standard deviation which incorporates multiple measurements in the same grain.

As shown in Fig. 5.2b, the surface microstructure after hydrogen charging shows that the hydride grains with {1$\bar{1}$0} normal parallel to **ND** in green IPF color have higher indexing rate and less distortion. Indeed, the misfit strain of the hydride grain with {1$\bar{1}$0} normal parallel to **ND** formed from OR2 favorable Ti grain can be easily accommodated though free surface. Besides, according to the results in Section 4.5, the hydride layer on the titanium grain with OR2 favorable orientation is almost composed of single hydride variant. However, in the hydride layer on the other grains, the complicate interactions between multiple hydride variants restrain the hydride growth and result in more remnant Ti matrices, which reduce the average hydride hardness. Some

defects, such as micro-cracks or void, produced by the hydride interactions can also decrease the value of indentation hardness.

#### 5.3.2.4 Comparison between α-Ti and δ-hydride

The change of indentation hardness with the *c*-axis declination angle Φ during hydrogen charging was studied. The hardness of 55 selected grains before and after charging are shown in Fig. 5.7 with red and blue points, respectively. The hardness of titanium matrix decreases with the increase of angle Φ, while the hardness values of hydrides are always higher than titanium with of relatively weak orientation dependence. The calculation error of the hydride hardness is larger due to the heterogeneous distribution of hydride precipitations inside grains. Thus, in general, the hardness change is larger with the increase of declination angle, which is much smaller in softer orientation than in the harder orientation of titanium grain. Obviously, the formation of hydride reduces the anisotropy of titanium grains. As discussed in Section 5.3.2.2, the orientation dependence of indentation hardness in α-Ti is due to the anisotropic activation of slip systems under indentation load. Thus, the reduced anisotropy during hydrogenation means the brittle nature and apparent suppression of hydride precipitation on both activation and motion of slip systems.

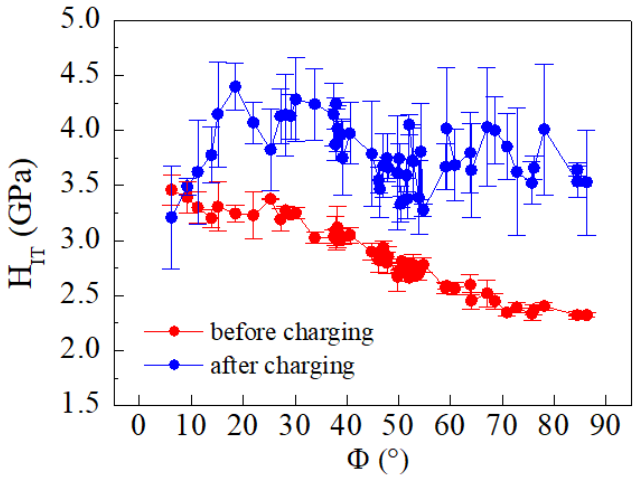


**Fig. 5.7** The change of $H_{IT}$ on sample surface before and after hydrogenation. Error bars are ± one standard deviation which incorporates multiple measurements in the same grain.

## 5.4 Tensile test

### 5.4.1 Tensile property influenced by hydrogen charging

To explore the influence of hydrogen charging on the tensile property, two samples with and without hydrogenation are stretched to break. The tensile curves are shown in Fig. 5.8. There

appears not obvious difference between two curves. According to Fig. 4.8, the thickness of hydride layer formed on the sample surface is around 7 μm, while the sample thickness is 0.5 mm. The hydride layer is too thin to influence the tensile property. However, after tensile deformation, extremely different surface microstructures of the two samples can be observed under SEM, as shown in Fig. 5.9.

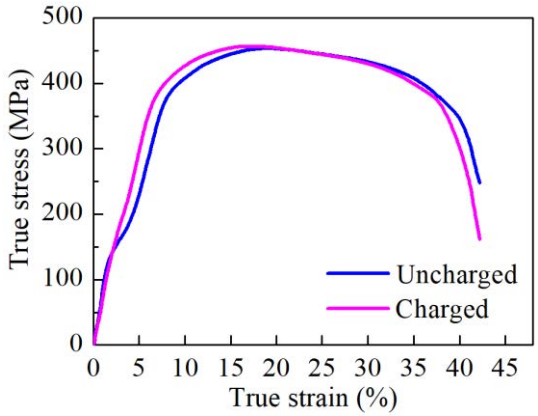


**Fig. 5.8** Tensile curve of the sample with and without hydrogen charging

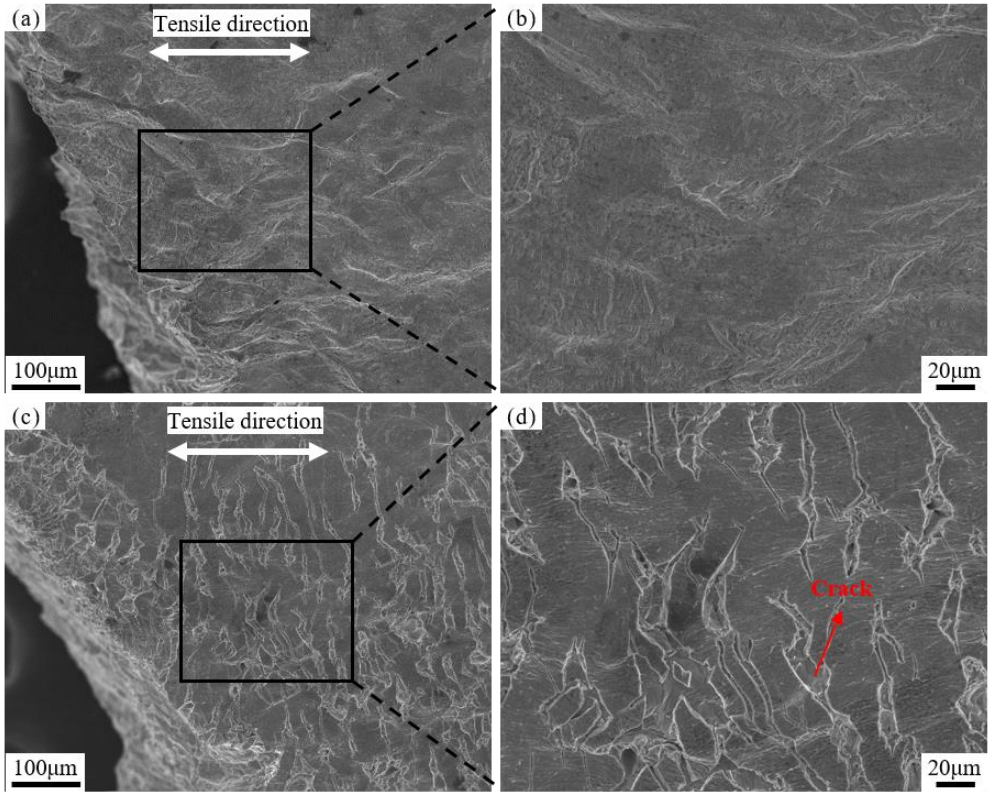


**Fig. 5.9** SEM images of lateral surface near fractured edge **(a)** Pre-charged sample. **(b)** Magnified microstructure of the area marked in (a). **(c)** Post-charged sample. **(d)** Magnified microstructure of the area marked in (c).

Fig. 5.9 shows the microstructures of lateral surfaces near fractured edges. For uncharged sample, ductile microstructure can be observed in Fig. 5.9 a and b. In contrast, amounts of micro cracks perpendicular to tensile direction take place in the hydride layer on the sample surface (see Fig. 5.9c and d). The brittle hydride layer with lower toughness cannot accommodate the large tensile deformation inside titanium matrix leading to the nucleation of micro-cracks.

### 5.4.2 Interaction between hydride and plastic deformation modes

Although the hydrides show extremely low ductility in Fig. 5.9, some studies proposed that hydrides have a certain ability to deform [117,118]. The interaction between dislocation and OR1 hydride has been investigated by Chen et al. [117,118] under SEM and TEM techniques. They found that OR1 hydride has a good deformability because of the coherent interface between OR1 hydride and titanium matrix. However, only a very small fraction of OR2 hydride was observed in their experiments, thus the related research on OR2 hydride is lacking. According to our previous results, OR2 hydride is the dominant hydride phase formed by hydrogen charging on **ND** surface. The OR2 hydride interactions with plastic deformation modes play an important role on the mechanical property of hydrogenated titanium. Some special hydride interactions with slip and twin in the **TD** tensile sample are researched in this section.

#### 5.4.2.1 Hydride-dislocation interaction

In previous research, SEM observation can clearly catch the slip traces on deformed sample [160]. By the combination of SEM and EBSD measurement, the type of slip mode can be determined. The microstructure of the interactions between OR2 hydrides and dislocations are shown in Fig. 5.10. The IPF map in Fig. 5.10a presents two parallel hydride platelets and the hydride variant is $B_2$. After tensile deformation, two types of activated slip modes intersecting with hydrides are labeled by green and blue lines, respectively (see Fig. 5.10b). IGMA analysis [1] of EBSD date is used to explore the active slip mode. The lower cutoff misorientation angle in IGMA analysis is taken as 1.2º, because of the limited angular resolution of the EBSD analysis. The IGMA distributions of material-point pairs between 1.2º and 2º is enough for the investigation of active slip mode, while the larger in-grain misorientation angle (>2º) is due to the deformation bands. Strong intensity around <0001> is observed in the 1.2º-2º IGMA distribution in Fig. 5.10c, the predominant slip mode is prismatic <***a***> slip by matching the Taylor axis in Table 1.1 (Chapter 1) to IGMA map. Besides, there appears no obvious distribution of slip bands inside the grain. To

further determine the slip system, SF criterion and trace analysis method are used. $(1\bar{1}00)$ $[11\bar{2}0]$ (P<***a***>$_1$) and $(10\bar{1}0)$ $[1\bar{2}10]$ (P<***a***>$_2$) are the activated slip systems with the largest two SF values, respective 0.44 and 0.42. The poles of prismatic <***a***> slip planes and slip directions are shown in the $\{10\bar{1}0\}$ and $<1\bar{2}10>$ pole figure (see Fig. 5.10d), where the poles in blue and green circles represent the activated slip systems P<***a***>$_1$ and P<***a***>$_2$. After that, the individual slip system can be determined according to the slip trace in the SEM image and pole figures. More P<***a***>$_1$ dislocations with larger SF value are generated in the deformed grain.

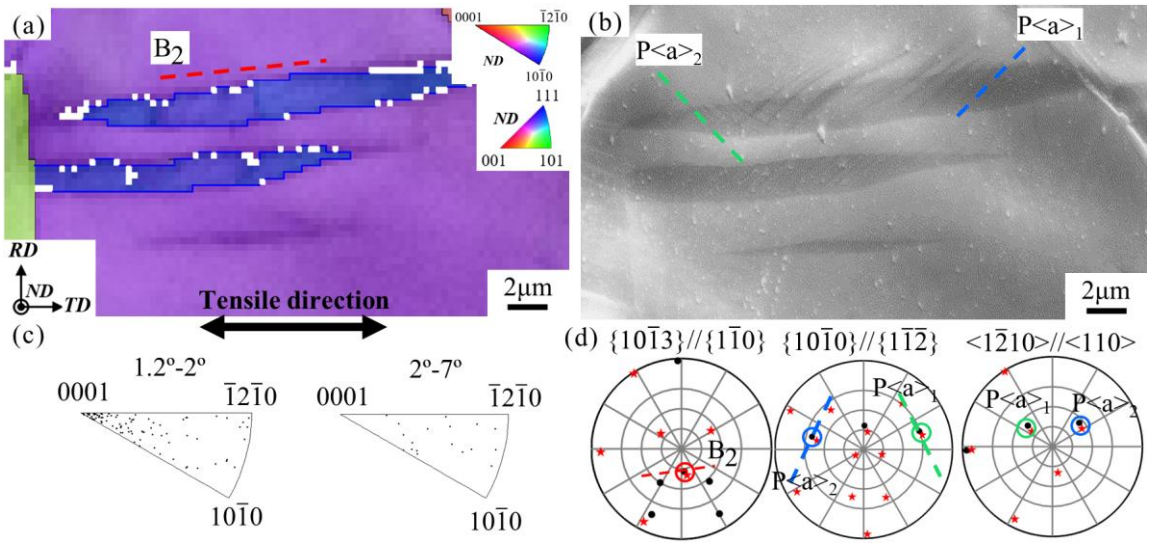


**Fig. 5.10** Microstructure of deformed grain with OR2 hydrides **(a)** IPF map and **(b)** corresponding SEM image. Grain boundaries and hydride interface are colored by black and blue, respectively. Dotted lines are the trace of hydride and slip plane. **(c)** The IGMA distribution for the deformed titanium grain. **(d)** Pole figures of $\{10\bar{1}3\}$, $\{10\bar{1}0\}$ planes and $<1\bar{2}10>$ directions. The black dots represent the plane and direction of α-Ti matrix and the red dots are δ-hydrides. (Euler angle of Ti grain: 4.9º, 60.1º, 27.4º)

Prismatic <***a***> slip is the most common slip systems in α-Ti at room temperature, which can be activated and move fast in the deformed grain. From the SEM image in Fig. 5.10b, the slip traces near hydrides are clearer than titanium matrix showing the obstruction and pinning of dislocation gliding by hydride plates. Furthermore, the obvious transmission of prismatic slip from titanium matrix into hydride precipitation is observed. As shown in Fig. 5.10d, the slip plane $\{10\bar{1}0\}$ and direction $<1\bar{2}10>$ of titanium are parallel to $\{1\bar{1}\bar{2}\}$ plane and <110> direction of hydride, respectively. According to the work of Conforto and Caillard [91], the interface is coherent and favorable for the slip transmission. In FCC crystal, slip generally occurs on {111} planes in $<1\bar{1}0>$ directions (on close-packed planes in close-packed directions) and the majority of prismatic <***a***>

slips in titanium under low plastic strain are screw slips. Thus, the slip transmission processed can be followed by the cross-slip process from $\{1\bar{1}\bar{2}\}$ into $\{111\}$ plane inside hydride.

A deformed grain with more severe slip bands is shown in Fig. 5.11. According to the IGMA distribution are presented in Fig. 5.11c, prismatic <***a***> slip and corresponding slip bands are formed. The dominant slip system in Fig. 5.11b is $(1\bar{1}00)$ $[11\bar{2}0]$ (P<***a***>$_1$) with the highest SF of 0.37, while obvious dislocation transmissions happen. Especially, another slip system, $(01\bar{1}0)$ $[\bar{2}110]$ (P<***a***>$_3$) with a lower SF of 0.18, induced at hydride interface by the impinging of P<***a***>$_1$ slip bands is observed in the black box. Normally, due to the local stress fluctuation near boundary, the deformation in polycrystalline materials is heterogeneous [24,25,161]. During deformation, the hydride precipitation on the grain boundary is under more complicated stress states than the intragranular ones leading to the activated low SF slip (P<***a***>$_3$) by the impingement of slip bands.

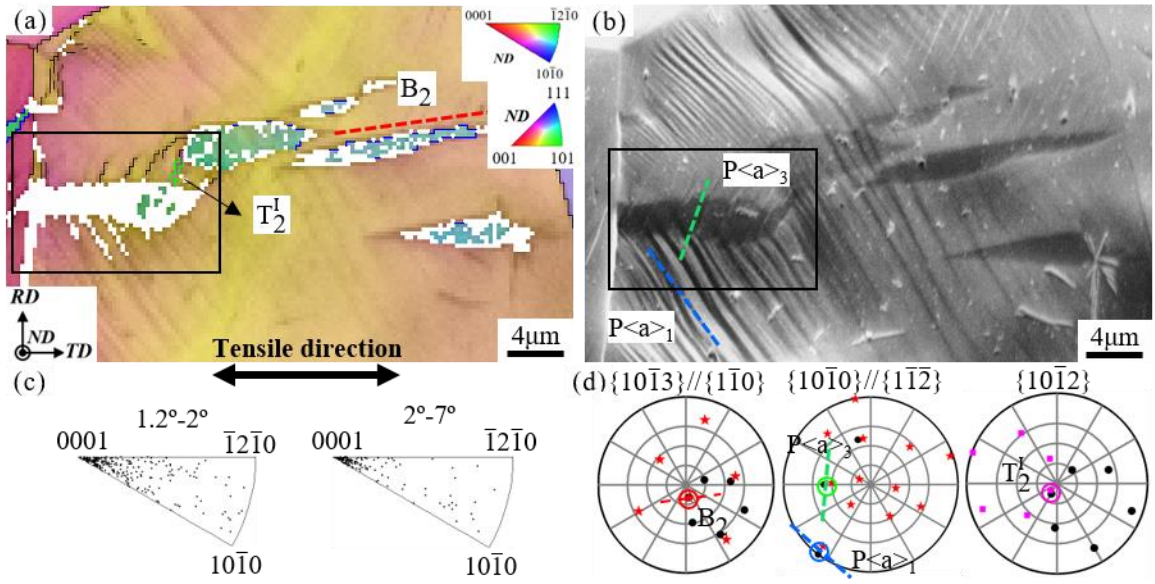


**Fig. 5.11 (a)** IPF map and **(b)** corresponding SEM image of deformed grain with OR2 hydrides. Grain boundaries, hydride and $\{10\bar{1}2\}$ twin interface are colored by black, blue and green, respectively. The dotted line shows the trace of hydride and slip plane. **(c)** The IGMA distribution for the grain after tensile deformation. **(d)** Pole figures of $\{10\bar{1}3\}$, $\{10\bar{1}0\}$ and $\{10\bar{1}2\}$ planes. The black dots represent the plane and direction of α-Ti matrix and the red dots are δ-hydrides. (Euler angle of Ti grain: 53.2º, 40.1º, 60.3º)

The stress concentration of the intergranular hydride in the black box is further confirmed by EBSD map in Fig. 5.11a. The intergranular hydride with slip transmission are nearly non-indexed, which can be seen as the reasons for the hydride induced micro-crack or void nucleation. Besides,

the movement of P<***a***>$_3$ dislocations with low SF is restricted. Dislocation walls formed by the accumulation of P<***a***>$_3$ dislocations are identified as small grain boundaries (>5º) on the upside of the intergranular hydride. Interestingly, a nucleation of {10$\bar{1}$2} tension twin ($T_2^I$) is formed in the area of P<***a***>$_3$ dislocation walls. As researched in Section 4.4.1.1 of Chapter 4, {10$\bar{1}$2} tension twin can be induced by OR2 hydride with hydride-twin pairs of $B_i$-$T^I_{i+3}$. Thus, the $T_2^I$ tension twin in Fig. 5.11a is neither induced by $B_2$ hydride nor by external force due to the negative SF value of -0.18. It can be derived that the $T_2^I$ twin nucleation is stimulated by the local stress concentration of P<***a***>$_3$ dislocations, which is not stable and will be detwinned after a larger elongation.

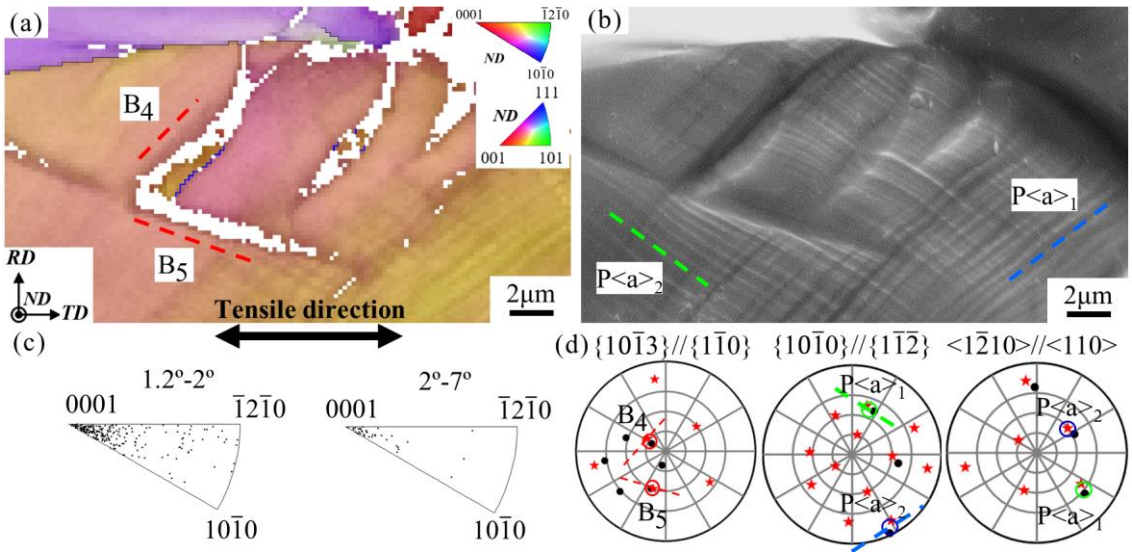


**Fig. 5.12 (a)** IPF map and **(b)** corresponding SEM image of deformed grain with OR2 hydrides. Grain boundaries and hydride interface are colored by black and blue, respectively. Dotted lines are the trace of hydride interface and slip plane. **(c)** The IGMA distribution for the deformed grain. **(d)** Pole figures of {10$\bar{1}$3}, {10$\bar{1}$2} planes and <10$\bar{1}$2> directions. The black dots represent the plane and direction of α-Ti matrix and the red dots are δ-hydrides. (Euler angle of Ti grain: 114.3º, 140.1º, 58.4º)

The grain in Fig. 5.12 is favorable for two dominant slip systems. The $B_4$ and $B_5$ hydrides in Fig. 5.12a have much lower indexing rate than the hydride interacting with single slip mode (see Fig. 5.10a and Fig. 5.11a). The non-indexed $B_5$ is determined by the combination of hydride variant selection in Section 3.6.2 of Chapter 3 and trace analysis of hydride interface through pole figure in Fig. 5.12d. The intersecting slip traces in Fig. 5.12b belong to prismatic <***a***> slip systems according to IGMA distribution. After SF and slip trace analysis, the slip systems parallel blue dotted line are (1$\bar{1}$00) [11$\bar{2}$0] (P<***a***>$_1$) with Schmid factor of 0.30 and the ones parallel green line

are $(10\bar{1}0)$ $[1\bar{2}10]$ (P<***a***>$_2$) with 0.27 SF value. Both of them are dominant slip systems in the grain due to the similar SF values.

The interaction between two slip systems impedes the movement and transmission of dislocations across hydride leading to large strain incompatibility between hydride and matrix. Furthermore, the slip traces of P<***a***>$_1$ and P<***a***>$_2$ are nearly parallel to the interface traces of respective $B_4$ and $B_5$ hydrides, indicating large interaction area between dislocation line and hydride plate interface. Therefore, hydride induced hardening is more serious in this grain. As for the grains in Fig. 5.10 and Fig. 5.11, the angles between hydride and slip trace are larger, and the contact areas of slip lines are close to the thickness direction of hydride plate. The smaller interaction area and lower hydride induced hardening reduce the strain incompatibility at hydride-titanium interface.

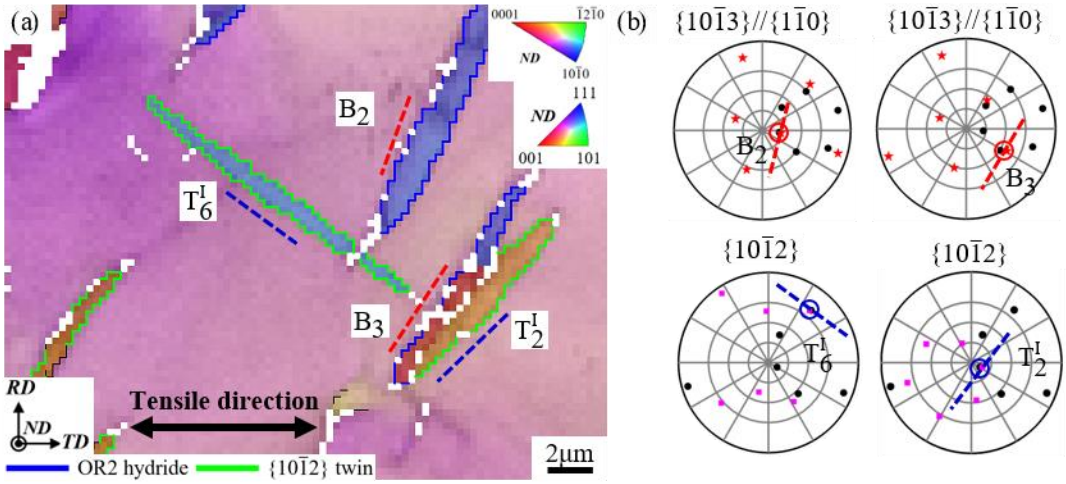


**Fig. 5.13 (a)** IPF map of deformed grain with hydrides. Grain boundaries, hydride and {10$\bar{1}$2} twin interface are colored by black, blue and green, respectively. The dotted line shows the trace of hydride interface and twin plane. **(b)** Pole figures of {10$\bar{1}$3} and {10$\bar{1}$2} planes. The black dots represent the plane of α-Ti matrix and the color dots are the planes of δ-hydride or twin. (Euler angle of Ti grain: 99.1°, 52.0°, 41.3°)

### 5.4.2.2 Hydride-twin interaction

{10$\bar{1}$2} tension twin is the most common twin in α-Ti at room temperature when the *c*-axis of grain is under extraction. Twins prefer to nucleate in the regions of stress concentration, grain boundaries and dislocation cells. Fig. 5.13 shows the deformed grain containing both {10$\bar{1}$2} twin and OR2 hydride. The variants of hydride precipitations are $B_2$ and $B_3$, while the two activated twin variants are $T_2^I$ and $T_6^I$ with the SF values of respective 0.17 and 0.29. The six {10$\bar{1}$2} twin

variants can be found in Table 4.1 in Chapter 4. Due to the positive SF, their strain contributions are in accordance with external macroscopic strains. As shown in Fig. 5.13a, $T_2^I$ variant is stimulated at the interface of $B_3$ hydride. The misfit dislocations around hydride plate can be the origins of the twin nucleation. Thus, hydride interface is also found to be taken as the preferential nucleation position for twinning in the deformed grains. Lee et al [162] investigate the effects of hydride precipitation on the mechanical properties of Zr alloys with uniaxial tensile tests at room temperature. With increasing hydrogen concentrations, yield strengths tend to decrease gradually. The decreased yield strength can be due to the misfit dislocation emission and preferential twin nucleation induced by hydride transformation.

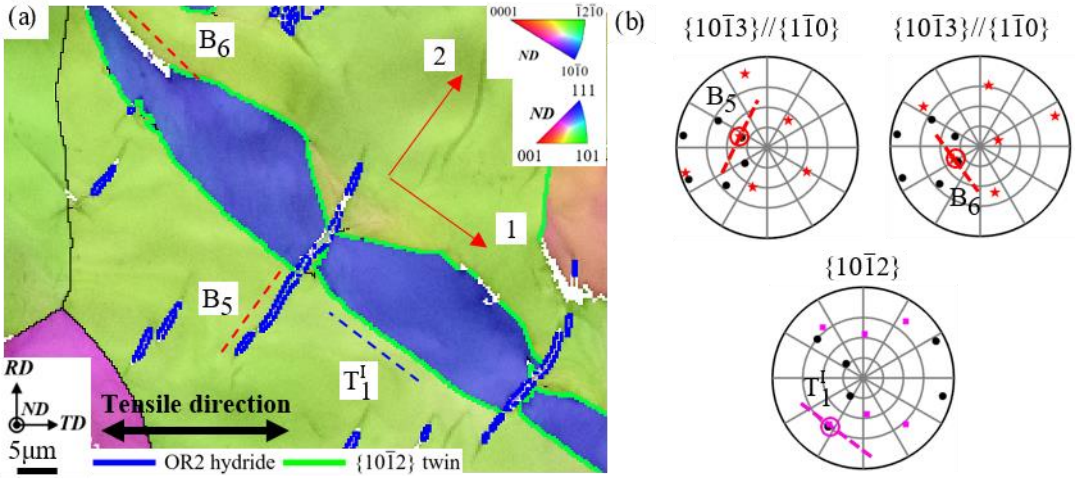


**Fig. 5.14 (a)** IPF map of deformed grain with hydrides. Grain boundaries, hydride and {10$\bar{1}$2} twin interface are colored by black, blue and green, respectively. The dotted line shows the trace of hydride interface and twin plane. **(b)** Pole figures of {10$\bar{1}$3} and {10$\bar{1}$2} planes. The black dots represent the plane of α-Ti matrix and the color dots are the planes of δ-hydrides or twin. (Euler angle of Ti grain: 97.3°, 122.1°, 0.3°)

Hydride precipitation can also impede the growth and thickening of deformation twin, which depends on the orientation between twin and hydride variants. A large {10$\bar{1}$2} tension twin is identified in Fig. 5.14a, where the twin variant is $T_1^I$ with the largest SF (0.35) and two hydride variants are $B_5$ and $B_6$. $B_5$ and $B_6$ are parallel to the thickness and length direction of twin lath, respectively. The larger contact area between $B_6$ and twin results in the higher stress concentration and thus low indexing rate of $B_6$, while the thickening of twin lath is restrained by $B_6$ hydride. Besides, the twin lath is separated into three parts by two $B_5$ hydrides. Near junction zone, the twin tends to be much narrower and the $B_5$ hydride plates are slightly sheared. The pinning effect of $B_5$ hydride on twin is more significant on both the twin growth and thickening.

Furthermore, the growth direction of twin can be determined according to Fig. 5.14a. The lower twin interface is relatively straight, while the upper interface is irregular, thus the thickening direction of twin is mainly in "2" direction (red arrow) in Fig. 5.14a. The limitation of the $T_1^I$ twin thickening is likely due to the back stress produced by grain boundary close to the lower twin interface indicating that the growing away from the grain boundary is energy favorable. Furthermore, the major shear direction of this twin is along "1" direction (left to right). At contact zones between twin and $B_5$ hydride, there appears larger gaps on the right side of hydride plate. It can be derived that the twin shear is interrupted by a hydride plate and accumulates at the intersection. When the shear accumulation reaches a critical level, the twin will cross or bypass the hydride plate and leave a gap at the junction.

## 5.5 Chapter summary

In this Chapter, the mechanical properties of titanium hydride were investigated by nano-indentation tests and tensile deformation.

The indentation hardness ($H_{IT}$) and modulus ($E^*$) of titanium surface were measured after every 8 h hydrogen charging to examine the evolution of mechanical properties. The hardness clearly tends to increase while modulus decreases until 16 h charging, after that, both of them maintain a constant level. The hydrogen-induced hardening and elastic modulus reduction are mainly due to the formation of hydride precipitation.

The indentation hardness of individual titanium grains is strongly dependence on the orientation of indentation direction. The average hardness of titanium matrix is 2.8 ± 0.3 GPa. The $H_{IT}$ value monotonously decreases from 3.5 to 2.3 GPa as the indentation direction (stress axis) deviates from *c*-axis. The *c*-axis parallel to stress axis is the hardest orientation and the $<10\bar{1}0>$ or $<1\bar{2}10>$ along stress axis is softest orientation for indentation test. The orientation dependent $H_{IT}$ is mainly attributed to the anisotropic activation of slip systems in α-titanium. In the hardest grain, $<\boldsymbol{c}+\boldsymbol{a}>$ slip is most favorable system, the larger CRSS for activation of $<\boldsymbol{c}+\boldsymbol{a}>$ results in higher applied stress from indentation test. $<\boldsymbol{a}>$ slip systems with low CRSS are easier to be activated by indentation loading in soft grain.

The orientation dependent hardness of δ-hydride formed after 168 h charging is less sensitive than α-Ti. The average $H_{IT}$ value of δ-hydride is 3.8 ± 0.3 GPa, which is much higher than titanium matrix showing the hard nature of hydride phase. OR2 hydride with $\{1\bar{1}0\}$ parallel to surface,

formed in the titanium grain with OR2 favorable orientation, has slightly larger $H_{IT}$ values. During hydrogenation, the larger hardness increase in the titanium grain with softer orientation than that with harder orientation finally result the weakened anisotropy on the post-charged surface.

The tensile morphologies near fracture edge were observed on the pre- and post-H-charged titanium surface. Plenty of cracks are induced in the brittle hydride layer on the charged surface to accommodate the large tensile strain. Although the poor deformability of hydride layer, the interactions between dislocations and twins also occur for hydride platelets. During tensile deformation, the predominant slip mode in the titanium grain is prismatic <***a***> slip. The transmission of prismatic slip from titanium matrix into hydride precipitation was observed, because of the coherent interface ($\{10\bar{1}0\}//\{1\bar{1}\bar{2}\}$ and $<1\bar{2}10>// <110>$). The hydride near grain boundary has higher stress concentration, which can induce the activation of another slip systems during the impingement of heavy slip bands. Besides, when a grain has more than one predominant slip mode, larger strain incompatibility between hydride and matrix restrain the slip transmission.

The nucleation of $\{10\bar{1}2\}$ tension twin at the hydride interface was observed in the deformed titanium grain. Hydride precipitation can impede both the growth and thickening of deformation twin. The hydride plate parallel to the length direction restrains the twin thickening and the hydride plate perpendicular to the thickness direction hinders both twin growth and thickening. These obstruction effect of hydride on twin can finally result in the stronger work hardening of titanium sample.

# Chapter 6 Conclusions and prospects

Contents



## 6.1 Conclusions

In the present work, a thorough experimental and theoretically crystallographic study has been conducted on hydride phase transformation in commercial pure titanium using the method of electrolytic hydrogen charging. The interaction of hydride precipitation with plastic deformation and the mechanical properties influenced by hydride transformation were investigated.

***Orientation dependence and variant selection of OR1 and OR2 hydride transformation***

Two orientation relationships of α-titanium/δ-hydride transition (OR1: {0001}//{001} $<1\bar{2}10>$//<110> with interface plane $\{10\bar{1}0\}$//$\{1\bar{1}0\}$, and OR2: ({0001}//$\{1\bar{1}1\}$ $<1\bar{2}10>$//<110> with interface plane $\{10\bar{1}3\}$//$\{1\bar{1}0\}$) are predominant on diffusion surfaces through interrupted in-situ EBSD measurement. The texture of ND surface is more favorable for hydride precipitation than RD surface. OR1 hydride transition in α-Ti is less favorable than OR2 due to its large distortion on the basal plane.

The grain orientations with $\{10\bar{1}0\}$ and $\{10\bar{1}3\}$ interface planes parallel to the diffusion surface are most favorable for OR1 and OR2 hydride transition, respectively. However, *c*-axis and *a*-axis of α-Ti grains parallel to the diffusion direction are the most unfavorable orientations for the formation of hydride precipitation. The calculation of anisotropic strain caused by hydride transition in α-Ti matrix indicates that the direction with largest misfit strain is $\{10\bar{1}0\}$ interface plane normal for OR2 hydride transformation and $\{10\bar{1}3\}$ interface plane normal for OR1. Thus, the grains which are more favorable for hydride formation can more effectively accommodate the strain of OR1 and OR2 hydride transition through the diffusion surface.

There appear three types of hydride platelet microstructures: parallel hydride platelets (Type I), crossed hydride platelets (Type II) and clustered hydride platelets (Type III). The hydride variants with interface plane most parallel to the diffusion surface is selected due to the highest

capacity of strain release. In the OR1 and OR2 favorable grain, only one or two hydride variants are activated and then quickly grow up to cover the whole grain. For the grain with basal plane parallel to the sample surface, all the OR2 hydride variants can be formed. The interaction between the multiple variants leads to that the grain is the non-indexed after hydrogen charging. The reason for lots of remnant α-Ti matrix in the grain with *a*-axis parallel to the surface normal is the difficulties on the growth of the formed clusters including both OR1 and OR2 hydride.

***Accommodation mechanism for hydride phase transformation***

Due to the large misfit strain of hydride transformation, certain accommodation operations are necessary for the strain relaxation. $\{10\bar{1}2\}$ extension and $\{11\bar{2}2\}$ contraction twins are observed at the interface of OR2 hydride platelets. $\{10\bar{1}2\}$ twin prefers to be formed in the grain with ***c***-axis parallel to diffusion direction and $\{11\bar{2}2\}$ twin is in the grain with transition orientation between OR1 and OR2 favorable ones. The twin variant with larger $D_{13}^{H\text{-}T}$ and $D_{33}^{S}$ is selected due to the highest accommodation capacity for local distortion of the nucleated hydride platelet. $\{10\bar{1}1\}$ twin is observed inside hydride layer near diffusion surface, which is activated by the accumulative stress inside Ti matrix in favor of the further growth of hydride precipitation.

Anisotropic hydride interaction was observed on the cross section of hydride layer. The hydride layer in the grains with the orientations of $<\bar{1}2\bar{1}0>$ and/or $<10\bar{1}0>$ parallel to diffusion direction mainly consists of OR1 hydride. Three symmetric OR1 variants are usually precipitated together to accommodate the large misfit strain.The grains with $\{10\bar{1}3\}$ and/or basal plane parallel to diffusion surface are favorable for the OR2 hydride layer. OR3 was observed at the edge of OR2 hydride layer, which is formed by the interaction of OR2 hydride variants and stress concentration on the diffusion surface.

Fine grain sample with larger volume of grain boundaries are more favorable for hydride transformation. The formation of intergranular hydride pair is one type of grain boundary accommodation behavior during hydrogenation. Adjacent hydrides prefer to be formed at the grain boundary with both the low θc ($< 30^{o}$) and the high θc ($75^{o} < \theta c < 85^{o}$). The reason for the preference at low $\theta_c$ boundaries is the aligned {0001} slip plane of grains on both sides of grain boundary. Prismatic slip induced by *c*-axis dilatation of neighbor grain results in amount of hydride pairs at the high $\theta_c$ boundaries ($75^{o} < \theta c < 85^{o}$).

***Mechanical properties of hydride phase***

The mechanical property evolution of titanium surface with hydrogen charging time was investigated by nanoindentation tests. During hydrogenation, the nanohardness ($H_{IT}$) clearly tends to increase while elastic modulus decreases until 16 h charging, after that, both of them maintain a constant level. The hydrogen-induced hardening and elastic modulus reduction are mainly due to the formation of hydride precipitation.

The indentation hardness of individual titanium grains is strongly dependent on the orientation of indentation direction. The average hardness of titanium matrix is 2.8 ± 0.3 GPa. The $H_{IT}$ value monotonously decreases from 3.5 to 2.3 GPa as the indentation direction (stress axis) deviates from *c*-axis. The *c*-axis parallel to stress axis is the hardest orientation and the $<10\bar{1}0>$ or $<1\bar{2}10>$ along stress axis is softest orientation for indentation test. The orientation dependent $H_{IT}$ is mainly attributed to the anisotropic activation of slip systems in α-titanium.

The orientation dependent hardness of δ-hydride formed after 168 h charging is less sensitive than α-Ti. The average $H_{IT}$ value of δ-hydride is 3.8 ± 0.3 GPa, which is much higher than titanium matrix showing the hard nature of hydride phase. OR2 hydride with $\{1\bar{1}0\}$ parallel to surface, formed in the titanium grain with OR2 favorable orientation, has slightly larger $H_{IT}$ values. During hydrogenation, the larger hardness increase in the titanium grain with softer orientation finally result the weakened anisotropy on the post-charged surface.

The tensile morphologies near fracture edge were observed on the pre- and post-H-charged titanium surface. Plenty of cracks are induced in the brittle hydride layer on the charged surface to accommodate the large tensile strain inside Ti matrix. Although the poor deformability of hydride layer, the interactions between dislocations and twins were also occur for hydride platelets. During tensile deformation, the predominant slip mode in the titanium grain is prismatic $<\boldsymbol{a}>$ slip. The transmission of prismatic slip from titanium matrix into hydride precipitation was observed. The hydride near grain boundary has higher stress concentration, which can induce the activation of another slip systems during the impingement of heavy slip bands. Besides, when the grain has more than one predominant slip mode, larger strain incompatibility between hydride and matrix restrain the slip transmission.

The nucleation of $\{10\bar{1}2\}$ tension twin at the hydride interface was observed in the deformed titanium grain. Hydride precipitation can impede both the growth and thickening of deformation twin. The hydride plate parallel to the length direction restrains the twin thickening and the hydride plate perpendicular to the thickness direction hinders both twin growth and thickening. These obstruction effects of hydride on twin are the reason for the hydrogen-induced hardening in α-Ti.

## 6.2 Prospects

1. Quantitative measurements of lattice orientation have now been made available with the rapid development of advanced characterization tools, such as the EBSD employed here in this work. The geometric relationship in ORs could be changed due to elastic energies that arise from elastic distortion and dislocations. A mechanics analysis of their contributions can and should be performed. For example, the elastic distortion will certainly lead to small deviation from ORs, and this should be quantified.

2. Hydride reorientation happens when hydride phase transformation is carried out under external stress. The applied stress can change the nucleation driving force and thus change the macro interface of hydride precipitation. In this work, hydrogen charging is performed under stress-free condition. In the future, the stress can be applied during electrolytic hydrogen charging, the influence of the direction and magnitude of applied stress on the reorientation of hydride platelet need detailed investigation.

3. Characterization of hydride precipitation should be done at atomic scale by simulation and high resolution TEM. The mechanism of hydride induced twinning and hydride interaction are still unclear. The deformation modes activated beneath indenter should be further observed under nano-level characterization. The stress field around hydride precipitation with and without deformation should be investigated.

# References

[1] Y.B. Chun, M. Battaini, C.H.J. Davies, S.K. Hwang, Distribution Characteristics of In-Grain Misorientation Axes in Cold-Rolled Commercially Pure Titanium and Their Correlation with Active Slip Modes, Metall. Mater. Trans. A. 41 (2010) 3473–3487.

[2] G.Y. Chin, W.L. Mammel, Competition among basal, prism, and pyramidal slip modes in hcp metals, Metall. Mater. Trans. B. 1 (1970) 357–361.

[3] A. Akhtar, Basal slip and twinning in α-titanium single crystals, Metall. Trans. A. 6 (1975) 1105.

[4] M.H. Yoo, C.T. Wei, Slip modes of hexagonal-close-packed metals, J. Appl. Phys. 38 (1967) 4317–4322.

[5] N. Munroe, X. Tan, H. Gu, Orientation dependence of slip and twinning in HCP metals, Scr. Mater. 36 (1997).

[6] S.G. Hong, S.H. Park, C.S. Lee, Role of {10-12} twinning characteristics in the deformation behavior of a polycrystalline magnesium alloy, Acta Mater. 58 (2010) 5873–5885.

[7] D. Shechtman, D.G. Brandon, Orientation dependent slip in polycrystalline titanium, J. Mater. Sci. 8 (1973) 1233–1237.

[8] D. Hull, D.J. Bacon, Introduction to dislocations, Butterworth-Heinemann, 2001.

[9] J.W. Edington, K.C.T. Russell, Practical electron microscopy in materials science, Macmillan International Higher Education, 1977.

[10] H. Li, C.J. Boehlert, T.R. Bieler, M.A. Crimp, Examination of the distribution of the tensile deformation systems in tension and tension-creep of Ti-6Al-4V (wt.%) at 296 K and 728 K, Philos. Mag. 95 (2015) 691–729.

[11] A. Orozco-Caballero, D. Lunt, J.D. Robson, J. Quinta da Fonseca, How magnesium accommodates local deformation incompatibility: A high-resolution digital image correlation study, Acta Mater. 133 (2017) 367–379.

[12] Z. Chen, S.H. Daly, Active slip system identification in polycrystalline metals by digital image correlation (DIC), Exp. Mech. 57 (2017) 115–127.

[13] M.H. Yoo, Slip, twinning, and fracture in hexagonal close-packed metals, Metall. Trans. A. 12 (1981) 409–418.

[14] L. Hu, S. Jiang, S. Liu, Y. Zhang, Y. Zhao, C. Zhao, Transformation twinning and deformation twinning of NiTi shape memory alloy, Mater. Sci. Eng. A. 660 (2016) 1–10.

[15] S. Xu, M. Gong, Y. Jiang, C. Schuman, J.S. Lecomte, J. Wang, Secondary twin variant selection in four types of double twins in titanium, Acta Mater. 152 (2018) 58–76.

[16] S. Xu, M. Gong, C. Schuman, J.-S. Lecomte, X. Xie, J. Wang, Sequential {10-12} twinning stimulated by other twins in titanium, Acta Mater. 132 (2017) 57–68.

[17] S. Xu, P. Zhou, G. Liu, D. Xiao, M. Gong, J. Wang, Shock-induced two types of {10-12} sequential twinning in Titanium, Acta Mater. 165 (2019) 547–560.

[18] S. Godet, L. Jiang, A.A. Luo, J.J. Jonas, Use of Schmid factors to select extension twin variants in extruded magnesium alloy tubes, Scr. Mater. 55 (2006) 1055–1058.

[19] S. Wang, C. Schuman, L. Bao, J.S. Lecomte, Y. Zhang, J.M. Raulot, M.J. Philippe, X. Zhao, C. Esling, Variant selection criterion for twin variants in titanium alloys deformed by rolling, Acta Mater. 60 (2012) 3912–3919.

[20] C. Schuman, L. Bao, J. Sébastien Lecomte, Y. Zhang, J. Marc Raulot, M. Jeanne Philippe, C. Esling, A new variant selection criterion for twin variants in titanium alloys (Part 1), Adv. Eng. Mater. 13 (2011) 1114–1121.

[21] C. Schuman, L. Bao, J.S. Lecomte, Y. Zhang, J.M. Raulot, M.J. Philippe, C. Esling, A new variant selection criterion for twin variants in titanium alloys (part 2), Adv. Eng. Mater. 14 (2012) 304–311.

[22] C.N. Tomé, X.F. Bi, Z. Zhang, J. Wang, A. Kumar, H.C. Wu, S.X. Mao, Rolling-induced Face Centered Cubic Titanium in Hexagonal Close Packed Titanium at Room Temperature, Sci. Rep. 6 (2016) 1–8.

[23] É. Martin, L. Capolungo, L. Jiang, J.J. Jonas, Variant selection during secondary twinning in Mg-3%Al, Acta Mater. 58 (2010) 3970–3983.

[24] J.J. Jonas, S. Mu, T. Al-Samman, G. Gottstein, L. Jiang, Ė. Martin, The role of strain accommodation during the variant selection of primary twins in magnesium, Acta Mater. 59 (2011) 2046–2056.

[25] S. Wang, Y. Zhang, C. Schuman, J.S. Lecomte, X. Zhao, L. Zuo, M.J. Philippe, C. Esling, Study of twinning/detwinning behaviors of Ti by interrupted in situ tensile tests, Acta Mater. 82 (2015) 424–436.

[26] I.J. Beyerlein, J. Wang, M.R. Barnett, C.N. Tomé, Double twinning mechanisms in magnesium alloys via dissociation of lattice dislocations, Proc. R. Soc. A Math. Phys. Eng. Sci. 468 (2012) 1496–1520.

[27] J.B. Hess, C.S. Barrett, Structure and nature of kink bands in zinc, JOM. 1 (1949) 599–606.

[28] K. Hagihara, T. Mayama, M. Honnami, M. Yamasaki, H. Izuno, T. Okamoto, T. Ohashi, T. Nakano, Y. Kawamura, Orientation dependence of the deformation kink band formation behavior in Zn single crystal, Int. J. Plast. 77 (2016) 174–191.

[29] T. Matsumoto, M. Yamasaki, K. Hagihara, Y. Kawamura, Configuration of dislocations in low-angle kink boundaries formed in a single crystalline long-period stacking ordered Mg-Zn-Y alloy, Acta Mater. 151 (2018) 112–124.

[30] S. Yamasaki, T. Tokuzumi, W. Li, M. Mitsuhara, K. Hagihara, T. Fujii, H. Nakashima, Kink Formation Process in Long-Period Stacking Ordered Mg-Zn-Y Alloy, Acta Mater. (2020).

[31] S. Jin, K. Marthinsen, Y. Li, Formation of {11-21} twin boundaries in titanium by kinking mechanism through accumulative dislocation slip, Acta Mater. 120 (2016) 403–414.

[32] M. Yamasaki, K. Hagihara, S.I. Inoue, J.P. Hadorn, Y. Kawamura, Crystallographic classification of kink bands in an extruded Mg-Zn-Y alloy using intragranular misorientation axis analysis, Acta Mater. 61 (2013) 2065–2076.

[33] L. Wang, J. Sabisch, E.T. Lilleodden, Kink formation and concomitant twin nucleation in Mg-Y, Scr. Mater. 111 (2016) 68–71.

[34] N.J. Lane, S.I. Simak, A.S. Mikhaylushkin, I.A. Abrikosov, L. Hultman, M.W. Barsoum, First-principles study of dislocations in hcp metals through the investigation of the {11-21} twin boundary, Phys. Rev. B. 84 (2011) 184101.

[35] P. Ehrlich, Solutions of oxygen in metallic titanium, Z. Anorg. u. Allgem. Chem. 247 (1941) 53–64.

[36] C. Domain, R. Besson, A. Legris, Atomic-scale Ab-initio study of the Zr-H system: I. Bulk properties, Acta Mater. 50 (2002) 3513–3526.

[37] R. Khoda-Bakhsh, D.K. Ross, Determination of the hydrogen site occupation in the α phase of zirconium hydride and in the α and β phases of titanium hydride by inelastic neutron scattering, J. Phys. F Met. Phys. 12 (1982) 15–24.

[38] D. Caillard, M. Gaumé, F. Onimus, Glide and cross-slip of a-dislocations in Zr and Ti, Acta Mater. 155 (2018) 23–34.

[39] J.P. Hirth, J. Lothe, Theory of dislocation, 1992.

[40] A.T. Churchman, The slip modes of titanium and the effect of purity on their occurrence during tensile deformation of single crystals, Proc. R. Soc. London. Ser. A. Math. Phys. Sci.

226 (1954) 216–226.

[41] Q. Yu, L. Qi, T. Tsuru, R. Traylor, D. Rugg, J.W. Morris, M. Asta, D.C. Chrzan, A.M. Minor, Origin of dramatic oxygen solute strengthening effect in titanium, Science (80-. ). 347 (2015) 635 LP – 639.

[42] A. de Crecy, A. Bourret, S. Naka, A. Lasalmonie, High resolution determination of the core structure of 1/3⟨1120⟩ {1010} edge dislocation in titanium, Philos. Mag. A. 47 (1983) 245–254.

[43] E. Clouet, D. Caillard, N. Chaari, F. Onimus, D. Rodney, Dislocation locking versus easy glide in titanium and zirconium, Nat. Mater. 14 (2015) 931–936.

[44] C. Domain, R. Besson, A. Legris, Atomic-scale ab initio study of the Zr–H system: II. Interaction of H with plane defects and mechanical properties, Acta Mater. 52 (2004) 1495–1502.

[45] N. Saini, C. Pandey, M.M. Mahapatra, Effect of diffusible hydrogen content on embrittlement of P92 steel, Int. J. Hydrogen Energy. 42 (2017) 17328–17338.

[46] R.P. Gangloff, Hydrogen assisted cracking of high strength alloys, Aluminum Co of America Alcoa Center Pa Alcoa Technical Center, 2003.

[47] C.J. McMahon, Hydrogen-induced intergranular fracture of steels, Eng. Fract. Mech. 68 (2001) 773–788.

[48] J. Venezuela, Q. Liu, M. Zhang, Q. Zhou, A. Atrens, The influence of hydrogen on the mechanical and fracture properties of some martensitic advanced high strength steels studied using the linearly increasing stress test, Corros. Sci. 99 (2015) 98–117.

[49] S.P. Lynch, Progress towards understanding mechanisms of hydrogen embrittlement and stress corrosion cracking, in: Corros. 2007, NACE International, 2007.

[50] S. Ramamurthy, A. Atrens, Stress corrosion cracking of high-strength steels, Corros. Rev. 31 (2013) 1–31.

[51] S.H. Zaferani, R. Miresmaeili, M.K. Pourcharmi, Mechanistic models for environmentally-assisted cracking in sour service, Eng. Fail. Anal. 79 (2017) 672–703.

[52] M. Koyama, C.C. Tasan, E. Akiyama, K. Tsuzaki, D. Raabe, Hydrogen-assisted decohesion and localized plasticity in dual-phase steel, Acta Mater. 70 (2014) 174–187.

[53] S. Thomas, N. Ott, R.F. Schaller, J.A. Yuwono, P. Volovitch, G. Sundararajan, N. V Medhekar, K. Ogle, J.R. Scully, N. Birbilis, The effect of absorbed hydrogen on the

dissolution of steel, Heliyon. 2 (2016) e00209.

[54] I.M. Robertson, P. Sofronis, A. Nagao, M.L. Martin, S. Wang, D.W. Gross, K.E. Nygren, Hydrogen Embrittlement Understood, Metall. Mater. Trans. A Phys. Metall. Mater. Sci. 46 (2015) 2323–2341.

[55] R.A. Oriani, Whitney Award Lecture—1987: Hydrogen—The Versatile Embrittler, CORROSION. 43 (1987) 390–397.

[56] H. Barthélémy, Effects of pressure and purity on the hydrogen embrittlement of steels, Int. J. Hydrogen Energy. 36 (2011) 2750–2758.

[57] T. Michler, J. Naumann, Hydrogen environment embrittlement of austenitic stainless steels at low temperatures, Int. J. Hydrogen Energy. 33 (2008) 2111–2122.

[58] L. Zhang, Z. Li, J. Zheng, Y. Zhao, P. Xu, C. Zhou, X. Li, Effect of strain-induced martensite on hydrogen embrittlement of austenitic stainless steels investigated by combined tension and hydrogen release methods, Int. J. Hydrogen Energy. 38 (2013) 8208–8214.

[59] C. Zhou, Y. Song, Q. Shi, S. Hu, J. Zheng, P. Xu, L. Zhang, Effect of pre-strain on hydrogen embrittlement of metastable austenitic stainless steel under different hydrogen conditions, Int. J. Hydrogen Energy. 44 (2019) 26036–26048.

[60] Y. Li, Y. Zhang, S. Han, Q. Wang, Research on the effect of aging time on the microstructure of 7055 aluminum alloy, Vacuum. 171 (2020) 108944.

[61] L. Huang, X. Hua, D. Wu, Z. Jiang, Y. Ye, A study on the metallurgical and mechanical properties of a GMAW-welded Al-Mg alloy with different plate thicknesses, J. Manuf. Process. 37 (2019) 438–445.

[62] Y. Han, S. Xue, R. Fu, P. Zhang, Effect of hydrogen content in ER5183 welding wire on the tensile strength and fracture morphology of Al–Mg MIG weld, Vacuum. 166 (2019) 218–225.

[63] K.R. Hebert, Trapping of hydrogen absorbed in aluminum during corrosion, Electrochim. Acta. 168 (2015) 199–205.

[64] R.S. Daum, D.W. Bates, D.A. Koss, A.T. Motta, The influence of a hydride layer on the fracture of zircaloy-4 cladding tubes, Argonne National Lab., IL (US), 2002.

[65] C.E. Ells, Hydride precipitates in zirconium alloys (A review), J. Nucl. Mater. 28 (1968) 129–151.

[66] A.T. Motta, L.-Q. Chen, Hydride formation in zirconium alloys, Jom. 64 (2012) 1403–1408.

[67] A.C. Wallace, G.K. Shek, O.E. Lepik, Effects of hydride morphology on Zr-2.5 Nb fracture toughness, in: Zircon. Nucl. Ind. Eighth Int. Symp., ASTM International, 1989.

[68] P.H. Davies, C.P. Stearns, Fracture toughness testing of Zircaloy-2 pressure tube material with radial hydrides using direct-current potential drop, in: Fract. Mech. Seventeenth Vol., ASTM International, 1986.

[69] B. Cox, Environmentally-induced cracking of zirconium alloys - A review, J. Nucl. Mater. 170 (1990) 1–23.

[70] M. Blat, L. Legras, D. Noel, H. Amanrich, Contribution to a better understanding of the detrimental role of hydrogen on the corrosion rate of Zircaloy-4 cladding materials, in: Zircon. Nucl. Ind. Twelfth Int. Symp., ASTM International, 2000.

[71] A.M. Garde, G.P. Smith, R.C. Pirek, Effects of hydride precipitate localization and neutron fluence on the ductility of irradiated Zircaloy-4, in: Zircon. Nucl. Ind. Elev. Int. Symp., ASTM International, 1996.

[72] O.N. Pierron, D.A. Koss, A.T. Motta, K.S. Chan, The influence of hydride blisters on the fracture of Zircaloy-4, J. Nucl. Mater. 322 (2003) 21–35.

[73] R.S. Daum, S. Majumdar, M.C. Billone, Mechanical properties of irradiated Zircaloy-4 for dry cask storage conditions and accidents, in: 2003 Nucl. Saf. Res. Conf. Washington, DC, 2003: pp. 85–96.

[74] R.S. Daum, S. Majumdar, Y. Liu, M.C. Billone, Radial-hydride embrittlement of high-burnup Zircaloy-4 fuel cladding, J. Nucl. Sci. Technol. 43 (2006) 1054–1067.

[75] N.A. Chapman, B. Côme, Natural Analogues in Radioactive Waste Disposal, Graham & Trotman, 1987.

[76] Q. Zhang, M. Zheng, Y. Huang, H.J. Kunte, X. Wang, Y. Liu, C. Zheng, Long term corrosion estimation of carbon steel, titanium and its alloy in backfill material of compacted bentonite for nuclear waste repository, Sci. Rep. 9 (2019) 1–18.

[77] F. Hua, K. Mon, P. Pasupathi, G. Gordon, D. Shoesmith, A review of corrosion of titanium grade 7 and other titanium alloys in nuclear waste repository environments, Corrosion. 61 (2005) 987–1003.

[78] R.W. Schutz, Corrosion of titanium and titanium alloys;(ASMI Handbook Committee, Met. Handbook, Corros. 13 (1987) 669–706.

[79] M.H.O. Könönen, E.T. Lavonius, J.K. Kivilahti, SEM observations on stress corrosion

cracking of commercially pure titanium in a topical fluoride solution, Dent. Mater. 11 (1995) 269–272.

[80] D.S. Shih, I.M. Robertson, H.K. Birnbaum, Hydrogen embrittlement of alpha titanium : in situ TEM studies, Acta Metall. 36 (1988) 111–124.

[81] M. Kappes, M. Iannuzzi, R.M. Carranza, Hydrogen Embrittlement of Magnesium and Magnesium Alloys: A Review, J. Electrochem. Soc. 160 (2013) C168–C178.

[82] J. Song, W.A. Curtin, Atomic mechanism and prediction of hydrogen embrittlement in iron, Nat. Mater. 12 (2013) 145–151.

[83] P.K. Pradhan, P.S. Robi, S.K. Roy, Micro void coalescence of ductile fracture in mild steel during tensile straining, Frat. Ed Integrità Strutt. 6 (2012).

[84] J. Venezuela, Q. Zhou, Q. Liu, H. Li, M. Zhang, M.S. Dargusch, A. Atrens, The influence of microstructure on the hydrogen embrittlement susceptibility of martensitic advanced high strength steels, Mater. Today Commun. 17 (2018) 1–14.

[85] F. Yunchang, D.A. Koss, The influence of multiaxial states of stress on the hydrogen embrittlement of zirconium alloy sheet, Metall. Trans. A. 16 (1985) 675–681.

[86] J. Huez, A.L. Helbert, X. Feaugas, I. Guillot, M. Clavel, Damage process in commercially pure α-titanium alloy without (Ti40) and with (Ti40-H) hydrides, Metall. Mater. Trans. A. 29 (1998) 1615–1628.

[87] H.K. Birnbaum, Mechanical properties of metal hydrides, J. Less-Common Met. 104 (1984) 31–41.

[88] I.M. Robertson, T. Tabata, W. Wei, F. Heubaum, H.K. Birnbaum, Hydrogen embrittlement and grain boundary fracture, Scr. Metall. 18 (1984) 841–846.

[89] D.O. Northwood, U. Kosasih, Hydrides and delayed hydrogen cracking in zirconium and its alloys, Int. Met. Rev. 28 (1983) 92–121.

[90] S. Banerjee, P.B.T.-P.M.S. Mukhopadhyay, eds., Chapter 8 - Interstitial Ordering, in: Phase Transform., Pergamon, 2007: pp. 717–781.

[91] E. Conforto, D. Caillard, A fast method for determining favourable orientation relationships and interface planes: Application to titanium-titanium hydrides transformations, Acta Mater. 55 (2007) 785–798.

[92] A. Bourret, A. Lasalmonie, S. Naka, In-situ high resolution observation of hydride precipitation in titanium, Scr. Metall. 20 (1986) 861–866.

[93] H. Numakura, M. Koiwa, Hydride precipitation in titanium, Acta Metall. 32 (1984) 1799–1807.

[94] E. Conforto, D. Caillard, Edge-to-edge matching at Ti-TiH interfaces: kinetics of hydride growth and clustering of precipitates with different orientation relationships, Solid State Phenom. 172–174 (2011) 242–247.

[95] O.T. Woo, G.C. Weatherly, C.E. Coleman, R.W. Gilbert, The precipitation of γ-deuterides (hydrides) in titanium, Acta Metall. 33 (1985) 1897–1906.

[96] J. Bair, M. Asle Zaeem, D. Schwen, Formation path of δ hydrides in zirconium by multiphase field modeling, Acta Mater. 123 (2017) 235–244.

[97] K.G. Barraclough, C.J. Beevers, Some observations on the phase transformations in zirconium hydrides, J. Nucl. Mater. 34 (1970) 125–134.

[98] A. Aladjem, Zirconium-Hydrogen, Solid State Phenom. 49–50 (1996) 281–330.

[99] Z. Zhao, Z. Zhao, M. Blat-Yrieix, J.-. Morniroli, A. Legris, L. Thuinet, Y. Kihn, A. Ambard, L. Legras, Characterization of Zirconium Hydrides and Phase Field Approach to a Mesoscopic-Scale Modeling of Their Precipitation, in: B. Kammenzind, M. Limbäck (Eds.), Zircon. Nucl. Ind. 15th Int. Symp., ASTM International, West Conshohocken, PA, 2009: pp. 29–50.

[100] G.C. Weatherly, The precipitation of γ-hydride plates in zirconium, Acta Metall. 29 (1981) 501–512.

[101] J. Wen, N. Allain, E. Fleury, Determination of orientation relationships between FCC-hydride and HCP-titanium and their correlation with hydrides distribution, J. Alloys Compd. 817 (2020) 153297.

[102] I. Guillot, X. Feaugas, M. Clavel, Dislocation-hydride interactions at low plastic strain in titanium, Scr. Mater. 44 (2001) 1011–1017.

[103] G.J.C Carpenter, The precipitation of γ-hydride plates in zirconium, Acta Metall. 29 (1978) 501.

[104] G.M. Han, Y.F. Zhao, C.B. Zhou, D.Y. Lin, X.Y. Zhu, J. Zhang, S.Y. Hu, H.F. Song, Phase-field modeling of stacking structure formation and transition of δ-hydride precipitates in zirconium, Acta Mater. 165 (2019) 528–546.

[105] F. Long, D. Kerr, G. Domizzi, Q. Wang, M.R. Daymond, Microstructure characterization of a hydride blister in Zircaloy-4 by EBSD and TEM, Acta Mater. 129 (2017) 450–461.

[106] T.W. Heo, K.B. Colas, A.T. Motta, L.Q. Chen, A phase-field model for hydride formation in polycrystalline metals: Application to δ-hydride in zirconium alloys, Acta Mater. 181 (2019) 262–277.

[107] S. Wang, F. Giuliani, T. Ben Britton, Microstructure and formation mechanisms of δ-hydrides in variable grain size Zircaloy-4 studied by electron backscatter diffraction, Acta Mater. 169 (2019) 76–87.

[108] C.M. Silva, F. Ibrahim, E.G. Lindquist, J.W. McMurray, C.D. Bryan, Brittle nature and the related effects of zirconium hydrides in Zircaloy-4, Mater. Sci. Eng. A. 767 (2019) 138396.

[109] W. Qin, N.A.P. Kiran Kumar, J.A. Szpunar, J. Kozinski, Intergranular δ-hydride nucleation and orientation in zirconium alloys, Acta Mater. 59 (2011) 7010–7021.

[110] R.K. Sharma, S. Sunil, B.K. Kumawat, R.N. Singh, A. Tewari, B.P. Kashyap, Influence of hydride orientation on fracture toughness of CWSR Zr-2.5%Nb pressure tube material between RT and 300 °C, J. Nucl. Mater. 488 (2017) 231–244.

[111] M.I. Luppo, A. Politi, G. Vigna, Hydrides in α-Ti: Characterization and effect of applied external stresses, Acta Mater. 53 (2005) 4987–4996.

[112] Y. Udagawa, M. Yamaguchi, H. Abe, N. Sekimura, T. Fuketa, Ab initio study on plane defects in zirconium–hydrogen solid solution and zirconium hydride, Acta Mater. 58 (2010) 3927–3938.

[113] K. Tougou, T. Onitsuka, K. Fukumoto, M. Uno, H. Muta, The study of hardening evaluation of pure Zr with δ-hydrides generation by the dynamic in-situ metallic structure observation and nano-indentation hardness test, J. Nucl. Mater. 511 (2018) 284–296.

[114] I. Guillot, X. Feaugas, M. Clavel, Dislocation-hydride interactions at low plastic strain in titanium, Scr. Mater. 44 (2001) 1011–1017.

[115] C.Q. Chen, S.X. Li, K. Lu, The deformation behaviors of gamma hydrides in titanium under cyclic straining, Acta Mater. 51 (2003) 931–942.

[116] C.Q. Chen, S.X. Li, Tensile and low-cycle fatigue behaviors of commercially pure titanium containing γ hydrides, Mater. Sci. Eng. A. 387–389 (2004) 470–475.

[117] C.Q. Chen, S.X. Li, K. Lu, Dislocation interaction with hydrides in titanium containing a low hydrogen concentration, Philos. Mag. 84 (2004) 29–43.

[118] C.Q. Chen, S.X. Li, H. Zheng, L.B. Wang, K. Lu, An investigation on structure, deformation and fracture of hydrides in titanium with a large range of hydrogen contents, Acta Mater. 52

(2004) 3697–3706.

[119] J. Wen, N. Allain, E. Fleury, Hydrogen evolution and its effects on cold rolling behavior in commercial pure titanium, Mater. Charact. 121 (2016) 139–148.

[120] J. Wen, N. Main, E. Fleury, The effect of hydrogen-deformation interactions on recrystallization of β-21S titanium alloys, Proc. 13th World Conf. Titan. (2016) 275–280.

[121] Y.Z. Chen, H.P. Barth, M. Deutges, C. Borchers, F. Liu, R. Kirchheim, Increase in dislocation density in cold-deformed Pd using H as a temporary alloying addition, Scr. Mater. 68 (2013) 743–746.

[122] G.M. Pharr, A. Bolshakov, Understanding nanoindentation unloading curves, J. Mater. Res. 17 (2002) 2660–2671.

[123] G.M. Pharr, W.C. Oliver, F.R. Brotzen, On the generality of the relationship among contact stiffness, contact area, and elastic modulus during indentation, J. Mater. Res. 7 (1992) 613–617.

[124] B. Taljat, G.M. Pharr, Development of Pile-up During Spherical Indentation of Elastic-Plastic Solids, Int. J. Solids Struct. - INT J SOLIDS STRUCT. 41 (2004).

[125] M.Y. N'jock, D. Chicot, J.M. Ndjaka, J. Lesage, X. Decoopman, F. Roudet, A. Mejias, A criterion to identify sinking-in and piling-up in indentation of materials, Int. J. Mech. Sci. 90 (2015) 145–150.

[126] A.E. Giannakopoulos, S. Suresh, Determination of elastoplastic properties by instrumented sharp indentation, Scr. Mater. 40 (1999) 1191–1198.

[127] W.C. Oliver, G.M. Pharr, Measurement of hardness and elastic modulus by instrumented indentation: Advances in understanding and refinements to methodology, J. Mater. Res. 19 (2004) 3–20.

[128] G. Hochstetter, A. Jimenez, J.L. Loubet, Strain-rate effects on hardness of glassy polymers in the nanoscale range. Comparison between quasi-static and continuous stiffness measurements, J. Macromol. Sci. 38 (1999) 681–692.

[129] G. Constantinides, K.S. Ravi Chandran, F.-J. Ulm, K.J. Van Vliet, Grid indentation analysis of composite microstructure and mechanics: Principles and validation, Mater. Sci. Eng. A. 430 (2006) 189–202.

[130] B. Rother, H.A. Jehn, Coating and interface characterization by depth-sensing indentation experiments, Surf. Coatings Technol. 85 (1996) 183–188.

[131] B. Beausir and J.-J. Fundenberger, Analysis tools for electron and X-ray diffraction, ATEX - software, Université de Lorraine - Metz, 2017.

[132] A.G. Khachaturyan, Theory of Structural Transformations in Solids John Wiley & Sons Inc, New York. (1983).

[133] L. Euler, Formvlae generales pro translatione qvacvnqvve corporvm rigidor, Novi Comment. Acad. Sci. Petropolitanae. 20 (1776) 189–207.

[134] H.J. Bunge, C. Esling, J. Muller, The role of the inversion centre in texture analysis, J. Appl. Crystallogr. 13 (1980) 544–554.

[135] H.J. Bunge, C. Esling, J. Muller, The influence of crystal and sample symmetries on the orientation distribution function of the crystallites in polycrystalline materials, Acta Crystallogr. Sect. A Cryst. Physics, Diffraction, Theor. Gen. Crystallogr. 37 (1981) 889–899.

[136] S.I. Wright, M.M. Nowell, S.P. Lindeman, P.P. Camus, M. De Graef, M.A. Jackson, Introduction and comparison of new EBSD post-processing methodologies, Ultramicroscopy. 159 (2015) 81–94.

[137] G.J.C. Carpenter, The dilatational misfit of zirconium hydrides precipitated in zirconium, J. Nucl. Mater. 48 (1973) 264–266.

[138] Q. Wang, S. Xu, J.S. Lecomte, C. Schuman, L. Peltier, X. Shen, W. Song, Crystallographic orientation dependence of hydride precipitation in commercial pure titanium, Acta Mater. 183 (2020) 329–339.

[139] M.A. Rodríguez, Anticipated degradation modes of metallic engineered barriers for high-level nuclear waste repositories, JOM. 66 (2014) 503–525.

[140] J.S. Bradbrook, G.W. Lorimer, N. Ridley, The precipitation of zirconium hydride in zirconium and zircaloy-2, J. Nucl. Mater. 42 (1972) 142–160.

[141] V. Perovic, G.C. Weatherly, C.J. Simpson, Hydride precipitation in α/β zirconium alloys, Acta Metall. 31 (1983) 1381–1391.

[142] Y.J. Li, Y.J. Chen, J.C. Walmsley, R.H. Mathinsen, S. Dumoulin, H.J. Roven, Faceted interfacial structure of $\{10\bar{1}1\}$ twins in Ti formed during equal channel angular pressing, Scr. Mater. 62 (2010) 443–446.

[143] D.H. Shin, I. Kim, J. Kim, Y.S. Kim, S.L. Semiatin, Microstructure development during equal-channel angular pressing of titanium, Acta Mater. 51 (2003) 983–996.

[144] M.A. Kumar, I.J. Beyerlein, R.J. Mccabe, C.N. Tome, Grain neighbour effects on twin transmission in hexagonal close-packed materials, Nat. Commun. 7.1 (2016) 1–9.

[145] L. Wang, R.I. Barabash, Y. Yang, T.R. Bieler, M.A. Crimp, P. Eisenlohr, W. Liu, G.E. Ice, Experimental Characterization and Crystal Plasticity Modeling of Heterogeneous Deformation in Polycrystalline α-Ti, Metall. Mater. Trans. A. 42 (2011) 626–635.

[146] G.M. Hommer, A.L. Pilchak, A.P. Stebner, Normalized resolved shear stress calculations for single crystals subjected to multiaxial loading, Materialia. 2 (2018) 53–57.

[147] S. Yamanaka, K. Yoshioka, M. Uno, M. Katsura, H. Anada, T. Matsuda, S. Kobayashi, Isotope effects on the physicochemical properties of zirconium hydride, J. Alloys Compd. 293 (1999) 908–914.

[148] E. Conforto, B.-O. Aronsson, A. Salito, C. Crestou, D. Caillard, Rough surfaces of titanium and titanium alloys for implants and prostheses, Mater. Sci. Eng. C. 24 (2004) 611–618.

[149] E. Conforto, D. Caillard, B.-O. Aronsson, P. Descouts, Crystallographic properties and mechanical behaviour of titanium hydride layers grown on titanium implants, Philos. Mag. 84 (2004) 631–645.

[150] C. Fizanne-Michel, M. Cornen, P. Castany, I. Péron, T. Gloriant, Determination of hardness and elastic modulus inverse pole figures of a polycrystalline commercially pure titanium by coupling nanoindentation and EBSD techniques, Mater. Sci. Eng. A. 613 (2014) 159–162.

[151] H. Somekawa, T. Mukai, Nanoindentation creep behavior of grain boundary in pure magnesium, Philos. Mag. Lett. 90 (2010) 883–890.

[152] J.J. Xu, H.Y. Cheung, S.Q. Shi, Mechanical properties of titanium hydride, J. Alloys Compd. 436 (2007) 82–85.

[153] D. Setoyama, J. Matsunaga, H. Muta, M. Uno, S. Yamanaka, Mechanical properties of titanium hydride, J. Alloys Compd. 381 (2004) 215–220.

[154] S.-Q. Shi, M.P. Puls, Fracture strength of hydride precipitates in Zr–2.5 Nb alloys, J. Nucl. Mater. 275 (1999) 312–317.

[155] F.C.S. Carvalho, J.F. Labuz, Experiments on effective elastic modulus of two-dimensional solids with cracks and holes, Int. J. Solids Struct. 33 (1996) 4119–4130.

[156] J.S. Weaver, M.W. Priddy, D.L. McDowell, S.R. Kalidindi, On capturing the grain-scale elastic and plastic anisotropy of alpha-Ti with spherical nanoindentation and electron back-scattered diffraction, Acta Mater. 117 (2016) 23–34.

[157] G.B. Viswanathan, E. Lee, D.M. Maher, S. Banerjee, H.L. Fraser, Direct observations and analyses of dislocation substructures in the α phase of an α/β Ti-alloy formed by nanoindentation, Acta Mater. 53 (2005) 5101–5115.

[158] K.E.K. Amouzou, T. Richeton, A. Roth, M.A. Lebyodkin, T.A. Lebedkina, Micromechanical modeling of hardening mechanisms in commercially pure α-titanium in tensile condition, Int. J. Plast. 80 (2016) 222–240.

[159] S. Pathak, S.R. Kalidindi, N.A. Mara, Investigations of orientation and length scale effects on micromechanical responses in polycrystalline zirconium using spherical nanoindentation, Scr. Mater. 113 (2016) 241–245.

[160] K. Wang, Z. Yan, Y. Zhou, S. Wei, X. Wang, R. Xin, Q. Liu, Slip initiation in interlayered β and corresponding slip transfer during compression of a lamellar-structure titanium alloy, Results Phys. 18 (2020) 103276.

[161] H. Qin, J.J. Jonas, H. Yu, N. Brodusch, R. Gauvin, X. Zhang, Initiation and accommodation of primary twins in high-purity titanium, Acta Mater. 71 (2014) 293–305.

[162] H. Lee, K. Kim, J.-S. Kim, Y.-S. Kim, Effects of hydride precipitation on the mechanical property of cold worked zirconium alloys in fully recrystallized condition, Nucl. Eng. Technol. 52 (2020) 352–359.

# Publication List

1. **Qian Wang**, Shun Xu, Jean-Sébastien Lecomte, et al. Crystallographic orientation dependence of hydride precipitation in commercial pure titanium. Acta Materialia, 183 (2020) 329–339.
2. **Qian Wang**, Jean-Sébastien Lecomte, Christophe Schuman, et al. The mechanical property evolution and grain boundary accommodation during hydride transformation in commercial pure titanium. Accepted.
3. **Qian Wang**, Jean-Sébastien Lecomte, Christophe Schuman, et al. Microstructure evolution of commercial pure titanium during interrupted in-situ tensile. Accepted.
4. **Qian Wang**, Jean-Sébastien Lecomte, Christophe Schuman, et al. Multi-dimensional morphology of hydride diffusion layer and associated sequential twinning in commercial pure titanium. Under review.

# Appendix

**Matlab script for Fig. 3.4b (OR1 hydride):**

```
a_alpha=0.295;b_alpha=0.295;c_alpha=0.468;
a_gamma=0.420;c_gamma=0.470;
a_delta=0.440;
sq2=sqrt(2);sq3=sqrt(3);sq6=sqrt(6);
% lattice dilatation from HCP Ti to FCT hydride
r1=sq6*a_gamma/3/a_alpha;r2=sq2*a_gamma/2/a_alpha;r3=c_gamma/c_alpha;
M1=[r1 0 0;0 r2 0;0 0 r3];
% lattice dilatation from FCT to FCC hydride
s1=a_delta/a_gamma;s2=a_delta/a_gamma;s3=a_delta/c_gamma;
M2=[s1 0 0;0 s2 0;0 0 s3];
% calculate deformation gradient tensor
F2=M2*M1;
disp('deformation gradient tensors in hydride frame');
disp(F2);
IN=[1 0 -1 0;0 1 -1 0;-1 1 0 0];% interface normal
for i=1:3
    in=IN(i,:);
    E_T_H=[sqrt(3)/2 0 0;-1/2 1 0;0 0 c_alpha/a_alpha];%miller to crystal frame, a2//-12-10
    M43_uvtw=[2 1 0 0;1 2 0 0;0 0 0 1]; %4-index to 3-index
    in=E_T_H*M43_uvtw*in';
    x=in./norm(in);
    z=[0 0 1]';
    y=cross(z,x);
    Rhc=[x y z];
    FP{i}=inv(Rhc)*F2*Rhc;
end
disp('deformation gradient tensors of six OR2 variants');
celldisp(FP);
% calculate misfit strain of P1 variant
CS = crystalSymmetry('6/mmm', [a_alpha b_alpha c_alpha], 'X||a*', 'Y||b', 'Z||c', 'mineral', 'Ti-Hex',
'color', 'light blue');
sR = CS.fundamentalRegion;
h = Miller (plotS2Grid( sR,'resolution', 2.5*degree), CS);
x=vector3d(h);
[m,n]=size(x);
x2=[];
f=[];
for i=1:m
   for j=1:n
      x1(1)=x(i,j).x;x1(2)=x(i,j).y;x1(3)=x(i,j).z;
      x2=FP{1}*x1';
      f(:,1)=(norm(x2)-norm(x1))/norm(x1)*100;
      max(f);
```

```
        eps(i,j)=max(f);
    end
end
maxvalue1=max(max(eps));
minvalue1=min(min(eps));
disp('max strain value of P1 variant (%)');
disp(maxvalue1);
disp('min strain value of P1 variant (%)');
disp(minvalue1);
% draw IPF of P1 variant
figure
hold on
contourf(h,eps,'antipodal');
hold on
annotate([Miller(0,0,0,-1,CS,'UVTW'),Miller(-1,2,-1,0,CS,'UVTW'),Miller(1,0,-
1,0,CS,'UVTW')],'all','symmetrised','labeled','BackgroundColor','w')
colorbar
caxis([-5 21]);
hold off
drawNow(gcm,'figSize','normal');
outputFile = ['OR1 strain IPF of variant 1.jpg'];
saveas(gcf,outputFile);
% calculate misfit strain of three OR1 variants
sR = CS.fundamentalRegion
h = Miller (plotS2Grid( sR,'resolution', 2.5*degree), CS)
x=vector3d(h)
[m,n]=size(x);
x2=[];
f=[];
   for i=1:m
      for j=1:n
         x1(1)=x(i,j).x;x1(2)=x(i,j).y;x1(3)=x(i,j).z;
         for s=1:3
         x2=FP{s}*x1';
         f(:,s)=(norm(x2)-norm(x1))/norm(x1)*100;
         end
      max(f);
      eps(i,j)=max(f);
       end
   end
maxvalue3=max(max(eps));
minvalue3=min(min(eps));
disp('max strain value of six variants (%)');
disp(maxvalue3);
disp('min strain value of six variants (%)');
disp(minvalue3);
% draw IPF of three OR1 variants
```

```
figure
hold on
contourf(h,eps,'antipodal');
hold on
annotate([Miller(0,0,0,-1,CS,'UVTW'),Miller(-1,2,-1,0,CS,'UVTW'),Miller(1,0,-
1,0,CS,'UVTW')],'all','symmetrised','labeled','BackgroundColor','w')
colorbar
caxis([-5 22]);
hold off
drawNow(gcm,'figSize','normal');
outputFile = ['OR1 strain IPF of three variants.jpg'];
saveas(gcf,outputFile);
```

**Matlab script for Fig. 3.4d (OR2 hydride):**

```
a_alpha=0.295;b_alpha=0.295;c_alpha=0.468;
a_gamma=0.420;c_gamma=0.470;
a_delta=0.440;
sq2=sqrt(2);sq3=sqrt(3);sq6=sqrt(6);
I=eye(3);
% structure transformation from HCP to FCT/FCC
p0=[0 0 1];
d0=[1 0 0]';
n=a_alpha/sq3/c_alpha;
S=I+n*d0*p0;
% lattice dilatation from HCP Ti to FCT hydride
dax=sq3*a_alpha;day=a_alpha;daz=c_alpha;
dgx=sqrt(a_gamma^2/2+c_gamma^2);dgy=a_gamma/sq2;dgz=2*sqrt(2*a_gamma^2+c_gamma^
2)/3;
r1=dgx/dax;r2=dgy/day;r3=dgz/daz;
M1=[r1 0 0;0 r1 0;0 0 r2];
% transformation from FCT to FCC hydride
ddx=sq6*a_delta/2;ddy=a_delta/sq2;ddz=2*a_delta/sq3;
s1=ddx/dgx;s2=ddy/dgy;s3=ddz/dgz;
M2=[s1 0 0;0 s1 0;0 0 s2];
% calculate deformation gradient tensor
F1=M2*M1*S;
disp('deformation gradient tensors in hydride frame');
disp(F1);
SD=[1 0 -1 0;0 1 -1 0;-1 1 0 0;-1 0 1 0;0 -1 1 0;1 -1 0 0];%shear direction
for i=1:6
    sd=SD(i,:);
    E_T_H=[sqrt(3)/2 0 0;-1/2 1 0;0 0 c_alpha/a_alpha];%miller to crystal frame, a2//-12-10
    M43_uvtw=[2 1 0 0;1 2 0 0;0 0 0 1]; %4-index to 3-index
    sd=E_T_H*M43_uvtw*sd';
    x=sd./norm(sd);
```

```
    z=[0 0 1]';
    y=cross(z,x);
    Rhc=[x y z];
    FB{i}=inv(Rhc)*F1*Rhc;
end
disp('deformation gradient tensors of six OR2 variants');
celldisp(FB);
% calculate misfit strain of variant 1
CS = crystalSymmetry('6/mmm', [a_alpha b_alpha c_alpha], 'X||a*', 'Y||b', 'Z||c', 'mineral', 'Ti-Hex',
'color', 'light blue');
sR = CS.fundamentalRegion;
h = Miller(plotS2Grid(sR,'resolution',2.5*degree),CS);
x=vector3d(h);
[m,n]=size(x);
x2=[];
f=[];
for i=1:m
   for j=1:n
       x1(1)=x(i,j).x;x1(2)=x(i,j).y;x1(3)=x(i,j).z;
       x2=FB{1}*x1';
       f(:,1)=(norm(x2)-norm(x1))/norm(x1)*100;
       max(f);
       eps(i,j)=max(f);
    end
end
maxvalue1=max(max(eps));
minvalue1=min(min(eps));
disp('max strain of B1 variant (%)');
disp(maxvalue1);
disp('min strain of B1 variant (%)');
disp(minvalue1);
% draw IPF of B1 variant
figure
hold on
contourf(h,eps,'antipodal');
hold on
plot(Miller(1,0,-1,3,CS),'labeled','grid','backgroundcolor','w');
hold on
annotate([Miller(0,0,0,-1,CS,'UVTW'),Miller(-1,2,-1,0,CS,'UVTW'),Miller(1,0,-
1,0,CS,'UVTW')],'all','symmetrised','labeled','BackgroundColor','w')
colorbar
caxis([-10 28]);
hold off
drawNow(gcm,'figSize','normal');
outputFile = ['OR2 strain IPF of variant 1.jpg'];
saveas(gcf,outputFile);
% calculate misfit strain of six variants
```

```
sR = CS.fundamentalRegion;
h = Miller(plotS2Grid(sR,'resolution',2.5*degree),CS);
x=vector3d(h);
[m,n]=size(x);
x2=[];
f=[];
for i=1:m
    for j=1:n
        x1(1)=x(i,j).x;x1(2)=x(i,j).y;x1(3)=x(i,j).z;
        for s=1:6
            x2=FB{s}*x1';
            f(:,s)=(norm(x2)-norm(x1))/norm(x1)*100;
        end
        max(f);
        eps(i,j)=max(f);
    end
end
maxvalue6=max(max(eps));
minvalue6=min(min(eps));
disp('max strain of six variants (%)');
disp(maxvalue6);
disp('min strain of six variants (%)');
disp(minvalue6);
% draw IPF of six OR2 variants
figure
hold on
contourf(h,eps,'antipodal');
hold on
K=Miller({1,0,-1,3},{0,1,-1,3},{-1,1,0,3},{-1,0,1,3},{0,-1,1,3},{1,-1,0,3},CS);
plot(K,'labeled','grid','backgroundcolor','w');
hold on
annotate([Miller(0,0,0,-1,CS,'UVTW'),Miller(-1,2,-1,0,CS,'UVTW'),Miller(1,0,-
1,0,CS,'UVTW')],'all','symmetrised','labeled','BackgroundColor','w')
colorbar
caxis([-10 28]);
hold off
drawNow(gcm,'figSize','normal');
outputFile = ['OR2 strain IPF of six variants.jpg'];
saveas(gcf,outputFile);
```